

Universidade de São Paulo
Instituto de Astronomia, Geofísica e Ciências Atmosféricas
Departamento de Astronomia

Marina Trevisan

**Formação e Evolução de Galáxias: Populações
Estelares na Via Láctea, Galáxias Elípticas e
Propriedades de Galáxias em Grupos.**

São Paulo

2012

Marina Trevisan

**Formação e Evolução de Galáxias: Populações
Estelares na Via Láctea, Galáxias Elípticas e
Propriedades de Galáxias em Grupos.**

Thesis presented in partial fulfillment of the requirements for the degree of Doctor in Sciences at the University of São Paulo, Institute of Astronomy, Geophysics and Atmospheric Sciences, Department of Astronomy.

Research field: Astronomy

Advisor: Prof.^a Dr.^a Beatriz Barbuy

São Paulo

2012

To Clara

Acknowledgments

I would like to thank my supervisor, Beatriz Barbuy, whose expertise and support made this thesis possible. Her dedication has always inspired me to never give up.

I am truly indebted and thankful to Reinaldo de Carvalho. Although he has never formally been my supervisor, his advise, encouragement and support have been present since the very beginning of my enterprise in Astronomy.

I would like to show my gratitude to Ignacio Ferreras for accepting me at University College London. Always armed with insightful comments, he made six months spent in London worth much longer.

I am grateful to Ignacio de la Rosa, Francesco la Barbera, Kjell Eriksson, Bengt Gustafsson, André Ribeiro and Paulo Lopes for the insightful discussions and all the knowlegde shared.

I would like to acknowledge the financial support from FAPESP, under the fellowship number 2008/50198-3.

Very special friends were present during these years. I would like to thank Camilla Danielski, Linda Cremonesi, and Barbara Grasso, for the great time during my experience in London. Thanks for Bruno Dias, for his support, friendship and our endless discussions about everything. I would like to thank my family for their eternal support. Iracema and Olívio; my parents and stepparents, Maria, Gilberto, Hamilton and Rosana; my brothers, Júlio, Gustavo, Miltinho, and Antônio, and my sister, Gabi. A special thanks for all of them. Last but not least, I wish to thank Fábio, who in difficult times was always there to remind me that it all worth it.

Resumo

Entender como as galáxias se formam e evoluem ao longo do tempo é um dos maiores desafios da cosmologia moderna. Vários processos estão presentes na formação de galáxias, tais como o *feedback* de supernovas e núcleos galácticos ativos, evolução química e dinâmica, e também efeitos ambientais. Esta tese abrange estes processos, a partir de um ponto de vista observacional. A Via Láctea tem um papel fundamental na compreensão dos vários processos envolvidos na formação de uma galáxia, e começamos nosso projeto estudando nossa própria galáxia. Diferentes processos deixam assinaturas típicas na distribuição de velocidades e metalicidades das estrelas. Por esta razão, combinando cinemática e abundâncias químicas, foi possível determinar a origem de uma amostra de estrelas velhas e ricas em metais. Compreender como e onde essas estrelas se formaram está intimamente relacionado com mecanismos presentes na evolução do disco Galáctico. Apesar de não podermos observar estrelas individuais em galáxias distantes, somos capazes de inferir a história de formação destas galáxias combinando modelos de população estelar simples, de forma a reproduzir o espectro observado. Usando esta metodologia, foi possível traçar a história de formação estelar de galáxias elípticas, e dessa forma restringir os mecanismos de *feedback* que regulam a formação de estrelas em halos. No cenário Λ CDM, as estruturas menores são formadas primeiro, e então elas se agrupam, formando assim estruturas cada vez maiores. As galáxias, ao serem incorporadas à sistemas maiores, sofrem os efeitos de diversos processos que atuam em ambientes de alta densidade, mudando assim suas propriedades. Desta forma, a evolução das galáxias e a formação de estruturas em grande escala andam lado a lado, como mostramos em nosso estudo de propriedades de galáxias em grupos. Exploramos a distribuição espacial das galáxias na vizinhança de grupos, e também usamos a distribuição de velocidades das galáxias para determinar o estágio evolutivo do grupo. Foram encontradas correlações importantes entre o estágio evolutivo do grupo e as populações de galáxias

que nestes residem.

Abstract

Understanding the way galaxies form and evolve throughout the cosmic time remains one of the greatest challenges of modern cosmology. Several processes are known to play a role in the formation of galaxies, such as feedback de supernovae and active galactic nuclei, chemical and dynamical evolution and environmental effects. This thesis encompasses these processes, from an observational point of view. The Milky Way plays a pivotal role in understanding the various processes involved in the formation of a galaxy, and we start our understanding program by studying our own Galaxy. Different formation processes leave typical signatures in the velocity and metallicity distribution of stars. For this reason, we were able to trace the origin of old and metal-rich stars by combining their kinematics and chemical abundances. Understanding how and where these stars were formed is closely related to mechanisms driving the evolution of the Galactic disk. Although we cannot observe individual stars in distant galaxies, only the integrated spectra, we are able to infer the mass assembly history of galaxies by combining single stellar population (SSP) models that reproduce the observed spectrum. Using this methodology, we traced the star formation history of elliptical galaxies and, by studying the signatures left in the star formation history, we were able to constrain the feedback mechanisms regulating the star formation within haloes. In the Λ CDM scenario, small scale structures are formed first, and then they merge forming larger and larger structures. Therefore, galaxies join more and more massive systems, and processes operating in these high-density environments change their properties. For this reason, galaxy evolution and formation of large-scale structures go hand in hand, as we show in our study of properties of galaxies in groups. We explored the spatial distribution of galaxies within and in the surrounding of groups, and we also used the velocity distribution of galaxies as a probe of the evolutionary stage of the group. We found important correlations between the evolutionary stage of the group and the population of galaxies residing within it.

List of Figures

1.1	The Milky Way galaxy	22
1.2	Figure illustrating the great variety of galaxies	23
1.3	Large scale structure as mapped with galaxy positions	24
1.4	Flow chart illustrating the evolution of an individual galaxy	29
1.5	Flow chart illustrating how to model SSP spectra	30
1.6	The Hubble sequence	37
1.7	Fundamental plane of elliptical galaxies	39
1.8	Star formation history of different types of galaxies	41
2.1	Toomre diagram of stars of the Geneva-Copenhagen Survey	54
2.2	Photometric temperatures of SMR stars	57
2.3	Comparison between trigonometric gravities from HIPPARCOS parallaxes and isochrone gravities	59
2.4	Temperatures vs. gravities diagram	60
2.5	Process of selection for stable Fe I and Fe II lines	62
2.6	Equivalent widths measurements from ARES and IRAF for the solar spectrum . .	63
2.7	Equivalent widths measurements from ARES and IRAF for for the stars HD 11608, HD 77338, and HD 81767	63
2.8	Ratio of opacities computed using the BSYN/EQWI and ABON2 codes for an Fe I line at $\lambda = 5861.11 \text{ \AA}$ for the solar model	64
2.9	Abundances versus $\log(W/\lambda)$ and excitation/ionization equilibrium for HD 26151	66
2.10	Excitation equilibrium as a function of temperature, gravity and metallicity . . .	67
2.11	Fe I abundance vs. temperatures	68

2.12	Differences between photometric and excitation temperatures <i>vs.</i> metallicities . . .	69
2.13	Ionization equilibrium as a function of temperature, gravity, and metallicity . . .	70
2.14	Relative differences between temperatures, gravities, and metallicities derived in the present work and from the PASTEL catalogue	73
2.15	Solar spectra in the region of the 6319 Å Mg triplet	75
2.16	Spectrum of HD 201237 in the region of the 6319 Å Mg triplet	76
2.17	Process of selection of stable lines of Ti I, Si I, and Ca I	78
2.18	Abundances of C, O, Mg, Si, Ca, Ti, and Ni <i>vs.</i> temperature	79
2.19	Abundances of C, Ca, and Ti <i>vs.</i> temperature after the correction	79
2.20	Comparison of abundances with other studies	81
2.21	Abundances of C, O, Ni, Mg, Ca, Si, and Ti <i>vs.</i> metallicities	82
2.22	UV plane and Toomre diagram	83
2.23	UVW velocities <i>vs.</i> α -Fe ratio	84
2.24	Ages <i>vs.</i> metallicities and α -Fe ratio	85
2.25	Ages <i>vs.</i> metallicities and α -Fe ratio of stars belonging to thin disk, thick disk, and intermediate populations	86
2.26	Abundances of O, Ni, Mg, Ca, Si, and Ti <i>vs.</i> metallicities	87
2.27	Mean Galactocentric distance <i>vs.</i> metallicities and α -Fe ratio	88
3.1	Scaling relations	93
3.2	Fraction of assembled stellar mass as a function of redshift	94
3.3	Mass-weighted metallicity as a function of stellar population age	99
4.1	Example of anisotropy signal detection for mock fields	103
4.2	Phase-space diagram of Group 91	105
4.3	Galaxy distribution around Group 91	106
4.4	Anisotropy profile of Group 91 and ratio of eigenvalues $q = \lambda_1/\lambda_2$ as a function of the radius	110
4.5	Distances of galaxies to the center of the groups and absolute magnitudes as a function of η	111
4.6	Global anisotropy versus the fraction of η_1 galaxies	112

4.7	Additional trends in our sample with respect the fraction of η_1 galaxies and to the fraction of galaxies within R_{200}	113
4.8	3D plot in velocity dispersion, radius and mass space	115
5.1	Composite groups velocity dispersion as a function of the absolute magnitude in the R band	122
5.2	Composite groups velocity dispersion as a function of the normalized radial distances to the group centers	122
5.3	B-R color of galaxies in the composite groups as a function of the normalized radial distances to the group centers	123
5.4	Absolute magnitude in R band as a function of the normalized radial distances to the group centers	123
6.1	Histograms of radial velocities for all non-Gaussian groups	131
6.2	DPM density probability decomposition	132
6.3	Histograms for Gaussian and non-Gaussian groups	134
6.4	Phase space diagrams for a typical Gaussian, non-Gaussian and modes systems .	136
A.1	Structure of the code	178
A.2	Best fit between synthetic and observed spectra	179

List of Tables

2.1	Sample stars in common with the Geneva-Copenhagen survey	47
2.2	Velocity ellipsoids for the thin disk, thick disk, and halo	50
2.3	Mean data for the thin, thick, and intermediate populations	52
2.4	Mean kinematical data for our sample, compared with kinematic groups studied by Famaey et al. (2005)	55
2.5	Gravity variations with stellar parameters	58
2.6	Abundances obtained with two different codes	65
2.7	Data from the PASTEL catalogue	71
2.8	Nickel blend at 6300 Å	74
2.9	Lines at the 6319 Å region	77
2.10	Comparison of abundances with other studies	80
3.1	Stellar population properties as a function of stellar mass.	98
4.1	Properties of groups	107
5.1	Mean properties of groups	120
6.1	Main properties of groups	126
6.2	Main properties of individual modes	133
A.1	Solar abundances obtained with the code	178
B.1	Log of spectroscopic observations	181
B.2	Basic stellar data	184
B.3	Kinematical data	186

B.4	Selected data from the PASTEL catalogue	188
B.5	Si, Ca, and Ti line list	191
B.6	Fe I and Fe II line list	193
B.7	Photometric and adopted spectroscopic stellar parameters	197
B.8	Final abundances of C, Ni, O and Mg	199
B.9	Final abundances of Ca, Si and Ti	201

Contents

1. <i>Introduction</i>	21
1.1 Galaxy formation and evolution: an overview	23
1.1.1 Density fluctuations and structure formation	24
1.1.2 Gas cooling and star formation	25
1.1.3 Feedback processes	27
1.1.4 Chemical evolution	27
1.1.5 Stellar Population Synthesis	28
1.1.6 Dynamical evolution	31
1.1.7 Environment effects	31
1.2 How to study galaxy formation?	32
1.2.1 Milky Way	32
1.2.2 Properties of galaxies	36
1.2.3 Galaxies at high redshift	42
1.2.4 Models and simulations of galaxy formation	42
1.3 What will be addressed in this thesis?	43
2. <i>Old and very metal-rich stars in the solar neighbourhood</i>	45
2.1 Introduction	45
2.2 Sample selection	46
2.3 Observations and reductions	48
2.4 Kinematics	48
2.4.1 Galactic orbits	49

2.4.2	Thin and thick disk membership probabilities	50
2.5	Stellar parameters	53
2.5.1	Temperatures	55
2.5.2	Surface gravities	57
2.5.3	Metallicities	60
2.5.3.1	Metallicities from two different codes	64
2.5.4	Checks on excitation and ionization equilibria	65
2.5.5	Stellar masses and ages	67
2.5.6	Final parameters and comparison with other studies	70
2.6	Abundance determination	72
2.6.1	Carbon, oxygen, magnesium, and calcium	72
2.6.2	Silicon, titanium and nickel	76
2.6.3	Spurious abundance trends and errors	77
2.6.4	Final abundances and comparison with other studies	78
2.7	Discussion	80
2.7.1	Comparison with thin and thick disk stars	81
2.7.2	Comparison with bulge stars	84
2.7.3	Theoretical predictions	86
2.8	Summary and conclusions	89
3.	<i>Constraints on feedback processes during the formation of early-type galaxies</i>	91
3.1	Introduction	91
3.2	Sample description	92
3.3	Stellar content	95
3.4	Results and discussion	96
3.4.1	Star formation history	96
3.4.2	Constraints of feedback processes	98
4.	<i>Galaxy distribution and evolution around a sample of 2dF groups</i>	101
4.1	Introduction	101
4.2	Methodology and data	102
4.2.1	Probing anisotropy around groups	102

4.2.2	The 2dF sample	104
4.2.3	Description of one group + surroundings field	108
4.3	Anisotropy and galaxy evolution	110
4.3.1	Characterizing galaxies around groups	110
4.3.2	Global anisotropy, galaxy evolution, and dynamics	111
4.4	Discussion	114
5.	<i>Segregation Effects According to the Evolutionary Stage of Galaxy Groups</i>	117
5.1	Introduction	117
5.2	Data and Methodology	118
5.2.1	2PIGG sample	118
5.2.2	Classifying groups	119
5.2.3	Composite groups	119
5.3	Segregation Analysis	120
5.4	Discussion	121
6.	<i>Non-Gaussian velocity distributions – The effect on virial mass estimates of galaxy groups</i>	125
6.1	Introduction	125
6.2	Data and Methodology	126
6.2.1	2PIGG sample	126
6.3	Non-Gaussianity and Mass	129
6.3.1	The mass bias	129
6.3.2	Exploring non-Gaussianity	129
6.3.3	The mass bias revisited	130
6.4	Discussion	135
7.	<i>Conclusions & Perspectives</i>	139
	<i>Bibliography</i>	143

<i>Appendix</i>	175
<i>A. Code for χ^2-minimization between observed and synthetic spectra</i>	<i>177</i>
<i>B. Tables</i>	<i>181</i>

Introduction

Our understanding of the nature of galaxies has dramatically increased in recent decades. Initially thought to be objects inside the Milky Way, it was not until the 1920s, when Hubble identified some Cepheid variables in the Andromeda galaxy, that astronomers became convinced that most of observed “nebulous” objects were independent systems. Less than 100 years later, using high resolution spectroscopy and imaging, and large surveys with almost one million galaxies, we are now able to explore in detail the properties of these systems up to high redshifts.

Throughout the last century, many studies have treated the question of how these objects were formed and how they evolved. One of the most important progress in this area was the establishment of the Λ CDM cosmological model. In this scenario, the matter of the universe consists of ordinary baryonic matter and a “dark” component. The formation of the dark matter component of galaxies has been well explored by using high-resolution simulations on supercomputers (Springel et al., 2005). However, the assembly of the baryonic component is regulated by a number of non-linear processes, such as shocking and cooling of gas, star formation, feedback by supernovae and active galactic nuclei, chemical enrichment, and stellar evolution. Many of these processes are still far from being fully understood, and the way in which galaxies form and evolve remains the most challenging problem in cosmology today. Motivated by these challenges, in this thesis, we address key aspects of galaxy formation from an observational point of view, by studying stars in the Milky Way, stellar populations in early-type galaxies, and the properties of galaxies in groups.

The Milky Way provides an unique opportunity to explore in detail the formation and evolution of spiral galaxies. Our Galaxy is shown in Figure 1.1. It is possible to resolve individual objects, such as stars, nebulae, star forming regions, and the content of the interstellar medium

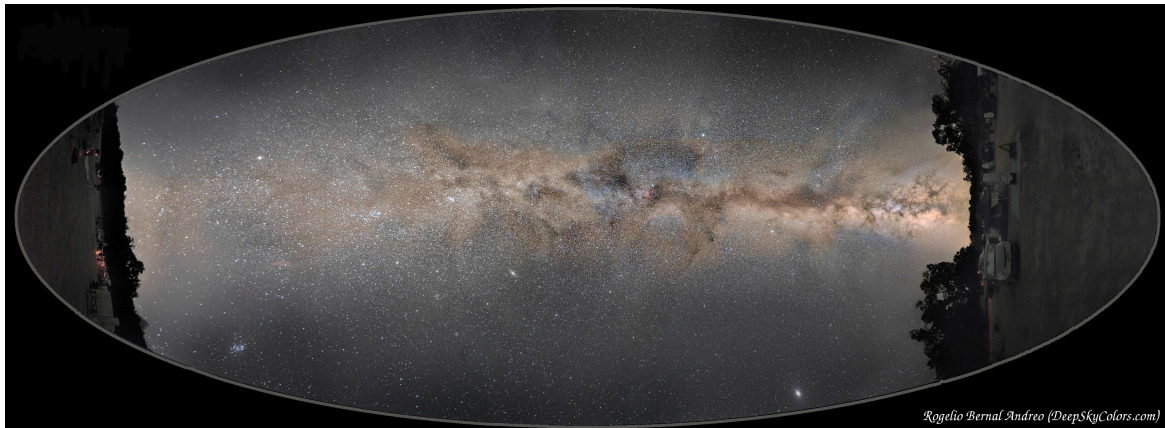


Figure 1.1: The Milky Way. Our Galaxy can be seen and studied in such a detail not possible for any other galaxy. Image credit & copyright: Rogelio Bernal Andreo (DeepSkyColors.com)

(ISM). Therefore, it is the only galaxy in which we can study in detail several astrophysical processes relevant for galaxy formation. Besides, it is possible to use the six-dimensional phase-space (position and velocity) for large numbers of individual stars, combined with their chemical abundances, to trace the formation history of the Milky Way in a way impossible for any other galaxy.

The understanding of how our own Galaxy was formed is a starting point in constructing a more general scenario of galaxy formation. The Milky Way is known to be of a specific type among a very diverse class of objects, as illustrated in Figure 1.2. It is necessary a wide range of parameters (such as luminosities, surface brightness, radius, morphology) to characterize a given galaxy. As we will see in this thesis, several parameters are correlated with each other, and galaxies usually are represented by scaling laws. These relations should be closely related to the mechanisms driving their formation. Any successful model of galaxy formation must be able to reproduce the galaxy properties and the relations among them.

Galaxies are not randomly distributed in space, but they tend to gather together in larger structures, such as groups and clusters. There are several observational evidences that the environment where galaxies reside affects their evolution, changing their properties. Understanding the mechanisms responsible for these changes is vital for a fully knowledge of how galaxies evolve. In addition, galaxies are not only interesting by their own; they also play a central role in the study of the structure and evolution of the Universe. They are tracers of the large-scale structures of the Universe, as shown in Figure 1.3, and detailed studies of their distribution can

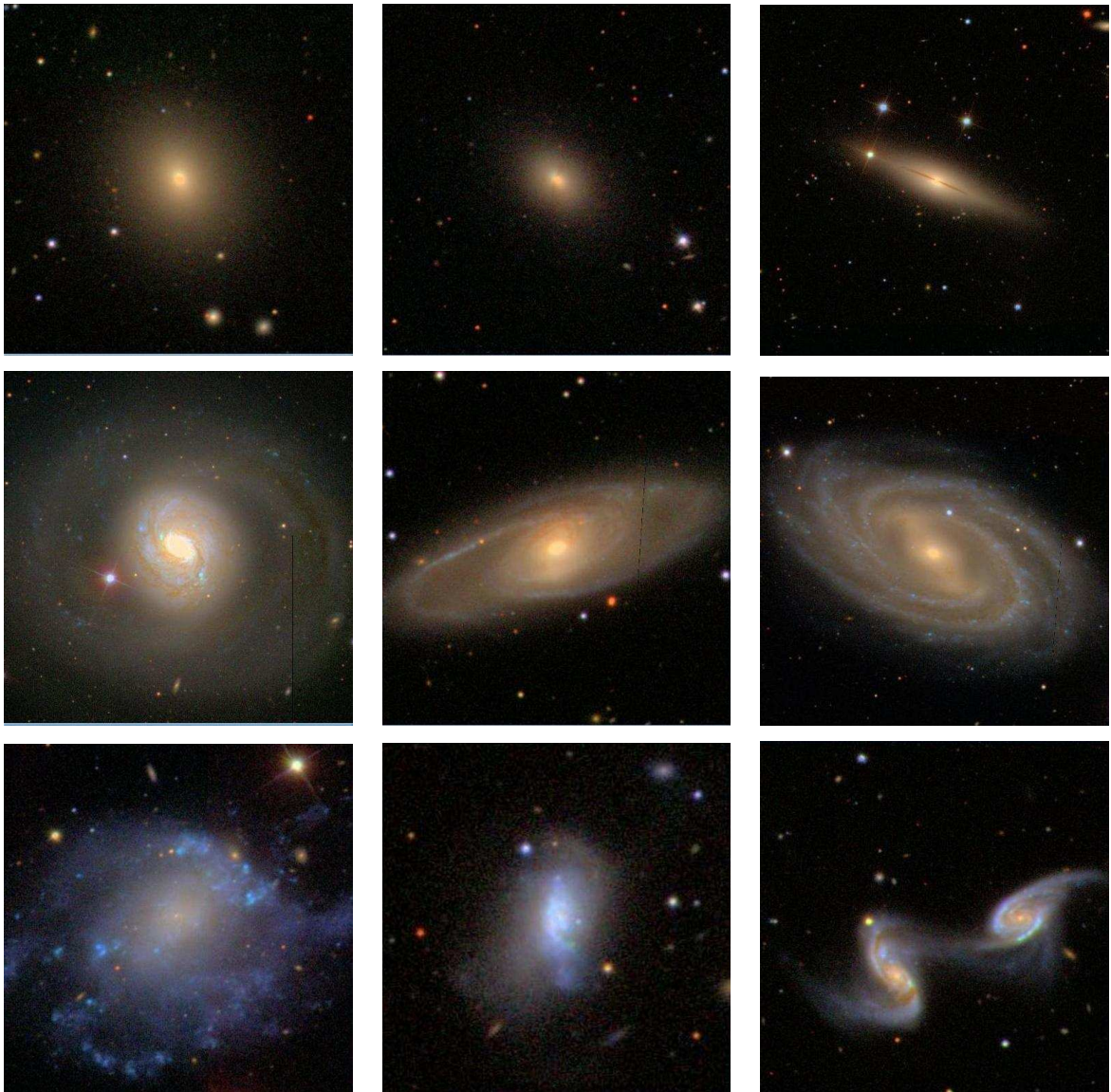


Figure 1.2: Figure illustrating the great variety of galaxies. Types shown here include: elliptical and lenticular (*first row*), spiral galaxies (*second row*), irregular and interacting galaxies (*third row*). Images Credit: Sloan Digital Sky Survey.

provide valuable constraints on how larger and larger systems are formed.

1.1 Galaxy formation and evolution: an overview

The way galaxies were formed and how they acquired the appearance they have today is the main goal of the study of galaxy formation. For this purpose, it is necessary to understand the evolution of the universe as a whole, including both large-scale structure formation and baryonic processes. In this Section, we outline the basic elements which are most relevant to this work.

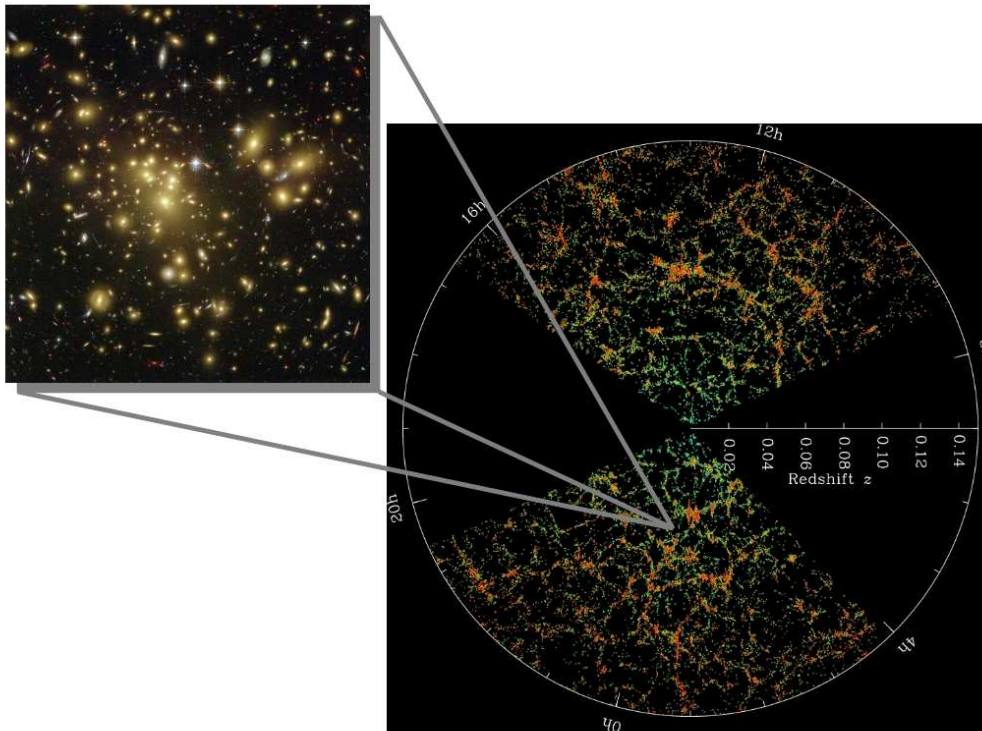


Figure 1.3: Galaxies are usually gathered together in groups and clusters, and they are tracers of the large-scale structures of the Universe. This Figure shows details of the Clusters Abell 1689 and slices through the SDSS 3-dimensional map of the distribution of galaxies. *Image Credit:* NASA, N. Benitez (JHU), T. Broadhurst (Racah Institute of Physics/The Hebrew University), H. Ford (JHU), M. Clampin (STScI), G. Hartig (STScI), G. Illingworth (UCO/Lick Observatory), the ACS Science Team and ESA (**Abell 1689**); M. Blanton and the Sloan Digital Sky Survey (**map of the distribution of galaxies**).

1.1.1 Density fluctuations and structure formation

Under the most accepted scenario today, the formation of structures in the universe is seeded by small matter density perturbations that grow with time. It is intuitive: a region with density slightly higher than the background attracts matter from its surroundings and becomes denser. In an expanding universe, however, the expansion slows the growth rate, and that's why the exact rate depends on the cosmological model describing the space-time properties on large scales. A very simple way to understand this is as follows. Imagine a sphere with a radius $R(t)$ and density $\rho = \bar{\rho}(1 + \delta)$, where $\bar{\rho}$ is the mean density of the universe and $\delta \ll 1$. By conservation of the mass within the sphere, in a static Universe, it is easy to see that the relation between the radius of the sphere and the density fluctuation is $R(t) \propto [1 + \delta(t)]^{-1/3}$. However, in an expanding Universe, the radius of the sphere also increases following the Hubble expansion, and

$R(t) \propto a(t) [1 + \delta(t)]^{-1/3}$, where $a(t)$ is the scale factor, which determines the way the Universe expands. Hence, while a gravitational instability that arises from an overdensity causes the contraction of the sphere, the expansion tends to increase the sphere radius. If $\delta(t) > 0$, the radius will grow less rapidly than the expansion of the Universe. For this reason, a region with an overdensity will become even denser as the Universe expands. When the density becomes sufficiently high ($\delta \sim 1$), the perturbation detaches from the expansion and starts to collapse (“turn-around”), and it marks the transition from an almost linear to a strongly non-linear regime.

In the very early universe, during the recombination epoch, as the free electrons were being captured by atomic nuclei, the universe became more and more transparent: the amount of photon scattering decreased dramatically. Scattering less, photons could diffuse much greater distances from high density regions of space to low density ones, equaling the fluctuation amplitudes of regions with a characteristic scale (Silk, 1968). In an universe composed only by baryonic matter, nonlinear structures, such as galaxies, would not be formed. A non-baryonic component, which does not interact with the radiation field, is thus required. The “dark matter” (DM) fluctuations were able to grow, forming DM haloes. Shortly after recombination ($z \sim 1100$), the baryons fall into the potential well of the haloes and together they grow into the structures we observe today.

The way structures grow during the linear regime is mostly determined by the underlying cosmological model. However, during the nonlinear phase, the way the structure grows and evolve is mostly determined by the matter content of the halo, specially baryonic process. Some of these processes are outlined below. Baryonic processes are usually treated in a simplified manner in models and simulations, therefore, constraints from observations are of paramount importance.

1.1.2 Gas cooling and star formation

After the recombination epoch, the gas falls into the potential well of the dark haloes. If the cooling is effective, star formation takes place, and galaxies are formed. Several cooling mechanisms can play a role. At high redshifts, the density of the cosmic microwave background (CMB) photons is still sufficiently high so that the inverse Compton scattering of CMB photons by electrons can be an efficient cooling mechanism. However, bremsstrahlung emission from free electrons is the main cooling process responsible for the cooling of the fully ionized gas

within massive haloes ($T_{\text{vir}} \gtrsim 10^7 \text{ K}$). In the temperature range of $10^4 \text{ K} < T_{\text{vir}} < 10^6 \text{ K}$, the main mechanisms are the decay of excited atoms (neutral or partially ionized) or emission through the recombination of electrons and ions. Metallicity plays an important role in this temperature range, since different atomic species have different excitation energies. In low mass haloes ($T_{\text{vir}} \lesssim 10^4 \text{ K}$), where the gas is almost completely neutral, the emission of fine and hyperfine structure transitions of heavy elements, if present, or rotational and vibrational lines of molecules can be also a cooling channel.

During the gas accretion into haloes, the gas cloud may fragment into small, high-density cores that can form stars. Ideally, we should have star formation laws derived from basic physical principals. However, many details regarding the physical processes involved are still not fully understood, and we use empirical laws instead. There are two very important ingredients in the the star formation process:

- Star formation rates (SFR). The SFR is usually related to the gas surface density $\dot{\Sigma}_{\star} \propto \Sigma_{\text{gas}}^n$, known as Schmidt law of star formation (Schmidt, 1959). Kennicutt (1998) analysed a variety of star-forming galaxies and found the best fit of $n = 1.4$. Although the Schmidt law is successful in many star-forming systems, it does not apply to dwarf galaxies. In these objects, the star formation efficiency is much lower than in normal larger galaxies (e.g. Panter et al., 2007).
- Initial mass function (IMF). The IMF is the distribution in mass of a newly formed stellar population (see Chabrier, 2005, for a review). Based on observations in the solar neighborhood, Salpeter (1955) first estimated the IMF as $\phi(m) dm \propto m^{-\alpha} dm$, with $\alpha = 1.35$ for stars in the mass range of $0.4 < m < 10M_{\odot}$. The function $\phi(m) dm$ determines the relative number of stars born with masses between m and $m + dm$. There are other relations for the IMF which are commonly used in the literature: Miller/Scalo (Miller & Scalo, 1979), Scalo (Scalo, 1986), Kroupa (Kroupa, 2002), and Chabrier (Chabrier, 2003). All these IMFs are similar at $m > 1 M_{\odot}$, but there is a significant difference among them at the low mass end. There are several uncertainties regarding the IMF, including the its dependence with metallicity and whether or not it is universal. For example, recent studies suggest a change of the IMF from low- to high-mass early-type galaxies (van Dokkum & Conroy, 2011), and for different morphological types (Auger et al., 2010; Spiniello et al., 2011; Dutton et al., 2011).

1.1.3 Feedback processes

Shortly after stars are formed, the most massive ones explode in supernovae (SN) events. The enormous amount of energy produced by these events heats the surrounding gas, blowing it out of the galaxy through galactic winds. The gas may be heated by the energy liberated by the accretion of matter to supermassive black holes (SMBH) that reside at the centers of almost all massive galaxies. These feedback mechanisms regulate the star formation efficiency within DM haloes. Simulations of galaxy formation and semi-analytical models have shown that it is only within haloes in a mass range around $M_{\text{halo}} \sim M_{\text{shock}} \sim 10^{12} M_{\odot}$ where baryons can form stars efficiently (Cattaneo et al., 2011; Moster et al., 2010; Bouché et al., 2010; Guo et al., 2011). Above this limit, gravitational shock heating and AGN feedback suppress the gas accretion (Dekel & Birnboim, 2006; Kereš et al., 2005, 2009; Birnboim & Dekel, 2003; Cattaneo et al., 2009, 2011; Oser et al., 2010). For galaxies within haloes with masses below $\sim 10^{12} M_{\odot}$, the energy liberated by supernova explosions can eject the gas from haloes with circular velocity $\lesssim 100 \text{ km s}^{-1}$, quenching the star formation within these systems (Dekel & Silk, 1986). Besides, supernova feedback is a fundamental process in order to reproduce the observed Tully–Fisher relation of spiral galaxies (e.g. de Rossi et al., 2010).

Although it has become clear over the years that feedback processes play an important role in galaxy formation (see e.g. Silk, 2011), we are still far from understanding which processes dominate, and when and how exactly they operate. Furthermore, to make accurate predictions for their effects, one also needs to know how often they occur. For supernovae this requires a prior understanding of the star-formation rates and the IMF. For AGN it requires understanding how, when and where supermassive black holes form, and how they accrete mass.

1.1.4 Chemical evolution

Chemical elements in the Universe can be formed through three main processes: primordial nucleosynthesis, stellar nucleosynthesis and interstellar nucleosynthesis. The first process occurred during the first three minutes of the Universe, when the matter was very hot and dense. This process produced primarily Hydrogen ($\sim 75\%$) and Helium ($\sim 25\%$), with a very small amount of D, ^3He , ^4He , and ^7Li . No heavier elements were produced, since there are no stable elements of mass 5 and 8. Spallation, the interaction between cosmic rays and the ISM gas, produces the light elements lithium, beryllium and boron (Audouze, 1986). Heavy elements are

formed in the interior of stars, or during SN events (see e.g. Matteucci, 2006). Stars with mass in the range $0.8 \lesssim M \lesssim 8M_{\odot}$ produce mainly helium, carbon, nitrogen and s-process elements (barium, yttrium, strontium). Type II supernovae ($M \gtrsim 8M_{\odot}$) are the main responsible for the synthesis of α -elements, also produce part of Fe and Fe-peak elements, and r-process elements (europium, barium). Type Ia supernovae produce mainly Fe-peak elements. When stars expel mass in stellar winds, or in supernova explosions, they enrich the interstellar medium (ISM) with newly synthesized metals.

Evolution of the chemical composition of the gas and stars in galaxies is important for several reasons. First, the luminosity and color of a stellar population depend not only on its age and IMF, but also on the metallicity of the stars. The cooling efficiency of gas also depends on its metallicity (more metal-enriched gas cools faster). Besides, the interstellar extinction caused by small particles of heavy elements can significantly reduce the brightness of a galaxy.

The chemical enrichment of a galaxy involves several ingredients, as illustrated in Figure 1.4. First, it is necessary to know the initial conditions, i.e. whether the first stars were formed from primordial gas (mainly H and He) or from gas pre-enriched by products from some neighboring more evolved system. Since the chemical enrichment of a galaxy depends on the products of stellar nucleosynthesis, one needs to know the rate in which they are formed (SFR) and the distribution of masses (IMF). The amount of mass in synthesized metals that is ejected by stars is known as stellar yields (see e.g. Rauscher et al., 2002; Chieffi & Limongi, 2004; Nomoto et al., 2006). Stellar yields depend basically on the stellar mass, chemical composition, and mass loss history. In addition, other relevant processes, such as gas inflow and outflow, radial flows of gas and stars and accretion of material of other systems (mergers), should be taken into account.

Our own Galaxy plays an important role in understanding the chemical enrichment of galaxies, since we can trace its own chemical history in great detail by studying chemical abundances of individual stars directly. Knowing the chemical evolution of our Galaxy is indispensable for comprehending the chemical evolution of other galaxies.

1.1.5 *Stellar Population Synthesis*

We do not observe individual stars in distant galaxies, only the integrated spectra. The correct interpretation of the spectrum of a galaxy relies then on the knowledge of several ingredients and determining how to extract information from it (an ensemble of stars) is the main goal of stellar

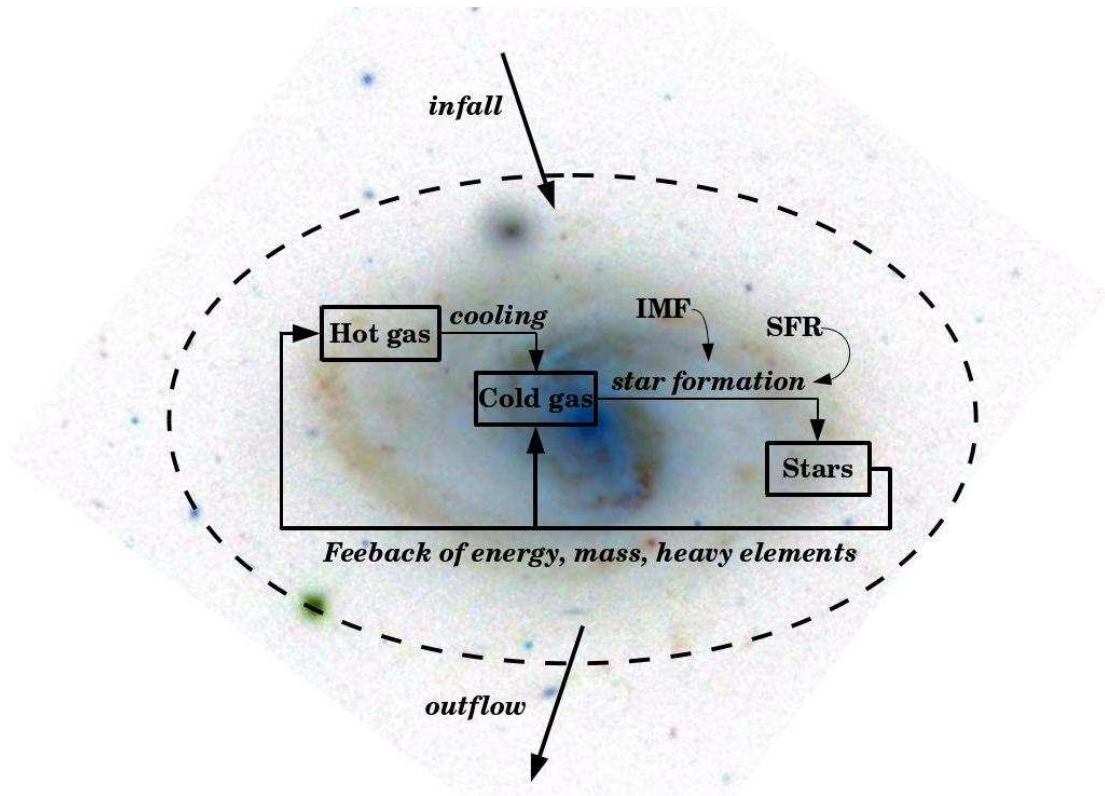


Figure 1.4: Flow chart illustrating the evolution of an individual galaxy. The hot gas within a galaxy cools and stars may be formed from the cold gas. Stars are formed with a given rate (SFR) and mass distribution (IMF). Also, they can eject mass and metals through stellar winds and in the final stage of their evolution, when they explode in a supernovae event depending on their mass. These SN explosions can eject mass out of galaxies (*outflows*), and gas from the intergalactic medium can be accreted (*infall*).

population studies. A single stellar population (SSP) is an important concept in stellar population studies. An SSP consists of an ensemble of stars which is formed from the same molecular cloud, at the same time. Therefore, all the stars have the same age and chemical composition, differing only in mass. Modeling the properties of SSPs (colors, luminosities and spectra) is important to understand stellar populations within galaxies, since we can reconstruct the complex star formation histories of galaxies by combining individual SSPs. The main ingredients to reproduce the characteristics of an SSP are the IMF, details of how stars evolve (evolutionary tracks), and libraries of stellar spectra. This is schematically illustrated in Figure 1.5.

Despite the great progress made in stellar population studies, this field still faces several challenges (see e.g. Charlot, 2010). One of them is to improve stellar population synthesis models with non-solar chemical abundance ratios. The present limitation relies on the libraries of stellar spectra, which is one of the main ingredients of stellar population synthesis models. We can

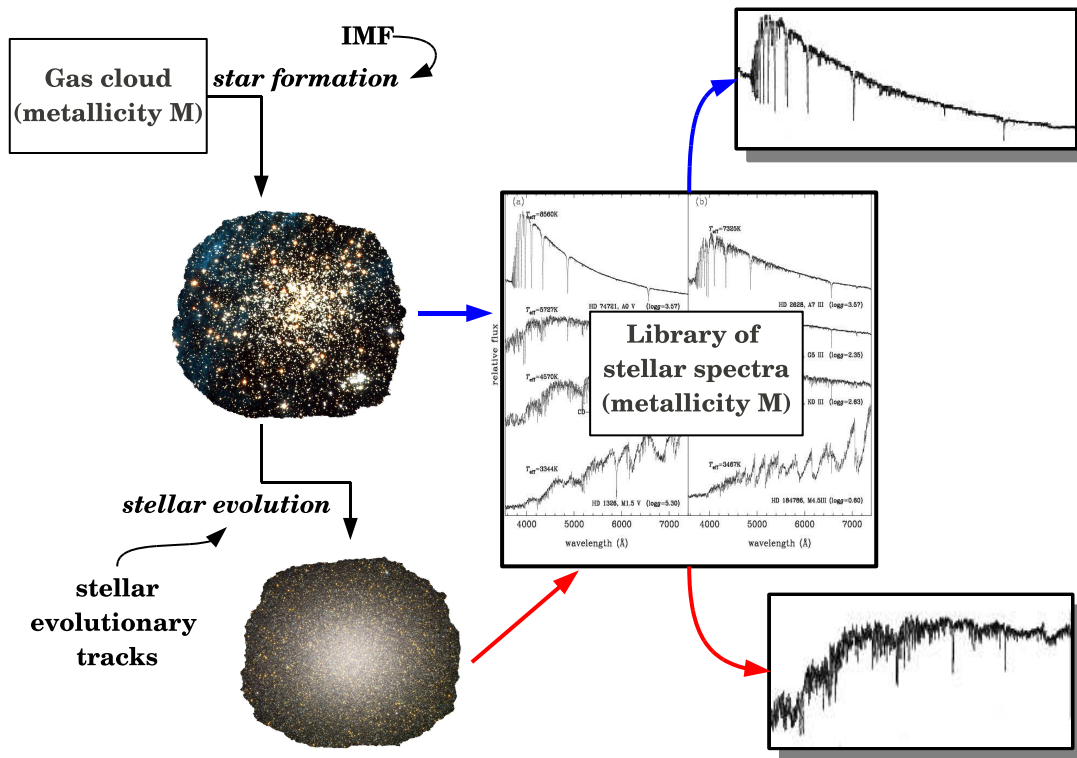


Figure 1.5: Flow chart illustrating how to model SSP spectra. *Images credit:* NGC 1850: ESA, NASA and Martino Romaniello (European Southern Observatory, Germany). NGC 5139: Martin Pugh (<http://www.martinpughastrophotography.id.au/>)

either use empirical or synthetic libraries to build stellar population models. One disadvantage of empirical libraries is the inability to extrapolate to abundance patterns that differ from those of the library stars, which are mainly from the solar neighborhood. Although synthetic libraries overcome this limitation of the empirical libraries, they rely on model atmospheres, which are subject to systematic uncertainties. Besides, computing a reliable high-resolution synthetic spectral library for a wide range of stellar parameters over a large spectral region requires building an extensive and reliable list of atomic and molecular line opacities, which are needed for an accurate reproduction of high-resolution spectra of real stars. Therefore, improvements in stellar population synthesis models with non-solar chemical abundance ratios can be made either by increasing the accuracy of synthetic stellar spectra or increasing the number of observed spectra of stars with non-solar abundances, e.g. metal-rich stars.

1.1.6 Dynamical evolution

Internal dynamical evolution can change the structure of galaxies. The tidal force caused by galaxy-galaxy interactions can remove dark matter, gas and stars from galaxies, and may also perturb their structure. In addition, instabilities within galaxies, such as bars and spiral arms, can redistribute mass and angular momentum within the galaxy, thereby changing its structure (e.g. Minchev & Famaey, 2010; Roškar et al., 2011). Hence, an important question is whether the morphologies of galaxies were set at formation, or are the result of secular evolution. An example is the bar-instability in disks, which may be responsible for the growth of a central ellipsoidal component, a so-called “pseudo-bulge” (Kormendy & Kennicutt, 2004; Gadotti, 2009). The redistribution of angular momentum, gas and stars within galaxies, can have important implications to models of chemical enrichment, and internal color, metallicity, and age gradients.

1.1.7 Environment effects

The evolution of galaxies within groups and clusters differs from that of galaxies in low-density environments. The major evidence is the morphology-density relation (Dressler, 1980). Colors, star formation rates, morphologies and gas content appear to be affected by local overdensities. Besides, Butcher & Oemler (1978) found that the fraction of blue galaxies within clusters increases with redshift. This indicates that galaxies in clusters rapidly evolve, most likely due to processes that operate in high-density regimes. There are several mechanisms that may account for these effects:

Tidal stripping Since galaxies are extended objects, the force exerted on one galaxy by another is not constant across its diameter. Therefore, this differential force cause tidal effects, and gas and stars from the outer parts of a galaxy can be removed.

Dynamical friction When a galaxy is moving through the intracluster medium (ICM), it loses kinetic energy due to interaction with the surrounding galaxies. To understand this effect, we can imagine a massive object moving through a cloud of small particles. These particles will be attracted by the massive object, gaining kinetic energy and momentum. By conservation of energy and momentum, the object loses it energy and slows its motion. This effect was first studied by Chandrasekhar (1943).

Galactic cannibalism The fate of a galaxy that loses much kinetic energy (by dynamical friction, for example) is to be merged with the central galaxy (Ostriker & Tremaine, 1975). The presence of bright cluster galaxies (BCG) in the center of clusters is the main evidence of this effect.

Galaxy harassment This effect corresponds to the removal of gas and stars from galaxies due to the cumulative effect of tidal interactions and high-speed encounters.

Ram-pressure stripping. The baryonic mass of a cluster is dominated by the hot gas ($T \sim 10^7 - 10^8$ K) in the intracluster medium (ICM). When a galaxy falls into a cluster, it may lose gas by the pressure exerted by the ICM gas. This effect is known as ram-pressure stripping, and it was first proposed by Gunn & Gott (1972).

Strangulation Several mechanisms acting in clusters can strip gas from galaxies. If the galaxy loses all its gas, the consequence is that star formation is quenched, and the galaxy becomes red over time. This process is called strangulation (Larson et al., 1980).

1.2 *How to study galaxy formation?*

What we have done so far is to describe in a schematic way all the processes involved during the formation of a galaxy. But how do we effectively study all this? The answer is that there is no unique way to address this issue. Instead, galaxy formation is a challenging problem whose solution requires an approach combining results from distinct areas: more specific studies of the Milky Way; studies of the structural properties of galaxies in different environments and despite their morphology; high spectral and spatial resolution observations of high redshift systems; and numerical simulations of the gravitational aggregation of dark matter and baryons. Below, we outline how each of these areas can contribute to assemble a complete picture of how galaxies form and evolve, and how they are possibly connected.

1.2.1 *Milky Way*

Our galaxy is known to be composed by four components, each with different structural, kinematic, and population characteristics: the bulge, the thin and the thick disks, and the stellar halo. A powerful way to constrain how each of these components were formed is to combine the

intrinsic properties of stars (e.g. chemical composition, age) and their kinematics. Historically, chemical and kinematic information were used as a basis to formulate the first galaxy formation models. In their classical paper, Eggen et al. (1962) analysed the properties and motion of ~ 200 dwarfs and showed that lower metallicity stars move on more highly eccentric orbits when compared to higher metallicity stars. The observed trends were interpreted as a signature that the stars now observed as a spheroidal halo were formed from the gas falling toward the galactic center in the radial direction. They proposed that the collapse of the galaxy in the radial direction was then stopped by rotation of the protogalaxy, and the disk was formed by the collapse from the halo onto a plane. However, from recent studies with large data sets and high resolution spectroscopy, we know that our Galaxy is a far more complex structure than suggested by these first models. We outline some recent results below.

Halo

The stellar halo represents only a small fraction of the Galactic total stellar mass, and it is composed by old, metal-poor stars, that move in high-eccentricity orbits. In the canonical model by Eggen et al. (1962), the halo component was formed during the rapid collapse of the protogalaxy. However, in the hierarchical galaxy formation scenario, stellar halos are also expected to contain debris of galaxies accreted through merger events. Since stellar haloes in distant galaxies are extremely difficult to detect due to their low surface brightness, the Milky Way halo contains unique fossil records of hierarchical galaxy formation. Indeed, there are several observational evidence in support of Λ CDM scenario, such as the detection of clumpiness in the phase space distribution of halo and disk stars (e.g. Majewski et al., 1996; Helmi & White, 1999; Chiba & Beers, 2000; Yanny et al., 2003; Helmi et al., 2006; Jurić et al., 2008; Bell et al., 2008), and the direct detection of satellite galaxies being accreted (e.g. Ibata et al., 1994; Martin et al., 2004; Zucker et al., 2006).

Recent studies suggest that the Galaxy halo is composed of at least two distinct stellar populations, each exhibiting different spatial distributions, orbits, and metallicities (Carollo et al., 2007; de Jong et al., 2010). For example, Carollo et al. analysed 20,000 stars from the SDSS/SEGUE (Yanny et al., 2009) and found that the halo population up to ~ 15 kpc (the inner-halo) are less metal-poor than the population beyond ~ 15 kpc (outer-halo). The distribution of metallicities for stars in the inner halo peaks at $[\text{Fe}/\text{H}] = -1.6$, while the distribution of the outer-halo stars

peaks at $[\text{Fe}/\text{H}] = -2.2$. In addition, the outer-halo comprises stars that exhibit a much more spherical spatial distribution when compared with the inner halo. This dichotomy indicates that the halo was formed through a process more complex than pure hierarchical accretions.

Simulations by De Lucia & Helmi (2008) suggest an explanation for this dichotomy. In their model, the stellar halo is mainly formed from a few massive satellites accreted early on during the galaxy's lifetime. The stars in the halo do not exhibit any metallicity gradient, but higher metallicity stars are more centrally concentrated than stars with lower abundances. The 'dual' nature of the stellar halo originates from a correlation between the stellar metallicity and the stellar mass of accreted galaxies. The most massive galaxies are more metal-rich than low mass systems. Since these massive galaxies decay through dynamical friction to the inner regions of the halo, this is where higher metallicity stars will be found preferentially. Despite these results being in qualitative agreement with recent observational measurements, higher resolution simulations are needed for this kind of study, and the exact origin of the Galactic stellar halo remains to be clarified.

Bulge

Bulges are commonly believed to form during the initial collapse of the protogalaxy and subsequent galaxy collisions and mergers (e.g. White & Rees, 1978; Matteucci & Brocato, 1990; Ferreras et al., 2003; Rahimi et al., 2010). Bulges formed in this way are commonly referred as "classical" bulges. However, secular mechanisms, such as bar-driven instabilities, can trigger star formation in Galactic centre, giving rise to a pseudo bulge (Kormendy & Kennicutt, 2004; Gadotti, 2009). Whether the bulge of the Milky Way is classical, pseudo-bulge or both is still matter of intense debate.

The very old, metal-rich and α -enhanced stellar population found in the bulge (McWilliam & Rich, 1994; Zoccali et al., 2006; Fulbright et al., 2007; Lecureur et al., 2007; Meléndez et al., 2008; Bensby et al., 2010) is consistent with a classical bulge. On the other hand, the boxy/peanut-like shape and cylindrical rotation of stars in the bulge (Howard et al., 2009; Shen et al., 2010) and the similarities between the bulge and the Galactic thick disk as observed in the solar neighborhood (Meléndez et al., 2008; Alves-Brito et al., 2010; Bensby et al., 2010; Gonzalez et al., 2011) lends strong support to the existence of a pseudo bulge. Recent studies of micro-lensed bulge stars (Bensby et al., 2011, 2012) show evidence for a bi-modal bulge

population: one with $[\text{Fe}/\text{H}] -0.6$ and a metal-rich population with $[\text{Fe}/\text{H}] +0.3$. This suggests that both a classical and a pseudo bulge coexist in the Galactic centre. Bensby et al. also find that the metal-rich population has a significant fraction of intermediate-age stars. There are evidences from outer galaxies that bars are associated with the intermediate-age stars. For example, Coelho & Gadotti (2011) studied a sample of 575 bulges with spectra from the SDSS by means of their stellar populations. They find that bulges within barred galaxies show an excess of stellar populations younger than ~ 4 Gyr.

The discussion regarding bulges of spiral galaxies is closely related to our understanding of how galaxies are formed. For example, Kormendy et al. (2010) study a sample of 19 massive spiral galaxies, and they find that 11 show no evidence for classical bulge. This is a challenge for galaxy formation theory. In the Λ CDM paradigm, high mass systems are produced mainly through mergers, and these events give rise to a classical bulge. Therefore it is difficult to explain a large number of massive bulgeless disks, since the absence of a classical bulge implies that no major merger occurred during the formation of these systems. However, recent simulations within large cubic volumes have shed some light on this issue. The existence of bulgeless massive spiral galaxies could be explained by the formation through cold streams (see Section 1.2.4), which can form high-mass systems with no mergers.

Disk

Since Gilmore & Reid (1983) identified that the disk is composed by a thin and a thick component, their properties have been the subject of several studies. The scale height of these two components is ~ 300 pc and ~ 900 pc for the thin and thick disk, respectively (e.g. Jurić et al., 2008). The thick disk seems to be composed by old, kinematically hot, metal poor stars with high α -Fe ratios. In the other hand, the thin disk is composed by younger and more metal rich stars when compared with the thick disk members. For this reason, they are commonly believed to be two distinct structures. However, detailed analysis of kinematics and chemical abundances of stars have shown the presence of an “intermediate” population between the thin and thick disk, i.e., stars which cannot be assigned to either of these components (e.g. Mishenina et al., 2004; Soubiran & Girard, 2005; Reddy et al., 2006). Indeed, studies of large data sets, such as the Geneva-Copenhagen Survey (Nordström et al., 2004; Holmberg et al., 2009) and SEGUE/SDSS (Yanny et al., 2009), have shown that the separation between thin and thick disk

is not straightforward (e.g. Jurić et al., 2008; Casagrande et al., 2011), a result with important implications for models of formation of the thin and the thick disk.

In models of the chemical evolution of the Galactic disk, it is generally assumed that the disk can be divided into concentric annuli, and each one evolves independently of the others (e.g. Pagel, 1997; Chiappini et al., 1997, 2001; Naab & Ostriker, 2006; Colavitti et al., 2008). In this scenario, the metallicity of stars formed in a given annulus depends on the annulus's radius and the time of their formation. However, several studies have shown that the age-metallicity relation presents a large scatter (e.g. Edvardsson et al., 1993). Besides, this simple scenario does not account for the presence of old and metal-rich stars in the Solar neighbourhood (Grenon, 1999, 2000; Feltzing & Gustafsson, 1998; Feltzing & González, 2001). In Chapter 2, we analysed a sample of old and metal-rich stars, which have thin disk abundances and thick disk kinematics. A comparison of α -element abundances of the sample stars with bulge stars shows that the oxygen is compatible with a bulge or inner thick disk origin. Our results suggest that models including radial mixing (Schönrich & Binney, 2009a,b; Villalobos et al., 2010, see also Section 1.1.6) and dynamical effects the bar/spiral arms might explain the presence of these old metal-rich dwarf stars in the solar neighbourhood. In addition, these models account for the scatter in the age-metallicity relation, also suggest that the thick disk originates from the thin disk, what explains the absence of a clear distinction between these two components. Although it is likely that radial mixing occurs, it is not clear how exactly it operates. Besides, many different processes enter the picture of disk formation and evolution, such as accretion of stars from disrupted satellites (Abadi et al., 2003a,b), and heating of the thin disk by minor mergers (Quinn et al., 1993; Kazantzidis et al., 2008). The upcoming large surveys, such as Gaia, will further constrain the interplay of various scenarios and, therefore, clarify the origin of the galactic disk.

1.2.2 *Properties of galaxies*

One of the most noticeable fact about galaxy populations is the existence of two basic galaxy types: spirals and ellipticals. Elliptical galaxies are approximately ellipsoidal systems supported by the random motions of their stars, and they have a smooth surface brightness profile. Spiral galaxies consists of flat, clumpy disks that are supported by rotation, and very often they have spiral arms. However, most of galaxies are not a pure elliptical or spiral (see e.g. Nair & Abraham, 2010). Figure 1.6 shows a classical scheme for classification of galaxies proposed by

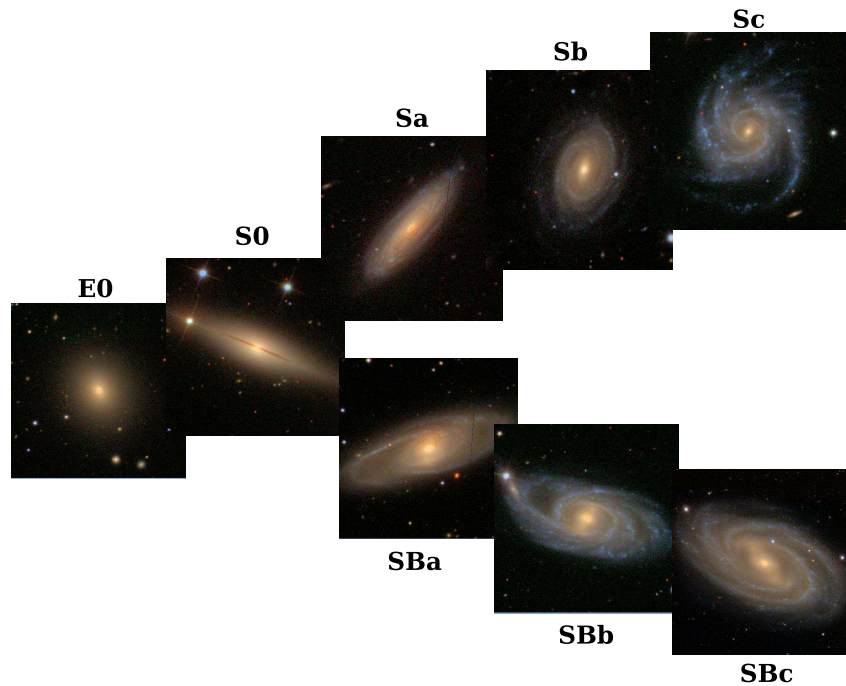


Figure 1.6: The Hubble sequence, starting with elliptical galaxies and ending with spiral systems.

Hubble in 1926. Hubble ordered the morphological types in a sequence, starting with elliptical galaxies and ending with spiral systems. For this reason, elliptical and lenticular system are usually called *early-type* galaxies, and spiral as *late-type*. The “fork” shape of this diagram accounts for the distinction between barred and unbarred spirals.

Galaxy properties, such as size, luminosity, surface brightness, rotation velocity (for disk galaxies) and velocity dispersion (for spheroidal systems) are known to follow scaling relations. The study of these relations provides a window into the processes that regulate galaxy formation, as described below.

Elliptical galaxies

Correlations between photometric and kinematic properties of elliptical galaxies have been empirically determined. For example, Faber & Jackson (1976) found that more luminous elliptical galaxies have larger central velocity dispersions

$$L \propto \sigma_0^\gamma \quad (1.1)$$

where $\gamma \sim 4$. This relation is known as Faber – Jackson relation. The mean surface brightness

within a given radius is defined by

$$\langle I \rangle_e = \frac{L}{2\pi R_e^2} \quad (1.2)$$

where L is total luminosity, R_e is the effective radius that encloses half of the total light, and $\langle I \rangle_e$ is given in flux units. The mean surface brightness can be written in units of mag arcsec², $\langle \mu \rangle_e \propto -2.5 \log \langle I \rangle_e$. Combining these relations, we have

$$\log R_e = a \log \sigma_0 + b \langle \mu \rangle_e + c \quad (1.3)$$

This equation defines the “fundamental plane” (FP) of elliptical galaxies. Figure 1.7 shows ordinary elliptical galaxies, dwarf ellipticals and classical bulges of spiral galaxies in the $[R_e, \sigma_0, \mu_e]$ space. There are several studies devoted to interpret the physical meaning of the FP (e.g. Faber et al., 1987; Djorgovski & de Carvalho, 1990; Jorgensen et al., 1996; Bernardi et al., 2003; La Barbera et al., 2010). If early-type galaxies are in virial equilibrium, $\sigma^2 \propto GM/R$, and correlations between $\log R_e, \log \sigma_0, \mu_e$ are, therefore, expected. The virial relation implies a constant mass-to-light ratio among elliptical galaxies. However, M/L presents a dependence on galaxy mass (e.g. Faber et al., 1987). This dependence can be interpreted as arising from differences in the dark matter fractions among early-type galaxies. Indeed, several studies have shown that the efficiency in which baryons are converted into stars within DM haloes varies with the halo mass (e.g. Cattaneo et al., 2011; Moster et al., 2010; Bouché et al., 2010; Guo et al., 2011), and feedback by supernovae and active galactic nuclei are believed to be responsible for this relation.

Spiral galaxies

Late-type galaxies are far more complex structures than elliptical and lenticular galaxies. Such as our own Galaxy, this class of objects might contain bulge, disk, bars, spiral arms and stellar halo. However, Tully & Fisher (1977) determined a simple empirical relationship between the intrinsic luminosity L (proportional to the stellar mass) of a spiral galaxy and its rotation velocity

$$L \propto V_{\max}^\alpha \quad (1.4)$$

where V_{\max} is the maximum of the rotation curve. Observed values of α lie in the range 2.5 – 4, and it is larger in redder bands (e.g. Pierce & Tully, 1992). This relation is known as the Tully–

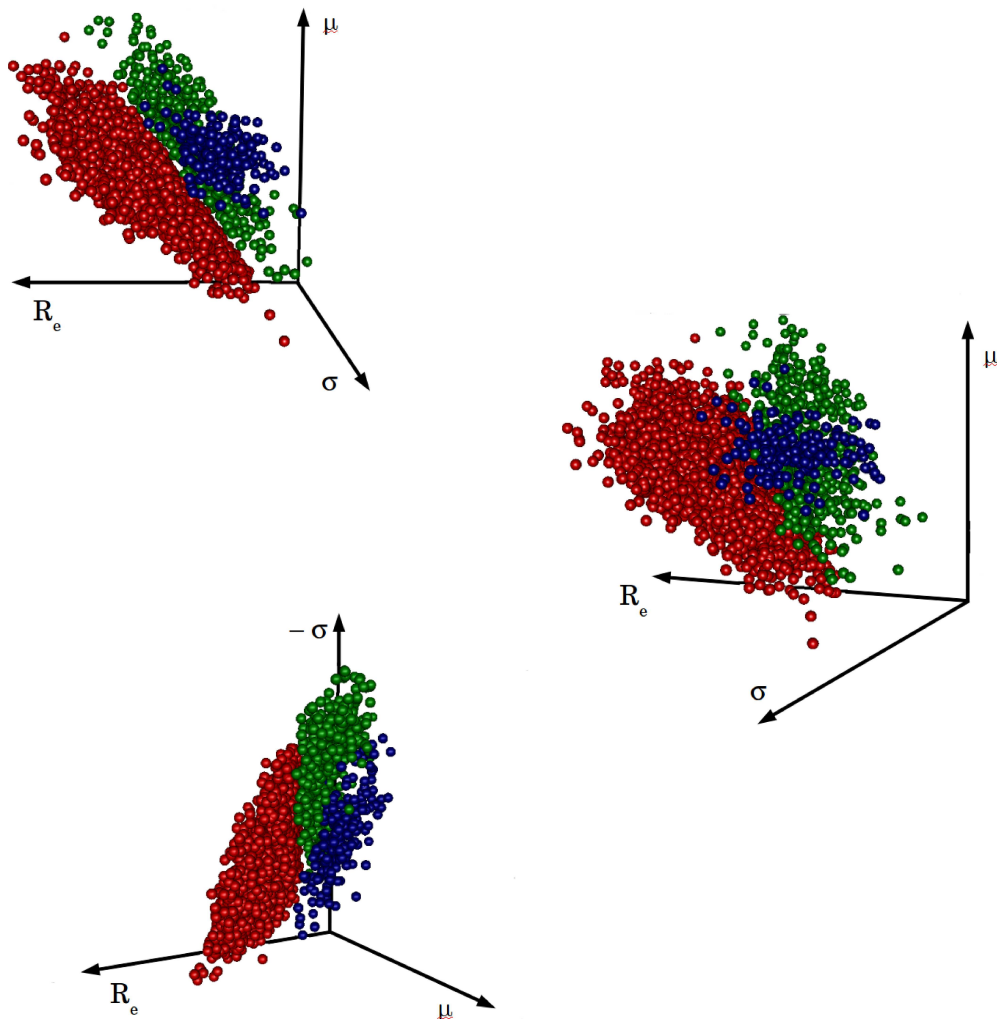


Figure 1.7: Fundamental plane of elliptical galaxies. Ordinary elliptical (La Barbera et al., 2010), dwarf elliptical (Trevisan et al., 2012a), and classical bulges of spiral galaxies (Gadotti, 2009) are represented by red, green and blue spheres, respectively.

Fisher relation. This relation is important for our understanding of formation and evolution of spiral galaxies, since it defines the relation between dynamical mass and luminosity. There are several studies devoted to the determination of the Tully–Fisher relation as a function of redshift (e.g. Puech et al., 2010; Fernández Lorenzo et al., 2010; Miller et al., 2011, 2012), environment (Biviano et al., 1990) and photometric band (e.g. Fernández Lorenzo et al., 2010).

Stellar populations in galaxies

As we saw in Section 1.2.1, the observation of individual stars is a powerful way to constraint formation scenarios. However, it is not possible to resolve individual stars in distant galaxies, only their integrated spectra. Information can be extracted from these spectra by means of stellar population studies, described in Section 1.1.5. By combining different SSP, we can trace the complex formation history of a galaxy, as shown in Figure 1.8. In this Figure, we show the star formation history (SFH) of spiral and elliptical galaxies (upper panels), as classified in the Galaxy Zoo project (Lintott et al., 2011, see Chapter 3 for a description of the galaxy sample presented in this Figure). Elliptical galaxies contain mainly old stellar populations, whereas spiral systems present an extended SFH. Lower panels in Figure 1.8 show the SFH of elliptical galaxies with different masses, where the *downsizing* effect is apparent.

Different mechanisms driving the formation of galaxies are expected to leave signatures in their SFH. Therefore, the analysis of stellar populations in galaxies is a powerful tool to study, characterize, and constrain several processes. In Chapter 3, we present a study of the relation between the curvature in the scaling relations and the stellar populations within galaxies. We find a clear difference between the age and metallicity distributions of the stellar populations in galaxies with masses above and beyond $M_{\star} \sim 3 \times 10^{10} M_{\odot}$, which suggests a sudden transition from a constant, highly efficient mode of star formation in high-mass galaxies, gradually decreasing towards the low-mass end of the sample, with half of the stars already in place by redshift $z \sim 2$ for all masses. The metallicity-age trend in low-mass galaxies is not compatible with infall of metal-poor gas, suggesting instead an outflow-driven relation.

Relation between galaxy properties and environment

The observed properties of galaxies have long been known to depend on the environment in which they reside. As structure grows, galaxies join more and more massive systems, therefore experiencing from low- to high-density environments during their lifetimes. In this context, the *nature* and *nurture* scenarios of galaxy evolution are inevitably intertwined, and the evolution of galaxy properties and the formation of large-scale structures go hand in hand.

In this work, we investigate the properties of galaxies within groups, and we find exciting results. We explore galaxy evolution and spatial patterns in the surroundings of a sample of 2dF groups, as described in Chapter 4. Our aim is to find evidence of galaxy evolution and clustering

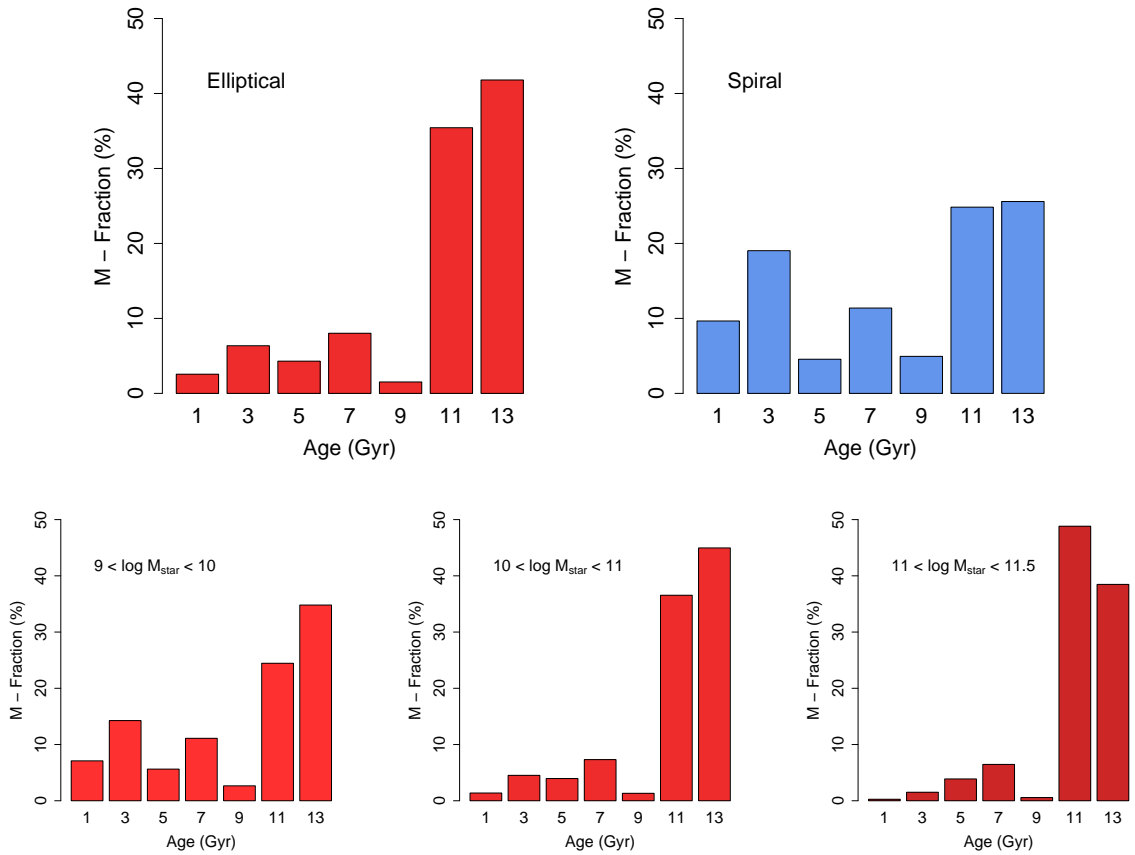


Figure 1.8: Star formation history of different types of galaxies. *Upper panels*: SFH of elliptical (*left*) and spiral galaxies (*right*). *Lower panels*: SFH of elliptical galaxies within three mass ranges.

out to 10 times the virial radius of the groups and so redefine their properties according to the spatial patterns in the fields and relate them to galaxy evolution. We found an important anticorrelation between anisotropy around groups and the fraction of early-type galaxies in these fields. Our results illustrate how the dynamical state of galaxy groups can be ascertained by the systematic study of their neighborhoods. This is an important achievement, since the correct estimate of the extent to which galaxies are affected by the group environment and follow large-scale filamentary structure is relevant to understanding the process of galaxy clustering and evolution in the Universe.

In Chapter 5, we study segregation phenomena in 57 groups selected from the 2PIGG catalog of galaxy groups. The dynamical state of the galaxy systems was determined after studying their velocity distributions. This analysis indicates that 84% of groups have galaxy velocities consistent with the normal distribution, while 16% of them have more complex underlying distributions. Properties of the member galaxies are investigated taking into account this classifica-

tion. Our results indicate that galaxies in Gaussian groups are significantly more evolved than galaxies in non-relaxed systems out to distances of $\sim 4R_{200}$, presenting significantly redder (B-R) colors. We also find evidence that galaxies with $M_R \leq -21.5$ in Gaussian groups are closer to the condition of energy equipartition.

The study of 9 galaxy groups with evidence for non-Gaussianity in their velocity distributions out to $4R_{200}$ is presented in Chapter 6. Statistical analysis indicates that non-Gaussian groups have masses significantly higher than Gaussian groups. We also have found that all non-Gaussian systems seem to be composed of multiple velocity modes. Besides, our results indicate that multimodal groups should be considered as a set of individual units with their own properties. In particular, we have found that the mass distribution of such units are similar to that of Gaussian groups. Our results reinforce the idea of non-Gaussian systems as complex structures in the phase space, likely corresponding to secondary infall aggregations at a stage before virialization. The understanding of these objects is relevant for cosmological studies using groups and clusters through the mass function evolution.

1.2.3 Galaxies at high redshift

Due to the finiteness of the speed of light, looking far away in space is also looking back in time. Therefore, we can follow the evolution of galaxies directly, in a statistical way, by observing these objects at different redshift. Besides, any successful model of galaxy formation should be able to predict the properties of galaxies at all redshifts.

Studies of distant objects have shown that the size of low-redshift early-type galaxies is twice larger than objects at $z \sim 1$ (e.g. Trujillo et al., 2007). It is still not clear which mechanism drives the evolution of the mass-size relation. Another important result concerns to the number density of massive objects at high-redshift. Several studies find an excess of high-mass galaxies when compared to what is predicted by current models (e.g. Conselice et al., 2007; Bertone & Conselice, 2009; Ferreras et al., 2009; Guo et al., 2010). Explaining these observations is closely connect to our understanding of how galaxies are formed.

1.2.4 Models and simulations of galaxy formation

In the last years, two approaches have been developed to study galaxy formation and evolution: *semi-analytic models* (Cole et al., 2000; Somerville et al., 2008; De Lucia & Blaizot, 2007;

Croton et al., 2006; Kang et al., 2005; Guo et al., 2010) and *direct cosmological simulations* (Oser et al., 2010; Pearce et al., 2001; Dave et al., 1997; Dolag et al., 2009; Wadsley et al., 2004; Kereš et al., 2005). Semi-analytic models use pre-calculated DM merger trees and follow the formation of galaxies with simplified analytic recipes. Direct cosmological simulations can follow the evolution of DM and gas components explicitly. However, the spatial and mass resolutions of the simulations are not high enough to accurately simulate low mass galaxies. Besides, more detailed processes in the simulations, such as star formation, supernovae and black hole feedback, are computed in a simplified manner.

Despite their limitations, both semi-analytic models and simulations are able to predict the evolution of galaxy properties over time. Recent simulations and theoretical models have shown that galaxies acquire most of their baryons via cold streams (Kereš et al., 2005; Dekel et al., 2009; Faucher-Giguère & Kereš, 2011). These cold streams correspond to intergalactic gas accreted by galaxies, which does not experience virial shock heating, and are mainly distributed along filaments. These streams can penetrate deep into the galaxy and form stars with high efficiency, due to the enhanced density of the cold gas along these filaments.

This stream-driven scenario for the formation of galaxies is an alternative to the merger picture. It can account for *i*) star-forming galaxies at high redshift, which are clumpy disk galaxies, incompatible with ongoing merger (Genzel et al., 2006; Förster Schreiber et al., 2006); *ii*) compact high-redshift spheroids, which cannot be explained by infrequent major merger (Kriek et al., 2006; van Dokkum et al., 2008); *iii*) number density of massive early-type galaxies at high-redshift (Conselice et al., 2007; Ferreras et al., 2009); *iv*) massive disk galaxies with no classical bulge (Kormendy et al., 2010; Howard et al., 2009). Despite the role that cold accretion is likely to play in galaxy formation, observations do not show clear signatures of infalling cold gas, which has been interpreted as a challenge for current models (e.g. Steidel et al., 2010). However, there are few studies of observational features of cold streams (Faucher-Giguère et al., 2010; Faucher-Giguère & Kereš, 2011; La Barbera et al., 2011), and no unambiguous interpretation of observations can be made.

1.3 What will be addressed in this thesis?

It should be clear from the above discussion that structure formation is a subject of great complexity, involving many strongly intertwined processes. In this thesis, we concentrate efforts

on studying our own Galaxy, early-type galaxies and galaxies residing in groups. Each of these studies constrains different processes, and they have their own challenges, as discussed in the following Chapters.

Stars can provide important information about the assembly of their host galaxies, since different formation processes leave typical signatures in their velocity and metallicity distributions. In Chapter 2, we study a sample of metal-rich stars in the Milky Way, and by combining chemical abundances and kinematics, we address processes driving the evolution of the Galactic disk.

We have studied the stellar content of early-type galaxies, and we have traced their star formation history and chemical enrichment. As we will show in Chapter 3, we are able to put constraints on feedback processes.

We have also investigated the properties of galaxies in groups. Galaxy evolution and spatial distribution in the surroundings of groups out to 10 times the virial radius are studied in Chapter 4. In Chapter 5, we explore properties of the member galaxies as a function of the dynamical state of the group. In Chapter 6, we present a study of galaxy groups with evidence for non-Gaussianity in their velocity distributions. These departures from Gaussianity can be interpreted as secondary infall aggregations at a stage before virialization.

Finally, in Chapter 7, we summarize and discuss future work and other closely related programs.

Old and very metal-rich stars in the solar neighbourhood¹

2.1 Introduction

The formation and properties of the thin and thick disks of our Galaxy have been the subject of several studies, and several scenarios have been proposed to explain their formation (e.g. Schönrich & Binney, 2009a,b; Villalobos et al., 2010, and references therein). In each scenario, typical signatures into the velocity and metallicity distribution of stars are imprinted. For this reason there have been numerous studies devoted to determination of the thick disk velocity ellipsoid and metallicity distribution, the study of the thin disk to the thick disk interface, abundance trends and correlations between abundance and kinematics, or the existence of gradients (e.g. Ivezić et al., 2008; Katz et al., 2011).

It is well-known that thick disk stars move on higher eccentricity orbits and present larger velocity dispersions than thin disk stars. The thick disk is a more slowly rotating stellar system than the thin disk, and as a whole it lags behind the local standard of rest by $\sim 50 \text{ km s}^{-1}$, while the thin disk component lags by only $\sim 12 \text{ km s}^{-1}$ (Soubiran et al., 2003; Robin et al., 2003). Thick disk stars also appear to be significantly older than thin disk ones (Fuhrmann, 1998).

On the other hand, the behaviour of the chemical abundance characteristics of these components still is a matter of debate. Some studies suggest that the thick disk component is composed mainly of metal-poor stars (e.g. Chiba & Beers, 2000; Reddy & Lambert, 2008), while metal-rich stars appear to be restricted to the thin disk, with a transition occurring at $[\text{Fe}/\text{H}] \sim -0.3$ (Mishenina et al., 2004; Reddy et al., 2006). Previous results show that thick disk stars exhibit a larger

¹ Chapter published as: Trevisan et al. 2011, A&A, 535, 42.

abundance of α -elements relative to iron than the thin disk members (Fuhrmann, 1998; Gratton et al., 2000; Ruchti et al., 2010). Bensby et al. (2003) and Feltzing et al. (2003) found that thick disk stars extend to solar metallicities, showing an inflexion in $[\alpha/\text{Fe}]$ vs. $[\text{Fe}/\text{H}]$ around $[\text{Fe}/\text{H}] \sim -0.5$, reaching the solar ratios at $[\text{Fe}/\text{H}] \sim 0.0$. Also, a new population has been identified in several studies: Reddy et al. (2006) and Haywood (2008) identify a population having thick disk kinematics but thin disk abundances (TKTA subsample in Reddy et al.). Mishenina et al. (2004) and Soubiran & Girard (2005) find metal-rich stars with kinematics of the thick disk.

A detailed study of stars with these properties can clarify the origin of this population. Therefore, in this work we study a sample of 71 metal-rich stars in terms of kinematics and abundances.

This Chapter is organized as follows. In Sect. 2.2, a description of the sample is presented, and the observations and reductions are described in Sect. 2.3. The Galactic orbits are derived in Sect. 2.4. Derivations of stellar parameters effective temperatures, gravities, and metallicities are given in Sect. 2.5. In Sect. 2.6, the element abundances are derived. In Sect. 2.7 the present results are compared with other samples from the literature, and we briefly discuss the possible origins of the identified stellar populations in the context of the Galaxy formation. Finally, results are summarized in Sect. 2.8.

2.2 *Sample selection*

Grenon (1972, 1989, 1990, 1998, 2000) selected 7824 high proper motion stars from the New Luyten's Two Tenths catalogue (NLTT) (a catalogue of nearby stars with proper motions $\mu > 0.18 \pm 0.02$ arcsec yr⁻¹) that have been included in the HIPPARCOS programme. Among these, radial velocities and Geneva photometry were gathered for 5443 stars. Only stars with parallaxes larger than 10 mas were kept for the study presented in Raboud et al. (1998). Among these, space velocities were measured for 4143 stars, and metallicities from Geneva photometry were gathered for 2619 of them. From their kinematics, Raboud et al. (1998) found that the old disk stars in this sample appeared to show a positive mean U motion. In particular, an imbalance between positive and negative U velocities was found for old disk stars selected in the parallax range 10 to 40 mas (with U positive in the direction of the anti-centre), reaching up to 50 km s⁻¹. After corrections for local motions, the U anomaly is $+29 \pm 2$ km s⁻¹ with respect to the Sun, and $+19 \pm 9$ km s⁻¹ with respect to the Galactic centre. Raboud et al. suggested that the metal-rich stars within this sample appear to wander from inside the bar, reaching the solar neighbourhood.

Table 2.1 - Sample stars in common with the Geneva-Copenhagen survey (Holmberg et al., 2009).

Star	R_{\min} (kpc)	ΔR_{\min} (kpc)	R_{\max} (kpc)	ΔR_{\max} (kpc)	e	Δe	Z_{\max} (kpc)	ΔZ_{\max} (kpc)
HD 9424	3.44	-0.35	8.28	0.47	0.41	0.07	0.08	0.03
HD 13386	4.74	-0.41	8.02	0.55	0.26	0.07	0.10	0.15
HD 25061	4.94	-0.23	9.20	0.44	0.30	0.04	0.04	0.15
HD 26151	6.39	-0.19	9.27	0.41	0.18	0.04	0.07	0.00
HD 35854	6.54	-0.36	8.02	0.53	0.10	0.06	0.17	-0.13
HD 82943	6.96	-0.25	8.23	0.41	0.08	0.05	0.03	0.16
HD 86249	8.00	0.51	8.78	0.21	0.05	-0.02	0.24	0.19
HD 90054 ^a	3.39	-0.33	8.02	0.50	0.41	0.06	0.18	0.13
HD 95338	2.98	-0.30	8.02	0.53	0.46	0.06	0.74	0.14
HD 104212	3.81	-0.63	7.98	0.53	0.35	0.11	0.24	0.36
HD 107509	3.43	-0.42	8.03	0.53	0.40	0.08	0.25	0.19
HD 148530	3.76	-0.20	9.12	0.59	0.42	0.04	0.51	0.17
HD 171999 ^b	3.94	-0.45	7.97	0.52	0.34	0.08	0.06	0.16
HD 180865	4.41	-0.30	8.02	0.50	0.29	0.06	0.11	0.15
HD 181433	6.72	0.07	10.06	0.41	0.20	0.01	0.27	-0.24
HD 218750	4.52	-0.54	8.16	0.53	0.29	0.08	0.30	-0.22
HD 224383	3.84	-0.38	8.59	0.44	0.38	0.07	0.09	0.02
Average		-0.28 ± 0.26		0.48 ± 0.09		0.06 ± 0.03		0.08 ± 0.16

Notes. $\Delta = \text{Our} - \text{GCS}$. ^(a)Binary. ^(b)Spectroscopic binary.

A subsample of 202 of these stars was selected for this project by M. Grenon when gathering the oldest disk stars, with high metallicities and eccentricities, as well as thin disk very metal-rich stars. We were able to obtain high-resolution spectra for 100 of them using the FEROS spectrograph at the 1.5m ESO telescope at La Silla, during an IAG/ON and ON/ESO agreement in 1999-2002.

The Geneva photometry was used by Grenon (1978) to derive the effective temperatures, absolute magnitudes, and metallicities, with internal errors of 20 – 40 K on effective temperature T_{eff} , 0.03 – 0.05 dex on metallicity [M/H] and 0.15 on V magnitudes.

For the present analysis, we selected the 71 most metal-rich stars of the sample of 100 observed stars, indicated by Geneva photometry to have $[\text{Fe}/\text{H}] > 0.00$. A study of α -elements vs. $[\text{Fe}/\text{H}]$ in their full metallicity range, for 36 among the 100 observed such stars, covering $-0.8 <$

$[\text{Fe}/\text{H}] < +0.4$, was presented by Pompéia et al. (2003). There are 12 stars in common between the present sample and Pompéia et al. (2003), where another 24 stars with metallicities below solar, were also analysed, with the aim of identifying the downturn knee of $[\alpha/\text{Fe}]$ vs. $[\text{Fe}/\text{H}]$, as discussed in Sect. 2.7. All the stars in the sample have parallaxes larger than 10 mas, with errors of 6% in average.

2.3 Observations and reductions

Optical spectra were obtained using the Fiber Fed Extended Range Optical Spectrograph (FEROS) (Kaufer et al., 2000) at the 1.52 m telescope at ESO, La Silla. The total wavelength coverage is 3560-9200 Å with a resolving power of $(R=\lambda/\Delta\lambda) = 48,000$. Two fibres, with entrance aperture of 2.7 arcsec, simultaneously recorded star light and sky background. The detector is a back-illuminated CCD with 2948 x 4096 pixels of 15 μm size.

Reductions were carried out through a pipeline package for reductions (DRS) of FEROS data, in MIDAS environment. The pipeline performs the subtraction of bias and scattered light in the CCD, orders extraction, flatfielding and wavelength calibration with a ThAr calibration frame. The data reduction proceeded in the IRAF environment as follows. The spectra were cut into parts of 500 Å each using the SCOPY task, and the normalization was carried out with the CONTINUUM task. Spectra of rapidly rotating hot B stars at similar airmasses as the target were also observed, in order to correct for telluric lines using the TELLURIC task. The radial and heliocentric velocities, v_r and v_{Helio} , were determined using the RVCORRECT task. The standard errors of the velocities are $\sim 0.2 \text{ km s}^{-1}$. Typical signal-to-noise ratios of the spectra were obtained considering average values at different wavelengths. The mean signal-to-noise ratio for the sample stars is ~ 100 , as reported in Table B.1.

2.4 Kinematics

Grenon (1999) found that the high metallicity stars in the sample have low maximum height from the Galactic plane Z_{max} , and their turn-off location indicated an age of ~ 10 Gyr. The identification of an old population with such a high metallicity and low Z_{max} is unexpected. In order to investigate the kinematical properties of the sample stars, we derive the Galactic orbits in Sect. 2.4.1, using the GRINTON integrator (Carraro et al., 2002; Bedin et al., 2006). In Sect. 2.4.2,

we separate the sample into thin disk and thick disk stars, based on kinematical criteria. We assigned a probability of each star belonging to either the thin or the thick disk, assuming that the space velocities of each population follow a Gaussian distribution as defined by Soubiran et al. (2003).

2.4.1 Galactic orbits

Grenon (1999) derived U , V , W space velocities for all the sample stars. U , V , W are defined in a right-handed Galactic system with U pointing outwards the Galactic centre, V in the direction of rotation and W towards the north Galactic pole. We used the GRINTON integrator to calculate the Galactic orbits, with these velocities and the HIPPARCOS parallaxes. This code integrates the orbits back in time for several Galactic revolutions and returns the minimum and maximum distances from the Galactic centre (R_{\min} , R_{\max}), maximum height from the Galactic plane (Z_{\max}) and the eccentricity e of the orbit. Before using the observed space motions, these were transformed to the local standard of rest. We used a solar motion of $(-10.0, 5.3, 7.2)$ km s^{-1} (Dehnen & Binney, 1998). The gravitational potential used in the orbit integration is a simple one (Allen & Santillan, 1991), for which a circular rotation speed of 220 km s^{-1} and a disk volume density of $0.15 M_{\odot} \text{ pc}^{-3}$ are adopted and a solar Galactocentric distance $R_{\odot} = 8.5 \text{ kpc}$ is assumed.

Uncertainties in the orbital parameters were obtained using the bootstrapping technique, as follows. We integrated the orbit of each star 500 times. At each integration, the input parameters, U , V , W velocities and the parallax π , were varied following a normal distribution with mean X and standard deviation of σ_X , where X is the parameter value and σ_X the error associated with it. The final orbital parameters R_{\min} , R_{\max} , Z_{\max} , and eccentricity, and their errors were then computed as the mean and standard deviation of the output values of these 500 realizations. Uncertainties in R_{\min} , R_{\max} , and Z_{\max} are typically $\approx 0.30 \text{ kpc}$, 0.60 kpc , and 0.05 kpc , respectively. The derived orbital parameters are listed in Table B.3. Our sample contains 17 stars in common with the Geneva-Copenhagen survey (Holmberg et al., 2009), hereafter referred to as GCS, as listed in Table 2.1. We compared the orbital parameters derived here with the values from the GCS survey. We found that our R_{\min} distances are $\sim 6\%$ lower and R_{\max} are $\sim 5\%$ higher on average. For the orbit eccentricities, we derived values which are $\sim 16\%$ higher than eccentricities from GCS. The maximum height from the Galactic plane from GCS are $\sim 80 \text{ pc}$ lower ($\sim 30\%$) than our sample, on average.

Table 2.2 - Velocity ellipsoids for the thin disk, thick disk, and halo.

Component	σ_U	σ_V	σ_W	V_{lag}	Fraction
Thin disk ^a	39	20	20	-7	0.85
Thick disk ^a	63	39	39	-46	0.15
Halo ^b	131	106	85	-220	0.006

Notes. ^(a)Soubiran et al. (2003). ^(b)Robin et al. (2003).

^(c)Famaey et al. (2005)

It is important to stress that the gravitational potential used in the orbit integration does not take the Galactic bar into account. The bar potential could affect the orbits of our stars, since R_{min} are as close as 3-4 kpc from the Galactic centre.

2.4.2 Thin and thick disk membership probabilities

Identifying stellar populations in velocity space is not straightforward. Thus, before discussing whether the sample stars belong to the thin or thick disk, we must analyse the criteria used to define the membership probabilities.

The separation between thin and thick disks can be done either by selecting stars based on their kinematics, using chemical composition criteria, or a combination of both. Usually, separation based only on kinematics or abundances are not equivalent: thick (thin) disk samples selected on kinematical criteria can contain stars with thin (thick) chemical abundances (e.g. Mishenina et al., 2004; Reddy et al., 2006). Some authors argue that, since the chemical composition of a star does not change with time, while kinematics may change, the selection based on abundances is more reliable. On the other hand, if we want to trace the formation of the disk components through the study of the chemical abundances of their stars, the abundances must not be used to define these components. Therefore, here we assign the probability of each star belonging to either the thin disk or the thick disk by adopting the kinematical approach used in previous studies by Bensby et al. (2004), Mishenina et al. (2004), and Reddy et al. (2006). The procedure relies on the assumption that the space velocities of each population follow a Gaussian distribution, with given mean values and dispersions σ_U , σ_V , σ_W . The equations determining the probabilities are

$$p_{\text{thin}} = f_1 \frac{p_1}{p}, \quad p_{\text{thick}} = f_2 \frac{p_2}{p}, \quad p_{\text{halo}} = f_3 \frac{p_3}{p} \quad (2.1)$$

where p_{thin} , p_{thick} , p_{halo} correspond to the probability that the star belongs to either the thin disk, thick disk or halo, respectively. Then, p and p_i are given by

$$p = f_1 p_1 + f_2 p_2 + f_3 p_3$$

and

$$p_i = \frac{1}{(2\pi)^{3/2} \sigma_{U_i} \sigma_{V_i} \sigma_{W_i}} \exp \left[-\frac{U^2}{2\sigma_{U_i}^2} - \frac{(V - V_{\text{lag}})^2}{2\sigma_{V_i}^2} - \frac{W^2}{2\sigma_{W_i}^2} \right]. \quad (2.2)$$

The parameters f_i are the relative densities of thin disk, thick disk, and halo stars in the solar neighbourhood. Since there is an overlap of the Gaussian distributions in velocity space, the definition of the thin and thick disk populations is very sensitive to the choice of parameters defining the Gaussian distributions and the population fractions. There are several studies devoted to determining of the velocity ellipsoids of the thin disk, thick disk, and halo components, as well as the population fractions in the solar neighbourhood. Here we compared studies by Soubiran et al. (2003) and Robin et al. (2003). We determined the probabilities using the values given in Table 2.2, where the velocity ellipsoids for the thin and thick disks were taken from Soubiran et al. (2003), and values from Robin et al. (2003) were used for the halo component. We also applied the same procedure to the thin disk, thick disk, and halo velocity dispersions and fractions from Robin et al. (2003): $(\sigma_U, \sigma_V, \sigma_W)_{\text{thin}} = (43, 28, 18) \text{ km s}^{-1}$ and $(\sigma_U, \sigma_V, \sigma_W)_{\text{thick}} = (67, 51, 42) \text{ km s}^{-1}$, $f_{\text{thin}} = 0.93$ and $f_{\text{thick}} = 0.07$.

As a test, we applied the procedure, using Soubiran et al. (2003) and Robin et al. (2003), to the GCS stars, and the results are shown in Figure 2.1. The decomposition of a larger sample into thin/thick disk makes the differences between Soubiran et al. (2003) and Robin et al. (2003) clearer. We considered that, if the probability of a star belonging to either the thin or thick disk is higher than 80%, then the star can be assigned to that component. If both p_{thin} and p_{thick} are lower than 80%, the star is classified as member of the intermediate population. Using velocity ellipsoids defined by Soubiran et al. (2003), we found that 81% of the GCS stars belong to the

Table 2.3 - Mean data for the thin, thick, and intermediate populations.

Group	Age (Gyr)	[Fe/H] (dex)	[α /Fe] (dex)	R_m^a (kpc)	U_{LSR}^b (km s ⁻¹)	V_{LSR}^b (km s ⁻¹)	W_{LSR}^b (km s ⁻¹)	e	Z_{max} (kpc)
Thin disk	7.8 ± 3.5	0.20 ± 0.22	-0.01 ± 0.05	8.2 ± 0.6	-10 ± 51	-19 ± 16	-11 ± 15	0.20 ± 0.08	0.21 ± 0.16
Thick disk	7.5 ± 3.1	0.22 ± 0.17	0.00 ± 0.04	6.3 ± 0.4	36 ± 43	-84 ± 17	-21 ± 23	0.40 ± 0.07	0.38 ± 0.40
Intermediate	6.8 ± 2.9	0.29 ± 0.17	-0.02 ± 0.03	7.3 ± 0.5	37 ± 61	-48 ± 13	-20 ± 14	0.29 ± 0.05	0.28 ± 0.22

Notes. ^(a)Mean Galactocentric distance, $R_m = (R_{\text{max}} + R_{\text{min}})/2$.

^(b)Space velocities with respect to the local standard of rest.

thin disk, 5% are thick disk stars, and 14% cannot be assigned to either of the components. The thin disk stars are restricted to $V > -50$ km s⁻¹. Using Robin et al. (2003), the following fractions were found: 92%, 2%, and 6% are thin, thick, and intermediate stars, respectively, and the thin disk stars can rotate as slowly as $V \sim -80$ km s⁻¹.

We then classified our 71 sample stars using velocity ellipsoids from Soubiran et al. (2003), and we found that 42 stars in the sample can be assigned to the thick disk, and 11 are more likely to be thin disk stars. The other 17 stars in the sample are intermediate between thin and thick disk components. Using Robin et al. (2003), we found that 16 stars in the sample belong to the thick disk, and 29 are more likely to be thin disk stars. The other 26 stars in the sample are not clearly members of either the thin or the thick disk components.

The same procedure (i.e., equations 2.1 and 2.2) was applied to the groups and stellar streams identified by Famaey et al. (2005). They applied a maximum-likelihood method to the kinematical data of 6691 K and M giants in the solar neighbourhood. They identified six kinematical groups: *i*) group Y, containing stars with “young” kinematics; *ii*) group HV, composed of high-velocity stars, which are probably mostly halo or thick disk stars; *iii*) group HyPl, the Hyades-Pleiades supercluster; *iv*) group Si, the Sirius moving group; *v*) group He, the Hercules stream; and *vi*) group B, which is composed of a “smooth” background in the UV plane, that are mostly thin disk stars. We obtained the probabilities of our sample stars belonging to these groups following the same procedure as above, assuming that the space velocities of each group follow a Gaussian distribution, with mean values, dispersions, and population fractions taken from Famaey et al.

As expected, neither of the sample stars belong to groups Y, HyPl, and Si, with probabilities below 1%. Only two stars have $p_Y > 1\%$: HD 35854 has $p_Y = 6\%$ and HD 82943 has $p_Y = 17\%$, respectively. Despite 11 stars in the sample having a probability of belonging to the Hercules

stream larger than 50%, neither of them satisfied our criteria $p_{\text{He}} > 80\%$ to be assigned to this group. Six stars in our sample appear to belong to the B group ($p_{\text{B}} > 80\%$), and 37 have kinematics compatible with the HV group ($p_{\text{HV}} > 80\%$). The other 28 stars in the sample cannot be assigned clearly to either of these groups.

The right-hand panel in Figure 2.1 presents the high velocity group, the B group and Hercules Stream stars, as classified by Famaey et al. (2005), and our sample star data overplotted in the Toomre diagram. In Table 2.4 the kinematics of our sample are compared with the data for 6030 stars from Famaey et al. (2005), where all the samples analysed show low maximum height above the plane. It appears that our sample is compatible with the high-velocity group (HV), and might be identified with that subpopulation. This group is probably composed of halo or thick-disk stars, and represents about 10% of the whole sample analysed by Famaey et al. (2005). Most stars assigned to the thick disk component, following the Soubiran et al. (2003) velocity distributions, are also members of the HV group.

The probabilities assumed for classifying the present 71 sample stars are those obtained with Soubiran et al. (2003) velocity ellipsoids, and not those suggested by Robin et al. (2003) (that give a low fraction of thick disk stars $f_{\text{thick}} = 0.07$). A higher fraction of nearby thick disk stars is supported by recent studies of the SDSS data (Jurić et al., 2008). Moreover, membership probabilities obtained with Soubiran et al. (2003) criteria are in better agreement with the more detailed analysis of the velocity space by Famaey et al. (2005). The final probabilities p_{thin} and p_{thick} are reported in Table B.3. In Table 2.3, we report the mean ages, metallicities, $[\alpha/\text{Fe}]$, space velocities, eccentricities, and maximum height above the Galactic plane for each of the populations: thin disk, thick disk, and intermediate. The stars with intermediate properties are so classified for having intermediate eccentricity, V velocity, Z_{max} , and R_{m} relative to the thick and thin disks.

2.5 Stellar parameters

A common method for deriving of stellar parameters relies on the abundances derived from Fe I and Fe II lines, by requiring excitation and ionization equilibria. In this work it was not assumed *a priori* that the absolute equilibria are reached, since this procedure could hide non-LTE effects, leading to misleading parameters. This choice is justified by previous work, which suggests that deviations from LTE are present in metal-rich dwarf stars (e.g. Feltzing & Gustaf-

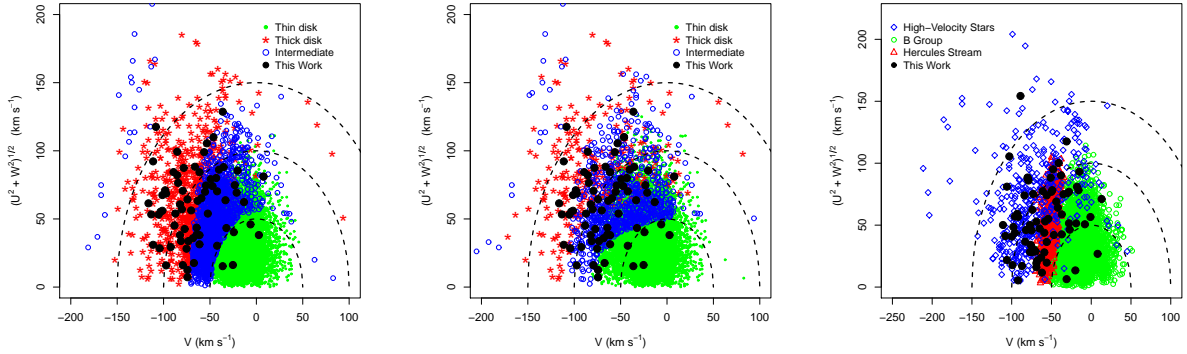


Figure 2.1: Toomre diagram of GCS stars. *Left and middle panels:* The thin/thick disk decomposition of GCS stars was performed using the velocity dispersions and star fractions from Soubiran et al. (2003) (*left*) and from Robin et al. (2003) (*middle*). The thin, thick, and intermediate stars of the GCS are represented by green dots, red stars, and open blue circles, respectively. The dashed lines indicate the total space velocity, $v_{\text{total}} = \sqrt{U^2 + V^2 + W^2}$, in steps of 50 km s^{-1} . *Right panel:* Toomre diagram showing the groups identified by Famaey et al. (2005): the Hercules stream (red open triangles), high-velocity stars (blue open diamonds), and B-group stars (green open circles). In all panels the present sample is indicated by black dots.

son, 1998; Meléndez & Ramírez, 2005). Therefore, the stellar temperatures and surface gravities were obtained without recourse to the Fe I and Fe II lines as follows.

- i)* The effective temperatures were calculated from the $(V-K_S)$ colour using the Casagrande et al. (2010, hereafter CRM10) colour-temperature relations, as described in Sect. 2.5.1.
- ii)* Then, $\log g$ is derived from masses and parallaxes. Using the HIPPARCOS parallaxes and the stellar masses from the Yonsei-Yale evolutionary tracks (Demarque et al., 2004), hereafter Y^2 , the surface gravities were derived following the procedure presented in Sect. 2.5.2.
- iii)* We used the metallicities from Geneva photometry as first guesses in steps *i* and *ii*.
- iv)* Then, fixing T_{eff} and $\log g$, the iron abundance and microturbulence velocity were derived from Fe I and Fe II lines, through local thermodynamic equilibrium (LTE) analysis, using the MARCS model atmospheres (Gustafsson et al., 2008). The microturbulence velocity was obtained by imposing constant iron abundance as a function of equivalent width (except for the cooler stars). The iron abundance and microturbulence velocity determinations are described in detail in Sect. 2.5.3.

Table 2.4 - Mean kinematical data for our sample, compared with kinematic groups studied by Famaey et al. (2005). Standard deviations are presented in parenthesis.

Kinematic group	$\langle U(\text{km s}^{-1}) \rangle$	$\langle V(\text{km s}^{-1}) \rangle$	$\langle W(\text{km s}^{-1}) \rangle$	$\langle Z_{\text{max}}(\text{pc}) \rangle$
present sample	17.6 (55.0)	-60.1 (29.7)	-10.6 (21.0)	330.0
HV Stars	18.5 (62.6)	-53.3 (37.2)	-6.6 (45.9)	208.1
B Group	2.9 (31.8)	-15.2 (17.6)	-8.2 (16.3)	196.1
Hercules Stream	42.1 (25.3)	-51.6 (7.1)	-8.1 (15.4)	132.9

Notes. HV refers to high-velocity stars.

- v) The Geneva metallicity was then replaced by the new iron abundance, to go through the whole iteration process
- vi) the procedure was repeated until there were no significant changes in (T_{eff} , $\log g$, $[\text{Fe}/\text{H}]$).

The changes on temperatures and gravities due to changes on metallicities are small, but not zero. Therefore, the procedure includes iteration to keep internal consistency. The final photometric parameters were tested against excitation and ionization equilibria, and T_{eff} and $\log g$ were further adjusted if necessary, as shown in Sect. 2.5.4. Only two stars in the sample required adjustments to be in satisfactory spectroscopic equilibrium.

We estimated ages for the sample stars, using the Y^2 isochrones. Details about the determination of stellar masses and ages are given in Sect. 2.5.5. Final considerations about the parameter determinations and comparison with other studies are presented in Sect. 2.5.6.

2.5.1 Temperatures

The basic photometric data used in temperature determinations are presented in Table B.2: photometric temperatures from Geneva photometry; V magnitudes (ESA, 1997); J and K_S magnitudes from 2MASS (Skrutskie et al., 2006); Bolometric correction BC_V from Alonso et al. (1995) (see Sect. 2.5.2); and HIPPARCOS parallaxes π (ESA, 1997). Errors of about 0.02 mag apply to V magnitudes; the errors on the other magnitudes are reported in Table B.2. The sample stars are all within 90 pc of the Sun and since interstellar reddening is usually zero for stars lying within 100 pc of the Sun (Schuster & Nissen, 1989), no reddening corrections were applied. We checked this assumption using the extinction law by Chen et al. (1998), and we verified that

the maximum reddening correction would be 0.1 mag for HD 104212. This level of extinction would raise the temperature by 130 K. Even so, excitation equilibrium was reached for this star (see Sect. 2.5.4). Thus, we adopted $A_V = 0$ for all the sample stars.

We derived temperatures from CRM10's colour-temperature calibrations. The results were compared with those determined with the widely adopted relations from Alonso et al. (1996, hereafter AAM96) and with temperatures from Geneva photometry, which are also available for all the sample stars.

CRM10 provide colour-temperature relations for Johnson V and 2MASS J and K_S magnitudes, so no magnitude system transformations are needed. To determine the photometric $T_{(J-K)}$ and $T_{(V-K)}$ temperatures from the colour-temperature calibrations described in AAM96, the following photometric system transformations were used. The J, K_S magnitudes and colours were transformed from the 2MASS system to CIT (California Institute of Technology) system, and from the latter to TCS (Telescopio Carlos Sánchez) system, with the relations established by Carpenter (2001) and Alonso et al. (1994). The transformations between the Johnson and TCS systems used the relations presented in Alonso et al. (1994).

Figure 2.2 presents the comparison between photometric temperatures. AAM96 relations give temperatures about 2% (~ 90 K) lower than CRM10 ones, in agreement with differences found by CRM10 between these two calibrations. As discussed in CRM10, the main source of differences between photometric T_{eff} scales is the absolute calibration of the photometric systems, which is essential when setting the zero point of the scale. The estimated zero point of the CRM10 scale is defined by a sample of solar twins, resulting in zero-point uncertainties of ~ 15 K. For AAM96 calibrations, this uncertainty is ~ 100 K (Casagrande et al., 2006, 2010). Moreover, AAM96 calibrations require photometric system transformations, which can introduce unnecessary errors. Therefore, the CRM10 calibrations were chosen for the effective temperature, and the $(V - K_S)$ colour calibration was preferred over the other colours, owing the extended base line, a confirmed lower $\sigma(T_{\text{eff}}) \sim 25$ K, and smaller dependence with $[\text{Fe}/\text{H}]$.

The internal errors in temperatures were computed considering the uncertainties in magnitudes and metallicities:

$$\sigma_{T_{\text{eff}}} = \frac{5040}{\theta^2} \left[\left(\frac{\partial \theta}{\partial [\text{Fe}/\text{H}]} \sigma_{[\text{Fe}/\text{H}]} \right)^2 + \left(\frac{\partial \theta}{\partial (V - K)} \sigma_{(V-K)} \right)^2 \right]^{1/2} \quad (2.3)$$

where $\sigma_{(V-K)}$ is the quadratic sum of errors in V and K_S magnitudes, and $\theta (= 5040/T_{\text{eff}})$ is

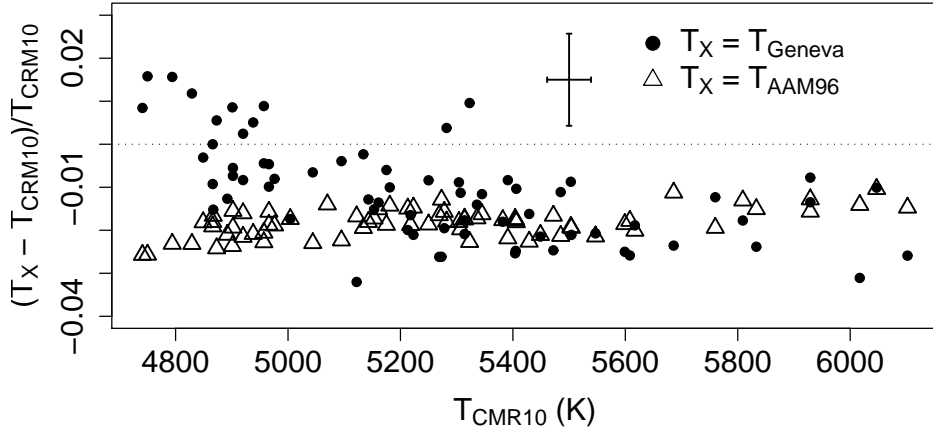


Figure 2.2: Photometric temperatures. The temperatures from CRM10 calibrations are compared with those from AAM96 relations (open triangles) and from Geneva photometry (filled circles). CRM10 temperatures are about 2% (~ 90 K) hotter than AAM96 ones.

a function of $(V - K)$ and $[\text{Fe}/\text{H}]$, as given in CRM10. Uncertainties in the zero point of the scale (15 K) and the calibration deviations (25 K, as given in Table 4 of CRM10) were added quadratically to the internal error. The final temperatures and errors are presented in Table B.7.

2.5.2 Surface gravities

The trigonometric surface gravities, $\log g$, were derived from HIPPARCOS parallaxes, π , through the standard formula

$$\log\left(\frac{g_\star}{g_\odot}\right) = 4 \log\left(\frac{T_{\text{eff},\star}}{T_{\text{eff},\odot}}\right) + 0.4(\mathcal{M}_{\text{Bol},\star} - \mathcal{M}_{\text{Bol},\odot}) + \log\left(\frac{M_\star}{M_\odot}\right), \quad (2.4)$$

where $T_{\text{eff},\star}$ and M_\star are the stellar temperature and mass, respectively, and the bolometric magnitude, $\mathcal{M}_{\text{Bol},\star}$, is given by

$$\mathcal{M}_{\text{Bol},\star} = V - A_V + \text{BC}_V + 5 \log \pi + 5.$$

The following values were adopted for the Sun: $T_{\text{eff},\odot} = 5777$ K, $\mathcal{M}_{\text{Bol},\odot} = 4.75$ (Barbuy, 2007) and $\log g_\odot = 4.44$. We used bolometric corrections BC_V from Alonso et al. (1995), where $(V-K)_\odot = 1.486$, $\text{BC}_{V,\odot} = -0.08$ were adopted.

Table 2.5 - Gravity variations with stellar parameters.

	ΔT_{eff}	ΔMass	$\Delta E(\text{B} - \text{V})$	$\Delta [\text{Fe}/\text{H}]$
	(-2 %)	(-5 %)	(+0.05 mag)	(-0.30 dex)
$\Delta \log g$ (dex)	-0.05	-0.02	0.01	< 0.01

Errors in gravities were calculated using the error propagation equation, derived from equation 2.4:

$$\sigma_{\log g}^2 = \sigma_M^2 \cdot k^2 \left(\frac{M_\odot}{M} \right)^2 + \sigma_{T_{\text{eff}}}^2 \cdot k^2 \left(\frac{4}{T_{\text{eff}}} \right)^2 + \sigma_\pi^2 \cdot k^2 \left(\frac{5}{\pi} \right)^2 + 2 \sigma_{M, T_{\text{eff}}}^2 \cdot k^2 \left(\frac{M_\odot}{M} \right) \left(\frac{4}{T_{\text{eff}}} \right) \quad (2.5)$$

where $k = \log e = 0.4343$, and errors in BC_V and magnitudes were considered to be small. The variables σ_M , $\sigma_{T_{\text{eff}}}$, and σ_π are errors in masses, temperatures, and parallaxes, respectively. Since we used the temperatures to get the masses from isochrones, the covariance between T_{eff} and mass, $\sigma_{M, T_{\text{eff}}}$, does not vanish. For each star, we took all the possible solutions $[M_i, T_{\text{eff},i}]$ within the error bars from the evolutionary tracks. Given that \overline{M} , $\overline{T_{\text{eff}}}$ are the respective mean values, the covariance can be obtained through

$$\sigma_{M, T_{\text{eff}}} = \left\langle (M_i - \overline{M}) \cdot (T_{\text{eff},i} - \overline{T_{\text{eff}}}) \right\rangle. \quad (2.6)$$

Table 2.5 presents the variations in $\log g$ with temperature, masses, $E(\text{B}-\text{V})$, and $[\text{Fe}/\text{H}]$. A temperature change of -2% (~ 100 K), which corresponds to the difference between CRM10 and AAM96 calibrations, would lead to lower stellar masses by 4% in average. The overall change in gravities is -0.05 dex on average. Despite the uncertainties involved in the determination of stellar masses, the effect on gravity is not significant: a 5% change in the masses would change gravities by only 0.02 dex. As described in Sect. 2.5.5, the masses estimated in this work have internal errors of about 3% and accuracy of 4%, resulting in a total uncertainty of about 5%. Effects of reddening corrections and changes in $[\text{Fe}/\text{H}]$ are not significant (0.01 and < 0.005 dex, respectively).

We checked the consistency between trigonometric gravities and evolutionary gravities. For this comparison, we used both Y^2 and Padova isochrones (Girardi et al., 2000). Padova gravities

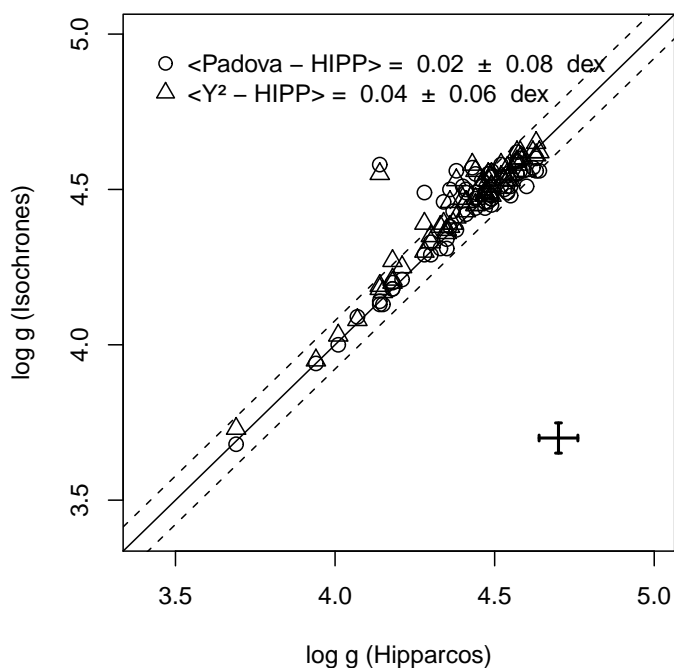


Figure 2.3: Comparison between trigonometric gravities from HIPPARCOS parallaxes and isochrone gravities. The open triangles represent the gravities obtained from Y^2 evolutionary tracks, and gravities from Padova isochrones are indicated by open circles. Solid and dashed lines show the very good agreement, with variations within ± 0.05 dex.

were obtained using the tool PARAM¹ (da Silva et al., 2006). The Y^2 gravities are the mean values of all the solutions within $T_{\text{eff}} \pm \sigma_{T_{\text{eff}}}$ and $M_{\text{abs}} \pm \sigma_{M_{\text{abs}}}$, where $\sigma_{T_{\text{eff}}}$ and $\sigma_{M_{\text{abs}}}$ are the errors in temperatures and absolute magnitudes. The agreement between both evolutionary (Y^2 , Padova) gravities and trigonometric gravities is excellent, as shown in Figure 2.3. A large difference of ~ 0.4 dex between HIPPARCOS and isochrones gravities was found for HD 201237. The photometry and/or Galactic extinction should not be the source of this discrepancy. This star has good quality photometry from the 2MASS catalogue; i.e., the photometric quality flags are set to A, and the errors on the magnitudes are ~ 0.02 mag. The reddening correction for this star is only $E(B-V) \sim 0.04$ mag, following the law by Chen et al. (1998), and this level of correction should not affect the stellar parameter determinations significantly. On the other hand, the HIPPARCOS parallax has a large error ($\sim 19\%$), which leads to an uncertainty of ~ 0.16 dex

¹ <http://stev.oapd.inaf.it/cgi-bin/param>

on gravity. Therefore, the parallax error is the most probable source of the discrepancy between HIPPARCOS and isochrones gravities. The stellar parameters found by Pompéia et al. (2002) for this star, $(T_{\text{eff}}, \log g, [\text{Fe}/\text{H}]) = (4950 \text{ K}, 4.10, -0.05)$, are in good agreement with those found in this work, $(4829 \text{ K}, 4.14, 0.00)$.

The final T_{eff} and $\log g$ parameters are presented in Figure 2.4, where Y^2 evolutionary tracks are shown for comparison.

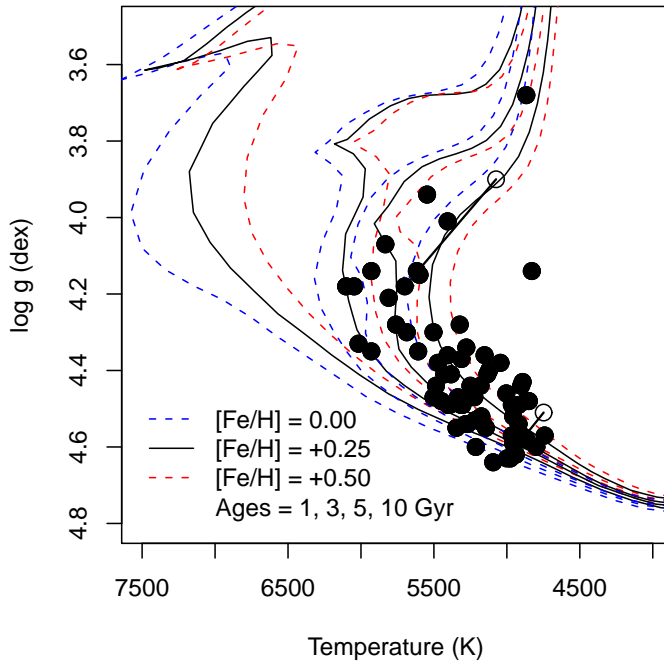


Figure 2.4: Temperatures vs. gravities. Y^2 isochrones representing different ages and metallicities are shown. The lines connecting an open and a filled circle depict changes in temperature and gravity of HD 94374 and HD 182572 to achieve excitation equilibrium (see text). The open circles indicate photometric temperatures obtained as described in Sect. 2.5.1; the filled circles correspond to the excitation-equilibrium values, which were adopted for these two stars.

2.5.3 Metallicities

We performed an LTE analysis to obtain the iron abundances from the measured equivalent widths. The calculations were carried out using the Meudon code ABON2 (Spite, 1967, and updates implemented since then). We used the MARCS 1D hydrostatic model atmospheres

(Gustafsson et al., 2008), obtained by interpolation for the appropriate parameters of the sample stars.

The list of neutral and ionized iron lines used in this work were based on the lists from Castro et al. (1997), Bensby et al. (2003) and Meléndez et al. (2009). The oscillator strengths, $\log gf$, adopted in this work were fitted in order to reproduce the solar iron abundance $(\text{Fe I}/\text{H})_{\odot} = 7.5^2$ (Grevesse & Sauval, 1998), using $T_{\text{eff}\odot} = 5777$ K, $\log g_{\odot} = 4.44$, and $\xi_{\odot} = 0.9$ km s⁻¹. The damping constants were computed when possible, using the collisional broadening theory of Barklem et al. (1998, 2000) and Barklem & Aspelund-Johansson (2005, and references therein).

The final iron line list comprises only lines that

- i*) are free of blends. We used an atlas of the solar photospheric spectrum (Wallace et al., 1998) and the VALD line lists (Kupka et al., 1999) to check for possible blends, and blended lines were discarded;
- ii*) have solar $W_{\lambda} < 100$ mÅ. For this range of W_{λ} , the astrophysical $\log gf$ values obtained from the solar equivalent widths are more reliable (for stronger lines oscillator strengths and broadening of wings have competing effects); and
- iii*) give systematically reliable abundances for the sample stars. Given that $\langle A \rangle_i$ is the iron abundance of each star, and $A_{\lambda i}$ is the abundance derived from an individual line, we checked the “quality” of the line by computing $A_{\lambda i} - \langle A \rangle_i$ for all the sample stars (Figure 2.5). This approach allows us to detect and exclude lines that give abundances systematically higher or lower than the abundance of the star by 0.15 dex and lines that seem to lead to inaccurate abundance values (deviation in $A_{\lambda i} - \langle A \rangle_i$ larger than 0.12 dex).

Atomic data adopted for the final iron line list are given in Table B.6. The equivalent widths of iron lines were measured using the automatic code ARES³ developed by Sousa et al. (2007). Given a reference line list and a list of input configuration parameters, ARES fits a continuum and measures W_{λ} by fitting a Gaussian profile.

We tested the dependence of W_{λ} on the choice of the ARES’s input parameters by comparing measurements made with different values, in particular the parameter required for the continuum definition (*rejt*) and the parameter that defines the wavelength interval around the line where the

² $(X/H) = \log(N_X/N_H) - 12$

³ <http://www.astro.up.pt/sousasag/ares/>

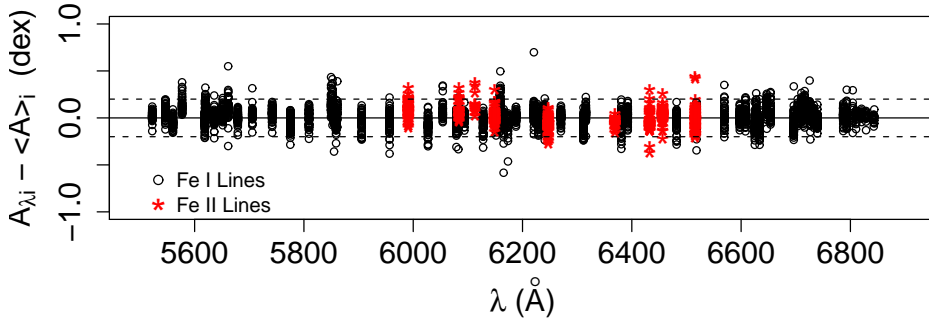


Figure 2.5: Process of selection for stable Fe I and Fe II lines. The iron abundance of each star, $\langle A \rangle_i$, is the average of abundances derived from individual lines, $A_{\lambda i}$. $A_{\lambda i} - \langle A \rangle_i$ values indicate deviations from the mean abundance value for each star. Fe I and Fe II lines are indicated as open circles and red stars, respectively.

computation will be conducted (*space*). By considering different values for these parameters in the intervals $0.993 < rejt < 0.999$ and $2 < space < 5 \text{ \AA}$, we obtained σ_{W_λ} , which is the standard deviation of the measurements. Despite the majority of the lines giving a stable result under different configurations, we found that some lines are very sensitive to the choice of these parameters. The differences between measurements made with different values of *rejt* and *space* can be as high as $\sigma_{W_\lambda} \sim 15 - 20\%$. To avoid the effect of these lines in computing of the final metallicity, for each line with $W_\lambda \pm \sigma_{W_\lambda}$, we computed the iron abundance $[\text{Fe}/\text{H}] \pm \sigma_{[\text{Fe}/\text{H}]}$. The final $[\text{Fe}/\text{H}]$ of each star was then considered as the weighted mean of the abundances, where $w = (1/\sigma_{[\text{Fe}/\text{H}]})$ were used as weights for each line.

The reliability of the ARES measurements was confirmed by comparing equivalent widths of iron lines measured with both ARES and the task SPLLOT in the IRAF context. Figures 2.6 and 2.7 present the good agreement between W_λ s measurements for the Sun and the stars HD 11608, HD 77338, and HD 81767.

We employed the equivalent widths of Fe I lines to derive the microturbulence velocity, ξ , by requiring independence between abundances and the reduced equivalent width, $\log(W_\lambda/\lambda)$. Only lines with $20 < W_\lambda < 100 \text{ m\AA}$ were used, since fainter lines show some scatter in the comparison between ARES and SPLLOT, and stronger lines are not well fitted by Gaussian profiles. No clear ξ velocities were found for our cooler stars ($T_{\text{eff}} < 5000 \text{ K}$). We considered that ξ can be defined as a function of temperature and gravity, and using stars with $T_{\text{eff}} > 5200 \text{ K}$, we defined $\xi = f(T_{\text{eff}}, \log g)$ and then extrapolated this function to $T_{\text{eff}} < 5200 \text{ K}$. We adopted 0.3 km

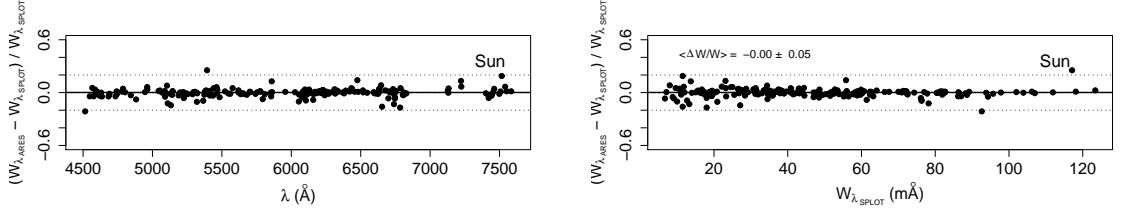


Figure 2.6: Equivalent widths measurements from ARES and IRAF for the solar spectrum. The relative differences, $(W_{\lambda_{\text{ARES}}} - W_{\lambda_{\text{IRAF}}})/W_{\lambda_{\text{IRAF}}}$, are given as a function of wavelength (*left*) and $W_{\lambda_{\text{IRAF}}}$ (*right*).

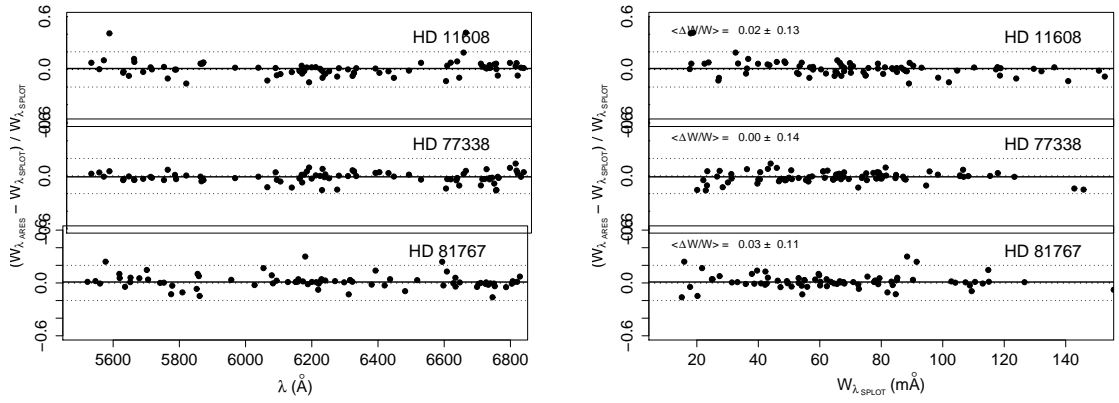


Figure 2.7: Same as Figure 2.6 for the stars HD 11608, HD 77338, and HD 81767.

s^{-1} from the extrapolation of our fit. The same problem was found by Feltzing & Gustafsson (1998) for their K dwarfs, and they adopted a constant value of 1 km s^{-1} . We found that this value is too high for our sample, leading to lower metallicities in this temperature range and, consequently, to a positive gradient $[\text{Fe}/\text{H}]$ vs. T_{eff} . A variation of $\Delta\xi = +0.2 \text{ km s}^{-1}$ leads to $\Delta[\text{Fe I, II}/\text{H}] = -0.05 \text{ dex}$. The errors in ξ were calculated considering the uncertainty in the slope of abundance vs. W_{λ} , and are typically 0.1 km s^{-1} .

To compute the errors in the final metallicity, the following sources of uncertainties were taken into account: *i*) uncertainties in the stellar parameters $[T_{\text{eff}}, v_t, \log g]$; *ii*) errors in the W_{λ} s measurements, which were estimated by considering several configurations of the ARES code as described above; and *iii*) uncertainties in $\log gf$ values, which were computed by considering errors in the solar W_{λ} s. The total errors are ~ 0.05 for $[\text{Fe I}/\text{H}]$ and 0.09 dex for $[\text{Fe II}/\text{H}]$.

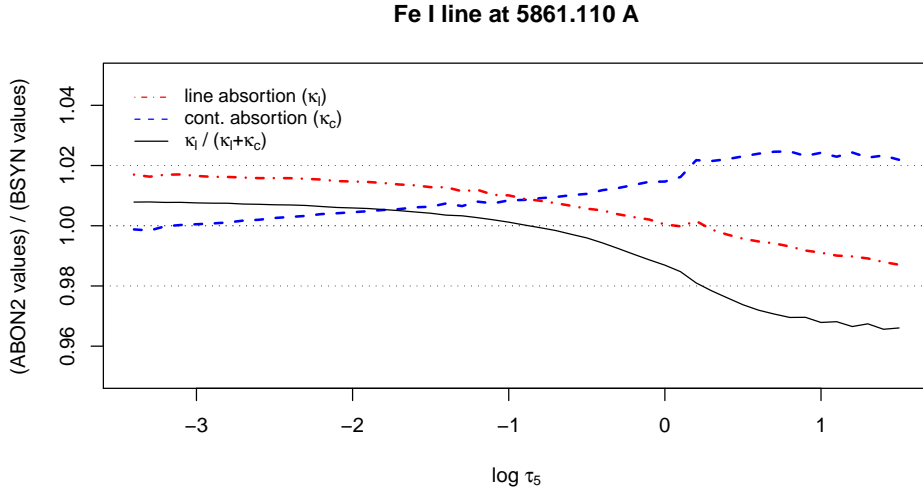


Figure 2.8: Ratio of opacities computed using the BSYN/EQWI (Edvardsson et al., 1993) and ABON2 (Spite, 1967) codes for an Fe I line at $\lambda = 5861.11 \text{ \AA}$ for the solar model.

2.5.3.1 Metallicities from two different codes

We proceeded with all the calculations described above using both the code by the Uppsala group BSYN/EQWI (Edvardsson et al., 1993, and updates since then) and the Meudon code ABON2 (Spite, 1967, and updates implemented since then). All steps of the calculation were carefully compared: optical depths of lines, continuum opacities κ_c , line broadening, and final abundances.

The dominating opacity source is the H^- bound-free absorption. The two codes consider different calculations for the H^- photo-detachment cross section σ_λ . The ABON2 code (Spite, 1967) adopts Geltman (1962) calculations, represented by the polynomial expressions from Gingerich (1964), while cross sections from Wishart (1979) are adopted in the BSYN/EQWI code (Edvardsson et al., 1993). Using these sources and considering a Fe I line at 5861 \AA and the solar atmosphere model, we found that differences in the continuum absorption are up to 4% in the upper atmospheric layers ($\tau_5 < -1$), and less than 1% in the bottom of the photosphere ($\tau_5 > 0$). We updated the ABON2 code (Spite, 1967) using new cross sections calculations from John (1988), which improve the agreement of κ_c between these two codes to $< 1\%$ at the upper layers with $\tau_5 < -1$ and $\sim 2\%$ at $\tau_5 > 0$ layers (Figure 2.8).

The line opacity (κ_l) calculated for an Fe I line at 5861 \AA is shown in Figure 2.8 with a solar model. We found that the ratio between line opacities, $\kappa_{l,\text{BSYN}}/\kappa_{l,\text{ABON2}}$, decreases with optical

Table 2.6 - Abundances obtained with two different codes.

Star	T_{eff} (K)	$\log g$	$\Delta[\text{Fe I}/\text{H}]^a$	$\Delta[\text{Fe II}/\text{H}]^a$
Sun	5777	4.44	0.00	0.00
HD 15133	5223	4.47	0.01	0.02
HD 77338	5346	4.55	0.01	0.01
HD 90054	6047	4.18	0.01	0.00
HD 177374	5044	4.38	0.01	0.02

Notes. ^(a) $\Delta[\text{Fe}/\text{H}] = [\text{Fe}/\text{H}]_{\text{BSYN}} - [\text{Fe}/\text{H}]_{\text{ABON2}}$.

depth. An agreement between their values in the two codes is found at $\log \tau_5 \approx 0$. The small discrepancy is mainly due to differences in the van der Waals broadening determinations. The ratio $\kappa_l/(\kappa_l + \kappa_c)$ is within 1% at layers with $\tau_5 < -1$.

The same analysis was carried out for other lines at different wavelengths and atmosphere models. Despite the small trends with λ and T_{eff} , Table 2.6 shows that the differences found between metallicities obtained with the two codes are within 0.02 dex.

2.5.4 Checks on excitation and ionization equilibria

Since we are using temperatures from photometric scales and trigonometric gravities, it is interesting to check whether excitation and ionization equilibria are reached. For each star, we plotted iron abundances vs. the excitation potential χ_{exc} (eV) and performed a linear fit between these two quantities (Figure 2.9 shows HD 26151 as an example). The excitation equilibria is indicated by the independence between abundances and χ_{exc} ; i. e., the slope b must be zero. Figure 2.10 presents the slope b as a function of temperature, gravity, and metallicity for all the sample stars. The slope exceeded 2σ from the mean value for two stars: HD 94374 and HD 182572. HD 182572 is a known variable, with an amplitude variation smaller than 0.2 mag. The photometric calibrations give $T_{\text{eff}} \approx 5070$ K, and the excitation temperature (5700 K) was adopted for this star. For G 161-029 no parallax measurement is available. Therefore spectroscopic T_{eff} and $\log g$ were adopted for these three stars.

In addition to these outlier stars in Figure 2.10, we found small trends between the slope b and temperatures/gravities. This was also found by Feltzing & Gustafsson (1998) in their analysis of 47 metal-rich stars. On the other hand, the trend between b and $[\text{Fe}/\text{H}]$ is very small; thus,

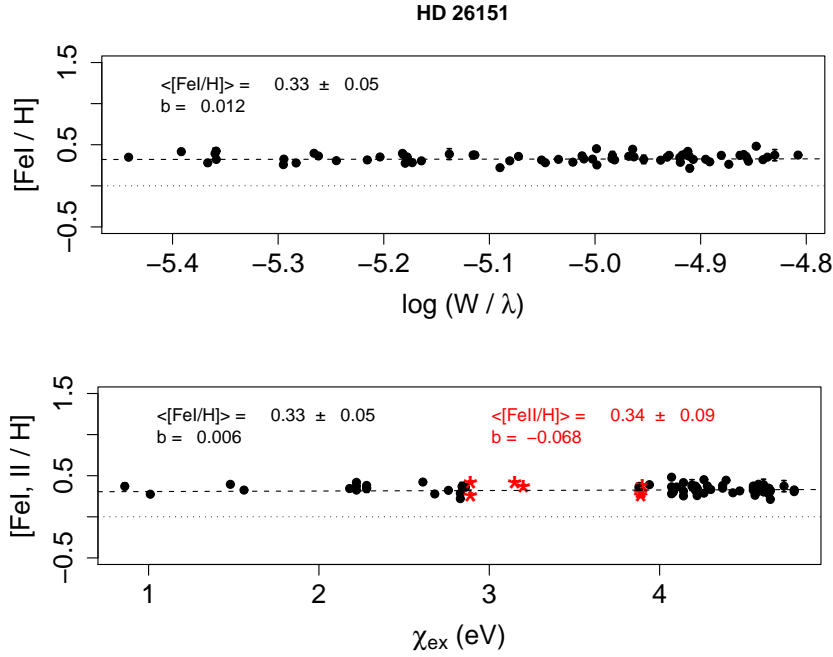


Figure 2.9: Abundances versus normalized equivalent widths, $\log(W/\lambda)$ (top), and excitation/ionization equilibrium (bottom) shown for HD 26151, as an example. Red stars represent Fe II lines. The Fe I and Fe II abundances and linear coefficients b are given in the plots.

the effect of choosing photometric temperatures over excitation ones on the final metallicities should be negligible. We quantified this effect by obtaining the excitation temperatures by requiring zero slope from the excitation energy balance diagram, and we compared the excitation and photometric temperatures, as shown in Figure 2.12. The excitation temperatures agree well with the photometric ones. Differences between temperatures are all below $\pm 5\%$, except for the stars HD 94371 and HD 182572, for which the excitation temperatures were adopted. The mean difference is only 0.7%, with a standard deviation of 2.5%. For $[\text{Fe}/\text{H}] \gtrsim 0.4$, the photometric temperatures are systematically higher than excitation temperatures by an amount of 2% in average. If we consider 2% lower temperatures in these cases, the resulting change in abundance is ~ -0.05 dex. Finally, in Figure 2.11, we show that the iron abundances derived from Fe I show no obvious trend with T_{eff} .

Ionization equilibria, indicated by the difference between Fe I and Fe II abundances, is shown in Figure 2.13 for all the sample stars. We found an apparent overionization as compared to expectations from LTE calculations for the cooler stars ($T_{\text{eff}} \leq 5200$ K) in the sample, with an upper limit of $[\text{Fe II}/\text{Fe I}] < 0.2$ dex. Even though lines of ionized iron atoms are less susceptible

to non-LTE effects than Fe I (Thévenin & Idiart, 1999), we considered the abundances derived from Fe I lines to be the final metallicities of our stars, since Fe I lines are more numerous.

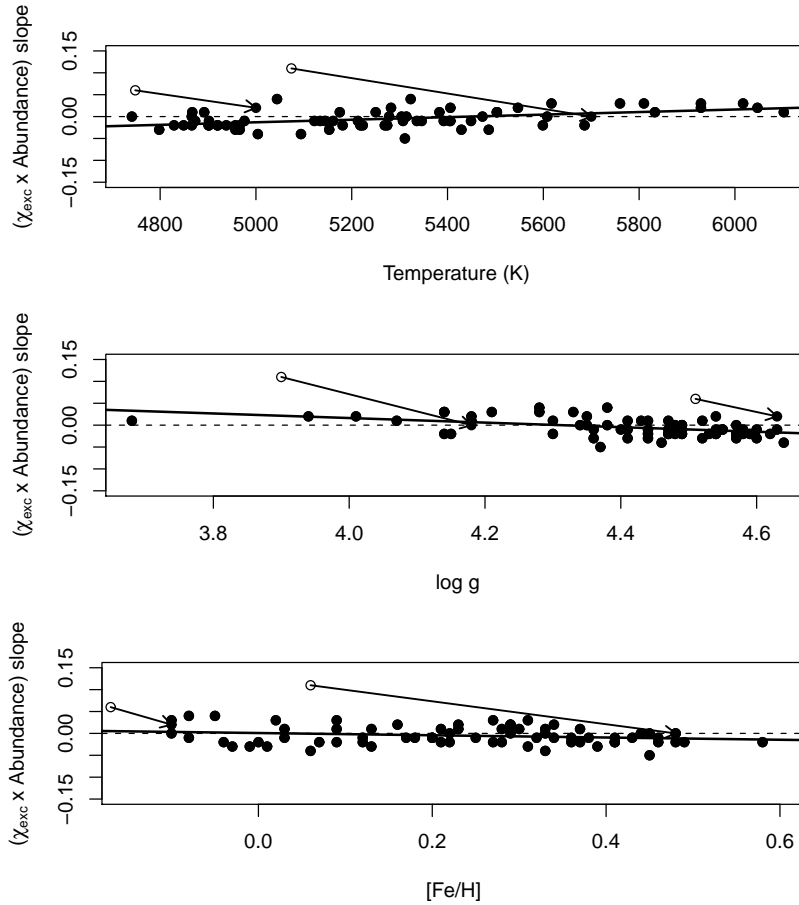


Figure 2.10: Excitation equilibrium as a function of temperature (*top*), gravity (*middle*), and metallicity (*bottom*). The dashed line indicates the perfect excitation equilibrium. The arrows indicate changes in temperature and gravity of HD 94374 and HD 182572 to achieve excitation equilibrium (see text). Open circles indicate photometric temperatures obtained as described in Sect. 2.5.1; filled circles correspond to the adopted, excitation-equilibrium values.

2.5.5 Stellar masses and ages

Isochrone fitting techniques can provide estimates of stellar masses and ages. Allende Prieto & Lambert (1999) compared masses derived from interpolation of isochrones and the direct estimates from observations in eclipsing spectroscopic binaries, and they concluded that masses can be estimated with uncertainties below 8%. More recently, Meléndez et al. (2011, in prep.)

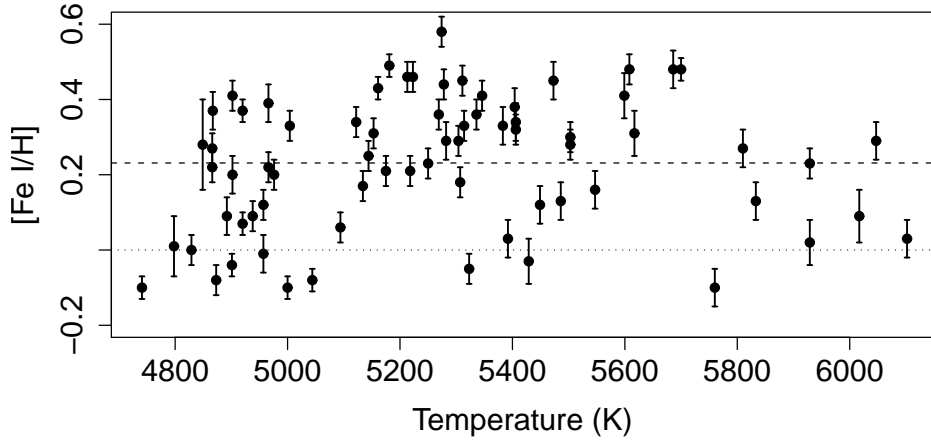


Figure 2.11: $[\text{Fe I}/\text{H}]$ vs. temperatures. Dashed and dotted lines indicate the mean iron abundance and $[\text{Fe}/\text{H}] = 0$, respectively.

show that masses and ages can be estimated with even higher accuracy, provided the isochrones are well calibrated to reproduce the solar ages and masses.

Therefore, we used a grid of Yonsei-Yale isochrones to determine the masses and ages for the sample stars. The isochrone points were characterized by the effective temperature (T_{eff}), the absolute magnitude (M_V), and the metallicity ($[\text{Fe}/\text{H}]$). Using T_{eff} , parallaxes, apparent magnitudes, and $[\text{Fe}/\text{H}]$ as input values, we recovered the possible solutions for $\log g$, masses, and ages, which are within the errors in T_{eff} , M_V and $[\text{Fe}/\text{H}]$, and computed the mean values. This procedure was repeated 200 times, and each time, the input values were varied following a normal distribution with mean X and standard deviation of σ_X , where X (with $X = T_{\text{eff}}$, M_V and $[\text{Fe}/\text{H}]$) is the parameter value and σ_X is the error associated with it. The internal errors on masses and ages were then computed as the standard deviation of the output values of these 200 realizations; errors of about 3% were found.

To check the accuracy of our mass determination method, we derived the masses of stars listed in Torres et al. (2010). These authors have produced the most recent compilation of high-accuracy mass determinations in binaries ($< 3\%$). We selected stars with temperatures and distances similar to those of our sample stars: parallaxes in the range 11 to 70 mas and temperatures from 4500 to 6500 K. We found 14 stars satisfying these criteria. Using the temperatures from these authors and solar metallicity, we derived the masses using the same method as was applied

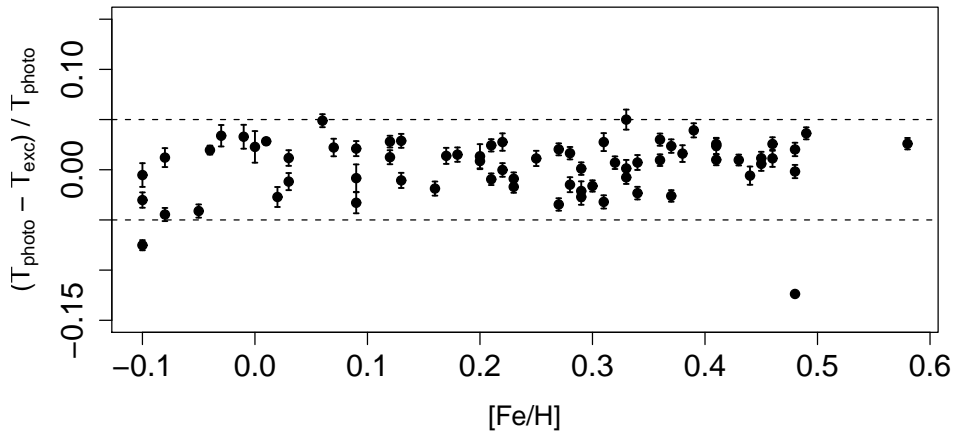


Figure 2.12: Differences between photometric and excitation temperatures vs. metallicities. The dashed lines indicate $\pm 5\%$.

to our stars. We found that masses obtained with Y^2 isochrones are 4% lower than masses from Torres et al., with a standard deviation of 5%. The good accuracy found in the present work comes from the narrower range of parameters considered here. Despite having found a systematic difference between masses from isochrones and those from dynamical considerations, no corrections were applied to the masses of our sample stars, since this difference would lead to lower $\log g$ only by an amount of < 0.02 dex, and the effect in the resulting abundances would be negligible. We added these uncertainties to the internal errors of masses and $\log g$.

We also derived the stellar masses from the Padova (Girardi et al., 2000) isochrones with the tool PARAM (da Silva et al., 2006) (see also Sect. 2.5.2). We found that masses estimated from Padova isochrones are $\sim 5\%$ lower than Y^2 masses, and this difference leads to lower gravities by ~ 0.02 dex.

Using the same procedure for mass determinations, we obtained the ages for all sample stars. The ages of 36 stars could be determined with errors smaller than 30%, and for 22 of them, the errors are within 20%. The stellar masses, ages, and their uncertainties for all sample stars are reported in Table B.7.

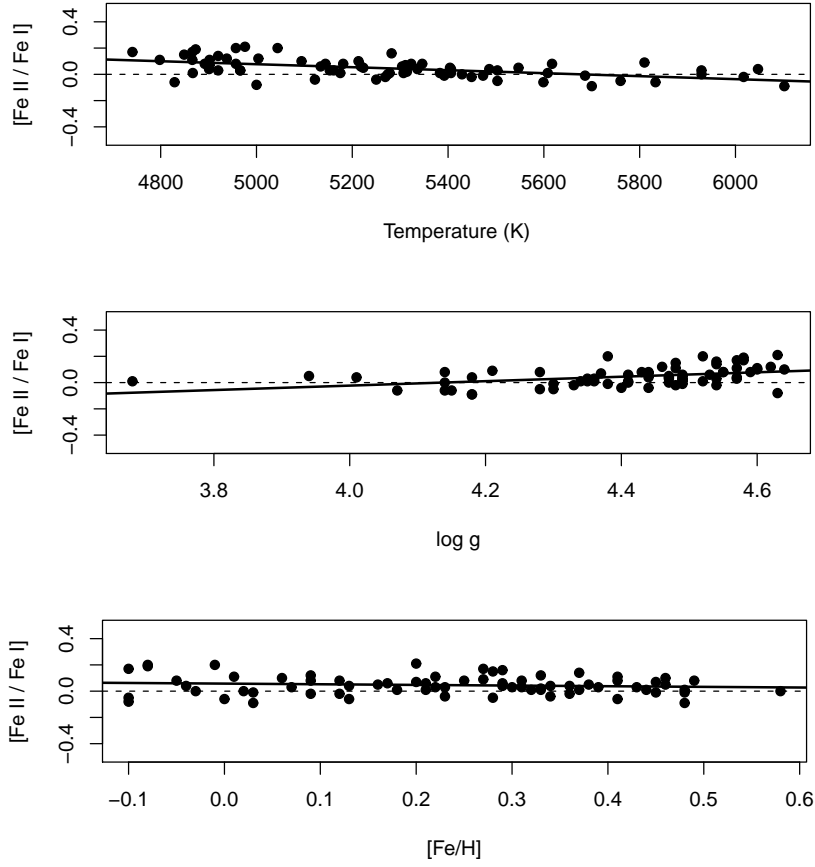


Figure 2.13: Ionization equilibrium as a function of temperature (*top*), gravity (*middle*), and metallicity (*bottom*). $[\text{Fe I}/\text{Fe II}]$ is the difference between abundances from neutral and single ionized iron lines, $[\text{Fe I}/\text{H}] - [\text{Fe II}/\text{H}]$.

2.5.6 Final parameters and comparison with other studies

The final adopted temperatures, gravities, and metallicities were compared with data available in the literature. For comparison purposes, the parameters (T_{eff} , $\log g$, $[\text{Fe}/\text{H}]$) were retrieved from the PASTEL catalogue (Soubiran et al., 2010), which compiles stellar atmospheric parameters obtained from the analysis of high-resolution, high signal-to-noise spectra. We only took into account analyses more recent than the year 1997 into account, keeping only from previous year the reference paper of McWilliam (1990). The parameters of 38 of our sample stars are available in this catalogue. Table 2.7 presents the mean values and standard deviations (when more than one value is available) of (T_{eff} , $\log g$, $[\text{Fe}/\text{H}]$). The differences are also reported. The selected list of stellar parameters given in this catalogue is reported in Table B.4.

Table 2.7 - Data from the PASTEL catalogue.

Star	T_{eff} (K)	ΔT_{eff} (K)	$\log g$	$\Delta \log g$	[Fe/H]	$\Delta[\text{Fe}/\text{H}]$
HD 8389	5330 ± 67	-56	4.44 ± 0.09	0.03	0.41 ± 0.09	0.17
HD 9424	5420 ± ...	29
HD 10576	5882 ± ...	47
HD 13386	5294 ± 95	-24	4.28 ± ...	0.26	0.26 ± ...	0.10
HD 15555	4855 ± 20	12
HD 25061	5321 ± ...	-14
HD 26151	5353 ± 22	30	4.39 ± 0.11	0.02	0.27 ± 0.01	0.06
HD 26794	4930 ± 29	-10	4.74 ± ...	-0.25	0.07 ± 0.04	0.00
HD 27894	4914 ± 54	6	4.30 ± 0.12	0.24	0.25 ± 0.07	0.12
HD 30295	5417 ± 74	-11	4.29 ± 0.30	0.07	0.22 ± 0.09	0.10
HD 31452	5262 ± ...	-12
HD 31827	5508 ± 150	100	4.12 ± 0.39	0.23	0.30 ± 0.15	0.17
HD 35854	4928 ± 32	-27	4.54 ± 0.11	0.04	-0.09 ± 0.06	0.05
HD 37986	5507 ± 66	-4	4.38 ± 0.06	0.09	0.27 ± 0.05	0.03
HD 39213	5372 ± 120	100	4.18 ± 0.25	0.20	0.28 ± 0.11	0.17
HD 39715	4816 ± 25	-75	4.75 ± ...	-0.18	-0.04 ± ...	-0.06
HD 77338	5290 ± 0	56	4.75 ± 0.21	-0.20	0.26 ± 0.06	0.15
HD 82943	6000 ± 44	-70	4.43 ± 0.08	-0.08	0.27 ± 0.04	-0.04
HD 86065	5026 ± ...	-88	4.50 ± ...	0.12	-0.06 ± ...	0.15
HD 86249	4961 ± ...	-4
HD 87007	5282 ± 29	0	4.55 ± 0.21	-0.01	0.27 ± 0.00	0.02
HD 90054	6080 ± ...	-33
HD 104212	5996 ± ...	-163
HD 107509	6069 ± ...	33
HD 120329	5636 ± ...	-19
HD 148530	5402 ± ...	-10
HD 149933	5735 ± ...	-249
HD 165920	5342 ± 5	-6	4.38 ± 0.02	0.09	0.30 ± 0.01	0.06
HD 171999	5288 ± 55	16	4.65 ± ...	-0.16	0.40 ± ...	-0.11
HD 180865	5255 ± ...	-37
HD 181234	5415 ± 121	-104	4.47 ± ...	-0.10	0.36 ± ...	0.09
HD 181433	4958 ± 6	-56	4.37 ± ...	0.20	0.33 ± ...	0.08
HD 182572	5583 ± 172	117	4.16 ± 0.17	0.02	0.38 ± 0.09	0.10
HD 197921	4948 ± ...	-82
HD 211706	6023 ± ...	-6

Table 2.7 - continued.

Star	T_{eff} (K)	ΔT_{eff} (K)	$\log g$	$\Delta \log g$	[Fe/H]	$\Delta[\text{Fe}/\text{H}]$
HD 218566	$4927 \pm \dots$	-78	$4.81 \pm \dots$	-0.33	$0.38 \pm \dots$	-0.10
HD 218750	$5227 \pm \dots$	-93
HD 224383	5751 ± 14	9	4.36 ± 0.06	-0.08	-0.06 ± 0.02	-0.04

The comparisons are presented in Figure 2.14. Differences between temperatures considered in the present work and those from the PASTEL catalogue do not exceed 2%, except for two stars (HD 31827 and HD 35854). We also found good agreement between gravities, with differences within ~ 0.2 dex.

The metallicities derived in this work are in good agreement with the values reported in the literature for $[\text{Fe}/\text{H}] \lesssim 0.3$. At higher metallicities ($[\text{Fe}/\text{H}] \gtrsim 0.3$), the abundances determined in this work are systematically higher than the values reported in the literature by ~ 0.1 dex on average. On the other hand, there are no systematic differences between temperatures and gravities for $[\text{Fe}/\text{H}] \gtrsim 0.3$; thus, it is unlikely that differences in stellar parameters are the source of our higher metallicities.

We also compared the present final metallicities and the photometric metallicities from the GCS survey. Our sample contains 17 stars in common with GCS, and the mean difference between the metallicities of these stars is $[\text{Fe}/\text{H}]_{\text{present}} - [\text{Fe}/\text{H}]_{\text{GCS}} = 0.08 \pm 0.12$. Improved new calibrations of the GCS data from Casagrande et al. (2011) brings the GCS metallicity scale into agreement with ours: using the temperatures from CRM10 calibrations, Casagrande et al. also found higher $[\text{Fe}/\text{H}]$ by an amount of 0.1 dex.

Finally, the metallicities derived from the Geneva photometry, presented in Table B.7, show differences of spectroscopic iron abundances derived in the present work being -0.12 ± 0.16 dex lower than the Geneva photometric metallicities.

2.6 Abundance determination

2.6.1 Carbon, oxygen, magnesium, and calcium

To derive the abundance of C, O, Mg, and Ca, we performed spectral synthesis, and the abundances were obtained by minimizing the χ^2 between the observed and synthetic spectra (see Appendix A). The synthetic spectra were obtained using the PFANT code described in Cayrel

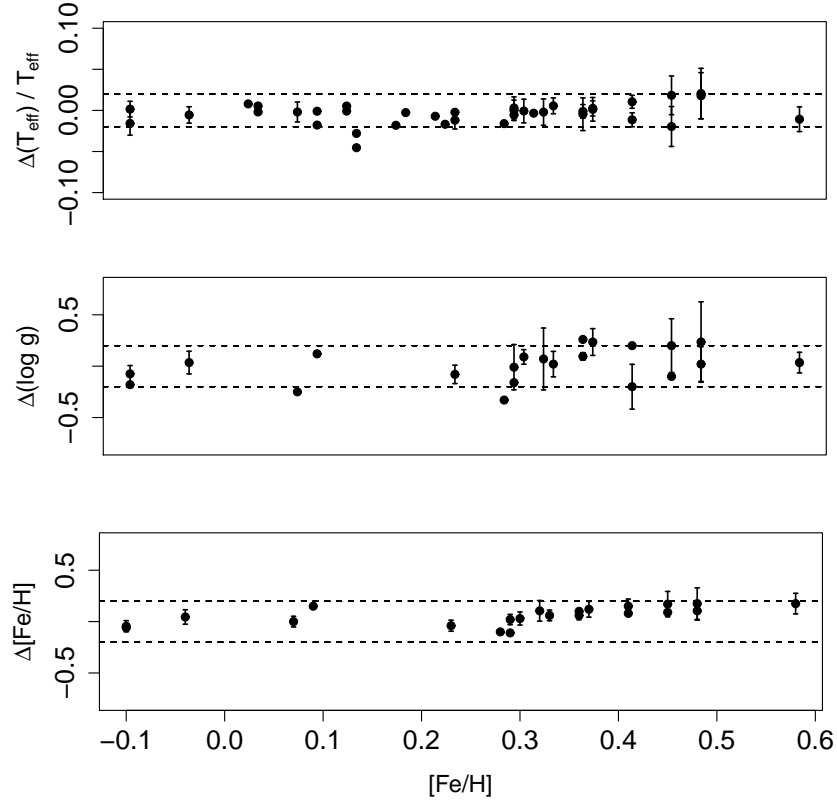


Figure 2.14: Relative differences between temperatures (*top*), gravities (*middle*), and metallicities (*bottom*) derived in the present work and from the PASTEL catalogue. Differences are *this work* - PASTEL. Dashed lines indicate $\pm 2\%$ in the T_{eff} panel and ± 0.2 dex in the $\log g$ and metallicity panels.

et al. (1991), Barbuy et al. (2003), and Coelho et al. (2005) which includes molecular lines in the ABON2 code (Sect. 2.5.3). Again, the same MARCS model atmospheres are employed.

Carbon

The carbon abundances were derived from the CI 5380 Å line, adopting the line list given in Spite et al. (1989). To check the atomic parameters, we derived the solar carbon abundance by χ^2 minimization between observed and synthetic solar spectra, obtaining $(\text{C}/\text{H})_{\odot} = 8.53$. This value is in good agreement with abundances from Grevesse et al. (1996), $(\text{C}/\text{H})_{\odot} = 8.55$, and Grevesse & Sauval (1998), $(\text{C}/\text{H})_{\odot} = 8.52$.

Table 2.8 - Nickel blend at 6300 Å.

Species	λ (Å)	χ_{exc} (eV)	$\log gf$
NiI	6300.335	4.27	-2.275
NiI	6300.355	4.27	-2.695
[OI]	6300.340	0.00	-9.820

Oxygen

The oxygen abundances were determined using the forbidden line at 6300 Å. The blend with nickel was taken into account using the atomic data from Bensby et al. (2004) (Table 2.8). Since previous studies suggest that the [Ni/Fe] ratio increases at higher metallicities (Bensby et al., 2005), the contribution of the Ni blend at 6300 Å may be important for our sample stars. For this reason, the abundances of Ni were previously derived, in order to consider the correct ratio [Ni/Fe] for each star.

To check the atomic parameters, we derived the solar oxygen abundance, obtaining $(O/H)_{\odot} = 8.63$. This value is in good agreement with $(O/H)_{\odot} = 8.66$ from Asplund et al. (2005).

Magnesium

The magnesium abundances were obtained using the triplet MgI lines at 6319 Å. A CaI line at 6318.3 Å showing autoionization effects, producing a $\sim 5\text{Å}$ broad line, can affect the determination of the continuum placement (e.g. Lecureur et al., 2007). The CaI autoionization line was treated by increasing its radiative broadening to reflect the much reduced lifetime of the level suffering autoionization compared with the radiative lifetime of this level. The radiative broadening had to be increased by 16 000 of its standard value ($\propto 1/\lambda^2$, based on the radiative lifetimes alone) to reproduce the CaI dip in the solar spectrum (Figure 2.15). In addition, the abundances of Ca of each star were derived before the calculations of the synthetic spectra at the 6319 Å region, in order to take the correct [Ca/Fe] ratio into account in the computation of the Ca line. Even if the majority of the stars in the sample are not affected, since their abundance ratios are close to solar ($[Ca/Fe] \sim 0.00$), for some of the sample stars the effect can be important. Figure 2.16 presents the spectrum of HD 201237 at the 6319 Å region. The contribution of the

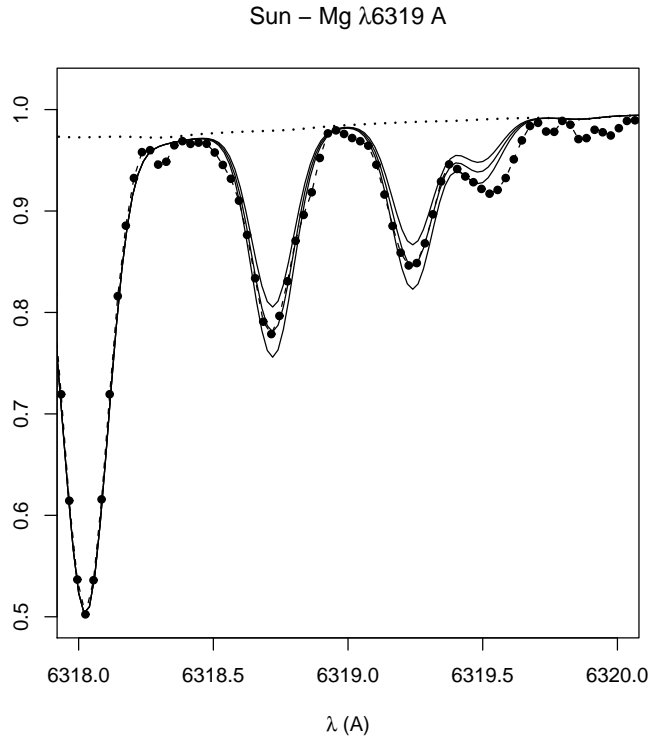


Figure 2.15: Solar spectra in the region of the 6319 Å Mg triplet. Solid lines indicate the synthetic spectra for $(\text{Mg}/\text{H}) = 7.50, 7.60, 7.70$; the dots indicate the observed spectrum. The dotted line shows the contribution of the CaI autoionization line.

CaI autoionization line is shown considering both $[\text{Ca}/\text{Fe}] = 0.00$ and $[\text{Ca}/\text{Fe}] = 0.37$. The latter is the abundance ratio of HD 201237 before the correction of the trend with temperature (Sect. 2.6.3). It is clear that the Ca abundance of this star must be taken into account to reproduce the CaI dip. The resulting differences in the Mg abundance considering solar and non-solar $[\text{Ca}/\text{Fe}]$ ratio are ~ 0.07 dex in average.

To check the atomic parameters of the lines at the MgI triplet region (Table 2.9), we derived the solar Mg abundance. We obtained $(\text{Mg}/\text{H})_{\odot} = 7.60$, in good agreement with $(\text{Mg}/\text{H})_{\odot} = 7.58$ from Grevesse & Sauval (1998).

Calcium

The CaI lines were selected from Bensby et al. (2004), Spite et al. (1987), and Barbuy et al. (2009), and they are listed in Table B.5. The $\log gf$ values were fitted to the solar line profiles, using $(\text{Ca}/\text{H})_{\odot} = 6.36$ (Grevesse & Sauval, 1998). The lines that give unreliable abundances

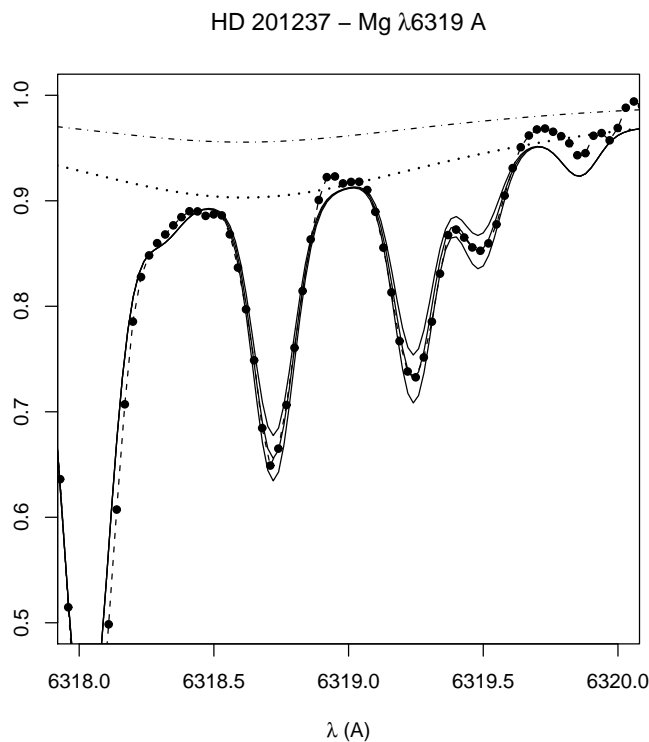


Figure 2.16: Spectrum of HD 201237 in the region of the 6319 Å Mg triplet. Solid lines indicate the synthetic spectra for $(\text{Mg}/\text{H}) = 7.53, 7.63,$ and 7.73 ; the dots indicate the observed spectrum. We considered the calcium abundance of HD 201237 to calculate the synthetic spectrum, and the contribution of the CaI autoionization line is represented by the dotted curve. The dot-dashed line indicates the CaI dip when we consider $[\text{Ca}/\text{Fe}] = 0.00$.

were identified using the same procedure as applied to Fe lines, and the differences $A_{\lambda i} - \langle A \rangle_i$ for all the sample stars are plotted in Figure 2.17.

2.6.2 Silicon, titanium and nickel

Silicon, titanium, and nickel abundances were determined by recovering the measured equivalent widths through LTE analysis with the ABON2 code (Spite, 1967). Again, the equivalent widths were measured with the ARES code, and errors in W_λ were estimated by carrying out the same procedure as described in Sect. 2.5.3. Ti, Si, and Ni spectral lines were selected from Bensby et al. (2004), Cohen et al. (2009), and Pompéia et al. (2007). Through a similar procedure used in the iron abundance determination, the $\log gf$ values were fitted to the solar equivalent widths, adopting $(\text{Ti}/\text{H})_\odot = 5.02$, $(\text{Si}/\text{H})_\odot = 7.55$ and $(\text{Ni}/\text{H})_\odot = 6.25$ (Grevesse & Sauval, 1998). The final line list and the astrophysical $\log gf$ values are presented in Table B.5.

Lines that give unreliable abundances were identified with the same procedure as used for

Table 2.9 - Lines at the 6319 Å region.

Species	λ (Å)	χ_{ex} (eV)	$\log gf$ (Sun)	$\log gf$ (NIST)	$\log gf$ (VALD)	$\log gf$ (BZO+09)
Fe I	6318.03	2.45	-1.80	-1.80	-2.26	...
TiI	6318.03	1.43	-0.94
CaI	6318.35	4.43	0.06	...	0.06	...
MgI	6318.72	5.11	-1.98	-2.10	-1.73	-2.10
MgI	6319.24	5.11	-2.23	-2.32	-1.95	-2.36
MgI	6319.49	5.11	-2.80	-2.80	-2.43	-2.80

Notes: BZO+09: Barbuy et al. (2009)

iron lines. We computed the differences between the abundance of each star, $\langle A \rangle_i$, and the abundance derived from an individual line, $A_{\lambda i}$. The differences $A_{\lambda i} - \langle A \rangle_i$ for all sample stars are plotted in Figure 2.17.

2.6.3 Spurious abundance trends and errors

Trends with effective temperature were found in previous studies. In an analysis of 1040 F, G, and K dwarf stars, Valenti & Fischer (2005) find that the abundances of Na, Si, Ti, Ni, and Fe present trends with the temperature of the star. Neves et al. (2009) derived the chemical abundances of 12 elements for a sample of 451 stars of the HARPS GTO planet search programme, and similar trends with temperatures were found.

To check such trends in our results, we plotted our final abundances against temperatures. Figure 2.18 shows the abundances vs. T_{eff} , and a significant trend is observed for C, Ca, and Ti abundances. Following a procedure similar to the one adopted by Valenti & Fischer (2005) and Meléndez & Cohen (2009), we corrected this trend by fitting a second-order polynomial and applied the correction for C, Ca, and Ti (Figure 2.19). We assumed that abundance trend corrections are zero at $T_{\text{eff}} = 5777$ K. This assumption eliminates the possibility that the Sun itself may have peculiar abundances (e.g. Allende Prieto et al., 2004).

The errors on abundances were estimated as follows. The errors on abundances of C, O, and Mg were derived by taking the uncertainties on the stellar parameters into account. Temperatures, gravities, and metallicities were varied individually according to their errors, and the

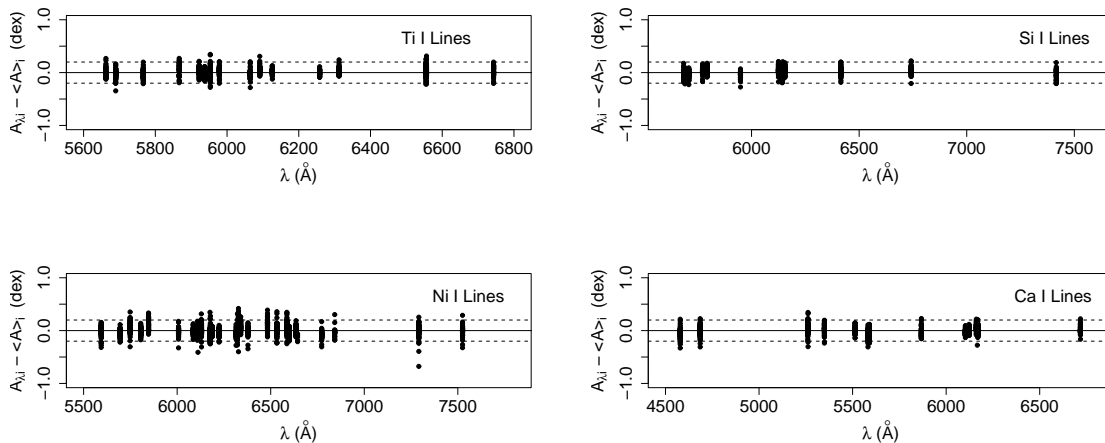


Figure 2.17: Process of selection of stable lines of Ti I, Si I, and Ca I. The dashed lines indicate ± 0.2 dex.

resulting variations on the abundance were added quadratically. This procedure were performed for ten stars in the sample, and the mean error was assumed to be the characteristic error for the sample stars (0.12, 0.17, and 0.08 dex for C, O, and Mg, respectively). More than one spectral line was used to derive the abundances of Ni, Si, Ca, and Ti, and for these elements, the errors are assumed to be the standard deviation of the abundances derived from individual lines. The errors on these four abundances are presented in Tables B.8 and B.9.

2.6.4 Final abundances and comparison with other studies

To test the reliability of our results, we compared the abundances derived in the present work and derivations from previous studies of Valenti & Fischer (2005) and Neves et al. (2009). Our sample contains 12 stars in common with the sample studied by Valenti & Fischer and eight in common with Neves et al. In Table 2.10, we give the mean difference between the abundance ratios $[X/Fe]$, and in Figure 2.20, these differences are shown as a function of $[Fe/H]$. Our results are in good agreement with the abundances derived by these authors. Differences are all within ~ 0.2 dex, and there is no evident trend with metallicity.

The final abundances relative to iron, $[X/Fe]$, vs. $[Fe/H]$ are presented in Figure 2.21. We plotted the abundances from Bensby et al. (2003), Bensby et al. (2004) and Mishenina et al. (2004, 2008), and Reddy et al. (2003, 2006) for a comparison. We applied the same procedure as described in Sect. 2.4.2 to separate the samples of these studies into thin disk, thick disk,

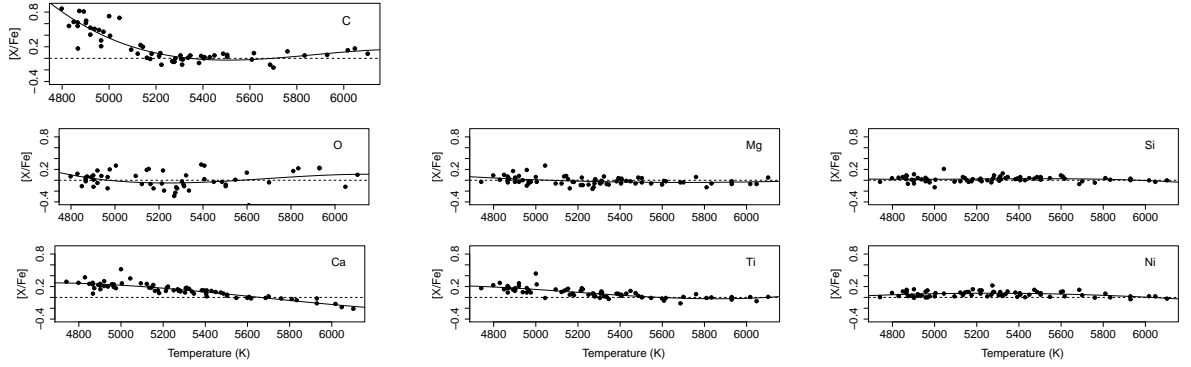


Figure 2.18: Abundances of C, O, Mg, Si, Ca, Ti, and Ni vs. temperature. A pronounced trend is observed for C, Ca and Ti.

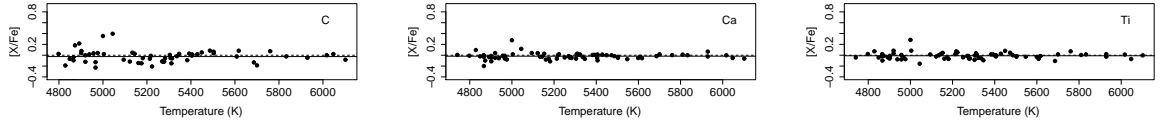


Figure 2.19: Abundances of C, Ca, and Ti vs. temperature after the correction. We considered the mean abundance in the range $5680 < T_{\text{eff}} < 5880$ K as the zero point of the correction, which is -0.03 , -0.02 , and -0.01 for C, Ca, and Ti, respectively.

and intermediate populations⁴. We stress that the comparison must be considered carefully: different approaches and methods can lead to systematic differences between abundances from different authors. These systematic differences could be determined by direct comparison of abundances for stars in common with other samples. However, our sample contains only two stars in common with the sample of Bensby et al. (2004) and one in common with Mishenina et al. (2004, 2008), so that the systematic differences could not be quantified accurately. By comparing the abundances of these stars (even if they are so few), we found that our results are 0.04 dex lower than $[\alpha/\text{Fe}]$ ratios from these studies. Differences at this level do not affect the main conclusions of this work.

We found the following trends of $[\text{X}/\text{Fe}]$ vs. $[\text{Fe}/\text{H}]$ for each element:

Carbon: $[\text{C}/\text{Fe}]$ is a decreasing function of metallicity. The median value of $[\text{C}/\text{Fe}]$ at lower

⁴ To perform a consistent comparison, we re-classified the samples from these authors, using the same procedure as for our sample. Hereafter, the thin disk, the thick disk, and intermediate populations from Bensby et al. (2003, 2004), Mishenina et al. (2004, 2008), and Reddy et al. (2003, 2006) refer to the classification described in Sect. 2.4.2.

Table 2.10 - Comparison of abundances with other studies.

Reference	$\Delta[\text{Fe}/\text{H}]$	$\Delta[\text{Ca}/\text{Fe}]$	$\Delta[\text{Mg}/\text{Fe}]$	$\Delta[\text{Si}/\text{Fe}]$	$\Delta[\text{Ti}/\text{Fe}]$	$\Delta[\text{Ni}/\text{Fe}]$	#
Valenti & Fischer (2005)	0.01 ± 0.07	0.02 ± 0.06	0.05 ± 0.05	0.06 ± 0.04	12
Neves et al. (2009)	0.10 ± 0.08	0.12 ± 0.11	0.04 ± 0.07	0.00 ± 0.04	-0.14 ± 0.09	0.02 ± 0.04	8

Notes. $\Delta[\text{X}/\text{Fe}] = \langle [\text{X}/\text{Fe}]_{\text{Our}} - [\text{X}/\text{Fe}]_{\text{Other}} \rangle$

metallicities ($[\text{Fe}/\text{H}] < 0.2$) is 0.03, while we found $[\text{C}/\text{Fe}] -0.07$ for the more metal-rich stars ($[\text{Fe}/\text{H}] > 0.2$).

Oxygen: $[\text{O}/\text{Fe}]$ decreases with increasing metallicity. Eight stars with metallicity $0.2 < [\text{Fe}/\text{H}] < 0.4$ have $[\text{O}/\text{Fe}] \approx 0.2$. Among these, five are assigned to the thick disk, two to the intermediate population, and one to the thin disk. This overabundance is within the errors; therefore higher S/N spectra would be interesting to verify their oxygen abundances with higher precision, since these could be a distinct category of stars, but there is no evidence for such a conclusion with the present data.

Nickel: The nickel-to-iron ratio is constant up to $[\text{Fe}/\text{H}] \sim 0.2$, and increases at higher metallicities. This trend has already been suggested by data from Bensby et al. (2004), and is confirmed here.

Magnesium, silicon, calcium, and titanium: The abundance of these elements present a low scatter and follows the general trend of thin disk stars.

2.7 Discussion

In the present work we concentrate efforts on studying metal-rich stars with $[\text{Fe}/\text{H}] > 0.0$, from a sample of high proper-motion, NLTT-selected stars as described in Sect. 2.2. In Pompéia et al. (2003), we studied the behaviour of $[\alpha/\text{Fe}]$ as a function of metallicity in the range $-0.8 < [\text{Fe}/\text{H}] < +0.4$, for stars with similar kinematics to the present sample. It was found that the enhancement of α -elements relative to Fe drops with increasing metallicity, reaching solar ratios at around $[\text{Fe}/\text{H}] \approx -0.4$ for Si, Ca, and Ti, and at $[\text{Fe}/\text{H}] \approx -0.2$ for Mg and O. This behaviour is compatible with the thick disk characteristics. Bensby et al. (2003) shows a drop in $[\alpha/\text{Fe}]$ at $[\text{Fe}/\text{H}] \approx -0.4$, reaching the solar ratio at $[\text{Fe}/\text{H}] \approx 0.0$. It was shown in Sect. 2.6 that α -

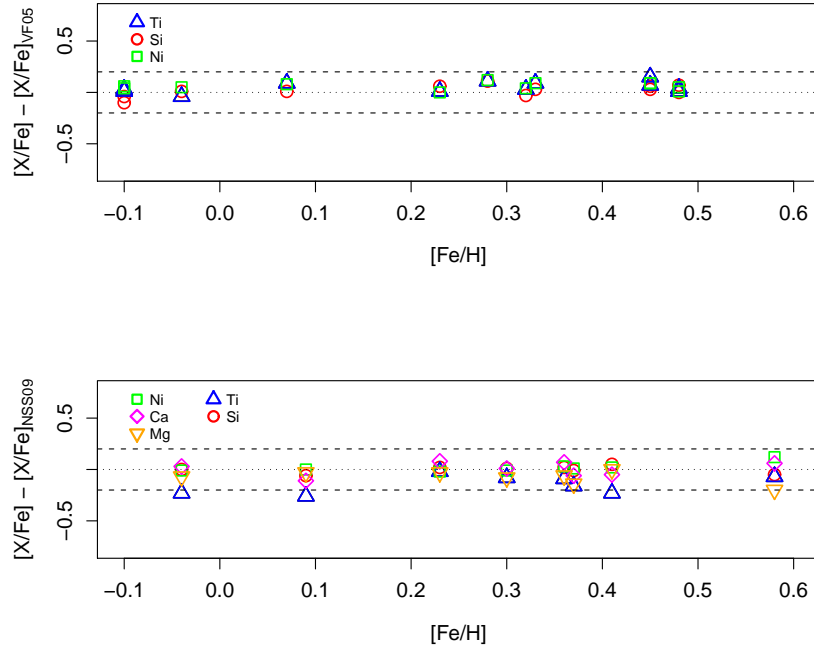


Figure 2.20: Comparison of abundances with other studies. The upper panel shows differences between our abundances of Si, Ti, and Ni and those from Valenti & Fischer (2005). The bottom panel presents the comparisons of Si, Ti, Ca, Mg, and Ni abundances from Neves et al. (2009).

element abundances are not enhanced in the metal-rich sample stars, a result compatible with the behaviour previously shown by Pompéia et al. (2003).

In terms of kinematical properties, we analysed the U, V, W velocities of the sample stars to identify members of the thick disk, thin disk and intermediate ones, according to definitions by Soubiran et al. (2003). The membership with thin or thick disk components discussed in Sect. 2.4.2 leads to 42 (59%) of the sample stars to be identified with the thick disk.

2.7.1 Comparison with thin and thick disk stars

We compared the characteristics of the sample stars with thin disk, thick disk, and intermediate populations from Bensby et al. (2003, 2004), Mishenina et al. (2004, 2008), and Reddy et al. (2006).

The sample is dominated by stars having the metallicities indicative of thin disk population, as seen by the behaviour of $[\alpha\text{-elements}/\text{Fe}]$ vs. $[\text{Fe}/\text{H}]$ presented in Figure 2.21. On the other hand, the kinematics of the sample stars would suggest membership with the thick disk, as shown

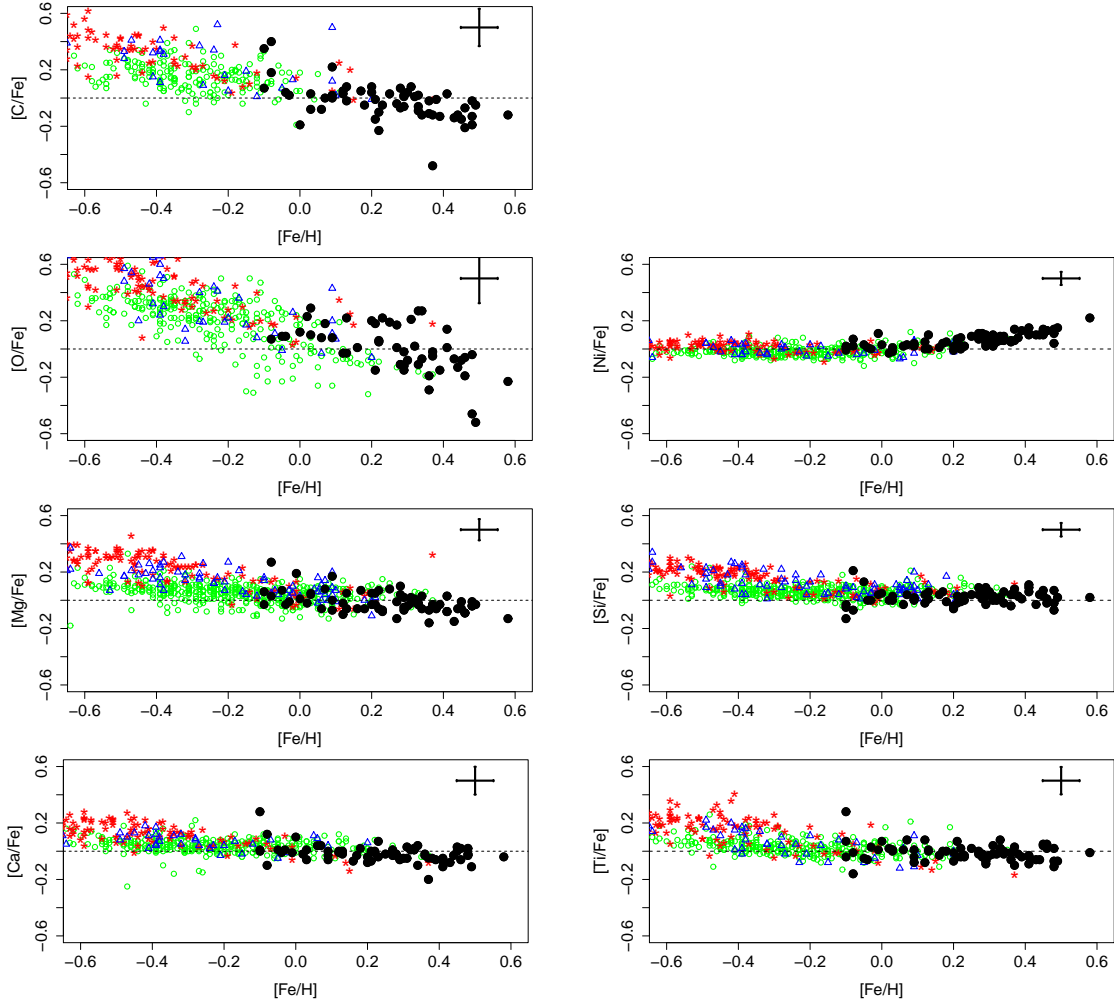


Figure 2.21: Abundances of C, O, Ni, Mg, Ca, Si, and Ti vs. metallicities. The abundances derived in this work (black circles) are compared with the thin (green circles), thick (red stars) disk stars, and the intermediate population (blue triangles) from Bensby et al. (2003, 2004), Mishenina et al. (2004, 2008), and Reddy et al. (2003, 2006).

in the UV plane and Toomre diagram (Figure 2.22). If confirmed as members of the thick disk, these metal-rich stars provide an interesting sample for testing models of thick disk formation. They show the kinematics of a thick disk, together with the metallicities and abundance ratios of thin disk stars.

In Figure 2.23, we show the space velocities U , V , and W against $[\alpha/\text{Fe}]$. The sample stars show a lower rotational velocity V than the thin disk stars. The $|W|$ velocity is somewhat higher than the thin disk, showing essentially only negative values, which may be further investigated in terms of migration effects in the Galaxy.

Grenon (1987) proposed that the average radius of the orbit, $R_m = (R_{\max} + R_{\min})/2$, is kept

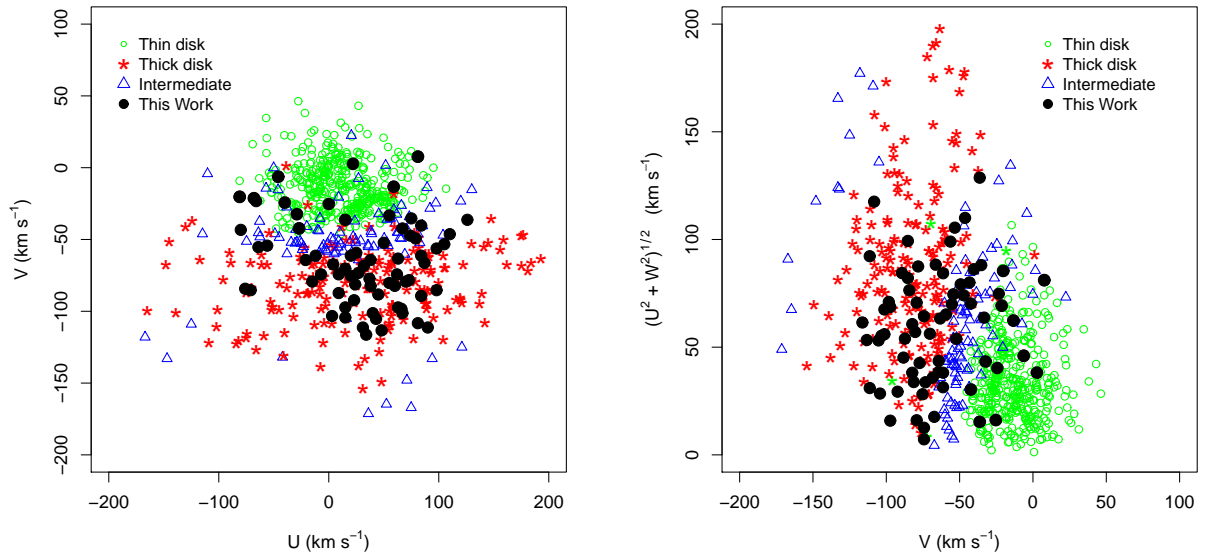


Figure 2.22: *Left*: UV plane. *Right*: Toomre diagram. In both panels, the present sample is indicated by black circles. The blue open circles and red stars are the thin and thick disks, respectively. The stars shown are the samples from Reddy et al. (2003, 2006), Mishenina et al. (2004, 2008), and Bensby et al. (2004). The velocities and population fractions used (Eqs. 2.1 and 2.2) were taken from Soubiran et al. (2003).

close to the initial galactocentric radius of the stellar birthplace. Therefore, we are able to use R_m to derive radial constraints, such as the abundance gradients for each population. Figure 2.27 shows how the metallicity and $[\alpha/\text{Fe}]$ vary with respect to R_m for thin, thick, and intermediate stars. The thin and thick disk stars appear to have $R_m \sim 8$ and 6 kpc, whereas the intermediate population has $R_m \sim 7$ kpc. These distances agree with R_m distances of our thin disk, thick disk, and intermediate subsamples. Therefore, we investigate whether R_m for each component remains the same when considering the more complete sample from GCS. This is shown in Figure 2.27 (right panels), and it is clear that the GCS data also show that thin, thick, and intermediate stars have these typical R_m values.

Figure 2.24 shows $[\text{Fe}/\text{H}]$ and $[\alpha/\text{Fe}]$ vs. the stellar ages. The ages of the sample stars span from ~ 2 to ~ 14 Gyr, with mean age of 7 to 8 Gyr. In this plot, the large symbols represent stars for which ages could be determined with uncertainties lower than 30%, and the remaining stars are shown as small symbols. The older stars in the sample present lower metallicities and higher α -element enhancement. To verify if different ages, $[\text{Fe}/\text{H}]$ and $[\alpha/\text{Fe}]$ correspond to different populations, in Figure 2.25 we show the same as Figure 2.24 for each subsample. Thin

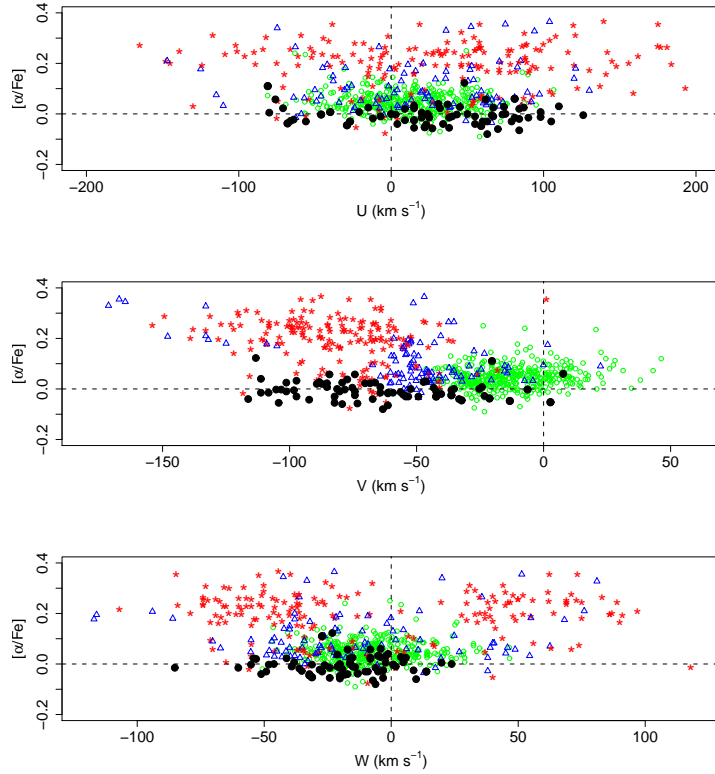


Figure 2.23: UVW vs. $[\alpha/\text{Fe}]$. The black circles show the present sample. Data from Reddy et al. (2003, 2006); Mishenina et al. (2004, 2008); Bensby et al. (2004) are shown as red stars (thick disk), open green circles (thin disk), and blue triangles (intermediate population).

disk, thick disk, and intermediate populations are indicated by different symbols. It seems that the three subsamples span the same range of ages, and the trends of decreasing metallicity with increasing age and increasing $[\alpha/\text{Fe}]$ with increasing age are observed for both thin and thick disk stars. Therefore, the evolution of abundances appear to be very similar for the three populations.

The maximum height from the Galactic plane Z_{max} of our selected 42 thick disk stars, of $Z_{\text{max}} = 380$ pc (Table 2.3), could be considered to be lower than a mean thick-disk height (e.g. Ivezić et al., 2008).

2.7.2 Comparison with bulge stars

Very metal-rich stars can be found in the Galactic bulge. In the most extensive high-resolution spectroscopic survey available so far, Zoccali et al. (2008) studied stars in three different fields along the Galactic minor axis and find that in the most central region of their bulge sample ($b = -4^\circ$), $\sim 30\%$ of the stars have $[\text{Fe}/\text{H}] > 0.2$, and more than 50% have $[\text{Fe}/\text{H}] > 0.0$. The

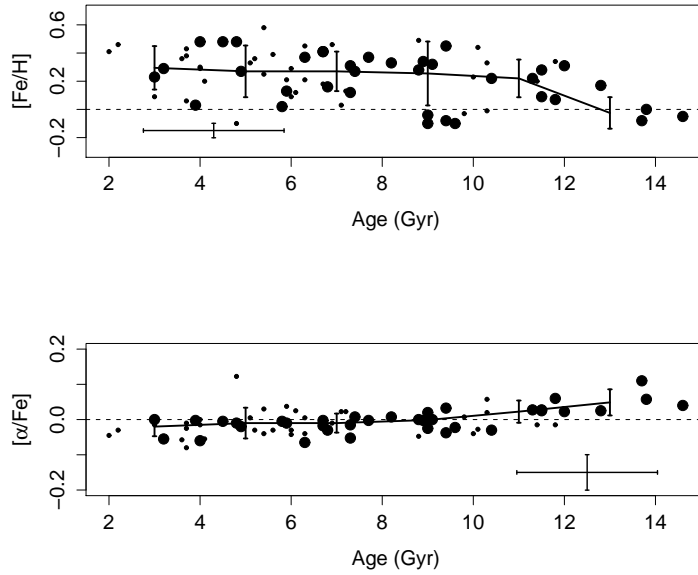


Figure 2.24: Ages vs. $[Fe/H]$ (top) and $[\alpha/Fe]$ bottom. The solid lines indicate the median value of $[Fe/H]$ and $[\alpha/Fe]$ in bins of 2 Gyr. Small symbols represent stars with age errors greater than 30%.

fraction of very metal-rich stars decreases with increasing Galactic latitudes. We investigate the similarity between the stars studied in this work and bulge stars.

Gonzalez et al. (2011) determined the abundances of the α elements Mg, Si, Ca, and Ti, and obtained a mean $[\alpha/Fe]$ ratio of bulge stars. At solar metallicities, the bulge stars are Mg-Si-Ca-Ti-enhanced by ~ 0.1 dex at the solar metallicity, when compared with our sample stars. However, the bulge stars are giants, and the present sample consists of dwarfs, therefore systematic effects of model atmospheres and other differences are expected on the abundance analysis.

Another interesting piece of information comes from the observation of microlensed dwarf and subgiant stars. In Figure 2.26 we show the abundances of O, Ni, Mg, Ca, Si, and Ti for 26 such stars, presented by Bensby et al. (2011), and we plot the abundances of our sample stars for comparison. Except for an enhanced Mg in a few of the microlensed dwarfs, the results for their six metal-rich stars are also compatible with the present results, therefore our metal-rich thick-disk star subsample could be identified with a bulge origin as well.

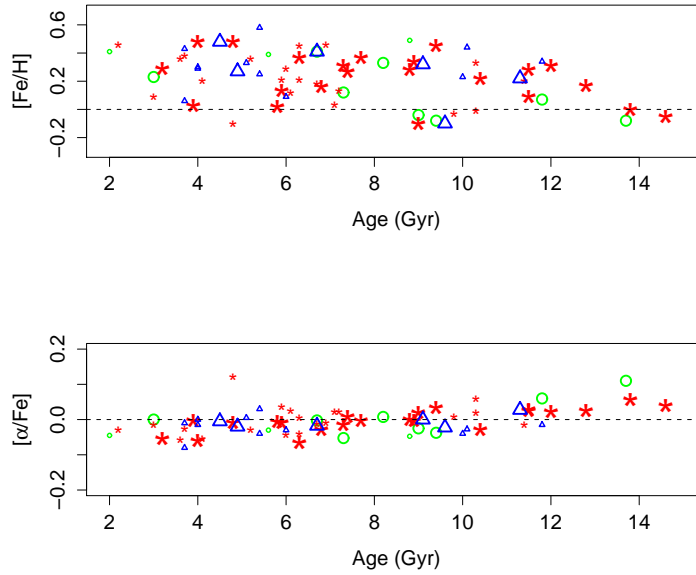


Figure 2.25: Ages vs. $[\text{Fe}/\text{H}]$ (top) and $[\alpha/\text{Fe}]$ bottom. Stars belonging to thin disk, thick disk, and intermediate populations are indicated as green circles, red stars, and blue triangles, respectively. Small symbols represent stars with age errors greater than 30%.

2.7.3 Theoretical predictions

The kinematical and chemical characteristics of the sample stars might be explained by models of radial migration of stars. Fux (1997) and Raboud et al. (1998) identified “hot” orbits produced by effects of the bar, moving stars between regions inside the bar, and outside corotation. Raboud et al. (1998) found that the old disk stars in their large sample appeared to show a positive mean U motion, with an imbalance between positive and negative U velocities reaching up to 50 km s^{-1} . A U anomaly of $+29 \pm 2 \text{ km s}^{-1}$ with respect to the Sun and $+19 \pm 9 \text{ km s}^{-1}$ with respect to the Galactic centre was identified. Raboud et al. suggest that the metal-rich stars within this sample appeared to wander from inside the bar, reaching the solar neighbourhood. Therefore, the kinematical anomaly for the old disk (see Sect. 2.2) detected by Raboud et al. could be a signature of the bar. More recently, Sellwood & Binney (2002) have shown that the transient spiral arms have a dominant effect on radial migration. If these mechanisms prove to be the origin of our thick disk sample stars, it could be that these stars are bulge or inner thick disk stars reaching the solar neighbourhood.

In recent years, radial migration has been the subject of several studies, such as Haywood

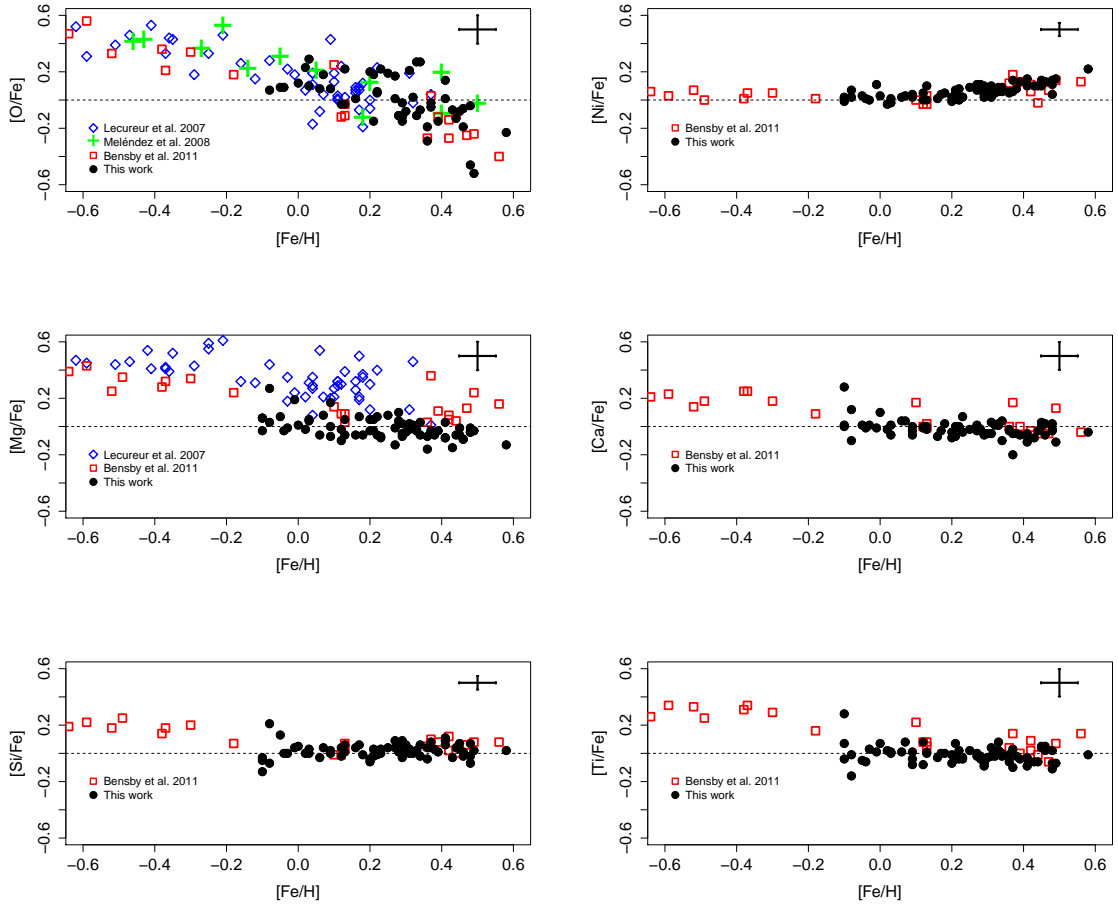


Figure 2.26: Abundances of O, Ni, Mg, Ca, Si, and Ti vs. $[Fe/H]$. Sample stars from thick disk are indicated as black dots, blue diamonds, green crosses, and red squares are bulge stars from Lecureur et al. (2007), Meléndez et al. (2008), and bulge microlensed dwarfs by Bensby et al. (2011), respectively.

(2008), Minchev & Famaey (2010), Schönrich & Binney (2009a,b), and Brunetti et al. (2010), among others. For example, Schönrich & Binney (2009b) predict that there are old very metal-rich stars in the solar neighbourhood, at a relatively low rotational velocity. In this case as well, these metal-rich stars would have an origin in the inner Galaxy.

Our subsample of 42 stars with kinematics of thick disk and solar α -to-Fe ratios seems to be similar to a sample identified by Haywood (2008): his identified subsample, shown as diamonds in his Figure 12, has kinematics of thick disk, $[\alpha/Fe] < +0.1$, and they are old with ages in the range 8-12 Gyr, ages characteristic of an old thin disk. Haywood (2008) assigns a status of transition objects between the two disks, but closer to an old thin disk. Despite the higher metallicity of our 42 such stars, they seem otherwise to be identical. It therefore seems that this

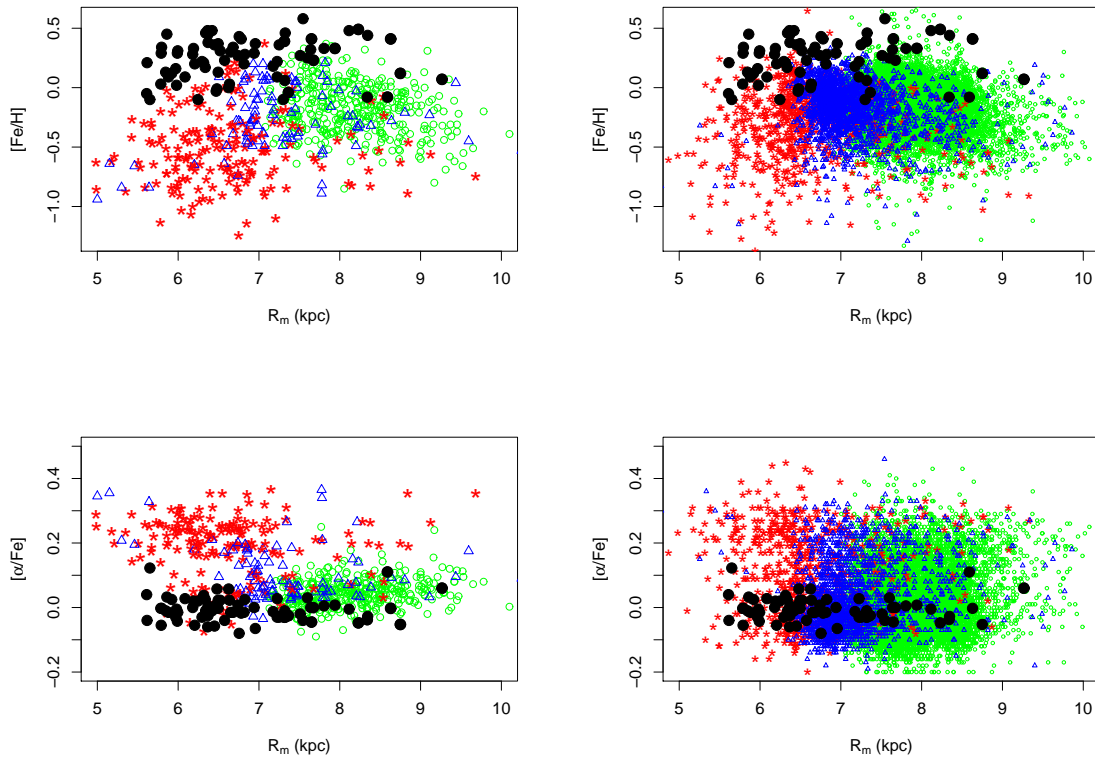


Figure 2.27: Mean Galactocentric distance vs. $[\text{Fe}/\text{H}]$ (top) and $[\alpha/\text{Fe}]$ (bottom). Panels on the right show the GCS stars. Stars belonging to thin disk, thick disk, and intermediate populations are indicated as green circles, red stars, and blue triangles, respectively.

subsample should be an inner disk, closer to the Galactic centre than Haywood’s subsample, an old thin disk component.

Indeed, radial migration from the inner disk (or bulge?) is the most probable origin of these stars. A need for more substantial radial mixing as first discussed in Wielen et al. (1996), was shown by Sellwood & Binney (2002) to be possible through the passage of recurrent transient spiral patterns. Lépine et al. (2003) and Roškar et al. (2011) present calculations demonstrating that resonant scattering with spiral arms trigger efficient migration of stars from regions at $R \sim 4\text{--}5$ kpc into the solar system region. Roskar et al. (2011) conclude that 50% of stars in the solar neighbourhood have come from $R < 6\text{kpc}$.

Radial migration of stars could be caused by spiral and/or bar resonance. Minchev & Famaey (2010) studied the combined effect of a central bar and spiral structure on the dynamics of a galactic disk, and they find that the spiral-bar resonance overlap induces a nonlinear

response leading to a strong redistribution of angular momentum in the disk. They show that a large population of stars from the bar's corotation resonance ($r \sim 4.5$ kpc) enters the solar circle (their Figure 6).

2.8 Summary and conclusions

In the present work, we analysed 71 metal-rich dwarf and turn-off stars, most of them old, selected from the high proper motion NLTT catalogue, as described in Raboud et al. (1998) (see Sect. 2.2). The aim of this work is to better understand these stellar populations, as well as to verify their high metallicities.

To be confident about the high-metallicity values, we compared the calculations carried out with two codes, from the Meudon (ABON2 code, Spite, 1967) and the Uppsala (BSYN/EQWI code, Edvardsson et al., 1993) groups, and the results are similar within $[\text{Fe}/\text{H}] \pm 0.02$. The metallicities derived are in the range $-0.10 < [\text{Fe I}/\text{H}] < +0.58$ from Fe I, and $-0.18 < [\text{Fe II}/\text{H}] < +0.56$ from Fe II.

The present sample was studied by means of their kinematics and abundances. Our sample of 71 metal-rich stars can be kinematically subclassified in samples of thick disk, thin disk, and intermediate stellar populations, with mean ages of about 7.8 ± 3.5 , 7.5 ± 3.1 , and 6.8 ± 2.9 Gyr, respectively. It seems definitely clear that some of the sample stars are quite old, and still quite metal rich. A most interesting feature of the sample stars is that 42 of them can be identified as belonging to the thick disk. In particular, 70% of the sample stars have space velocity $V < -50 \text{ km s}^{-1}$, which is more typical of a thick disk, but show solar α -to-iron ratios that are more compatible with thin disk members. This subsample appears similar to one identified by Haywood (2008), having kinematics of thick disk, together with $[\alpha/\text{Fe}] < +0.1$, and old ages in the range 8-12 Gyr; Haywood (2008) interprets these stars as old thin disk, or transition objects between the two disks, but as closer to an old thin disk. Our subsample has higher metallicities than Haywood's subsample and could have an origin closer to the Galactic centre than Haywood's old thin disk/transition component.

The presence of very metal-rich stars in the solar neighbourhood, at a relatively low rotational velocity give evidence of radial migration in the Galaxy, induced by the bar and/or interaction of bar and spiral arms, such as proposed by Fux (1997), Raboud et al. (1998), Sellwood & Binney (2002), Lépine et al. (2003), Haywood (2008), Minchev & Famaey (2010), (Schönrich & Binney,

2009a,b), or Brunetti et al. (2010).

Finally, we can conclude that the sample stars, all metal-rich, should be old thin stars from the inner disk, as suggested by Haywood (2008), including the 42 ones identified to have kinematics of the thick disk, and $[\alpha/\text{Fe}] < +0.1$. On the other hand, it is natural that the very metal-rich stars have low α -to-iron ratios, as discussed in Roskar et al. (2011), i.e. all stars with $[\text{Fe}/\text{H}] > 0$ show such low α -to-iron. In other words, the decreasing trend of $[\alpha\text{-elements}/\text{Fe}]$ with increasing metallicity means that the SNIa enrichment in iron occurs at the same pace for our sample, thick disk, and bulge stars.

Constraints on feedback processes during the formation of early-type galaxies¹

3.1 Introduction

The conversion of gas into stars in galaxies and the role of feedback mechanisms has been one of the key aspects of extragalactic astrophysics over the past decades. Several baryonic processes regulate the star formation efficiency within dark matter haloes. Simulations of galaxy formation and semi-analytical models have shown that it is only within haloes in a mass range around $M_{\text{halo}} \sim M_{\text{shock}} \sim 10^{12} M_{\odot}$ where baryons can form stars efficiently (Cattaneo et al., 2011; Moster et al., 2010; Bouché et al., 2010; Guo et al., 2011). Above this limit, gravitational shock heating and AGN feedback suppress the gas accretion (Dekel & Birnboim, 2006; Kereš et al., 2009, 2005; Birnboim & Dekel, 2003; Cattaneo et al., 2009, 2011). For galaxies within haloes with masses below $\sim 10^{12} M_{\odot}$, other processes are usually invoked to explain the star formation suppression. Reionization of the IGM suppresses gas accretion in haloes with circular velocity $\lesssim 40 \text{ km s}^{-1}$ (Mamon et al., 2010; Cattaneo et al., 2011). The energy liberated by supernova explosions can eject the gas from haloes with circular velocity $\lesssim 100 \text{ km s}^{-1}$, quenching the star formation within these systems (Dekel & Silk, 1986).

The fraction of mass acquired via mergers is also a function of stellar mass. For example, the semi-analytical models of De Lucia et al. (2006) show that the number of effective progenitors of galaxies with stellar masses $\lesssim 10^{11} M_{\odot}$ is less than two, while this number can be as large as five for galaxies with $M_{\star} \sim 10^{12} M_{\odot}$. According to Cattaneo et al. (2011), the dependence of feedback and merger processes on stellar mass defines three galaxy formation regimes. Stellar mass \sim

¹ Chapter to be published as: Trevisan et al. 2012, accepted for publication in The Astrophysical Journal Letters.

$10^{11}M_{\odot}$ marks the transition between two dominant mechanisms: gas accretion ($M_{\star} \lesssim 10^{11}M_{\odot}$) and gas-poor mergers ($M_{\star} \gtrsim 10^{11}M_{\odot}$). A third regime, set immediately below $\sim 10^{11}M_{\odot}$, is characterized by the increasing contribution of a population that was built by gas-rich mergers. The contribution of these mass-dependent processes can be an explanation for the well known dichotomy among early-type galaxies (e.g. Kang et al., 2007), supported by many observations, like e.g. a characteristic mass scale (Kauffmann et al., 2003), and a well-defined mass-metallicity relation (see e.g. Tremonti et al., 2004).

If the dichotomy originates from the mass-dependent role played by feedback, gas accretion, gas-rich and gas-poor mergers, we would expect to find signatures of these processes on the formation history of the galaxies along the different stellar masses. In this letter, the star formation history of a sample of galaxies in a wide range of stellar mass (from 10^9 to $10^{11.5}M_{\odot}$) has been examined for the presence of those signatures.

This Chapter is organized as follows: in Sect. 3.2, we describe the sample; in Sect. 3.3, we present a detailed study of the stellar populations using a spectral fitting code, which also is able to return the star formation history. Finally, we summarize and discuss our results in Sect. 3.4. Throughout the paper, we adopt a cosmology with $H_0 = 70 \text{ km s}^{-1} \text{ Mpc}^{-1}$, $\Omega_m = 0.3$ and $\Omega_{\Lambda} = 0.7$.

3.2 Sample description

Our sample of early-type galaxies was retrieved from SDSS-DR7 (Abazajian et al., 2009), selecting galaxies in the redshift range between 0.01 and 0.025, brighter than $m_{\text{petro},r} < 17.77$, where $m_{\text{petro},r}$ is the Petrosian magnitude in the r-band. This limit roughly corresponds to the magnitude at which the SDSS spectroscopy is complete (Strauss et al., 2002). The redshift limits chosen provide a 95% complete sample between $\mathcal{M}_{\text{petro},r} \sim -20$ and ~ -17.46 , where $\mathcal{M}_{\text{petro},r}$ is the k-corrected SDSS Petrosian absolute magnitude in r-band, obtained with the `kcorrect` code (version 4_2) of Blanton et al. (2003), choosing as reference the median redshift of the sample ($z_0=0.021$). See La Barbera et al. (2008) for details on the estimation of the completeness limits.

To select objects from the SDSS database, we define a flag mask, excluding those objects which are: *i*) blended, i. e., with more than one photometric peak¹; *ii*) too bright (detections of

¹ Since we are using objects from the primary catalog, this selection is equivalent to exclude objects with two or more peaks, which were not deblended

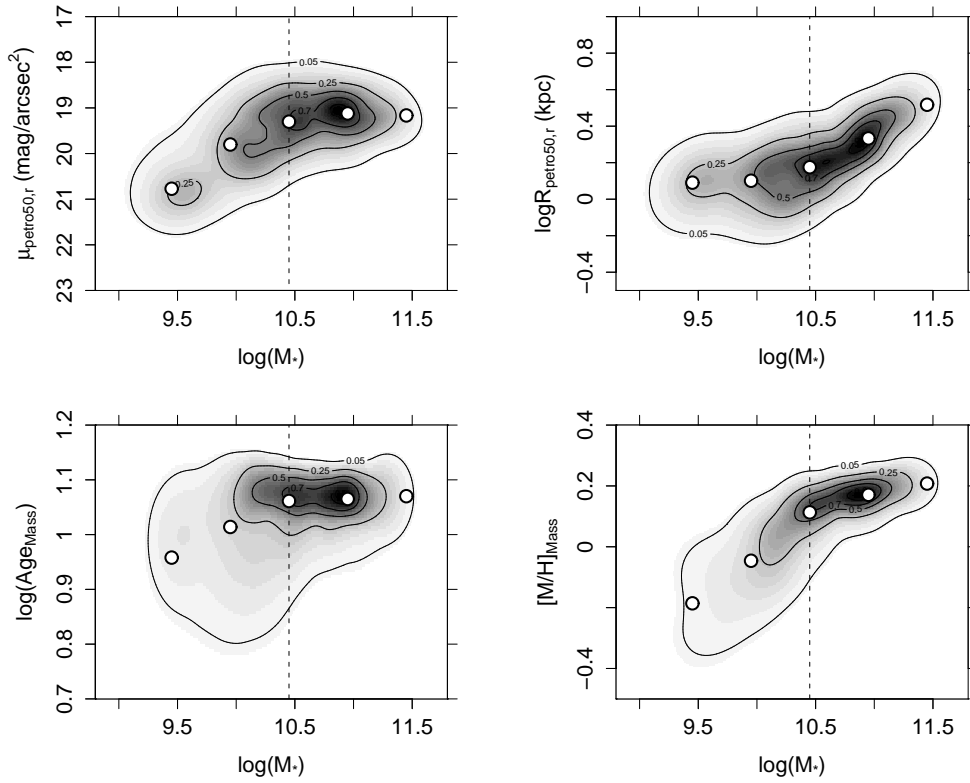


Figure 3.1: *Upper panels:* Scaling relations between stellar mass and surface brightness (left) or half-light radius (right). Both quantities are measured with respect to the Petrosian radius measured in the r band. *Bottom panels:* Mass-weighted average age (left) and metallicity (right), as obtained by the STARLIGHT spectral fitting code (see text for details). The grayscale corresponds to the density of points in each graph, with contour lines given at the 90, 70, 50, 25 and 5% levels with respect to the maximum value. The vertical dashed lines indicate $M_{\star} \sim 5 \times 10^{10} M_{\odot}$, which corresponds to the stellar mass of objects with $M_{\text{petro},r} = -20.2$, i.e. at the knee in the scaling relations. Median values obtained within mass bins (see Table 3.1) are shown in each panel as open dots.

> 200σ); *iii*) too large ($r > 4'$ or a deblend with $r > 1/2$ frame); *iv*) saturated; *v*) located close to the edge of a frame or *vi*) in a region where the sky measurement failed, thus the photometry is compromised; objects which *vii*) are part of the extended wing of a bright star or *viii*) which may be an electronic ghost of a bright star were also excluded. In addition, only objects with no spectroscopic warning on (i.e. `zWarning` attribute set to zero) were selected. This mask is used in a boolean expression in the main query, which returns 10187 objects.

Early-type galaxies obey well-studied scaling relations. Several morphological classification indicators have been proposed from the parameters of the SDSS pipeline (e.g. Strateva et al., 2001). However, it is still unclear whether these indicators can be applied to low mass systems. Previous work has shown that dwarf elliptical galaxies do not have the same surface brightness

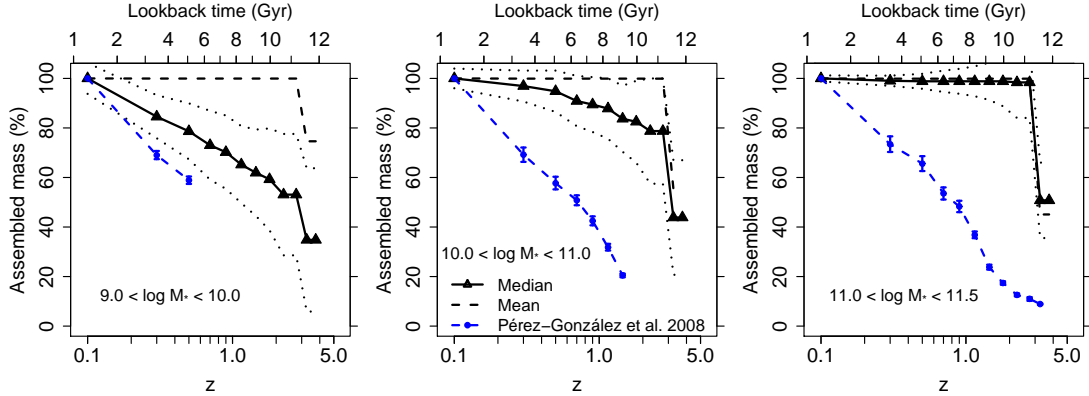


Figure 3.2: Fraction of assembled stellar mass as a function of redshift. The panels show the fraction of mass normalized by the mass of galaxies at $z \sim 0.1$. Triangles and solid lines show the mean values, dashed lines indicate the median values and the errors are represented by dotted lines. Results by Pérez-González et al. (2008) are indicated by solid circles with error bars.

profile as their giant counterparts (Graham & Guzmán, 2003), or similar star formation histories (Koleva et al., 2009), even featuring weak spiral structures (Lisker, 2009). Hence, we cannot use the standard SDSS attributes such as `eClass` or `fracDev`. Instead, visual inspection is the most reliable indicator of an early-type morphology. We use the classification from the Galaxy Zoo project (Lintott et al., 2011), and select only galaxies classified as elliptical. The Galaxy Zoo project collected simple morphological classifications of nearly 900,000 galaxies drawn from the Sloan Digital Sky Survey, contributed by hundreds of thousands of volunteers. This large number of classifications allows the exclusion of classifier error, and the measurement of the influence of subtle biases inherent in morphological classification. We found 10138 (99.7%) galaxies from our sample in the Galaxy Zoo database. Among them, 1359 are classified as ellipticals and 3313 as spirals. For the remaining 5466 galaxies, no reliable classification was possible.

In summary, our final sample is composed by 1328 objects between redshift 0.01 and 0.025, which are brighter than $\mathcal{M}_{\text{petro},r} = -17.46$ and visually classified as elliptical by the Galaxy Zoo project. A further visual inspection was carried out by the authors to confirm the morphological classification.

3.3 Stellar content

Age, metallicity, stellar mass and velocity dispersion were derived using the spectral fitting code STARLIGHT (Cid Fernandes et al., 2005). Before running the code, the observed spectra are corrected for foreground extinction and de-redshifted, and the models are degraded to match the wavelength-dependent resolution of the spectrum of each galaxy, as described in La Barbera et al. (2010).

We used SSP models based on the Medium resolution INT Library of Empirical Spectra (MILES, Sánchez-Blázquez et al., 2006), using the code presented in Vazdekis et al. (2010). We used version 9.1 of the models (Falcón-Barroso et al., 2011). The new version corrects some small errors in the radial velocities of the stars, has more accurate measurements of the spectral resolution of the stellar library, and gives a better absolute flux calibration. They have a spectral resolution of $\sim 2.5 \text{ \AA}$, almost constant with wavelength. A basis grid of 162 SSPs was selected, covering ages in the range of 0.07–12.6 Gyr, and with $[M/H] = -1.71, -1.31, -0.71, -0.38, 0.00,$ and $+0.20$. The models use a Kroupa (2001) Universal IMF with slope = 1.30, and isochrones by Girardi et al. (2000). The stellar masses – computed within the fiber aperture – are extended to the full extent of the galaxy by computing the difference between fiber and model magnitudes in the z band. The stellar mass is then $\log(M_\star) = \log(M_\star)' + 0.4 (m_{\text{fiber},z} - m_{\text{model},z})$.

We compare the results from STARLIGHT with different set-up parameters and different grids. We find no systematic trends, with differences typically within $\pm 20\%$. A detailed study of how results are affected by changes on the set-up parameters of STARLIGHT and different SSP model assumptions will be given in a forthcoming paper (Trevisan et al., in prep.). Variations in the SSP optical colors due to different IMF shapes are very small (see e.g. Vazdekis et al., 2010). Since STARLIGHT uses all the spectral information available, different IMF are not expected to affect our results. Hence, if a systematic change of the IMF is present (as suggested by, e.g. van Dokkum & Conroy, 2011) from low- to high-mass early-type galaxies, the net result would be a change of the stellar mass that corresponds to the position of the knee, keeping the derived stellar population properties presented here unchanged.

3.4 Results and discussion

In this letter, we study the star formation histories of a sample of ~ 1300 visually-selected elliptical galaxies by means of a spectral fitting method. For each galaxy we determine the stellar mass, metallicity, age and star formation history (SFH). Figure 3.1 shows both the photometric scaling relations (upper panels), along with the scaling of the derived average ages and metallicities, weighted in mass (bottom panels). The plots of surface brightness μ_{Petro} and Petrosian radius vs. stellar mass provide similar information, considering that μ_{Petro} is derived from Petrosian radius and luminosity, with the latter following the stellar mass of a galaxy. We bin the sample into five subsamples in stellar mass, indicated by blue dots in Figure 3.1. Table 3.1 presents the properties of the stellar populations for each bin. Regarding the age and metallicity scaling relation (bottom panels in Figure 3.1), a clear change in the slope of $[\text{M}/\text{H}]$ vs. stellar mass is apparent at $\sim 3 \times 10^{10} M_{\odot}$, equivalent to an absolute magnitude of $\mathcal{M}_{\text{dev},r} \sim -20.2$, below which the metallicity decreases linearly with mass. This corresponds approximately to the position of the knee seen in the photometric scale relations. The age distribution is more complex, with a homogeneous population of old galaxies for $M_{\star} \gtrsim 10^{10} M_{\odot}$, and an increased scatter towards younger ages with decreasing mass.

It is not clear whether the dichotomy in structural properties has the same origin as the stellar population properties (see e.g. Graham & Guzmán, 2003; Janz & Lisker, 2008; Côté et al., 2008). The fact that the knee in the photometric scaling relations has a counterpart in the stellar populations properties might indicate the processes regulating the star formation also affect the structural properties of galaxies. For example, feedback mechanisms might affect galaxy sizes, since the gas is pushed out of galaxies by outflows and might be converted into stars at large radii (e.g. Hills, 1980; Richstone & Potter, 1982; Fan et al., 2008, 2010; Damjanov et al., 2009).

3.4.1 Star formation history

Besides the averaged age and metallicity, spectral fitting provides a wealth of additional information on the star formation history of individual galaxies. For a given spectrum, a STARLIGHT run returns the contribution, as a percentage of mass, from each *basis* SSP. This distribution traces directly the star formation history. For each galaxy in the sample, we determine the “cumulative” mass fraction, i.e. the fraction of stars that are older than a given age, as a function of age. Then, we average the cumulative distributions over all galaxies within each mass bin. The

age of the distribution at the 50th and 80th percentiles in stellar mass is presented in Table 3.1. Galaxies with mass $\gtrsim 10^{10}M_{\odot}$ form their stars early and over a very short period of time, with 80% of their stars being older than ~ 11 Gyr. Galaxies in the low mass bins also have a very old stellar population. However, the time required to form 80% of the stellar mass is $\sim 5 - 6$ Gyr longer than that required by more massive galaxies. Hence, in early-type galaxies, *downsizing* should be interpreted as a more extended period of formation in low mass galaxies (instead of an overall later process of formation).

We compare our results with Pérez-González et al. (2008). Their study is based on a sample of ~ 28000 objects of all morphological types at $0 < z < 4$ to constrain the evolution of the stellar mass content in galaxies as a function of redshift. We rebin our sample into three subsamples with masses ranging from $\log(M_{\star}) = 9.0 - 10.0$, $10.0 - 11.0$, and $11.0 - 11.5$, which correspond to the first three bins of Pérez-González et al. (2008). Figure 3.2 shows the cumulative mass fractions as a function of redshift. In all three bins, early-type galaxies are formed in a much more efficient process, in contrast to the sample of Pérez-González et al. (2008), although the difference is more pronounced in the most massive bin. The large difference is due to the fact that their sample includes galaxies of all morphological types. In contrast, the analysis of the stellar populations of visually classified early-type galaxies at $z \lesssim 1$, yield a short-lived and early process of star formation (Ferrerias et al., 2009), consistent with our findings. Besides, the present sample is susceptible to aperture effects, since all galaxies are observed through a fiber with fixed angular diameter. Table 3.1 reports the mean aperture for each mass bin. The aperture A is defined as the ratio between the radius of the SDSS fiber and the half-light Petrosian radius measured in the r band, $A = R_{\text{fiber}}/R_{\text{petro50},r}$. The mean aperture varies from $A \sim 0.5$ in the first two bins to ~ 0.2 in the more massive bin. Assuming that the internal metallicity gradient of early-type galaxies varies from about -0.4 at high mass (La Barbera et al., 2011) to negligible at lowest mass (e.g. Koleva et al., 2011), the above variation of A would imply a change of ~ 0.16 in $[M/H]$, i.e. significantly smaller than that of ~ 0.5 seen for the range of masses in Table 3.1. Since age gradients are generally small in (massive) ETGs, aperture effects are also likely not to drive the variation of galaxy age with stellar mass. This conclusion is further supported by our analysis of the waveband dependence of the Fundamental Plane relation of bright ETGs (La Barbera et al., 2010), as we found that total (i.e. within an infinite aperture) metallicity and age do actually increase with stellar mass.

Table 3.1 - Stellar population properties as a function of stellar mass.

$\log(M_\star)$ interval	9.2 – 9.7	9.7 – 10.2	10.2 – 10.7	10.7 – 11.2	11.2 – 11.7
Number of objects	156	293	410	360	84
L-weighted Age (Gyr)	6.3 ± 3.6	8.0 ± 3.3	9.4 ± 2.3	9.6 ± 1.6	9.4 ± 1.2
M-weighted Age (Gyr)	8.6 ± 2.8	9.8 ± 2.4	10.7 ± 1.8	11.1 ± 1.4	11.3 ± 1.2
50% of stars older than (Gyr)	11.1	12.2	12.5	12.4	12.4
80% of stars older than (Gyr)	4.9	7.8	11.5	11.6	11.7
L-weighted [M/H]	-0.4 ± 0.2	-0.2 ± 0.2	0.0 ± 0.1	0.1 ± 0.1	0.1 ± 0.1
M-weighted [M/H]	-0.2 ± 0.2	-0.1 ± 0.1	0.1 ± 0.1	0.2 ± 0.0	0.2 ± 0.0
$R_{\text{fiber}}/R_{\text{petro50,r}}$	0.53 ± 0.19	0.54 ± 0.19	0.45 ± 0.15	0.31 ± 0.09	0.21 ± 0.05

3.4.2 Constraints of feedback processes

These results indicate that the processes regulating star formation in the low- and high-mass regimes are either different or they leave different signatures on the SFH. Tab. 3.1 shows that galaxies within the three more massive bins have similar ages and metallicities, with 80% of their stellar mass formed at approximately the same redshift. The ages and metallicities obtained are almost constant from the third to the fifth mass bins. On the other hand, the low mass bins show a gradual decrease of age and metallicity with decreasing stellar mass. Galaxies in all bins have roughly half of their stars formed before redshift $z \sim 2 - 3$. For the most massive galaxies, the additional 30% of the stars is formed within ~ 1 Gyr. Hence, the star formation in these galaxies after a redshift $z \sim 1$ can be considered “residual”. On the other hand, galaxies with mass ranging from $\log(M_\star) = 9.2$ to 9.7 have 80% of their star formed only at $z \sim 0.5$. Our results indicate that massive objects form faster and low mass systems have a more extended star formation history than suggested by models (e.g. De Lucia et al., 2006).

The feedback mechanism commonly invoked to explain the regulation of star formation in low mass systems is supernovae-driven winds (e.g. Larson, 1974; Ferrara & Tolstoy, 2000; Kereš et al., 2009). The chemical enrichment of low-mass galaxies indicate that the process regulating the star formation in these galaxies should be strong enough to eject metals out of the galaxy. However, it is not able to quench the star formation completely. Alternatively, these systems may be continuously being fuelled by infalling IGM gas at low metallicity.

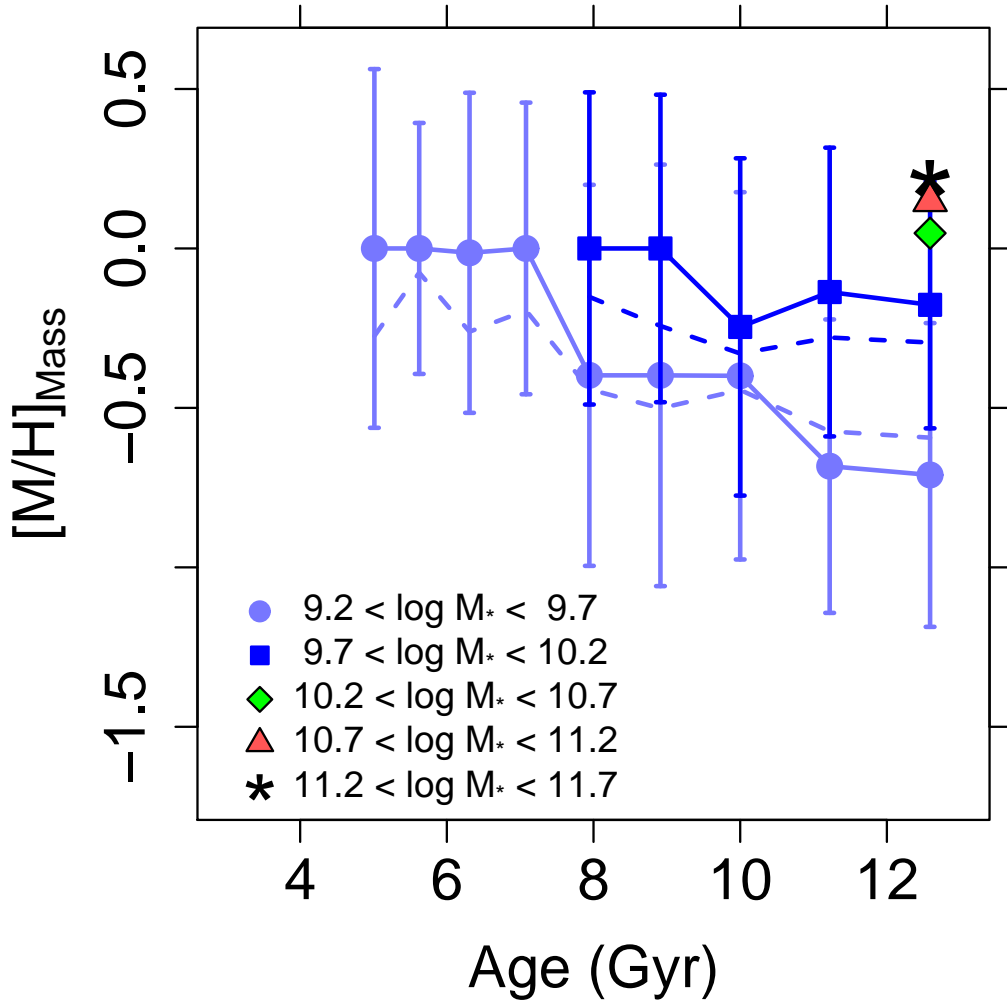


Figure 3.3: Mass-weighted metallicity as a function of stellar population age, in bins of stellar mass. The metal enrichment is shown until 80% of the mass is assembled. For this reason, only one point at 12.6 Gyr is shown for the three most massive bins. This corresponds to the age of the oldest SSP used in the spectral fitting. The solid (dashed) lines indicate the median (mean) values.

Figure 3.3 shows the mass-weighted $[M/H]$ as a function of stellar population age. The metal enrichment is shown up to the epoch when 80% of the stellar mass is formed. Galaxies in the three most massive bins form their stars very quickly, and 80% of their stars are older than 11 Gyr. For this reason, only one point is shown for these three bins. The figure shows a consistent trend of chemical enrichment, whereby the younger populations are more metal rich, an result that supports the idea that the mass-metallicity trend cannot be explained by the infall

of metal-poor gas, requiring instead a feedback mechanism that preferentially removes metals from low-mass galaxies. Supernova feedback can account for these “metal-enhanced outflows”. Since metals are formed in SN events, SN-driven winds are metal-enhanced with respect to the star-forming gas. Most of the metals mixed with the hot gas are able to leave the galaxy, whereas only a small fraction of cool ISM gas is lost (see e.g. Tremonti et al., 2004; Mac Low & Ferrara, 1999; Ferrara & Tolstoy, 2000). Aperture effect is not expected to affect these results, as galaxies in a given mass range have similar $r_{\text{fiber}}/r_{\text{petro}}$ ratios. In addition, the trend is not expected to be driven by the age-metallicity degeneracy, since in this case the same slope would be observed for all mass bins.

The SFH of high-mass galaxies indicate that their stars were already formed before $z \sim 2$. Several studies have shown that high mass systems are assembled mainly via mergers (De Lucia et al., 2006; Cattaneo et al., 2011). However, our results constrain the main epoch of growth via mergers to $z \gtrsim 2$, unless the mergers proceed mainly via gas poor progenitors, a requirement needed both to prevent young stars from forming and to keep the mass-metallicity relationship in place. Alternatively, these systems can be already in place at high redshift, as suggested by the weaker number density evolution with redshift for the most massive galaxies between $z \sim 1.5$ and 0. (see e.g. Conselice et al., 2007; Ferreras et al., 2009; Banerji et al., 2010).

The presence of galaxies with a high baryon content already in the form of stars at high redshift can be justified by the fact that the masses of the underlying dark matter haloes are above the threshold for virial shock heating. The cold mode of galaxy formation (Kereš et al., 2005; Guo et al., 2011; Dekel et al., 2009) can account for the required high star formation efficiency. However, it is still not clear how this process can result in the spheroidal morphologies we see already in place at $z \sim 1$.

Galaxy distribution and evolution around a sample of 2dF groups¹

4.1 Introduction

Small groups of galaxies contain about half of all galaxies in the Universe (e.g. Huchra & Geller, 1982; Geller & Huchra, 1983; Nolthenius & White, 1987; Ramella et al., 1989). They represent the link between galaxies and large-scale structures, and have at least two important features: galaxies inside groups interact more with each other than they do in the field; and groups have small crossing times, generally $\lesssim 0.1 H_0^{-1}$, indicating that they are dynamical units, that are possibly in virial equilibrium. However, the dynamical state of a galaxy group is not easy to determine. Group environments are unstable, the systems still may be separating from the cosmic expansion, collapsing, accreting new members, or merging with other groups to produce larger objects. Generally, the estimated properties of these systems are based on the assumption that groups of galaxies defined by friends-of-friends algorithm (and other clustering methods) are gravitationally bound objects. This is not completely true, since projection effects can dominate the statistics of these systems (e.g. Diaferio et al., 1993). In a Λ CDM cosmology, Niemi et al. (2007) showed that about 20% of nearby groups are not bound, but merely visual objects. There is no methodology for determining the dynamical status of galaxy groups. An interesting attempt at describing group evolution is the fundamental track diagram, a plane that follows the evolution of isolated galaxy systems in an expanding Universe (see Mamon, 1993). The plane is defined by the dimensionless crossing time and the dimensionless mass bias. This diagram, however, suffers from degeneracies between the expansion and early collapse phases,

¹ Chapter published as: Ribeiro et al. 2009, A&A, 505, 521

and also between the full collapse and rebound phases. Although most groups lie close to the fundamental track, there is a large scatter and the result is inconclusive (Mamon, 2007). Giuricin et al. (1988) applied a correction factor to the virial mass and assumed a specific model for the system evolution, but the model only accounted for internal gravitational forces and neglected tidal interactions with the neighborhoods. Galaxy groups, however, interact significantly with their surroundings. For instance, the shapes and galaxy flows around these systems are related to large-scale structures and are relevant to the internal dynamics of the groups (e.g. Paz et al., 2006; Ceccarelli et al., 2005; Plionis et al., 2004). Generally, one assumes that bound groups reach a quasi-equilibrium state in which galaxies have isotropic orbits with random phases. This happens after the scattering of galaxies by each other and by masses outside the group. If a group is isolated and remains fairly spherical, then its constituent galaxies are not deflected from their radial trajectories until the group has collapsed to a small fraction of its maximum radius. In this case, the collapse is violent and the group first reaches equilibrium at ~ 200 times the mean cosmic density. At the opposite extreme in which a nascent group is strongly influenced by surrounding objects, the collapse is gentle and the group attains equilibrium at lower density constraints. Hence, measuring environmental influence over galaxy systems can be a way of accessing their formation history and present dynamical state. In the present work, this important point is investigated where we study the surroundings of galaxy groups previously selected from 2dF by Tago et al. (2006). Using some tools of spatial statistical analysis, we examine the possible correlation between the anisotropy around groups and galaxy evolution. This relationship may shed some light on the dynamical state of galaxy groups.

This Chapter is organized as follows: in Sect. 4.2 we present the methodology and data used in this work; in Sect. 4.3, we present our results and explore the relation between anisotropy and galaxy evolution; in Sect. 4.4, we discuss our results.

4.2 Methodology and data

4.2.1 Probing anisotropy around groups

For the projected distribution, anisotropy can be probed by the reduced second-order moment measure \mathcal{K} of a point pattern (e.g. Stoyan & Stoyan, 1994). In this work, we estimate \mathcal{K} using the library **spatstat** within the R statistical package (see Baddeley, 2008). The command `Kmeasure`

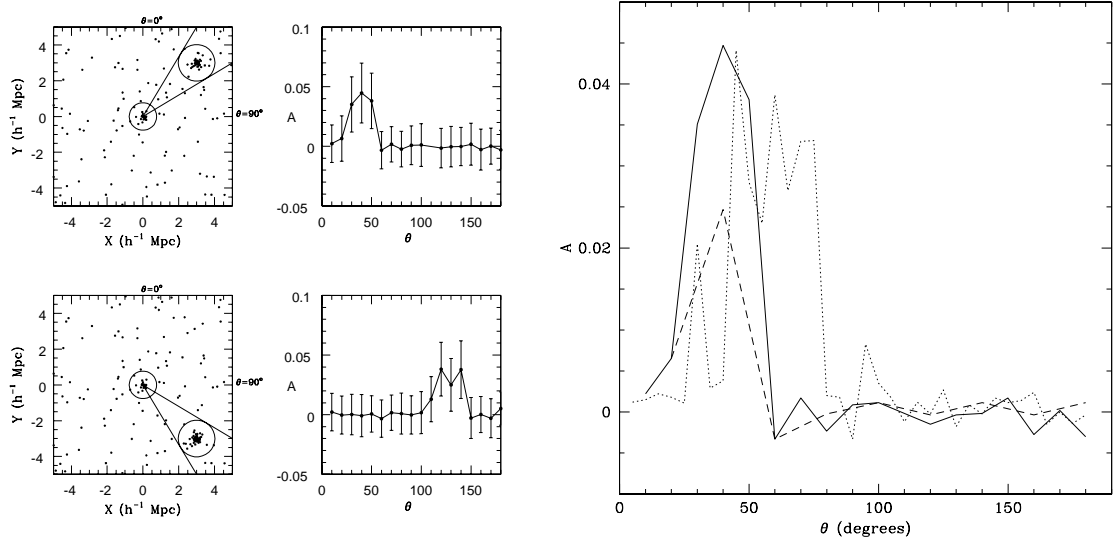


Figure 4.1: *Left panel:* example of anisotropy signal detection for mock fields consisting of Hernquist spheroids plus Poisson background. *Right panel:* detection of anisotropy using three angular steps: $\Delta\theta = 5^\circ$, 10° , and 20° , in dotted, solid, and dashed lines, respectively.

(spatstat) executes the following steps:

1. A point pattern is assumed.
2. A list of all pairs of distinct points in the pattern is produced.
3. The vectors that join the first point to the second point in each pair are computed.
4. These vectors are considered to be a new pattern of ‘points’.
5. A Gaussian kernel smoother is applied to them.

The algorithm approximates the point pattern and its window with binary pixel images, introduces a Gaussian smoothing kernel, and uses the Fast Fourier Transform to form a density estimate κ . The calculation takes into account the edge correction known as the “translation correction” (see Ripley, 1977). The density estimate of κ is returned in the form of a real-valued pixel image. The \hat{K} estimator is defined as the expected number of points lying within a distance r_{max} of a typical point, and with a displacement vector of orientation in the range $[\alpha, \beta]$. This can be computed by summing the entries over the relevant region, i.e, the sector of the disc of radius r centred on the origin with angular range $[\alpha, \beta]$. Hence, we can compute a measure of anisotropy (A) as integrals of the form

$$A \equiv \int_0^{r_{max}} \int_{\alpha}^{\beta} d\kappa(r, \theta). \quad (4.1)$$

Note that the second-order moment function K is used to test the hypothesis that a given planar point pattern is a realization of a Poisson process. Thus, the objective is to search for significant peaks in the integral given in Eq. (1) for angular steps $\Delta\theta = \beta - \alpha$. The uncertainty in the anisotropy measurement is computed directly from the variance in the pixel values in the corresponding circular sector. Of course, the choice of $\Delta\theta$ is arbitrary. In this work, we assume that $\Delta\theta = 10^\circ$, based on the following analysis.

Consider a controlled sample corresponding to a point pattern given by a Poisson distribution (100 points) plus a central group defined as a Hernquist spheroid (Hernquist, 1990). An additional group is located initially at $\sim 4h^{-1}$ Mpc around an angle of 45° , and then around an angle of 135° . In Figure 4.1, we present both the mock field and the anisotropy signal as a function of the angle for the two positions of the second group. It is clear from this figure that the second group produces significant anisotropy signal. To justify our choice of $\Delta\theta$, we present in Figure 4.1 (right panel) a reanalysis in the case of the second group at 45° for $\Delta\theta = 5^\circ, 10^\circ$, and 20° . For $\Delta\theta = 5^\circ$, we still detect the peak, but there are now secondary peaks and a more noisy behaviour for A . For $\Delta\theta = 20^\circ$, the peak is still there, but now less significant. This result suggests that in the limit of a too small value $\Delta\theta$, we have a noisy anisotropy curve (possibly with false peaks), while in the limit of very large $\Delta\theta$, the signal can be completely lost. In this work, we set $\Delta\theta = 10^\circ$ as a confidence scanning angle to probe anisotropy in galaxy fields of our sample.

4.2.2 The 2dF sample

We apply the anisotropy estimator to a sample consisting of 32 galaxy groups previously identified by Tago et al. (2006) applying the friends-of-friends algorithm to data from the 2dFGRS (Colless et al., 2001). This subset corresponds to those groups located in areas of at least 80% redshift coverage out to 10 times the virial radius roughly estimated from the projected harmonic mean. Group members and interlopers were redefined after the identification of gaps in the redshift distribution according to the technique described by Lopes et al. (2009a). Before selecting group members and rejecting interlopers we first refine the spectroscopic redshift of each group and identify its velocity limits. For this purpose, we employ the gap-technique described in Katgert et al. (1996) and Olsen et al. (2005) to identify gaps in the redshift distribution. A

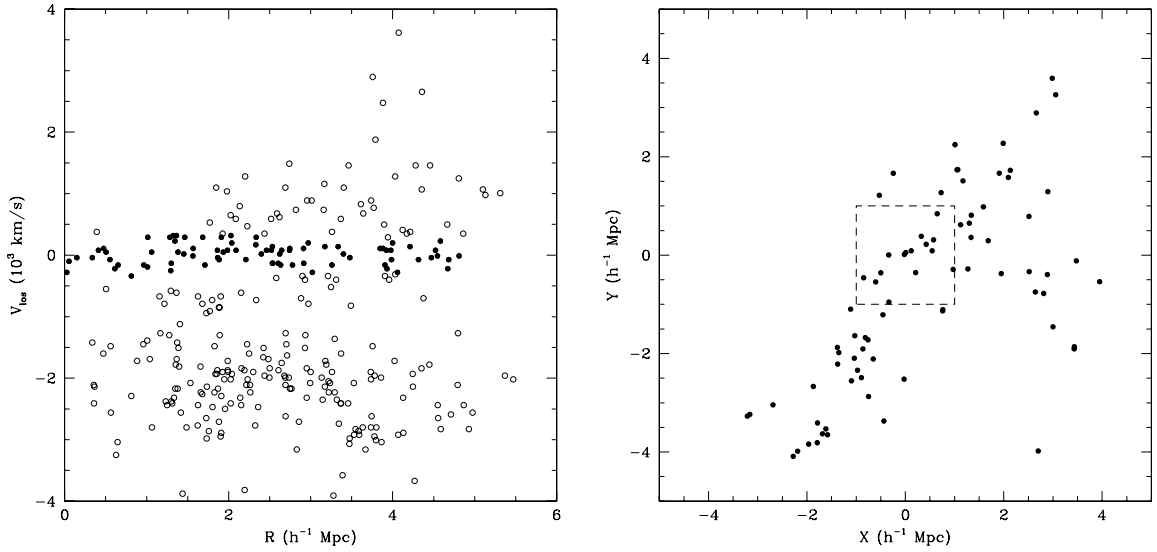


Figure 4.2: *Left panel:* phase-space diagram of Group 91 shown as an example. We consider the group center to derive the velocity and radial offsets. Group members (filled circles) are selected with a shifting gapper procedure. The interlopers are represented by open circles. *Right panel:* Group members with a central $1 h^{-1}$ Mpc square in dashed lines.

variable gap, called *density gap* (Adami et al., 1998), is considered. To determine the group redshift, only galaxies within $0.50 h^{-1}$ Mpc are considered. Details about this procedure are found in Lopes et al. (009a).

With the new redshift and velocity limits, we apply an algorithm for interloper rejection to define the final list of group members. We use the “shifting gapper” technique (Fadda et al., 1996), which consists of the application of the gap-technique to radial bins from the group center. We consider a bin size of $0.42 h^{-1}$ Mpc (0.60 Mpc for $h = 0.7$) or larger to ensure that at least 15 galaxies are selected. Galaxies not associated with the main body of the group are discarded. This procedure is repeated until the number of group members is stable and no further galaxies are eliminated as intruders. An example of the application of the shifting gapper procedure is seen in Figure 4.2 (right panel). The main difference from the study of Lopes et al. (009a) is that here we consider all galaxies within 10 times the virial radius (as listed in Tago et al. 2006). In Lopes et al. (009a), the interloper removal procedure was applied to galaxies within a maximum radius of $2.5 h^{-1}$ Mpc. Next, we estimate the velocity dispersions (σ) and physical radius (R_{200}) of each group. Finally, a virial analysis is performed for mass estimation (M_{200}). Further details regarding the interloper removal and estimation of global properties (σ , physical

Group 91

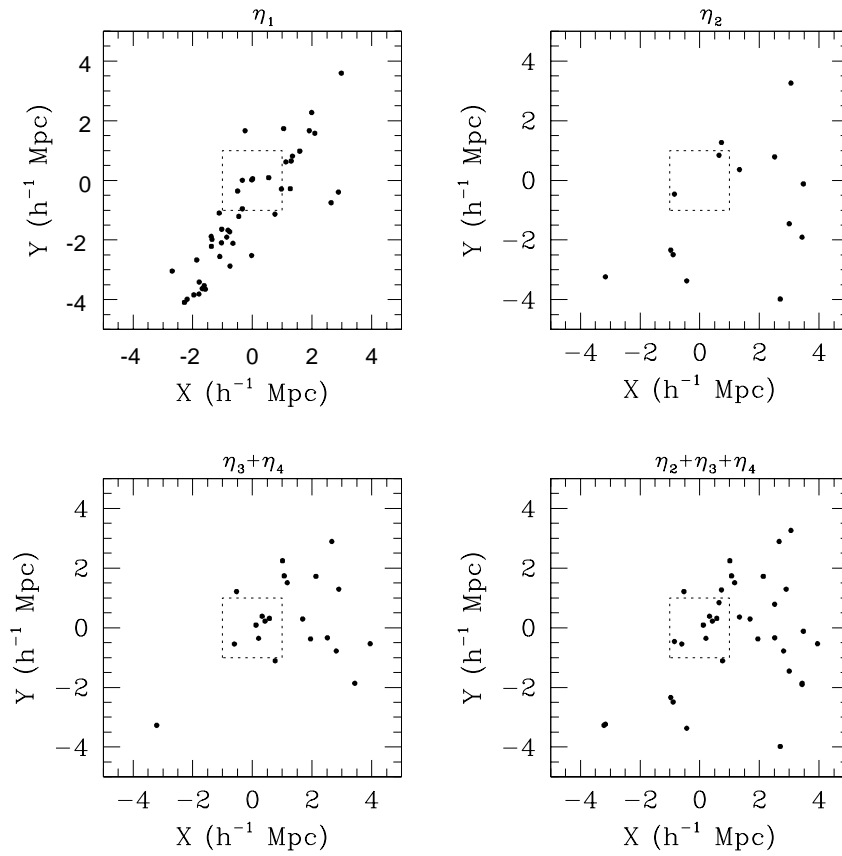


Figure 4.3: Galaxy distribution around Group 91 per η -type division with central $1 h^{-1}$ Mpc squares in dashed lines.

radius and mass) are found in Lopes et al. (009a).

The physical properties of these groups are presented in Table 4.1. The columns correspond to:

1. Group identification number;
2. RA (J2000.0) in degrees (mean of member galaxies);
3. DEC (J2000.0) in degrees (mean of member galaxies);
4. z , the new redshift, determined within $0.5 h^{-1}$ Mpc;
5. σ , the velocity dispersion in kms^{-1} (computed with the group members);
6. R_{200} in Mpc;

7. M_{200} ($10^{14} M_{\odot}$);
8. Number of member galaxies (after exclusion of interlopers);
9. Number of member galaxies within R_{200} ;
10. Global anisotropy (see definition in Section 2.3);
11. Fraction of η_1 galaxies (Section 2.3);
12. Fraction of galaxies within R_{200} .

Table 4.1 - Properties of groups.

Group	RA ($^{\circ}$)	DEC ($^{\circ}$)	z	σ (km s^{-1})	R_{200} (Mpc)	M_{200} ($10^{14} M_{\odot}$)	N	N_{200}	GA	f_{η_1}	f_{200}
23	168.608	-4.008	0.1010	264.202	0.65	0.35	16	13	2.894	0.645	0.812
59	162.581	-0.332	0.0949	221.623	0.55	0.21	13	10	3.263	0.687	0.769
60	162.231	0.936	0.1070	262.031	1.28	2.66	65	18	2.939	0.500	0.276
61	161.688	1.438	0.1068	290.062	1.20	2.19	73	22	4.152	0.550	0.301
63	160.890	1.555	0.1065	198.729	1.03	1.37	46	10	2.992	0.520	0.217
64	160.419	1.361	0.0726	169.913	0.79	0.61	43	14	2.903	0.625	0.325
83	174.909	-1.110	0.0777	236.053	0.99	1.20	54	20	2.746	0.541	0.370
86	180.818	0.882	0.0782	125.600	0.66	0.35	36	12	2.357	0.566	0.333
91	191.534	0.703	0.0892	155.980	0.89	0.88	80	9	3.483	0.562	0.112
95	191.946	-0.213	0.0898	219.657	0.95	1.06	58	20	2.409	0.541	0.344
137	23.602	-32.823	0.0646	362.672	1.08	1.51	45	25	3.690	0.500	0.555
139	32.829	-33.200	0.1065	179.301	0.84	0.75	34	12	3.235	0.604	0.352
182	6.925	-30.745	0.1066	279.339	1.34	3.01	74	18	2.553	0.479	0.243
187	10.290	-29.003	0.1089	165.089	0.90	0.93	59	12	2.654	0.562	0.203
188	14.169	-30.784	0.0769	256.686	1.16	1.94	64	17	1.917	0.500	0.265
189	9.426	-30.787	0.0613	249.968	0.93	0.98	36	15	3.259	0.541	0.416
193	17.559	-29.663	0.1074	151.658	0.82	0.71	46	11	3.724	0.604	0.239
195	15.688	-31.925	0.1087	222.339	0.98	1.21	40	16	2.759	0.541	0.400
208	36.363	-30.062	0.0723	270.511	0.82	0.68	26	16	2.194	0.625	0.615
216	47.233	-31.051	0.0650	222.393	1.09	1.55	59	16	3.593	0.550	0.271
225	328.094	-28.863	0.0929	197.640	0.97	1.14	45	17	2.517	0.583	0.377
245	352.361	-30.148	0.1057	378.582	1.60	5.16	58	12	2.168	0.479	0.206
249	355.576	-30.284	0.0619	234.400	1.01	1.24	45	24	3.115	0.562	0.533

Table 4.1 - continued.

Group	RA ($^{\circ}$)	DEC ($^{\circ}$)	z	σ (km s^{-1})	R_{200} (Mpc)	M_{200} ($10^{14} M_{\odot}$)	N	N_{200}	GA	f_{η_1}	f_{200}
250	355.214	-30.339	0.0801	246.493	0.71	0.43	22	14	1.855	0.645	0.636
256	10.190	-26.482	0.1121	342.401	1.31	2.83	57	15	3.091	0.479	0.263
258	9.870	-26.520	0.1009	158.659	0.66	0.36	19	8	3.615	0.666	0.421
264	26.607	-26.639	0.0600	301.131	0.98	1.14	22	13	3.717	0.604	0.590
266	32.245	-26.366	0.1162	271.840	0.83	0.72	17	10	2.157	0.562	0.588
269	42.215	-26.001	0.1052	239.011	1.05	1.47	39	11	2.986	0.500	0.282
278	334.293	-26.673	0.0598	315.139	1.07	1.47	37	15	2.351	0.520	0.405
280	343.716	-25.911	0.0805	168.699	0.74	0.51	23	12	2.690	0.566	0.521
281	343.461	-25.517	0.0899	234.579	1.06	1.48	48	19	2.711	0.541	0.395

4.2.3 Description of one group + surroundings field

The methodology presented in Sect. 4.2.1 is now applied to describe in detail the anisotropy features of Group 91 plus its neighborhood. This field is presented in Figure 4.3 (left panel), where equatorial coordinates were transformed to Cartesian ones using redshift information for a flat universe with $\Omega_m = 0.3$. We can see that the galaxy distribution is clearly anisotropic. In Figure 4.3, we present the same field, but now we identify differences in the general behaviour according to the galaxy spectral type defined by Madgwick et al. (2002). The η parameter is a measure of spectral type, which corresponds approximately to the following division:

$\eta_1 \longrightarrow$ E-S0 galaxies [$\eta < -1.4$]
$\eta_2 \longrightarrow$ Sa galaxies [$-1.4 \leq \eta < 1.1$]
$\eta_3 \longrightarrow$ Sb galaxies [$1.1 \leq \eta < 3.5$]
$\eta_4 \longrightarrow$ Scd galaxies [$\eta \geq 3.5$]

(Madgwick et al. (see 2002) for more details about the spectral type classification and data division by η).

In this work, we ascertain whether the anisotropy pattern is related to the galaxy types in the group + surroundings field. The anisotropy profile of Group 91 is presented in Figure 4.4 (left

panel), where we see the overall behavior in the small box and the behavior per type in colors (main box). Typically, our fields are so dominated by η_1 galaxies ($\sim 60\%$ in average) that the number of objects in the remaining bins are too small for comparisons between each other. Here, we just compare η_1 with the other types, according to $\eta_1 \times \eta_2$, $\eta_1 \times (\eta_3 + \eta_4)$, and $\eta_1 \times (\eta_2 + \eta_3 + \eta_4)$. To verify whether the respective profiles differ significantly from each other, we applied a bootstrap hypothesis test, assuming as the null hypothesis that the mean of the difference in the anisotropy signal between two populations is zero ($H_0 : \mu = 0$), while the alternative hypothesis is $\mu \neq 0$. A small p -value makes the null hypothesis appear implausible. Obtaining p can be done using the bootstrap resampling approach. In this work, based on 1,000 bootstrap sample replications, we obtain for Group 91: $\eta_1 \times \eta_2 : p=0.008$; $\eta_1 \times \eta_{34} : p=0.014$; and $\eta_1 \times \eta_{234} : p=0.015$. Taking the usual cutoff of $p = 0.05$ (5% significance level), we reject the null hypothesis in all cases and conclude that η_1 -type galaxies in this case have a distinctive spatial distribution. Additionally, determining the group + surroundings shape by diagonalizing the moments of the inertia tensor as a function of the radius, we find that there is an elongation jump close to R_{200} (see Figure 4.4, right panel). This suggests that the group is embedded in a highly anisotropic structure.

We applied this methodology to the remaining groups of our sample and found that only 15% of the groups (91,139,189,193, and 250) have a distinctive η_1 population. However, the number of fields with significant elongation is quite high. To help us understand that, we define a new quantity, the global anisotropy (GA) as

$$\text{GA} = \frac{\text{Max}(A) - \text{Median}(A)}{\sigma(A)}. \quad (4.2)$$

Basically, this is a measure of the relative importance of the anisotropy peak with respect to the entire profile. The values of GA are listed in Table 4.1. Here, we require that a significant elongation corresponds to $\text{GA} \geq 2$, i.e., $\text{Max}(A) \geq 2\sigma(A) + \text{Median}(A)$. Following this criterium, we have found that 94% of the fields have a high degree of elongation. Being more restrictive and setting $\text{GA} \geq 3$, 37% of the systems still have this alignment prominence. In our control sample of 1,000 Hernquist spheroids + Poisson background, we found just 12% of alignments by chance. Hence, we conclude that our sample consists of a significant number of group + surroundings predominantly elongated.

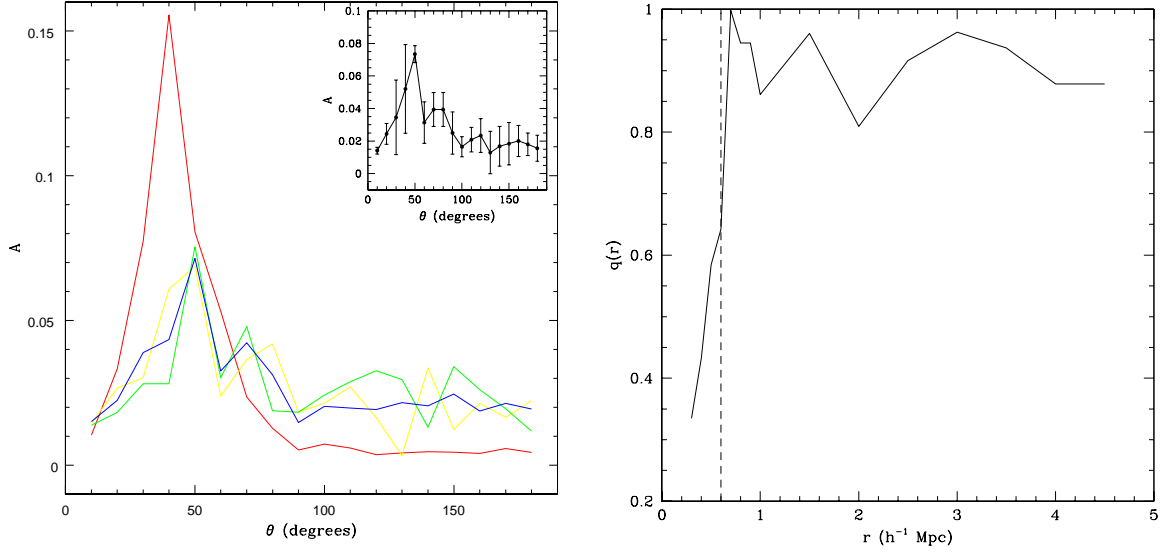


Figure 4.4: *Left panel:* anisotropy profile of Group 91. η_1 galaxies are in red; η_2 galaxies are in yellow; $\eta_3 + \eta_4$ galaxies are in green; and $\eta_2 + \eta_3 + \eta_4$ galaxies are in blue. The general behaviour is displayed in the small box. *Right panel:* ratio of eigenvalues $q = \lambda_1/\lambda_2$ as a function of the radius, obtained after diagonalizing the inertia tensor $\det(I_{ij} - \lambda^2 M) = 0$ (where M is a 2×2 unit matrix). The vertical dashed line indicates R_{200} .

4.3 Anisotropy and galaxy evolution

The intrinsic elongated shape of groups can be a very important factor when determining their dynamical state (e.g. Tovmassian & Plionis, 2009). In this section, we investigate a possible correlation between anisotropy and galaxy evolution for all galaxies in our sample.

4.3.1 Characterizing galaxies around groups

We use the spectral parameter η to characterize galaxy evolution around groups. We applied the Welch's t -test (Welch, 1947), also known as the F -test (Press et al., 1986), which is an adaptation of the Student's t -test, to the comparison of two samples (in this case $\eta < -1.4$ and $\eta \geq -1.4$) with unequal variance. This statistic tests the null hypothesis that the mean of each of the two samples are equal, assuming a normally distributed parent population. The test was applied in two ways: (i) testing the two samples by keeping the divisory line $\eta = -1.4$; (ii) testing data iteratively in samples defined by one of the other quantities (M_B , $B - R$, and distance to the center of the groups, d_c). In the second case, the two data sets are redefined for increasing (or decreasing) values of the quantity, so we can find the corresponding divisory line (i.e., the first value in which the null hypothesis is rejected).

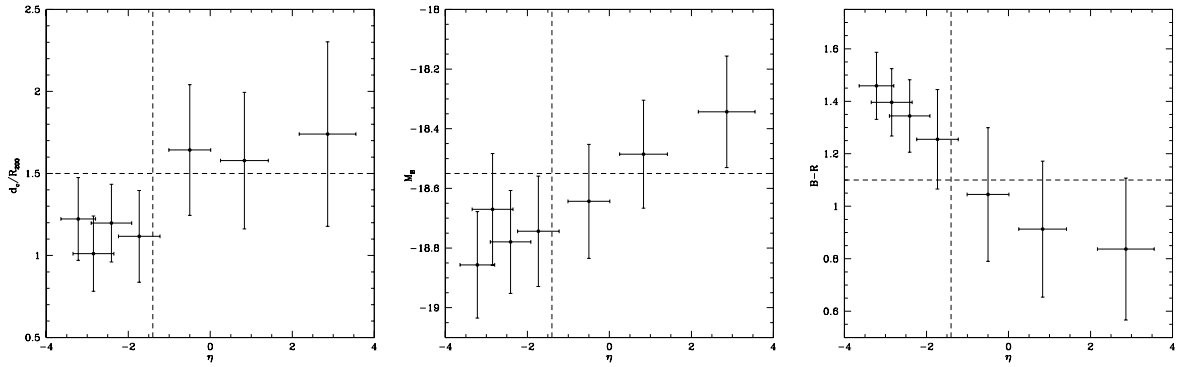


Figure 4.5: Distances of galaxies to the center of the groups (normalized by R_{200}) as a function of η (left panel). Absolute magnitudes as a function of η (middle panel). B-R color as a function of η (right panel). Dashed lines divide data into two groups statistically distinct.

We first probe the distribution of galaxies as a function of the distances to the center of the groups. To illustrate our results more clearly, galaxies were sorted in η and divided into seven subgroups with the same number of objects. In Figure 4.5 (left panel), we see that low η (early type) galaxies are more concentrated than high η objects. We verified a corresponding horizontal line at $d_c/R_{200} = 1.5$, where data can be divided into two statistically distinct groups, after a t -test ($p = 1.78 \times 10^{-5}$). This expected result is just a manifestation of the morphology-density (radius) relation (e.g. Dressler, 1980). We also find that our sample is dominated by dwarf galaxies ($M_B \geq -20$ for $\sim 90\%$ of the sample) and that low η galaxies are more luminous than the remainder (see Figure 4.5, middle panel), where a horizontal line at $M_B = -18.55$ divides data into two subgroups that are statistically distinct ($p = 1.02 \times 10^{-7}$). Finally, the distribution of (B-R) color indicates two distinct groups at B-R=1.1 ($p = 8.07 \times 10^{-5}$), where low η galaxies are redder than the rest (see Figure 4.5, right panel). Thus, our sample is dominated by dwarfs, and low η objects are more central, luminous and redder than the other galaxies.

4.3.2 Global anisotropy, galaxy evolution, and dynamics

Now, we wish to study the possible correlation between galaxy evolution and anisotropy. We verified that the fraction of η_1 galaxies around groups exhibits a significant correlation with GA. This result, presented in Figure 4.6 (right panel), suggests that a relation exists between the shape of groups + surroundings, and their star formation rate. More anisotropic fields have a lower fraction of η_1 galaxies (the F -test presents $p = 0.0036$ for a linear fit). We also divide

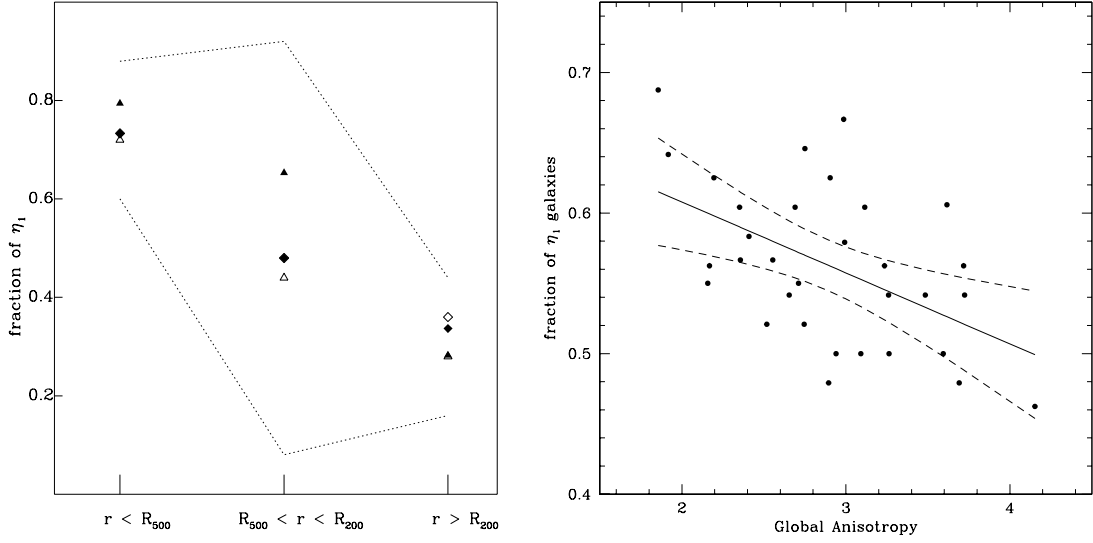


Figure 4.6: *Left panel:* global anisotropy versus the fraction of η_1 galaxies. Best fit linear is in solid lines, while 95% confidence levels contours are presented as dashed lines. *Right panel:* distance against the fraction of η_1 galaxies, now divided in GA quartiles (open and filled losangles, open and filled triangles). Dotted lines show the typical errors for each distance range.

galaxies into GA quartiles and probe their distribution with distance to the center. This is also presented in Figure 4.6 (left panel), where we see no significant difference between the GA quartiles with increasing radius. The general behaviour just reproduces the morphology-density (radius) relation.

The η_1 galaxy fraction in the fields is a good indicator of evolution, since the morphology-density relation appears to imply that late become early type galaxies. We now present some additional trends in our data associated to this quantity. In Figure 4.7, we see that f_{η_1} is anticorrelated with σ ($p=0.0066$) and N ($p=2.8 \times 10^{-5}$). That is, cold groups evolving in poorer environments contain a higher fraction of η_1 galaxies. At the same time, f_{η_1} is correlated with f_{200} ($p=0.0002$): groups in which more galaxies are inside R_{200} exhibits a higher fraction of η_1 galaxies (Figure 4.7). Finally, f_{200} is anticorrelated with N ($p=1.8 \times 10^{-8}$), (see also in Figure 4.7). This all means that rich fields harbour less concentrated galaxy systems with fewer η_1 galaxies, i.e., less evolved groups. These fields are also more anisotropic, containing hotter groups, which is more consistent with a scenario where galaxies move along the elongation direction, as expected in dynamical young systems that form by anisotropic accretion of matter along filamentary large-scale structures (e.g. Tovmassian & Plionis, 2009).

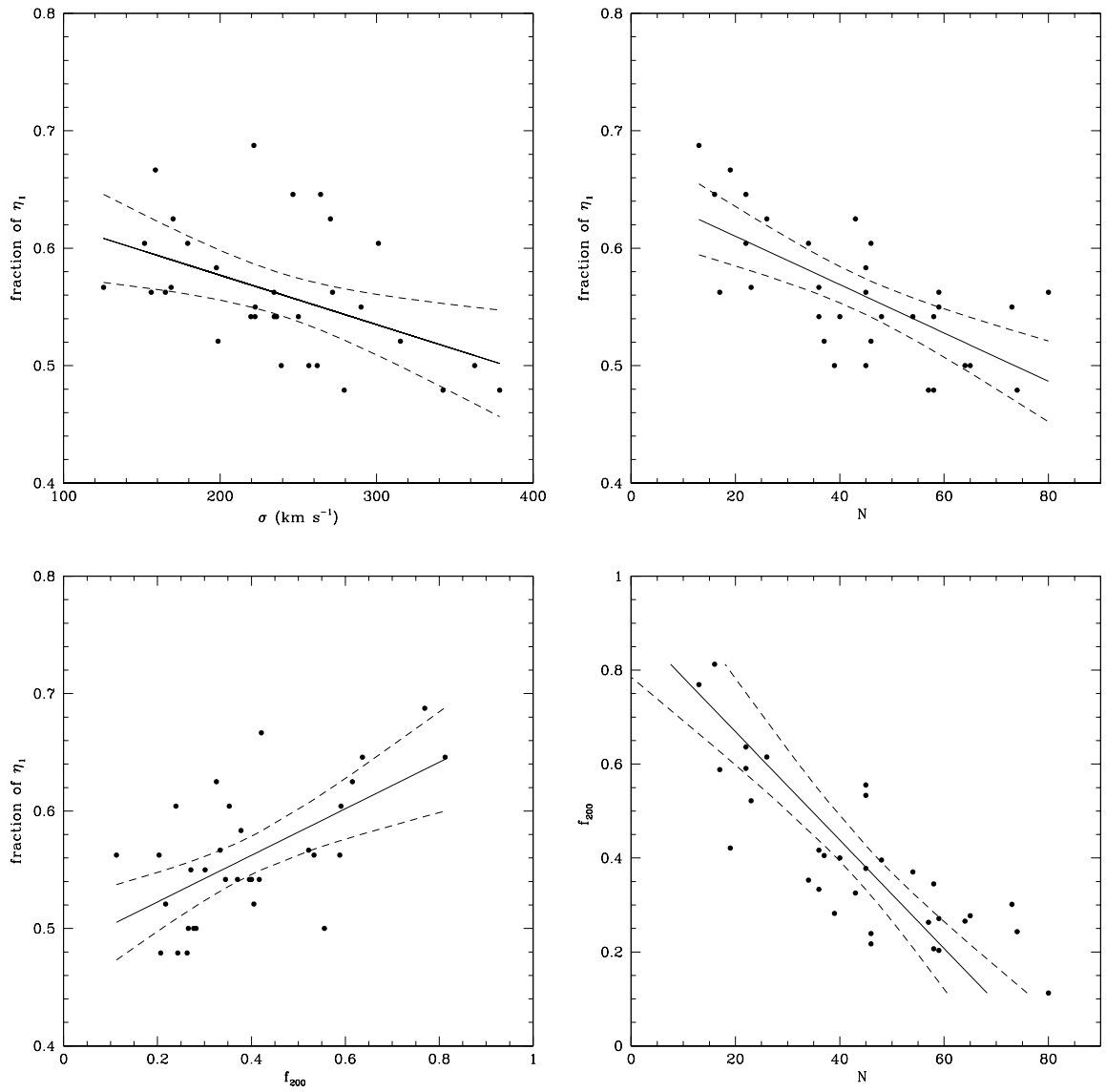


Figure 4.7: Additional trends in our sample with respect the fraction of η_1 galaxies and to the fraction of galaxies within R_{200} . 95% confidence levels contours are presented as dashed lines.

Trying to extend this scenario into a more dynamical work, we consider the behaviour of galaxy groups in the $(\sigma, R_{200}, M_{200})$ space (see Figure 4.8). We note that most of the groups settle onto a fitted plane given by $M_{200} = 0.001\sigma + 3.985R_{200} - 2.792$ ($p=1.2\times 10^{-15}$, for a F-statistic). Dividing groups according to their galactic content, i.e., the fraction of η_1 galaxies, we can see a clear difference in the group distribution on this plane. Open circles denote groups with $f_{\eta_1} > 0.55$, which are distributed more to the left and bottom of the plane, while filled circles represent groups with $f_{\eta_1} \leq 0.55$, predominantly located to the right and top of the plane (0.55 is the median value for f_{η_1}). The existence of a plane in the $(\sigma, R_{200}, M_{200})$ space indicates that groups are sufficiently evolved for their properties to be well correlated in this dynamical frame. We note, however, that f_{η_1} is related to entire fields, and not only to groups. Hence, different loci on this plane for low and high f_{η_1} fields indicate a relation between the groups and their surroundings. Recall that f_{η_1} is also anticorrelated with GA, another field (not group) measurement. Hence, a tantalizing view of this result is that we have groups in different dynamical states approximately along the diagonal from the top-right to the bottom-left corners of the fitted plane. This is not exactly an evolutionary track, but an indicator of how anisotropy, galactic content, and dynamics are intimately connected during the formation of galaxy systems.

4.4 Discussion

The spatial distribution of galaxies traces the shape of the dark matter potential in which they are embedded. Simulations show that dark matter halos are not spherical, as one would expect from dark matter dissipationless nature, but they are strongly flattened triaxial ellipsoids (Dubinski & Carlberg, 1991, e.g.). Groups are probably the most suitable objects to use in studying the shapes of dark matter halos, since they connect the general field of galaxies and large-scale structure. Indeed, any correlation between morphological properties of the groups and galaxy evolution can provide an indication of how matter assembles to form larger and larger galaxy systems, and how the environment affects galaxy evolution during this process.

In this work, we have introduced a new method to probe extended regions around galaxy groups. Based on the second moment of the Ripley function, the method allows us to define an operational anisotropy profile that indicates preferential directions around the systems. We also define a global anisotropy (GA) from the anisotropy profile, a quantity that can be compared to other properties of the groups. Galaxies in our 2dF group sample are distributed out to $\sim 10R_V$

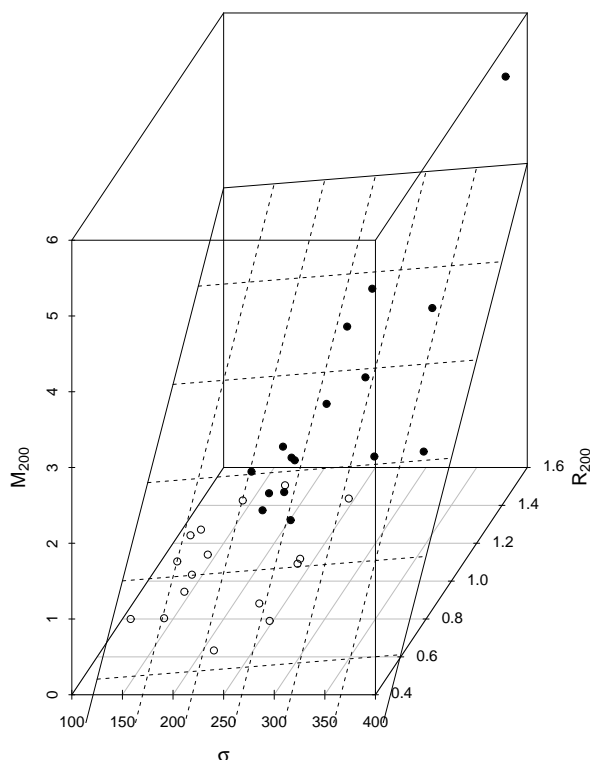


Figure 4.8: 3D plot in $[\sigma \text{ (km s}^{-1}), R_{200} \text{ (Mpc)}, M_{200} \text{ (} 10^{14} \text{ M}_{\odot})]$ space. Open circles denote groups with $f_{\eta_1} > 0.55$, while filled circles represent groups with $f_{\eta_1} \leq 0.55$.

around the center of the groups, so we have fairly extended samples of group+surrounding galaxies. We find that GA is correlated with the spectral parameter η (Madgwick et al., 2002), an indicator of the star formation rate of galaxies. Observations indicate that the lower star formation rate of group galaxies is visible out to $2R_{200}$ (Balogh et al., 1998), while Λ CDM numerical simulations show that particles that penetrate deep into dark matter halos travel out to $\approx 2.6R_{200}$ (Gill et al., 2005). In this work, we have found that galaxies represent two statistically distinct groups with a transition at $\eta = -1.4$ and $d_c = 1.5R_{200}$, a scale somewhat smaller (by 25%) than the observed radius for decreased star formation, but consistent with this value. At the same time, our sample by dwarf galaxies ($M_B > -20$ for $\sim 90\%$ of all objects) with statistical transition line at $M_B = -18.55$, such that the central galaxies are the most luminous as well. These are also redder than the more external ones, with a transition line at $B - R = 1.1$. All of this suggests that our sample consists mainly of dwarf ellipticals (dE). Interestingly, dE are potentially the only galaxy type whose formation is sensitive to global, rather than local, environment (Conselice, 2005).

In this context it is important to note that we found about 94% groups have significant elongation throughout the group and the surrounding fields ($GA \geq 2$), and a (negative) linear relation between GA and the fraction of η_1 galaxies. In the case when these objects are predominantly dEs, we conclude that these galaxies are tracing the anisotropic large-scale accretion of matter onto groups. We also know that the high dwarf-to-giant ratio observed in rich clusters suggests that cluster dE do not form in groups that later merge to build clusters (Conselice, 2005). Bright galaxies that follow the Kormendy relation (Kormendy, 1977) are indeed unlikely to have been formed by mergers of dwarf early-type systems (Evstigneeva et al., 2004). Likewise, our results indicate that a high number of dEs exist in both the groups and the flow of matter along the filamentary structure feeding these systems.

Segregation Effects According to the Evolutionary Stage of Galaxy Groups¹

5.1 Introduction

Groups of galaxies contain about half of all galaxies in the Universe (e.g. Huchra & Geller, 1982; Geller & Huchra, 1983; Nolthenius & White, 1987; Ramella et al., 1989). They represent the link between galaxies and large-scale structures and play an important role to galaxy formation and evolution. One of the most important questions about galaxy systems is related to segregation phenomena. The study of segregation effects is important to understand how system environment is transforming galaxies at the present epoch. Evidence for different loci in position and velocity spaces according to luminosity, spectral type and color of galaxies suggests ongoing evolution of clusters through the process of mergers, dynamical friction and secondary infall (Adami et al., 1998; Biviano et al., 2002). Segregation has also been observed in galaxy groups (e.g. Mahdavi et al., 1999; Carlberg et al., 2001), suggesting a continuum of segregation properties of galaxies from low-to-high mass systems (Girardi et al., 2003). However, the dynamical state of galaxy groups is not taken into account in these studies. Differences in segregation phenomena may emerge if one divides groups according to their evolutionary stage. Recently, Hou et al. (2009) have examined three goodness-of-fit tests (Anderson-Darling, Kolmogorov and χ^2 tests) to find which statistical tool is best able to distinguish between relaxed and non-relaxed galaxy groups. Using Monte Carlo simulations and a sample of groups selected from the CNOC2, they found that the Anderson-Darling (AD) test is far more reliable at detecting real departures from normality. Their results show that Gaussian and non-Gaussian groups

¹ Chapter published as: Ribeiro, Lopes & Trevisan 2010, MNRAS, 409, L124

present distinct velocity dispersion profiles, suggesting that discrimination of groups according to their velocity distributions may be a promising way to access the dynamics of galaxy systems. Extending up this kind of analysis to the outermost edge of groups one can probe the regions where they might not be in dynamical equilibrium. In this Chapter, we look for segregation effects in galaxy groups selected from the 2PIGG catalog (Eke et al., 2004), using 2dF data out to $4R_{200}$, and taking into account the evolutionary stage of the groups resulting from the AD test.

5.2 Data and Methodology

5.2.1 2PIGG sample

We use a subset of the 2PIGG catalog, corresponding to groups located in areas of at least 80% redshift coverage in 2dF data out to 10 times the radius of the systems, roughly estimated from the projected harmonic mean (Eke et al., 2004). The idea of working with such large areas is to probe the effect of secondary infall onto groups. Members and interlopers were redefined after the identification of gaps in the redshift distribution according to the technique described by Lopes et al. (2009a). Before selecting group members and rejecting interlopers we first refine the spectroscopic redshift of each group and identify its velocity limits. For this purpose, we employ the gap-technique described in Katgert et al. (1996) and Olsen et al. (2005) to identify gaps in the redshift distribution. A variable gap, called *density gap* (Adami et al., 1998), is considered. To determine the group redshift, only galaxies within $0.50 \text{ h}^{-1} \text{ Mpc}$ are considered. Details about this procedure are found in Lopes et al. (2009a); see also Ribeiro et al. (2009) for applications of this technique to 2dF galaxy groups. With the new redshift and velocity limits, we apply an algorithm for interloper rejection to define the final list of group members. We use the “shifting gapper” technique (Fadda et al., 1996), which consists of the application of the gap-technique to radial bins from the group center. We consider a bin size of $0.42 \text{ h}^{-1} \text{ Mpc}$ (0.60 Mpc for $h = 0.7$) or larger to ensure that at least 15 galaxies are selected. Galaxies not associated with the main body of the group are discarded. This procedure is repeated until the number of group members is stable and no further galaxies are eliminated as intruders. In the present work, we have sampled galaxies out to 10 times the harmonic mean radius of the systems, including galaxies whose distances to the centers can reach $\sim 8 \text{ Mpc}$. To avoid contamination of nearby structures, we select galaxies within the maximum radius $R_{max} = 4.0 \text{ Mpc}$ (see La Barbera et al.,

2010). After applying the shifting gapper procedure we have a list of group members and we call R_A the aperture equivalent to the radial offset of the most distant member (normally close to R_{max}). We estimate the velocity dispersion (σ) within R_A and then the physical radius (R_{200}) of each group. Finally, a virial analysis is performed for mass estimation (M_{200}). Further details regarding the interloper removal and estimation of global properties (σ , physical radius and mass) are found in Lopes et al. (2009a).

5.2.2 *Classifying groups*

The first step in our analysis is to apply the AD test (see Hou et al., 2009, for a good description of the test) to the velocity distributions of galaxies in groups. This is done for different distances, producing the following ratios of non-Gaussian groups: 6% ($R \leq 1R_{200}$), 9% ($R \leq 2R_{200}$), and 16% ($R \leq 3R_{200}$ and $R \leq 4R_{200}$). Approximately 90% of all galaxies in our sample have distances $\leq 4R_{200}$. This is the natural cutoff in space we have made in this work. Some properties of galaxy groups are presented in Table 5.1. We have classified groups according to the AD test (at 0.05 significance level) done at $R \leq 4R_{200}$, encompassing all groups with evidence for normality deviations. Properties of non-Gaussian (NG) groups in Table 5.1 were computed twice, with and without a correction based on iterative removal of galaxies whose absence in the sample cause the groups become Gaussian, following a procedure similar to Perea et al. (1990). The corrected properties are just those the system would have if it was made only with galaxies consistent with the normal velocity distribution. This correction allows one to honestly compare typical properties of G and NG groups. Not doing that, NG groups could have their properties overestimated by a factor of ~ 1.5 , taking all members within $4R_{200}$. After this procedure, we see in Table 5.1 that G and corrected NG groups have similar properties.

5.2.3 *Composite groups*

A suitable way to investigate galaxies in multiple galaxy systems is to combine them in stacked objects (Biviano et al., 1992). Thus, we built two composite groups, Gaussian–G (composed of 48 systems) and non-Gaussian–NG (composed of 9 systems). Galaxies in these composite groups have distances to group centers normalized by R_{200} and their velocities refers to the group median velocities and are scaled by the group velocity dispersions

Table 5.1 - Mean properties of groups.

Type	R_{200} (Mpc)	M_{200} ($10^{14} M_{\odot}$)	σ (km/s)	N_{200}	N_T
G	0.94 ± 0.31	0.88 ± 0.79	223 ± 89	10 ± 4	24 ± 11
NG	1.32 ± 0.27	1.41 ± 0.83	363 ± 99	12 ± 5	40 ± 12
NG _c	0.97 ± 0.23	0.95 ± 0.95	257 ± 76	10 ± 4	31 ± 10

$$u_i = \frac{v_i - \langle v \rangle_j}{\sigma_j} \quad (5.1)$$

where i and j are, respectively, the galaxy and the group indices. Velocity dispersions of the composite groups refer to the dimensionless quantity u_i . Absolute magnitudes, M_R , are obtained from Super-COSMOS R band, a 2dF photometric information. Cosmology is defined by $\Omega_m = 0.3$, $\Omega_{\lambda} = 0.7$, and $H_0 = 100 h \text{ km s}^{-1} \text{ Mpc}^{-1}$. Distance-dependent quantities are calculated using $h = 0.7$. All figures presented in the next section correspond to cumulative data in R/R_{200} or M_R . Error-bars in our analysis are obtained from a bootstrap technique with 1000 resamplings.

5.3 Segregation Analysis

Segregation analysis is a powerful tool to evaluate galaxy evolution in galaxy systems (e.g. Goto, 2005). We probe segregation phenomena out to $4R_{200}$, looking for differences in galaxies with respect to the dynamical state of the groups. First, we test the presence of luminosity segregation in the velocity space by computing the normalized velocity dispersion, σ_u , of the stacked G and NG groups. In Figure 5.1, we plot σ_u of the composite groups as a function of the absolute magnitude in the R band. We clearly see that, at $M_R \leq -21.5$, the velocity dispersions decreases towards brighter absolute magnitudes. On the other hand, for fainter absolute magnitudes, the velocity dispersions are approximately constant. More interestingly, although the result is similar for both stacked groups, for the NG group we see a steeper correlation in the bright end than that we see for the G group. If one assumes a constant galaxy mass-to-light ratio, energy equipartition implies $\sigma_u \propto 10^{0.2M_R}$ (e.g. Adami et al., 1998). The regression lines between $\log \sigma_u$ and M_R have slopes 0.18 ± 0.05 and 0.38 ± 0.03 , for G and NG groups, respectively. That is, the brightest galaxies are moving more slowly than other group galaxies. Such a segregation in the velocity space may be interpreted as evidence that these galaxies have reached

energy equipartition, as a consequence of dynamical friction (e.g. Capelato et al., 1981). In fact, the slope we found for galaxies in the G group is consistent with this interpretation. However, the steeper relation between σ_u and M_R probably indicates a departure from equipartition state for galaxies in the NG group. We also should note that, for $M_R \geq -21.5$, velocity dispersions are larger in the NG group. Therefore, although fainter galaxies both in G and NG groups seem to lie in the velocity equipartition state generated by violent relaxation, these galaxies in the NG group have more kinetic energy. A complementary view of this scenario follows from what is seen in Figure 5.2. Note that the velocity dispersion profiles show declining and rising trends, for G and NG groups, respectively. They approximately cross each other at $2.5R_{200}$ and then separate more and more for larger radii. This is consistent with the results of Hou et al. (2009), for the CNOC2 galaxy groups sample. Rising profiles are generally interpreted as a possible signature of mergers (Menci & Fusco-Femiano, 1996), which suggests a current intense phase of environmental influence on galaxies in the inner parts of non-Gaussian groups. Looking for a counterpart of these effects in color, we plot in Figure 5.3 the color profiles for the G and NG groups. They clearly reveal a stronger reddening towards the center for galaxies in the G group. Also, note that the profiles turn flat approximately at $3R_{200}$, but galaxies are still redder in Gaussian groups out to $4R_{200}$. This result indicates that non-Gaussian groups contain less evolved galaxies at the present epoch even in the outskirts. In fact, galaxies in the NG group are fainter than those in the G group for all radii, with luminosities presenting rising profiles in both cases (see Figure 5.4). Spearman tests indicate significant increasing trends up to $1R_{200}$ and $2.3R_{200}$ for the G and NG stacked systems, respectively.

5.4 Discussion

We have studied segregation effects in 57 galaxy groups selected from the 2PIGG catalog (Eke et al., 2004) using 2dF data out to $4R_{200}$. This means we probe galaxy distribution near to the turnaround radius, thus probably taking into account all members in the infall pattern around the groups (e.g. Rines & Diaferio, 2006; Cupani et al., 2008). Instead of focusing our analysis on choosing specific galaxy types to study segregation, we have used the dynamical state of galaxy systems to test for different levels of environmental influence on galaxies. The theoretical expectation is that the underlying velocity distribution is normal for systems in dynamical equilibrium. Using the AD test, we divided the sample in Gaussian and non-Gaussian groups.

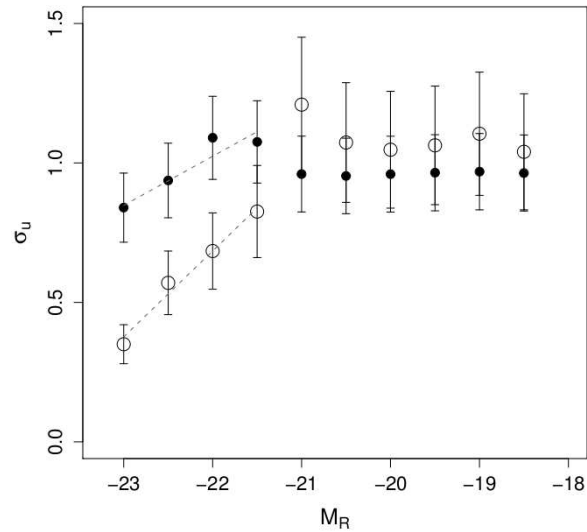


Figure 5.1: Composite groups velocity dispersion as a function of the absolute magnitude in the R band. Filled circles denote galaxies in G groups, while open circles denote galaxies in NG groups. Dashed lines indicate the regression fits for galaxies with $M_R \leq -21.5$.

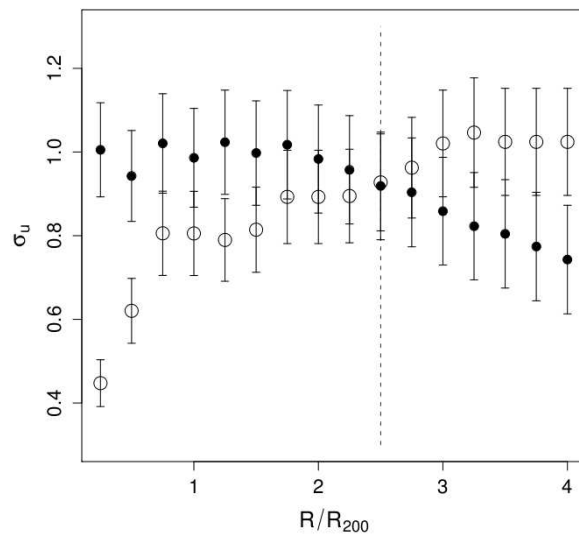


Figure 5.2: Composite groups velocity dispersion as a function of the normalized radial distances to the group centers. Filled circles denote galaxies in G groups, while open circles denote galaxies in NG groups.

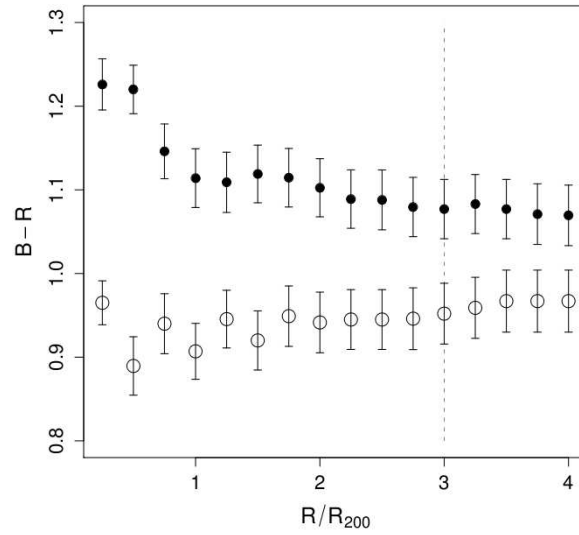


Figure 5.3: B-R color of galaxies in the composite groups as a function of the normalized radial distances to the group centers. Filled circles denote galaxies in G groups, while open circles denote galaxies in NG groups.

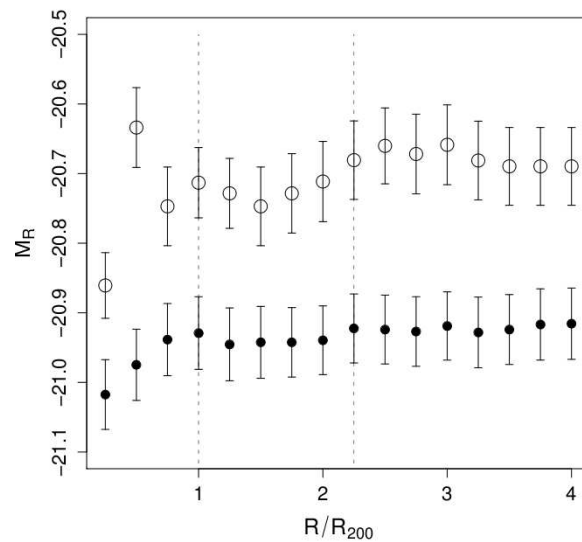


Figure 5.4: Absolute magnitude in R band as a function of the normalized radial distances to the group centers. Filled circles denote galaxies in G groups, while open circles denote galaxies in NG groups.

These were used to build the composite G and NG groups. Some general results we found were expected: segregation in velocity space (galaxies brighter than $M_R = -21.5$ are moving more slowly than other group galaxies); and color and luminosity gradients towards the center of the groups. However, important differences emerge when we compare the behaviour of galaxies in G and NG groups. For instance, color gradient and overall reddening are stronger in the case of the G group out to large distances, showing a significant raise of more evolved galaxies from non-relaxed to relaxed systems (Figure 5.3). This is consistent with the luminosity profiles, indicating that galaxies in the G group are significantly brighter than those in the NG group (Figure 5.4). On the other hand, the rising velocity dispersion profile for galaxies in the NG group indicate that, though less evolved now, galaxies in non-Gaussian systems may be undergoing a more intense phase of interactions in their inner parts at the present epoch (Figure 5.2). These results are in agreement with the work of Popesso et al. (2007), in which Abell clusters with an abnormally low X-ray luminosity for their mass have a higher fraction of blue galaxies, and are characterized by leptokurtic (more centrally concentrated than a Gaussian) velocity distribution of their member galaxies in the outskirts ($1.5 < R/R_{200} \leq 3.5$), as expected for systems undergoing a phase of mass accretion. This also fairly agrees with Osmond & Ponman (2004) who have found that groups with an abnormally low velocity dispersion relative to their X-ray properties have a higher fraction of spirals and could be dynamically unrelaxed. The low velocity dispersions are probably consequence of the interactions in the inner part of the groups. Since they only considered the central group regions and the brightest galaxies, our analysis suggests that they may have found unrelaxed systems, but could have underestimated the global velocity dispersions of these groups (see Table 5.1 and Figure 5.2).

Taken together, these facts point out a scenario where young systems have galaxies bluer and fainter up to large radii ($\sim 4R_{200}$), possessing lower velocity dispersions in the inner parts (and higher velocity dispersions in the outer parts) in comparison to more evolved systems. This latter result is also related to the segregation detected in the velocity space. Galaxies brighter than $M_R = -21.5$ are moving more slowly than other group galaxies, but the relation $\sigma_u - M_R$ is steeper for non-Gaussian groups, indicating a departure from the energy equipartition expectation – $\sigma_u \propto 10^{0.2M_R}$ (see Figure 5.1). Our work suggests that the slope of the relation $\sigma_u - M_R$ could be used to determine the evolutionary stage of galaxy groups.

Non-Gaussian velocity distributions – The effect on virial mass estimates of galaxy groups¹

6.1 Introduction

Groups of galaxies contain most of galaxies in the Universe and are the link between individual galaxies and large-scale structures (e.g. Huchra & Geller, 1982; Geller & Huchra, 1983; Nolthenius & White, 1987; Ramella et al., 1989). The dissipationless evolution of these systems is dominated by gravity. Interactions over a relaxation time tend to distribute the velocities of the galaxy members in a Gaussian distribution (e.g. Bird & Beers, 1993). Thus, a way to access the dynamical stage of galaxy groups is to study their velocity distributions. Evolved systems are supposed to have Gaussian velocity distributions, while those with deviations from normality are understood as less evolved systems. Hou et al. (2009) have examined three goodness-of-fit tests (Anderson-Darling, Kolmogorov and χ^2 tests) to find which statistical tool is best able to distinguish between relaxed and non-relaxed galaxy groups. Using Monte Carlo simulations and a sample of groups selected from the CNOC2, they found that the Anderson-Darling (AD) test is far more reliable at detecting real departures from normality in small samples. Their results show that Gaussian and non-Gaussian groups present distinct velocity dispersion profiles, suggesting that discrimination of groups according to their velocity distributions may be a promising way to access the dynamics of galaxy systems.

Recently, Ribeiro et al. (2010) extended up this kind of analysis to the outermost edge of groups to probe regions where galaxy systems might not be in dynamical equilibrium. They found significant segregation effects after splitting up the sample in Gaussian and non-Gaussian

¹ Chapter published as: Ribeiro, Lopes & Trevisan 2011, MNRAS, 413, L81

systems. In the present work, we try to further understand the nature of non-Gaussian groups. In particular, we investigate the problem of mass estimation for this class of objects, and their behaviour in the phase space. The Chapter is organized as follows: in Section 6.2 we present data and methodology; Section 6.3 contains a statistical analysis with sample tests and multimodality diagnostics for non-Gaussian groups; finally, in Section 6.4 we summarize and discuss our findings.

6.2 Data and Methodology

6.2.1 2PIGG sample

We use a subset of the 2PIGG catalog, corresponding to groups located in areas of at least 80% redshift coverage in 2dF data out to 10 times the radius of the systems, roughly estimated from the projected harmonic mean (Eke et al., 2004). The idea of working with such large areas is to probe the effect of secondary infall onto groups. Members and interlopers were redefined after the identification of gaps in the redshift distribution according to the technique described by Lopes et al. (2009a). Finally, a virial analysis is performed to estimate the groups' properties. See details in Lopes et al. (2009b), Ribeiro et al. (2009), and Ribeiro et al. (2010). We have classified the groups after applying the AD test to their galaxy velocity distributions (see Hou et al., 2009, for a good description of the test). This is done for different distances, producing the following ratios of non-Gaussian groups: 6% ($R \leq 1R_{200}$), 9% ($R \leq 2R_{200}$), and 16% ($R \leq 3R_{200}$ and $R \leq 4R_{200}$). We assume this latter ratio (equivalent to 9 systems) as the correct if one desires to extend up the analysis to the regions where galaxy groups might not be in dynamical equilibrium. Approximately 90% of all galaxies in the sample have distances $\leq 4R_{200}$. This is the natural cutoff in space we have made in this work. Some properties of galaxy groups are presented in Table 6.1, where non-Gaussian groups are identified with an asterisk. Cosmology is defined by $\Omega_m = 0.3$, $\Omega_\lambda = 0.7$, and $H_0 = 100 h \text{ km s}^{-1} \text{ Mpc}^{-1}$. Distance-dependent quantities are calculated using $h = 0.7$.

Table 6.1 - Main properties of groups.

Group	R_{200} (Mpc)	M_{200} ($10^{14} M_\odot$)	σ (km/s)	N_{memb}	N_{200}
55	0.689	0.400	173.203	16	9
60	0.664	0.359	120.395	41	12

Table 6.1 - continued.

Group	R_{200} (Mpc)	M_{200} ($10^{14} M_{\odot}$)	σ (km/s)	N_{memb}	N_{200}
84	1.025	1.326	224.715	54	10
91	0.848	0.754	164.293	34	4
102*	1.550	4.602	433.218	32	8
130	0.999	1.245	240.908	43	11
138*	1.271	2.578	348.885	74	14
139	0.997	1.250	235.740	39	12
169	0.765	0.573	225.212	9	4
177*	1.178	2.100	336.309	45	14
179*	1.663	5.897	471.352	23	10
181	1.247	2.488	393.379	29	12
188	0.514	0.174	153.714	8	2
191	0.707	0.456	268.517	14	10
197	0.897	0.930	297.903	13	7
204	1.493	4.333	473.813	33	12
209	0.680	0.407	132.095	15	4
222	1.243	2.494	315.355	22	8
236	1.258	2.575	331.308	19	7
271	0.968	1.093	240.691	41	15
326	0.648	0.333	167.764	21	7
352*	1.656	5.618	496.694	31	13
353	0.873	0.826	220.025	34	12
374	0.902	0.919	217.038	21	10
377	0.480	0.138	132.466	13	5
387	0.649	0.345	125.308	32	5
398	0.781	0.601	182.800	29	12
399	0.917	0.973	183.397	34	7
409	1.078	1.583	251.071	64	11
410	0.847	0.769	199.465	42	8
428	1.201	2.191	342.440	26	14

Table 6.1 - continued.

Group	R_{200} (Mpc)	M_{200} ($10^{14} M_{\odot}$)	σ (km/s)	N_{memb}	N_{200}
435	0.606	0.283	123.549	23	4
444	0.820	0.697	244.491	13	7
447*	1.169	2.032	296.919	37	6
453	0.827	0.720	271.840	17	10
455	1.588	5.088	454.227	65	15
456	0.319	0.041	58.138	16	3
458	0.642	0.336	115.674	18	4
466	1.507	4.381	554.511	23	13
471	1.128	1.832	399.078	22	14
475*	1.152	1.952	294.413	28	6
479	0.806	0.671	160.887	17	6
480	0.923	1.006	272.058	23	12
482	0.663	0.373	202.903	17	9
484	1.099	1.702	268.116	32	7
485	1.679	6.076	559.140	29	18
488	1.220	2.334	326.566	42	12
489	0.872	0.852	188.283	30	6
493	1.170	2.061	323.268	30	10
504	1.319	2.985	429.207	30	13
505*	1.176	2.111	336.804	20	7
507*	1.459	4.036	436.498	27	11
513	0.724	0.495	178.637	19	6
515	1.117	1.817	298.220	30	13
519	0.808	0.689	207.011	17	4
525	0.495	0.158	108.230	9	3
536	2.003	10.576	676.902	45	24

6.3 Non-Gaussianity and Mass

6.3.1 The mass bias

We consider the two sample statistical problem for the Gaussian (G) and NG (non-Gaussian) subsamples. We choose the mass resulting from the virial analysis as the property to illustrate the comparison between the subsamples. Both Kolmogorov-Smirnov (KS) and Cramer-von Mises (CvM) tests reject the hypothesis that the NG subsample is distributed as the G subsample, with p-values 0.00001 and 0.00029, respectively. For these tests, we have used 1000 bootstrap replicas of each subsample to alleviate the small sample effect. The result indicates an inconsistency between the mass distributions of G and NG groups. This could represent a real physical difference or, more probably, an indication of a significant bias to higher masses in NG groups. The median mass for this subsample is $\langle M_{200}^{NG} \rangle = 2.57 \times 10^{14} M_{\odot}$, while it is $\langle M_{200}^G \rangle = 8.85 \times 10^{13} M_{\odot}$ for the G subsample, thus $\langle M_{200}^{NG} \rangle$ is larger by a factor of ~ 2.9 . In the following, we investigate this mass bias looking for features in the velocity distributions of galaxy groups.

6.3.2 Exploring non-Gaussianity

The shape of velocity distributions may reveal a signature of the dynamical stage of galaxy groups. For instance, systems with heavier tails than predicted by a normal parent distribution may be contaminated by interlopers. Otherwise, systems with lighter tails than a normal may be multimodal, consisting of overlapping distinct populations (Bird & Beers, 1993, e.g.). We now try to understand the mass bias in the NG subsample by studying non-Gaussianity in the velocity distributions. Since we have carefully removed interlopers from each field (see Section 6.2.1 and Lopes et al., 009a), we consider here that the most probable cause of normality deviations in our sample is due to a superposition of modes in the phase space (e.g. Diemand & Kuhlen, 2008). Visual inspection of radial velocity histograms of NG systems suggests that multi-peaks really happen in most cases (see Figure 6.1).

We statistically check multimodality by assuming the velocity distributions as Gaussian mixtures with unknown number of components. We use the Dirichlet Process mixture (DPM) model to study the velocity distributions. The DPM model is a Bayesian nonparametric methodology that relies on Markov Chain Monte Carlo (MCMC) simulations for exploring mixture models with an unknown number of components (Diebolt & Robert, 1994). It was first formalised in

Ferguson (1973) for general Bayesian statistical modeling. The DPM is a distribution over k -dimensional discrete distributions, so each draw from a Dirichlet process is itself a distribution. Here, we assume that a galaxy group is a set of k components, $\sum_{i=1}^k \pi_i f(y|\theta_i)$, with galaxy velocities distributed according to Gaussian distributions with mean and variance unknown. In this framework, the numbers π_i are the mixture coefficients that are drawn from a Dirichlet distribution. In the DPM model, the actual number of components k used to model data is not fixed, and can be automatically inferred from data using the usual Bayesian posterior inference framework. See Neal (2000) for a survey of MCMC inference procedures for DPM models.

In this work, we find k using the R language and environment (R Development Core Team) under the `dpmixsim` library (da Silva, 2009). The code implements mixture models with normal structure (conjugate normal-normal DPM model). First, it finds the coefficients π_i , and then separates the components of the mixture, according to the most probable values of π_i , in the distributional space, leading to a partition of this space into regions (da Silva, 2009). The results can be visually analysed by plotting the estimated kernel densities for the MCMC chains. In Figure 6.2, we show the DPM diagnostics for each group, that is, the deblended modes in the velocity distributions. We have found the following number of modes per group: 4/102, 3/138, 3/177, 2/179, 5/352, 3/447, 2/475, 3/505, 3/507. Therefore, all non-Gaussian groups in our sample are multimodal (reaching a total of 28 modes) according to the DPM analysis. Unfortunately, we cannot compute the physical properties of 13 modes, due to intrinsic scattering in velocity data (and/or to the smallness of the modes – those with less than 4 members). The properties of the other 15 modes are presented in Table 6.2.

6.3.3 The mass bias revisited

Now, we perform again the statistical tests, comparing the distribution of mass in NG and G with the new sample (see Figure 6.3). First, we compare the NG subsample and the sample of modes (M). Both KS and CvM tests reject the hypothesis that M is distributed as NG, with $p=0.0211$ and $p=0.0189$, respectively. Then, we compare G and M. Now, the tests accept the hypothesis that M is distributed as G, with $p=0.4875$ and $p=0.4695$. Hence, the distribution of the modes deblended from non-Gaussian groups are themselves mass distributed as Gaussian groups. Also, the median mass of the M sample is $\langle M_{200}^M \rangle = 1.33 \times 10^{14} M_{\odot}$, a value larger than $\langle M_{200}^G \rangle$ only by a factor ~ 1.5 (before deblending groups the factor was ~ 2.9). This consistency

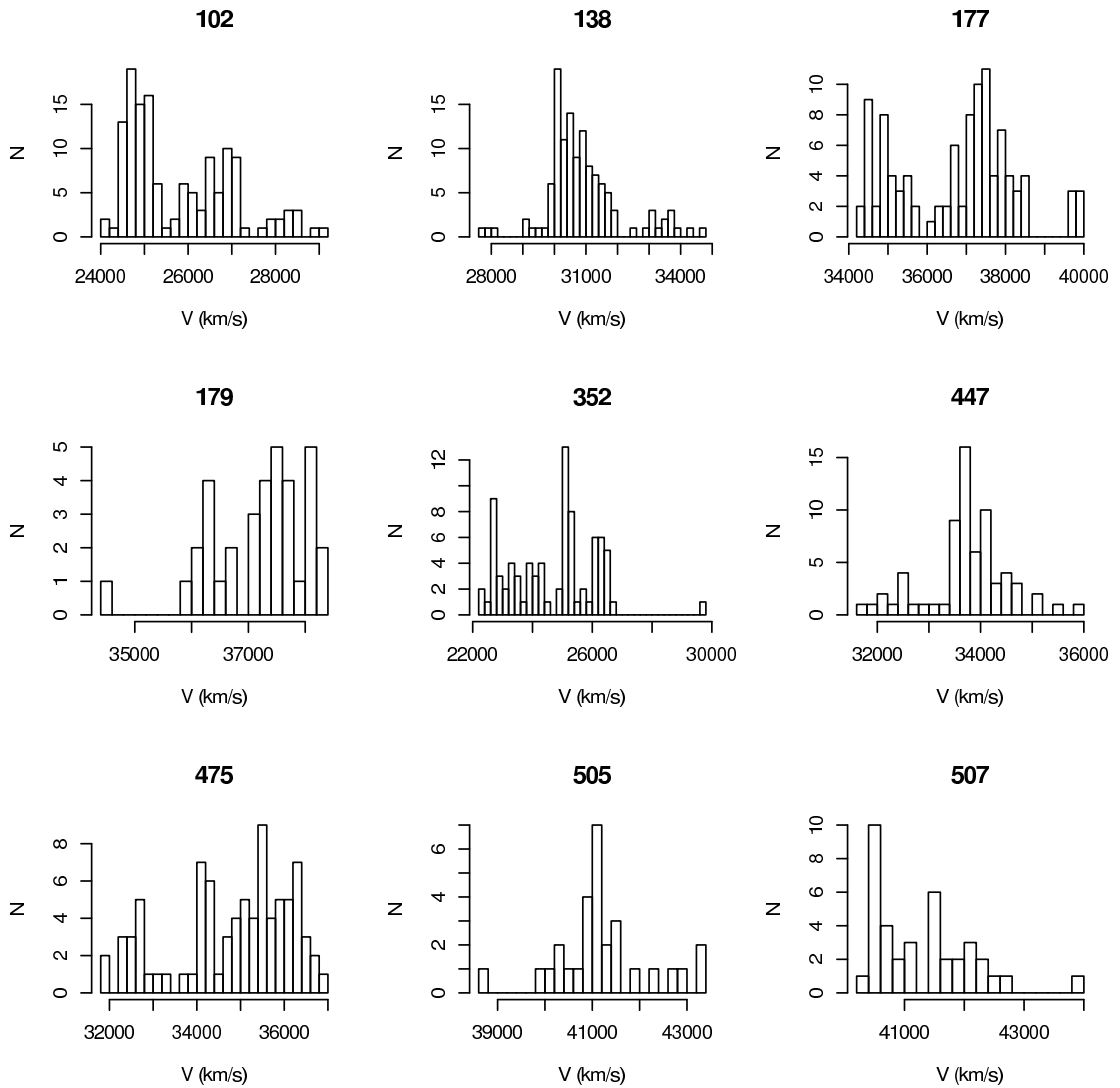


Figure 6.1: Histograms of radial velocities for all non-Gaussian groups.

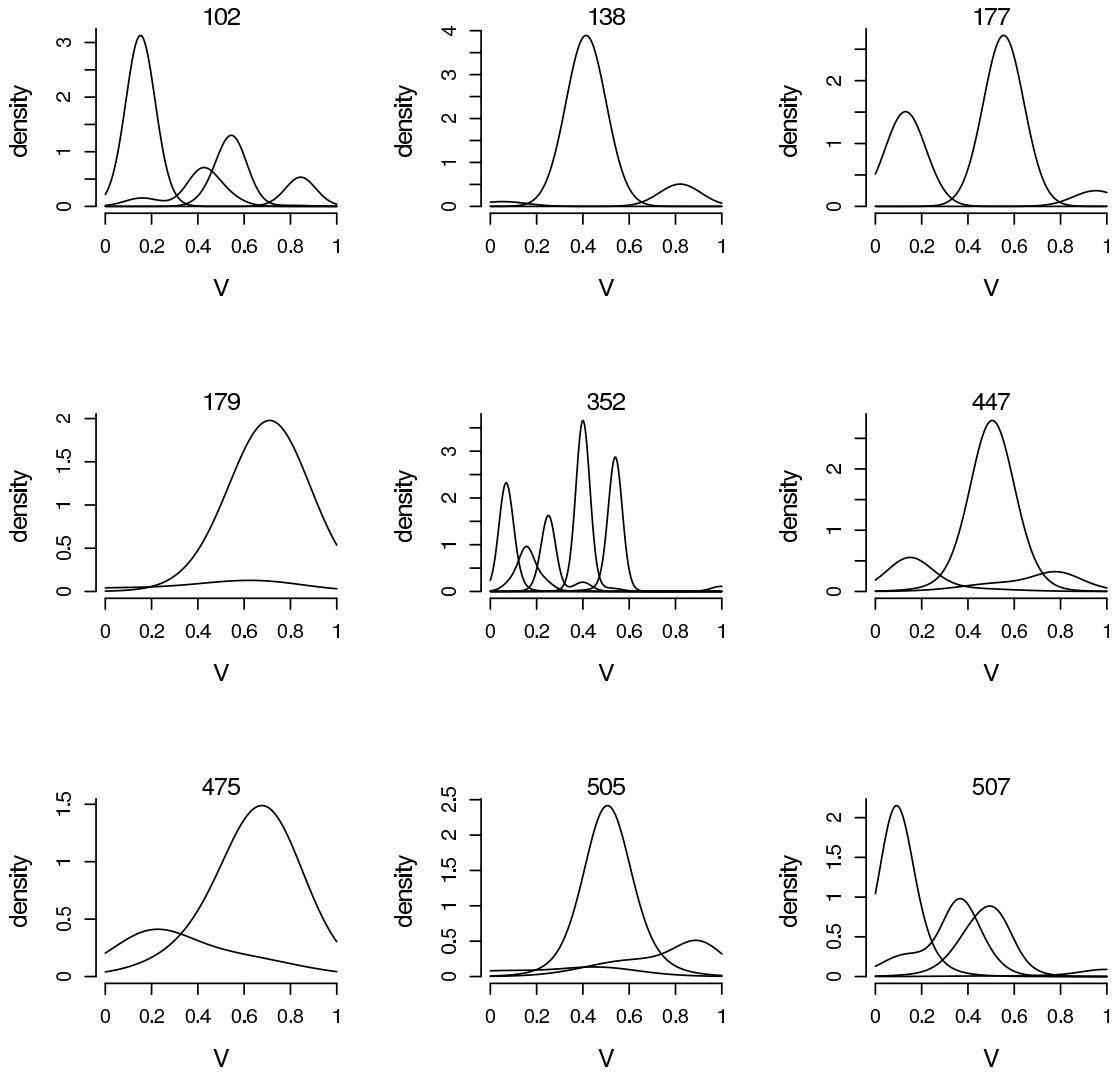


Figure 6.2: DPM density probability decomposition. Velocities are rescaled to the $[0,1]$ interval.

between G and M objects indicate that non-Gaussian groups are a set of smaller systems, probably forming an aggregate out of equilibrium. Indeed, groups are the link between galaxies and larger structures. Thus, our results suggest we are witnessing secondary infall (the secondary modes) onto a previously formed (or still forming) galaxy system (the principal mode). Naturally, we cannot discard the possibility of NG groups being unbound systems of smaller groups seen in projection, although the properties of the independent modes are quite similar to those found in physically bound groups.

Table 6.2 - Main properties of individual modes.

Mode	R_{200} (Mpc)	M_{200} ($10^{14} M_{\odot}$)	σ (km/s)	N_{200}
102 _a	1.077	1.549	337.482	21
102 _b	0.728	0.477	153.372	4
138 _a	1.550	4.677	498.927	35
177 _a	1.249	2.481	369.569	11
177 _b	1.212	2.289	362.462	14
179 _a	1.326	3.001	336.265	8
352 _a	0.487	0.142	158.571	6
352 _b	0.941	1.033	218.210	6
352 _c	0.697	0.416	208.670	3
352 _d	0.558	0.213	181.206	5
447 _a	1.016	1.330	240.437	3
447 _b	1.192	2.155	441.382	5
475 _a	1.500	4.308	470.516	19
475 _b	2.345	16.347	829.977	10
505 _a	0.928	1.040	228.411	3

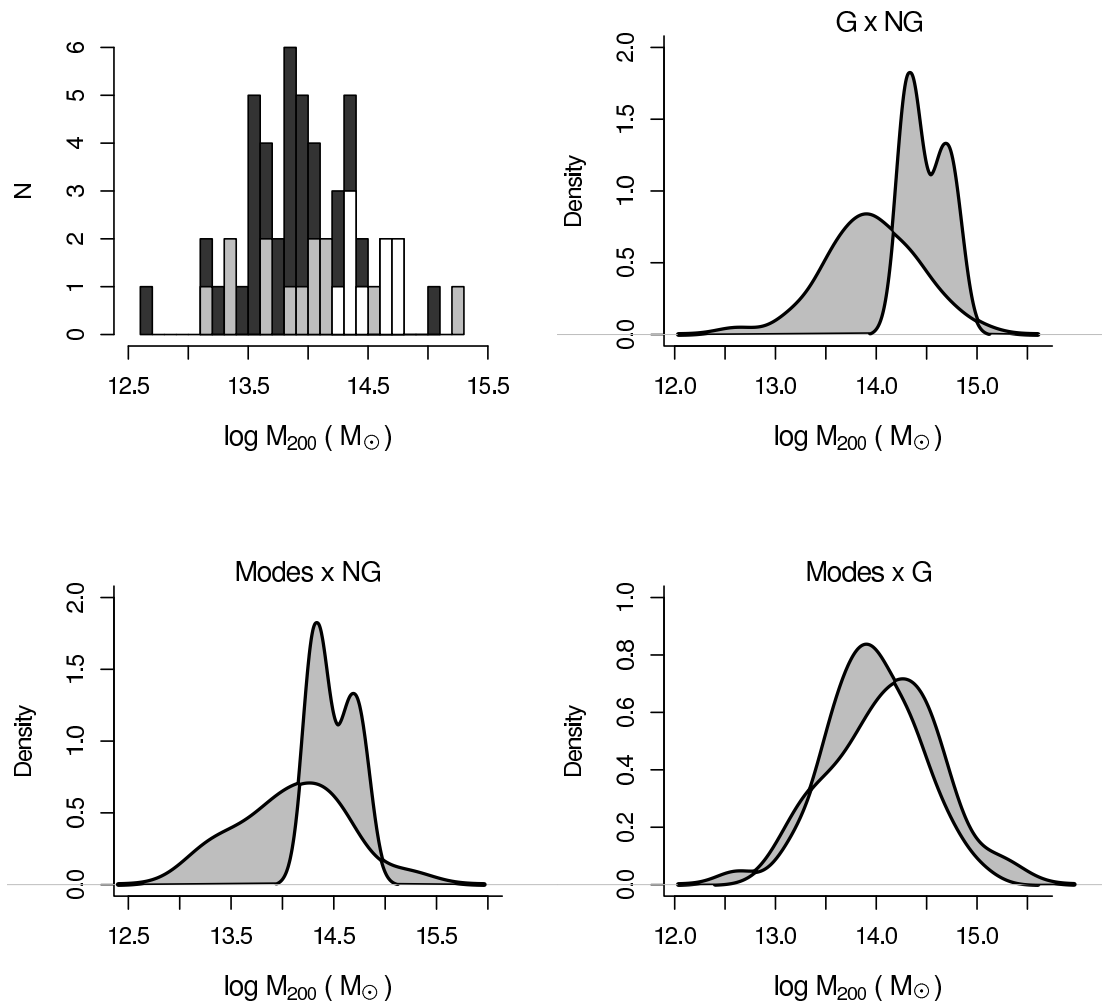


Figure 6.3: Histograms for Gaussian (dark gray) and non-Gaussian (white) groups. Histogram of modes is plotted in light gray. Density probability comparison among systems. Intersections areas are in white.

6.4 Discussion

We have classified galaxy systems after applying the AD normality test to their velocity distributions up to the outermost edge of the groups. The purpose was to investigate regions where galaxy systems might not be in dynamical equilibrium. We have studied 57 galaxy groups selected from the 2PIGG catalog (Eke et al., 2004) using 2dF data out to $4R_{200}$. This means we probe galaxy distributions near to the turnaround radius, thus probably taking into account all members in the infall pattern around the groups (e.g. Rines & Diaferio, 2006; Cupani et al., 2008). The corresponding velocity fields depend on the local density of matter. High density regions should drive the formation of virialized objects, whereas low density environments are more likely to present streaming motions, i.e., galaxies falling toward larger potential wells constantly increasing the amplitude of their clustering strength (e.g. Diaferio & Geller, 1997).

We have found that 84% of the sample is composed of systems with Gaussian velocity distributions. These systems could result from the collapse and virialization of high density regions with not significant secondary infall. They could be groups surrounded by well organized infalling motions, possibly reaching virialization at larger radii. Theoretically, in regions outside R_{200} , we should apply the non-stationary Jeans formalism, leading us to the virial theorem with some correction terms. These are due to the infall velocity gradient along the radial coordinate and to the acceleration of the mass accretion process (see Cupani et al., 2008). Their contribution is likely to be generally negligible in the halo core where the matter is set to virial equilibrium and to become significant in the halo outskirts where the matter is still accreting (see e.g. Cupani et al., 2008). However, a slow and well organized infalling motion to the center of the groups could diminish the importance of the correction terms, i.e., the systems could be in a quasi-stationary state outside R_{200} . The high fraction of groups immersed in such surroundings suggests that ordered infalling motion around galaxy groups might happen quite frequently in the Universe.

In any case, Gaussian groups can be considered as dynamically more evolved systems (see Ribeiro et al., 2010). The remaining 16% of the sample is composed of non-Gaussian groups. We found that these systems have masses significantly larger than Gaussian groups. This biasing effect in virial masses is basically due to the higher velocity dispersions in NG groups. Ribeiro et al. (2010) found that NG groups have rising velocity dispersion profiles. A similar result was found by Hou et al. (2009). Rising velocity dispersion profiles could be related to the higher

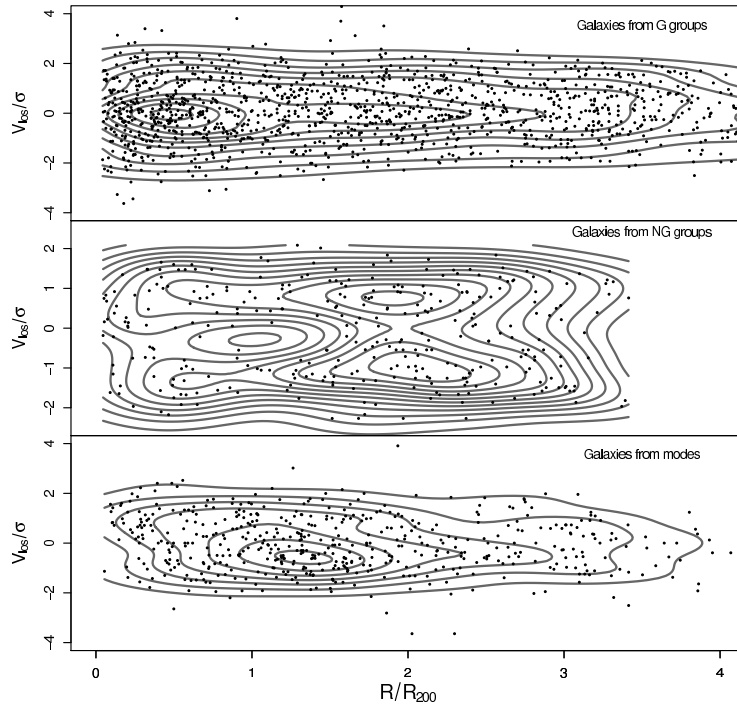


Figure 6.4: Phase space diagrams for a typical Gaussian (*upper box*), non-Gaussian (*middle box*) and modes (*lower box*) systems. Density contours indicate galaxy concentration across the diagrams. Distances to the center of the systems are normalized by R_{200} . Radial velocities are subtracted from the median velocity and divided by the velocity dispersion of the groups.

fraction of blue galaxies in the outskirts of some galaxy systems (see Ribeiro et al., 2010; Popesso et al., 2007).

At the same time, the NG subsample is composed of multipeak objects, identified by the DPM model analysis applied to the velocity space. These results indicate that secondary infall might be biasing the mass estimates of these groups. Thus, the NG systems could result from the collapse of less dense regions with significant secondary infall input. Contrary to Gaussian groups, the surroundings of NG systems do not seem to be in a quasi-stationary state. They are dynamically complex. Actually, we have found these groups can be modelled as assemblies of smaller units. After deblending groups into a number of individual modes, we have verified that the mass distribution of these objects is consistent with that of Gaussian groups, suggesting that each unit is probably a galaxy group itself, a system formed during the streaming motion toward the potential wells of the field.

Our results reinforce the idea of NG systems as complex structures in the phase space out to $4R_{200}$. This scenario is illustrated in Figure 6.4, where we show the stacked G and NG groups,

and the stacked modes. Galaxies in these composite groups have distances and line-of-sight velocities with respect to the centers normalized by R_{200} and σ , respectively. In the upper box, we present the G stacked group. Note that galaxies are extensively concentrated in the phase space diagram, with a single density peak near to $0.5R_{200}$, revealing a well organized system around this point. Also, note that the density peak has $V_{los}/\sigma \approx 0$. Contour density lines suggest that ordered shells of matter are moving toward the center. A different result is found for the NG stacked group. In the middle box of Figure 6.4, we see a less concentrated galaxy distribution, with less tight density contour levels, presenting a density peak slightly larger than R_{200} , and two additional peaks, around $2R_{200}$, possibly interacting with the central mode. The additional peaks are not aligned at $V_{los}/\sigma \approx 0$, suggesting a less symmetrical galaxy distribution in the phase space. These features suggest that non-Gaussian systems are distinct, and dynamically younger than Gaussian groups, which agrees well with the results of Ribeiro et al. (2010). Also in Figure 6.4, we present the modes stacked system in the lower box. Similar to the Gaussian case, we have a single peak in the phase space, near to $1.5R_{200}$. Galaxy distribution however is still less symmetrical than in Gaussian groups, with the peak not aligned at $V_{los}/\sigma \approx 0$. This suggests that, although more organized than NG systems, modes are probably dynamically distinct and younger than Gaussian groups as well.

Our work points out the importance of studying NG systems both to possibly correct their mass estimates and multiplicity functions, as well as to better understand galaxy clustering at group scale. Understanding of these objects is also relevant for cosmological studies using groups and clusters through the evolution of the mass function (Voit, 2005). Using systems with overestimated properties may lead to a larger scatter in the mass calibration (Lopes et al., 2009b) and could also affect the mass function estimate (Voit, 2005).

Conclusions & Perspectives

In this research program, we address key aspects of how galaxies form and evolve, by studying stars in the Milky Way, stellar populations in early type galaxies, and properties of galaxies in groups. We outline the main results below.

To probe the formation history of different stellar populations within our Galaxy, in Chapter 2, a detailed analysis of a sample of very metal-rich stars is carried out. We derive the metallicities, abundances of α elements, ages, and Galactic orbits. We confirm the high metallicity of these stars reaching up to $[\text{Fe I}/\text{H}] = 0.58$, and the sample of metal-rich dwarfs can be kinematically subclassified in samples of thick disk, thin disk, and intermediate stellar populations. All sample stars show solar α -Fe ratios, and most of them are old and still quite metal rich. The orbits suggest that the thin disk, thick disk and intermediate populations were formed at Galactocentric distances of ~ 8 kpc, ~ 6 kpc, and ~ 7 kpc, respectively. The mean maximum height of the thick disk subsample of $Z_{\text{max}} \sim 380$ pc, is lower than for typical thick disk stars. A comparison of α -element abundances of the sample stars with bulge stars shows that the oxygen is compatible with a bulge or inner thick disk origin. Our results suggest that models of radial mixing and dynamical effects of the bar and bar/spiral arms might explain the presence of these old metal-rich dwarf stars in the solar neighbourhood.

The chemical imprints these stars may, therefore, reveal valuable information about the formation and evolution of the still poorly understood inner disk. So far, only a few studies have been devoted to the determination of chemical abundances of stars in the inner parts of our Galaxy (e.g. Bensby et al., 2010). Besides, the majority of abundance studies have focused on elements with atomic number $Z \leq 30$, and heavy elements have been examined in a small number of metal-rich stars. For this reason, further analysis devoted to the determination of e.g. Fe-peak,

r- and s-process element abundances offers an opportunity to increase our understanding of this stellar population (Trevisan et al., 2012, in prep.).

In Chapter 3, we present exciting results concerning the stellar mass assembly and the chemical enrichment of other galaxies. We focus on the specific family of early-type galaxies, deriving the star formation histories of a complete sample of visually classified galaxies from SDSS-DR7 over the redshift range $0.01 < z < 0.025$, covering a stellar mass interval from 10^9 to $3 \times 10^{11} M_{\odot}$. Our sample features the characteristic “knee” in the surface brightness vs. mass distribution at $M_{\star} \sim 5 \times 10^{10} M_{\odot}$. We find a clear difference between the age and metallicity distributions of the stellar populations above and beyond this knee, which suggests a sudden transition from a constant, highly efficient mode of star formation in high-mass galaxies, gradually decreasing towards the low-mass end of the sample. At fixed mass, our early-type sample is more efficient in building up the stellar content at early times in comparison to the general population of galaxies, with half of the stars already in place by redshift $z \sim 2$ for all masses. The metallicity-age trend in low-mass galaxies is not compatible with infall of metal-poor gas, suggesting instead an outflow-driven relation.

Although internal processes, such as feedback by SN and AGN, migration of stars, chemical enrichment, etc., play a very important role in the formation of galaxies, it is well known that environmental effects might reshape these systems. To address this issue, we have examined the relation between the properties of galaxy groups and their members. In Chapter 4, we study galaxy evolution and spatial patterns in the surroundings of a sample of 2dF groups. Our aim is to find evidence of galaxy evolution and clustering out to 10 times the virial radius of the groups and so redefine their properties according to the spatial patterns in the fields and relate them to galaxy evolution. Group members and interlopers were redefined after the identification of gaps in the redshift distribution. We then used exploratory spatial statistics based on the second moment of the Ripley function to probe the anisotropy in the galaxy distribution around the groups. We found an important anticorrelation between anisotropy around groups and the fraction of early-type galaxies in these fields. Our results illustrate how the dynamical state of galaxy groups can be ascertained by the systematic study of their neighborhoods. This is an important achievement, since the correct estimate of the extent to which galaxies are affected by the group environment and follow large-scale filamentary structure is relevant to understanding the process of galaxy clustering and evolution in the Universe.

In Chapter 5, we study segregation phenomena in 57 groups selected from the 2PIGG catalog of galaxy groups. The dynamical state of the galaxy systems was determined after studying their velocity distributions. We have used the Anderson-Darling test to distinguish relaxed and non-relaxed systems. This analysis indicates that 84% of groups have galaxy velocities consistent with the normal distribution, while 16% of them have more complex underlying distributions. Properties of the member galaxies are investigated taking into account this classification. Our results indicate that galaxies in Gaussian groups are significantly more evolved than galaxies in non-relaxed systems out to distances of $\sim 4R_{200}$, presenting significantly redder (B-R) colors. We also find evidence that galaxies with $M_R \leq -21.5$ in Gaussian groups are closer to the condition of energy equipartition.

The study of 9 galaxy groups with evidence for non-Gaussianity in their velocity distributions out to $4R_{200}$ is presented in Chapter 6. This sample is taken from 57 groups selected from the 2PIGG catalog of galaxy groups. Statistical analysis indicates that non-Gaussian groups have masses significantly higher than Gaussian groups. We also have found that all non-Gaussian systems seem to be composed of multiple velocity modes. Besides, our results indicate that multimodal groups should be considered as a set of individual units with their own properties. In particular, we have found that the mass distribution of such units are similar to that of Gaussian groups. Our results reinforce the idea of non-Gaussian systems as complex structures in the phase space, likely corresponding to secondary infall aggregations at a stage before virialization. The understanding of these objects is relevant for cosmological studies using groups and clusters through the mass function evolution.

It should be clear from the results presented in this thesis that structure formation is a subject of great complexity, and that advances can be achieved by connecting fields that are tenuously related on initial inspection. In this context, the upcoming years will bring exciting opportunities for studies of galaxy formation. With current and future surveys, astronomers will have access to an incredibly large amount of information. However, the increasing quality and quantity of images, spectra and catalogs also represents new challenges. For example, a realistic forecast indicates that by 2020, more than 60 PB of archived data will be accessible to astronomers (Berriman & Groom 2011). The availability of this amount of data implies that astronomers must change the way they exploit the data, and the need for highly efficient tools to handle them is imminent. The astronomical community has already taken steps in this direction with

the development of Virtual Observatories (VO). VOs combine data archives and software tools, creating an environment where research programs can be conducted. Therefore, VOs represent a way to optimize - or even to make it feasible - the analysis of current and future data. In this scenario, future programs also involve the integration of software tools into VO environment, such as the PFANT code (see Chapter 2 and Appendix A) and STARLIGHT (see Chapter 3), in preparation for what lies ahead.

Bibliography

- Abadi M. G., Navarro J. F., Steinmetz M., Eke V. R., Simulations of Galaxy Formation in a Λ Cold Dark Matter Universe. I. Dynamical and Photometric Properties of a Simulated Disk Galaxy, *ApJ*, 2003a, vol. 591, p. 499
- Abadi M. G., Navarro J. F., Steinmetz M., Eke V. R., Simulations of Galaxy Formation in a Λ Cold Dark Matter Universe. II. The Fine Structure of Simulated Galactic Disks, *ApJ*, 2003b, vol. 597, p. 21
- Abazajian K. N., Adelman-McCarthy J. K., Agüeros M. A., Allam S. S., Allende Prieto C., An D., Anderson K. S. J., Anderson S. F., Annis J., Bahcall N. A., et al. et al. The Seventh Data Release of the Sloan Digital Sky Survey, *ApJS*, 2009, vol. 182, p. 543
- Adami C., Biviano A., Mazure A., Segregations in clusters of galaxies, *A&A*, 1998, vol. 331, p. 439
- Adami C., Mazure A., Biviano A., Katgert P., Rhee G., The ESO nearby Abell cluster survey. IV. The fundamental plane of clusters of galaxies, *A&A*, 1998, vol. 331, p. 493
- Allen C., Santillan A., An improved model of the galactic mass distribution for orbit computations, *RMxAA*, 1991, vol. 22, p. 255
- Allende Prieto C., Barklem P. S., Lambert D. L., Cunha K., S⁴N: A spectroscopic survey of stars in the solar neighborhood. The Nearest 15 pc, *A&A*, 2004, vol. 420, p. 183
- Allende Prieto C., Lambert D. L., Fundamental parameters of nearby stars from the comparison with evolutionary calculations: masses, radii and effective temperatures, *A&A*, 1999, vol. 352, p. 555

- Alonso A., Arribas S., Martínez-Roger C., Broad band JHK infrared photometry of an extended sample of late type dwarfs and subdwarfs., *A&AS*, 1994, vol. 107, p. 365
- Alonso A., Arribas S., Martínez-Roger C., Determination of bolometric fluxes for F, G and K subdwarfs, *A&A*, 1995, vol. 297, p. 197
- Alonso A., Arribas S., Martínez-Roger C., The empirical scale of temperatures of the low main sequence (F0V-K5V), *A&A*, 1996, vol. 313, p. 873
- Alonso A., Arribas S., Martínez-Roger C., The effective temperature scale of giant stars (F0-K5). I. The effective temperature determination by means of the IRFM, *A&AS*, 1999, vol. 139, p. 335
- Alves-Brito A., Meléndez J., Asplund M., Ramírez I., Yong D., Chemical similarities between Galactic bulge and local thick disk red giants: O, Na, Mg, Al, Si, Ca, and Ti, *A&A*, 2010, vol. 513, p. A35
- Asplund M., Grevesse N., Sauval A. J., The Solar Chemical Composition. In *Cosmic Abundances as Records of Stellar Evolution and Nucleosynthesis*, vol. 336 of *Astronomical Society of the Pacific Conference Series*, 2005, p. 25
- Audouze J., Nucleosynthesis of the Very Light ($A < 12$) and Trans Iron ($A > 60$) Nucleii. In *Saas-Fee Advanced Course 16: Nucleosynthesis and Chemical Evolution*, 1986, p. 431
- Auger M. W., Treu T., Gavazzi R., Bolton A. S., Koopmans L. V. E., Marshall P. J., Dark Matter Contraction and the Stellar Content of Massive Early-type Galaxies: Disfavoring "Light" Initial Mass Functions, *ApJL*, 2010, vol. 721, p. L163
- Baddeley A., *Analysing spatial point patterns in R*, 2008
- Balogh M. L., Schade D., Morris S. L., Yee H. K. C., Carlberg R. G., Ellingson E., The Dependence of Cluster Galaxy Star Formation Rates on the Global Environment, *ApJL*, 1998, vol. 504, p. L75
- Banerji M., Ferreras I., Abdalla F. B., Hewett P., Lahav O., Exploring the luminosity evolution and stellar mass assembly of 2SLAQ luminous red galaxies between redshifts 0.4 and 0.8, *MNRAS*, 2010, vol. 402, p. 2264

- Barbuy B., Division IV: Stars (Etoiles), Transactions of the International Astronomical Union, 2007, vol. XXVB, p. 135
- Barbuy B., Perrin M.-N., Katz D., Coelho P., Cayrel R., Spite M., Van't Veer-Menneret C., A grid of synthetic spectra and indices Fe5270, Fe5335, Mgb and Mg₂ as a function of stellar parameters and [alpha/Fe], A&A, 2003, vol. 404, p. 661
- Barbuy B., Zoccali M., Ortolani S., Hill V., Minniti D., Bica E., Renzini A., Gómez A., VLT-FLAMES analysis of 8 giants in the bulge metal-poor globular cluster NGC 6522: oldest cluster in the Galaxy?. Analysis of 8 giants in NGC 6522, A&A, 2009, vol. 507, p. 405
- Barklem P. S., Anstee S. D., O'Mara B. J., Line broadening cross sections for the broadening of transitions of neutral atoms by collisions with neutral hydrogen, Publications of the Astronomical Society of Australia, 1998, vol. 15, p. 336
- Barklem P. S., Aspelund-Johansson J., The broadening of Fe II lines by neutral hydrogen collisions, A&A, 2005, vol. 435, p. 373
- Barklem P. S., Piskunov N., O'Mara B. J., A list of data for the broadening of metallic lines by neutral hydrogen collisions, A&AS, 2000, vol. 142, p. 467
- Bedin L. R., Piotto G., Carraro G., King I. R., Anderson J., The absolute motion of the peculiar cluster NGC 6791, A&A, 2006, vol. 460, p. L27
- Bell E. F., Zucker D. B., Belokurov V., Sharma S., Johnston K. V., Bullock J. S., Hogg D. W., Jahnke K., de Jong J. T. A., Beers T. C., Evans N. W., Grebel E. K., Ž. Ivezić Koposov S. E., Rix H.-W., Schneider D. P., Steinmetz M., Zolotov A., The Accretion Origin of the Milky Way's Stellar Halo, ApJ, 2008, vol. 680, p. 295
- Bensby T., Adén D., Meléndez J., Gould A., Feltzing S., Asplund M., Johnson J. A., Lucatello S., Yee J. C., Ramírez I., Cohen J. G., Thompson I., Bond I. A., Gal-Yam A., Han C., Sumi T., Suzuki D., Wada K., Miyake N., Chemical evolution of the Galactic bulge as traced by microlensed dwarf and subgiant stars. IV. Two bulge populations, A&A, 2011, vol. 533, p. A134
- Bensby T., Alves-Brito A., Oey M. S., Yong D., Meléndez J., The first chemical abundance analysis of K giants in the inner Galactic disc, A&A, 2010, vol. 516, p. L13

- Bensby T., Feltzing S., Gould A., Johnson J. A., Asplund M., Adén D., Meléndez J., Cohen J. G., Thompson I., Lucatello S., Gal-Yam A., Signatures of an intermediate-age metal-rich bulge population, ArXiv e-prints, 2012
- Bensby T., Feltzing S., Johnson J. A., Gould A., Adén D., Asplund M., Meléndez J., Gal-Yam A., Lucatello S., Sana H., Sumi T., Miyake N., Suzuki D., Han C., Bond I., Udalski A., Chemical evolution of the Galactic bulge as traced by microlensed dwarf and subgiant stars. II. Ages, metallicities, detailed elemental abundances, and connections to the Galactic thick disc, *A&A*, 2010, vol. 512, p. A41
- Bensby T., Feltzing S., Lundström I., Elemental abundance trends in the Galactic thin and thick disks as traced by nearby F and G dwarf stars, *A&A*, 2003, vol. 410, p. 527
- Bensby T., Feltzing S., Lundström I., Oxygen trends in the Galactic thin and thick disks, *A&A*, 2004, vol. 415, p. 155
- Bensby T., Feltzing S., Lundström I., Ilyin I., α -, r-, and s-process element trends in the Galactic thin and thick disks, *A&A*, 2005, vol. 433, p. 185
- Bernardi M., Sheth R. K., Annis J., Burles S., Eisenstein D. J., Finkbeiner D. P., Hogg D. W., Lupton R. H., Schlegel D. J., SubbaRao M., Bahcall N. A., Blakeslee J. P., et al. Early-Type Galaxies in the Sloan Digital Sky Survey. III. The Fundamental Plane, *AJ*, 2003, vol. 125, p. 1866
- Bertone S., Conselice C. J., A comparison of galaxy merger history observations and predictions from semi-analytic models, *MNRAS*, 2009, vol. 396, p. 2345
- Bird C. M., Beers T. C., Astronomical applications of distribution shape estimators, *AJ*, 1993, vol. 105, p. 1596
- Birnboim Y., Dekel A., Virial shocks in galactic haloes?, *MNRAS*, 2003, vol. 345, p. 349
- Biviano A., Girardi M., Giuricin G., Mardirossian F., Mezzetti M., Velocity segregation in galaxy clusters, *ApJ*, 1992, vol. 396, p. 35
- Biviano A., Giuricin G., Mardirossian F., Mezzetti M., The Tully-Fisher relation in different environments, *ApJS*, 1990, vol. 74, p. 325

-
- Biviano A., Katgert P., Thomas T., Adami C., The ESO Nearby Abell Cluster Survey. XI. Segregation of cluster galaxies and subclustering, *A&A*, 2002, vol. 387, p. 8
- Blackwell D. E., Lynas-Gray A. E., Determination of the temperatures of selected ISO flux calibration stars using the Infrared Flux Method, *A&AS*, 1998, vol. 129, p. 505
- Blanton M. R., Brinkmann J., Csabai I., Doi M., Eisenstein D., Fukugita M., Gunn J. E., Hogg D. W., Schlegel D. J., Estimating Fixed-Frame Galaxy Magnitudes in the Sloan Digital Sky Survey, *AJ*, 2003, vol. 125, p. 2348
- Bond J. C., Tinney C. G., Butler R. P., Jones H. R. A., Marcy G. W., Penny A. J., Carter B. D., The abundance distribution of stars with planets, *MNRAS*, 2006, vol. 370, p. 163
- Bouché N., Dekel A., Genzel R., Genel S., Cresci G., Förster Schreiber N. M., Shapiro K. L., Davies R. I., Tacconi L., The Impact of Cold Gas Accretion Above a Mass Floor on Galaxy Scaling Relations, *ApJ*, 2010, vol. 718, p. 1001
- Brunetti M., Chiappini C., Pfenniger D., Diffusion in barred-spiral galaxies, *ArXiv e-prints*, 2010
- Butcher H., Oemler J. A., The evolution of galaxies in clusters. I - ISIT photometry of C1 0024+1654 and 3C 295, *ApJ*, 1978, vol. 219, p. 18
- Capelato H. V., Gerbal D., Mathez G., Mazure A., Roland J., Salvador-Sole E., Theoretical multi-mass models for clusters of galaxies, *A&A*, 1981, vol. 96, p. 235
- Carlberg R. G., Yee H. K. C., Morris S. L., Lin H., Hall P. B., Patton D. R., Sawicki M., Shepherd C. W., Environment and Galaxy Evolution at Intermediate Redshift in the CNOC2 Survey, *ApJ*, 2001, vol. 563, p. 736
- Carollo D., Beers T. C., Lee Y. S., Chiba M., Norris J. E., Wilhelm R., Sivarani T., Marsteller B., Munn J. A., Bailer-Jones C. A. L., Fiorentin P. R., York D. G., Two stellar components in the halo of the Milky Way, *Nature*, 2007, vol. 450, p. 1020
- Carpenter J. M., Color Transformations for the 2MASS Second Incremental Data Release, *AJ*, 2001, vol. 121, p. 2851
- Carraro G., Girardi L., Marigo P., The intermediate-age open cluster NGC 2158, *MNRAS*, 2002, vol. 332, p. 705

- Casagrande L., Portinari L., Flynn C., Accurate fundamental parameters for lower main-sequence stars, *MNRAS*, 2006, vol. 373, p. 13
- Casagrande L., Ramírez I., Meléndez J., Bessell M., Asplund M., An absolutely calibrated T_{eff} scale from the infrared flux method. Dwarfs and subgiants, *A&A*, 2010, vol. 512, p. A54+
- Casagrande L., Schoenrich R., Asplund M., Cassisi S., Ramirez I., Melendez J., Bensby T., Feltzing S., New constraints on the chemical evolution of the solar neighbourhood and Galactic disc(s), *ArXiv e-prints*, 2011
- Castro S., Rich R. M., Grenon M., Barbuy B., McCarthy J. K., High-Resolution Abundance Analysis of Very Metal-rich Stars in the Solar Neighborhood, *AJ*, 1997, vol. 114, p. 376
- Cattaneo A., Faber S. M., Binney J., Dekel A., Kormendy J., Mushotzky R., Babul A., Best P. N., Brüggén M., Fabian A. C., Frenk C. S., Khalatyan A., Netzer H., Mahdavi A., Silk J., Steinmetz M., Wisotzki L., The role of black holes in galaxy formation and evolution, *Nature*, 2009, vol. 460, p. 213
- Cattaneo A., Mamon G. A., Warnick K., Knebe A., How do galaxies acquire their mass?, *A&A*, 2011, vol. 533, p. A5
- Cayrel R., Perrin M.-N., Barbuy B., Buser R., A grid of synthetic spectra for the determination of effective temperature, gravity and metallicity of F, G, and K stars. I - Description of the method. II - Application to 41 stellar spectra taken in the Basel field of SA 141, *A&A*, 1991, vol. 247, p. 108
- Ceccarelli M. L., Valotto C., Lambas D. G., Padilla N., Giovanelli R., Haynes M., Galaxy Peculiar Velocities and Infall onto Groups, *ApJ*, 2005, vol. 622, p. 853
- Chabrier G., Galactic Stellar and Substellar Initial Mass Function, *Publications of the Astronomical Society of the Pacific*, 2003, vol. 115, p. 763
- Chabrier G., The Initial Mass Function: from Salpeter 1955 to 2005. In *The Initial Mass Function 50 Years Later*, vol. 327 of *Astrophysics and Space Science Library*, 2005, p. 41
- Chandrasekhar S., Dynamical Friction. III. a More Exact Theory of the Rate of Escape of Stars from Clusters., *ApJ*, 1943, vol. 98, p. 54

- Charlot S., Concluding Remarks: Recent Achievements and Future Challenges in Stellar Population Studies. In IAU Symposium , vol. 262 of IAU Symposium, 2010, p. 303
- Chen B., Vergely J. L., Valette B., Carraro G., Comparison of two different extinction laws with HIPPARCOS observations, *A&A*, 1998, vol. 336, p. 137
- Chiappini C., Matteucci F., Gratton R., The Chemical Evolution of the Galaxy: The Two-Infall Model, *ApJ*, 1997, vol. 477, p. 765
- Chiappini C., Matteucci F., Romano D., Abundance Gradients and the Formation of the Milky Way, *ApJ*, 2001, vol. 554, p. 1044
- Chiba M., Beers T. C., Kinematics of Metal-poor Stars in the Galaxy. III. Formation of the Stellar Halo and Thick Disk as Revealed from a Large Sample of Nonkinematically Selected Stars, *AJ*, 2000, vol. 119, p. 2843
- Chieffi A., Limongi M., Explosive Yields of Massive Stars from $Z = 0$ to $Z = Z_{\text{solar}}$, *ApJ*, 2004, vol. 608, p. 405
- Cid Fernandes R., Mateus A., Sodr e L., Stasińska G., Gomes J. M., Semi-empirical analysis of Sloan Digital Sky Survey galaxies - I. Spectral synthesis method, *MNRAS*, 2005, vol. 358, p. 363
- Coelho P., Barbuy B., Meléndez J., Schiavon R. P., Castilho B. V., A library of high resolution synthetic stellar spectra from 300 nm to 1.8 μm with solar and α -enhanced composition, *A&A*, 2005, vol. 443, p. 735
- Coelho P., Gadotti D. A., Bars Rejuvenating Bulges? Evidence from Stellar Population Analysis, *ApJL*, 2011, vol. 743, p. L13
- Cohen J. G., Thompson I. B., Sumi T., Bond I., Gould A., Johnson J. A., Huang W., Burley G., Clues to the Metallicity Distribution in the Galactic Bulge: Abundances in MOA-2008-BLG-310S and MOA-2008-BLG-311S, *ApJ*, 2009, vol. 699, p. 66
- Colavitti E., Matteucci F., Murante G., The chemical evolution of a Milky Way-like galaxy: the importance of a cosmologically motivated infall law, *A&A*, 2008, vol. 483, p. 401

- Cole S., Lacey C. G., Baugh C. M., Frenk C. S., Hierarchical galaxy formation, *MNRAS*, 2000, vol. 319, p. 168
- Colless M., Dalton G., Maddox S., Sutherland W., Norberg P., Cole S., Bland-Hawthorn J., Bridges T., Cannon R., Collins C., Couch W., Cross N., et al. The 2dF Galaxy Redshift Survey: spectra and redshifts, *MNRAS*, 2001, vol. 328, p. 1039
- Conselice C., The role of dwarf galaxies in galaxy cluster evolution, *Highlights of Astronomy*, 2005, vol. 13, p. 328
- Conselice C. J., Bundy K., Trujillo I., Coil A., Eisenhardt P., Ellis R. S., Georgakakis A., Huang J., Lotz J., Nandra K., Newman J., Papovich C., Weiner B., Willmer C., The properties and evolution of a K-band selected sample of massive galaxies at $z \sim 0.4-2$ in the Palomar/DEEP2 survey, *MNRAS*, 2007, vol. 381, p. 962
- Côté P., Ferrarese L., Jordán A., Blakeslee J. P., Chen C.-W., Infante L., Mei S., Peng E. W., Tonry J. L., West M. J., Galaxy scaling relations from the ACS Virgo and Fornax Cluster Surveys: no evidence for a dwarf-giant dichotomy. In *IAU Symposium*, vol. 245 of *IAU Symposium*, 2008, p. 395
- Croton D. J., Springel V., White S. D. M., De Lucia G., Frenk C. S., Gao L., Jenkins A., Kauffmann G., Navarro J. F., Yoshida N., The many lives of active galactic nuclei: cooling flows, black holes and the luminosities and colours of galaxies, *MNRAS*, 2006, vol. 365, p. 11
- Cupani G., Mezzetti M., Mardirossian F., Mass estimation in the outer non-equilibrium region of galaxy clusters, *MNRAS*, 2008, vol. 390, p. 645
- da Silva A. F., , *Comput. Methods Programs Biomed.*, 2009, vol. 94, p. 1
- da Silva L., Girardi L., Pasquini L., Setiawan J., von der Lühe O., de Medeiros J. R., Hatzes A., Döllinger M. P., Weiss A., Basic physical parameters of a selected sample of evolved stars, *A&A*, 2006, vol. 458, p. 609
- Damjanov I., McCarthy P. J., Abraham R. G., Glazebrook K., Yan H., Mentuch E., Le Borgne D., Savaglio S., Crampton D., Murowinski R., Juneau S., Carlberg R. G., Jørgensen I., Roth K., Chen H.-W., Marzke R. O., Red Nuggets at $z \sim 1.5$: Compact Passive Galaxies and the Formation of the Kormendy Relation, *ApJ*, 2009, vol. 695, p. 101

-
- Dave R., Dubinski J., Hernquist L., Parallel TreeSPH, *New Astronomy*, 1997, vol. 2, p. 277
- de Jong J. T. A., Yanny B., Rix H.-W., Dolphin A. E., Martin N. F., Beers T. C., Mapping the Stellar Structure of the Milky Way Thick Disk and Halo Using SEGUE Photometry, *ApJ*, 2010, vol. 714, p. 663
- De Lucia G., Blaizot J., The hierarchical formation of the brightest cluster galaxies, *MNRAS*, 2007, vol. 375, p. 2
- De Lucia G., Helmi A., The Galaxy and its stellar halo: insights on their formation from a hybrid cosmological approach, *MNRAS*, 2008, vol. 391, p. 14
- De Lucia G., Springel V., White S. D. M., Croton D., Kauffmann G., The formation history of elliptical galaxies, *MNRAS*, 2006, vol. 366, p. 499
- de Rossi M. E., Tissera P. B., Pedrosa S. E., Impact of supernova feedback on the Tully-Fisher relation, *A&A*, 2010, vol. 519, p. A89
- Dehnen W., Binney J. J., Local stellar kinematics from HIPPARCOS data, *MNRAS*, 1998, vol. 298, p. 387
- Dekel A., Birnboim Y., Galaxy bimodality due to cold flows and shock heating, *MNRAS*, 2006, vol. 368, p. 2
- Dekel A., Birnboim Y., Engel G., Freundlich J., Goerdt T., Mumcuoglu M., Neistein E., Pichon C., Teyssier R., Zinger E., Cold streams in early massive hot haloes as the main mode of galaxy formation, *Nature*, 2009, vol. 457, p. 451
- Dekel A., Silk J., The origin of dwarf galaxies, cold dark matter, and biased galaxy formation, *ApJ*, 1986, vol. 303, p. 39
- Demarque P., Woo J., Kim Y., Yi S. K., Y^2 Isochrones with an Improved Core Overshoot Treatment, *ApJS*, 2004, vol. 155, p. 667
- di Benedetto G. P., Towards a fundamental calibration of stellar parameters of A, F, G, K dwarfs and giants, *A&A*, 1998, vol. 339, p. 858
- Diaferio A., Geller M. J., Infall Regions of Galaxy Clusters, *ApJ*, 1997, vol. 481, p. 633

- Diaferio A., Ramella M., Geller M. J., Ferrari A., Are groups of galaxies virialized systems?, *AJ*, 1993, vol. 105, p. 2035
- Diebolt J., Robert C. P., , *Journal of the Royal Statistical Society*, 1994, vol. 56, p. 363
- Diemand J., Kuhlen M., Infall Caustics in Dark Matter Halos?, *ApJL*, 2008, vol. 680, p. L25
- Djorgovski S., de Carvalho R., Optical Properties of Early Type Galaxies. In *Windows on Galaxies* , vol. 160 of *Astrophysics and Space Science Library*, 1990, p. 9
- Dolag K., Borgani S., Murante G., Springel V., Substructures in hydrodynamical cluster simulations, *MNRAS*, 2009, vol. 399, p. 497
- Dressler A., Galaxy morphology in rich clusters - Implications for the formation and evolution of galaxies, *ApJ*, 1980, vol. 236, p. 351
- Dubinski J., Carlberg R. G., The structure of cold dark matter halos, *ApJ*, 1991, vol. 378, p. 496
- Dutton A. A., Mendel J. T., Simard L., Evidence for a non-universal stellar initial mass function in low-redshift high-density early-type galaxies, *ArXiv e-prints*, 2011
- Edvardsson B., Andersen J., Gustafsson B., Lambert D. L., Nissen P. E., Tomkin J., The Chemical Evolution of the Galactic Disk - Part One - Analysis and Results, *A&A*, 1993, vol. 275, p. 101
- Eggen O. J., Lynden-Bell D., Sandage A. R., Evidence from the motions of old stars that the Galaxy collapsed., *ApJ*, 1962, vol. 136, p. 748
- Eke V. R., Baugh C. M., Cole S., Frenk C. S., Norberg P., Peacock J. A., Baldry I. K., Bland-Hawthorn J., Bridges T., Cannon R., Colless M., Collins C., Couch W., Dalton G., de Propris R., et al. Galaxy groups in the 2dFGRS: the group-finding algorithm and the 2PIGG catalogue, *MNRAS*, 2004, vol. 348, p. 866
- ESA The Hipparcos and Tycho Catalogues (ESA 1997), *VizieR Online Data Catalog*, 1997, vol. 1239, p. 0
- Evstigneeva E. A., de Carvalho R. R., Ribeiro A. L., Capelato H. V., Merging of low-mass systems and the origin of the Fundamental Plane, *MNRAS*, 2004, vol. 349, p. 1052

- Faber S. M., Dressler A., Davies R. L., Burstein D., Lynden-Bell D., Global scaling relations for elliptical galaxies and implications for formation. In *Nearly Normal Galaxies. From the Planck Time to the Present*, 1987, p. 175
- Faber S. M., Jackson R. E., Velocity dispersions and mass-to-light ratios for elliptical galaxies, *ApJ*, 1976, vol. 204, p. 668
- Fadda D., Girardi M., Giuricin G., Mardirossian F., Mezzetti M., The Observational Distribution of Internal Velocity Dispersions in Nearby Galaxy Clusters, *ApJ*, 1996, vol. 473, p. 670
- Falcón-Barroso J., Sánchez-Blázquez P., Vazdekis A., Ricciardelli E., Cardiel N., Cenarro A. J., Gorgas J., Peletier R. F., An updated MILES stellar library and stellar population models, *A&A*, 2011, vol. 532, p. A95
- Famaey B., Jorissen A., Luri X., Mayor M., Udry S., Dejonghe H., Turon C., Local kinematics of K and M giants from CORAVEL/Hipparcos/Tycho-2 data. Revisiting the concept of superclusters, *A&A*, 2005, vol. 430, p. 165
- Fan L., Lapi A., Bressan A., Bernardi M., De Zotti G., Danese L., Cosmic Evolution of Size and Velocity Dispersion for Early-type Galaxies, *ApJ*, 2010, vol. 718, p. 1460
- Fan L., Lapi A., De Zotti G., Danese L., The Dramatic Size Evolution of Elliptical Galaxies and the Quasar Feedback, *ApJL*, 2008, vol. 689, p. L101
- Faucher-Giguère C.-A., Kereš D., The small covering factor of cold accretion streams, *MNRAS*, 2011, vol. 412, p. L118
- Faucher-Giguère C.-A., Kereš D., Dijkstra M., Hernquist L., Zaldarriaga M., Ly α Cooling Emission from Galaxy Formation, *ApJ*, 2010, vol. 725, p. 633
- Favata F., Micela G., Sciortino S., The [Fe/H] distribution of a volume limited sample of solar-type stars and its implications for galactic chemical evolution., *A&A*, 1997, vol. 323, p. 809
- Feltzing S., Bensby T., Lundström I., Signatures of SN Ia in the galactic thick disk. Observational evidence from alpha -elements in 67 dwarf stars in the solar neighbourhood, *A&A*, 2003, vol. 397, p. L1

- Feltzing S., González G., The nature of super-metal-rich stars. Detailed abundance analysis of 8 super-metal-rich star candidates, *A&A*, 2001, vol. 367, p. 253
- Feltzing S., Gustafsson B., Abundances in metal-rich stars. Detailed abundance analysis of 47 G and K dwarf stars with $[Me/H] > 0.10$ dex, *A&AS*, 1998, vol. 129, p. 237
- Ferguson T. S., , *Annals of Statistics*, 1973, vol. 1, p. 209
- Fernández Lorenzo M., Cepa J., Bongiovanni A., Pérez García A. M., Lara-López M. A., Pović M., Sánchez-Portal M., Evolution of the infrared Tully-Fisher relation up to $z = 1.4$, *A&A*, 2010, vol. 521, p. A27
- Ferrara A., Tolstoy E., The role of stellar feedback and dark matter in the evolution of dwarf galaxies, *MNRAS*, 2000, vol. 313, p. 291
- Ferreras I., Lisker T., Pasquali A., Kaviraj S., Exploring the formation of spheroidal galaxies out to $z \sim 1.5$ in GOODS, *MNRAS*, 2009, vol. 395, p. 554
- Ferreras I., Pasquali A., Malhotra S., Rhoads J., Cohen S., Windhorst R., Pirzkal N., Grogin N., Koekemoer A. M., Lisker T., Panagia N., Daddi E., Hathi N. P., Early-Type Galaxies in the PEARS Survey: Probing the Stellar Populations at Moderate Redshift, *ApJ*, 2009, vol. 706, p. 158
- Ferreras I., Wyse R. F. G., Silk J., The formation history of the Galactic bulge, *MNRAS*, 2003, vol. 345, p. 1381
- Förster Schreiber N. M., Genzel R., Lehnert M. D., Bouché N., Verma A., Erb D. K., Shapley A. E., Steidel C. C., Davies R., Lutz D., Nesvadba N., Tacconi L. J., Eisenhauer F., Abuter R., Gilbert A., et al. SINFONI Integral Field Spectroscopy of $z \sim 2$ UV-selected Galaxies: Rotation Curves and Dynamical Evolution, *ApJ*, 2006, vol. 645, p. 1062
- Fuhr J. R., Wiese W. L., A Critical Compilation of Atomic Transition Probabilities for Neutral and Singly Ionized Iron, *Journal of Physical and Chemical Reference Data*, 2006, vol. 35, p. 1669
- Fuhrmann K., Nearby stars of the Galactic disk and halo, *A&A*, 1998, vol. 338, p. 161

-
- Fulbright J. P., McWilliam A., Rich R. M., Abundances of Baade's Window Giants from Keck HIRES Spectra. II. The Alpha and Light Odd Elements, *ApJ*, 2007, vol. 661, p. 1152
- Fux R., 3D self-consistent N-body barred models of the Milky Way. I. Stellar dynamics, *A&A*, 1997, vol. 327, p. 983
- Gadotti D. A., Structural properties of pseudo-bulges, classical bulges and elliptical galaxies: a Sloan Digital Sky Survey perspective, *MNRAS*, 2009, vol. 393, p. 1531
- Geller M. J., Huchra J. P., Groups of galaxies. III - The CfA survey, *ApJS*, 1983, vol. 52, p. 61
- Geltman S., That Bound-Free Absorption Coefficient of the Hydrogen Negative Ion., *ApJ*, 1962, vol. 136, p. 935
- Genzel R., Tacconi L. J., Eisenhauer F., Förster Schreiber N. M., Cimatti A., Daddi E., Bouché N., Davies R., Lehnert M. D., Lutz D., Nesvadba N., Verma A., Abuter R., Shapiro K., Sternberg A., Renzini A., et al. The rapid formation of a large rotating disk galaxy three billion years after the Big Bang, *Nature*, 2006, vol. 442, p. 786
- Gill S. P. D., Knebe A., Gibson B. K., The evolution of substructure - III. The outskirts of clusters, *MNRAS*, 2005, vol. 356, p. 1327
- Gilmore G., Reid N., New light on faint stars. III - Galactic structure towards the South Pole and the Galactic thick disc, *MNRAS*, 1983, vol. 202, p. 1025
- Gingerich O., Review of Opacity Calculations, *SAO Special Report*, 1964, vol. 167, p. 17
- Girardi L., Bressan A., Bertelli G., Chiosi C., Evolutionary tracks and isochrones for low- and intermediate-mass stars: From 0.15 to 7 M_{sun} , and from $Z=0.0004$ to 0.03, *A&AS*, 2000, vol. 141, p. 371
- Girardi M., Rigoni E., Mardirossian F., Mezzetti M., Morphology and luminosity segregation of galaxies in nearby loose groups, *A&A*, 2003, vol. 406, p. 403
- Giuricin G., Gondolo P., Mardirossian F., Mezzetti M., Ramella M., Groups of galaxies in the Local Supercluster - Some hypotheses on the evolutionary stage, *A&A*, 1988, vol. 199, p. 85

- Gonzalez O. A., Rejkuba M., Zoccali M., Hill V., Battaglia G., Babusiaux C., Minniti D., Barbey B., Alves-Brito A., Renzini A., Gomez A., Ortolani S., Alpha element abundances and gradients in the Milky Way bulge from FLAMES-GIRAFFE spectra of 650 K giants, *A&A*, 2011, vol. 530, p. A54
- González Hernández J. I., Bonifacio P., A new implementation of the infrared flux method using the 2MASS catalogue, *A&A*, 2009, vol. 497, p. 497
- Goto T., Velocity dispersion of 335 galaxy clusters selected from the Sloan Digital Sky Survey: statistical evidence for dynamical interaction and against ram-pressure stripping, *MNRAS*, 2005, vol. 359, p. 1415
- Graham A. W., Guzmán R., HST Photometry of Dwarf Elliptical Galaxies in Coma, and an Explanation for the Alleged Structural Dichotomy between Dwarf and Bright Elliptical Galaxies, *AJ*, 2003, vol. 125, p. 2936
- Gratton R. G., Carretta E., Matteucci F., Sneden C., Abundances of light elements in metal-poor stars. IV. [Fe/O] and [Fe/Mg] ratios and the history of star formation in the solar neighborhood, *A&A*, 2000, vol. 358, p. 671
- Grenon M., On Metal Rich and SMR Stars. In *IAU Colloq. 17: Age des Etoiles* , 1972, p. 55
- Grenon M., Photometric properties of G, K and M stars in relation to galactic structure and evolution, 1978
- Grenon M., The chemical evolution of the Galactic disc from the kinematics and metallicities of proper motion stars, *Ap&SS*, 1989, vol. 156, p. 29
- Grenon M., From halo to SMR stars. In *European Southern Observatory Conference and Workshop Proceedings* , vol. 35 of *European Southern Observatory Conference and Workshop Proceedings*, 1990, p. 143
- Grenon M., The Age of Old Galactic Populations, *Highlights of Astronomy*, 1998, vol. 11, p. 560
- Grenon M., The Kinematics and Origin of SMR Stars, *Ap&SS*, 1999, vol. 265, p. 331

-
- Grenon M., The Origin and Kinematical Evolution of SMR Stars. In *The Evolution of the Milky Way: Stars versus Clusters*, 2000, p. 47
- Grevesse N., Noels A., Sauval A. J., Standard Abundances. In *Cosmic Abundances*, vol. 99 of *Astronomical Society of the Pacific Conference Series*, 1996, p. 117
- Grevesse N., Sauval A. J., Standard Solar Composition, *SSRv*, 1998, vol. 85, p. 161
- Gunn J. E., Gott I. J. R., On the Infall of Matter Into Clusters of Galaxies and Some Effects on Their Evolution, *ApJ*, 1972, vol. 176, p. 1
- Guo Q., White S., Boylan-Kolchin M., De Lucia G., Kauffmann G., Lemson G., Li C., Springel V., Weinmann S., From dwarf spheroidals to cD galaxies: simulating the galaxy population in a Λ CDM cosmology, *MNRAS*, 2011, vol. 413, p. 101
- Guo Q., White S., Li C., Boylan-Kolchin M., How do galaxies populate dark matter haloes?, *MNRAS*, 2010, vol. 404, p. 1111
- Gustafsson B., Edvardsson B., Eriksson K., Jørgensen U. G., Nordlund Å., Plez B., A grid of MARCS model atmospheres for late-type stars. I. Methods and general properties, *A&A*, 2008, vol. 486, p. 951
- Haywood M., Radial mixing and the transition between the thick and thin Galactic discs, *MNRAS*, 2008, vol. 388, p. 1175
- Heiter U., Luck R. E., Abundance Analysis of Planetary Host Stars. I. Differential Iron Abundances, *AJ*, 2003, vol. 126, p. 2015
- Helmi A., Navarro J. F., Nordström B., Holmberg J., Abadi M. G., Steinmetz M., Pieces of the puzzle: ancient substructure in the Galactic disc, *MNRAS*, 2006, vol. 365, p. 1309
- Helmi A., White S. D. M., Building up the stellar halo of the Galaxy, *MNRAS*, 1999, vol. 307, p. 495
- Hernquist L., An analytical model for spherical galaxies and bulges, *ApJ*, 1990, vol. 356, p. 359
- Hills J. G., The effect of mass loss on the dynamical evolution of a stellar system - Analytic approximations, *ApJ*, 1980, vol. 235, p. 986

- Holmberg J., Nordström B., Andersen J., The Geneva-Copenhagen survey of the solar neighbourhood. III. Improved distances, ages, and kinematics, *A&A*, 2009, vol. 501, p. 941
- Hou A., Parker L. C., Harris W. E., Wilman D. J., Statistical Tools for Classifying Galaxy Group Dynamics, *ApJ*, 2009, vol. 702, p. 1199
- Howard C. D., Rich R. M., Clarkson W., Mallery R., Kormendy J., De Propris R., Robin A. C., Fux R., Reitzel D. B., Zhao H. S., Kuijken K., Koch A., Kinematics at the Edge of the Galactic Bulge: Evidence for Cylindrical Rotation, *ApJL*, 2009, vol. 702, p. L153
- Huchra J. P., Geller M. J., Groups of galaxies. I - Nearby groups, *ApJ*, 1982, vol. 257, p. 423
- Ibata R. A., Gilmore G., Irwin M. J., A dwarf satellite galaxy in Sagittarius, *Nature*, 1994, vol. 370, p. 194
- Ivezić Z., Sesar B., Jurić M., Bond N., Dalcanton J., et al. The Milky Way Tomography with SDSS. II. Stellar Metallicity, *ApJ*, 2008, vol. 684, p. 287
- Janz J., Lisker T., The Sizes of Early-Type Galaxies, *ApJL*, 2008, vol. 689, p. L25
- John T. L., Continuous absorption by the negative hydrogen ion reconsidered, *A&A*, 1988, vol. 193, p. 189
- Jorgensen I., Franx M., Kjaergaard P., The Fundamental Plane for cluster E and S0 galaxies, *MNRAS*, 1996, vol. 280, p. 167
- Jurić M., Ž. Ivezić Brooks A., Lupton R. H., Schlegel D., et al. The Milky Way Tomography with SDSS. I. Stellar Number Density Distribution, *ApJ*, 2008, vol. 673, p. 864
- Kang X., Jing Y. P., Mo H. J., Börner G., Semianalytical Model of Galaxy Formation with High-Resolution N-Body Simulations, *ApJ*, 2005, vol. 631, p. 21
- Kang X., van den Bosch F. C., Pasquali A., On the origin of the dichotomy of early-type galaxies: the role of dry mergers and active galactic nucleus feedback, *MNRAS*, 2007, vol. 381, p. 389
- Katgert P., Mazure A., Perea J., den Hartog R., Moles M., Le Fevre O., Dubath P., Focardi P., Rhee G., Jones B., Escalera E., Biviano A., Gerbal D., Giuricin G., The ESO Nearby Abell Cluster Survey. I. Description of the dataset and definition of physical systems., *A&A*, 1996, vol. 310, p. 8

- Katz D., Soubiran C., Cayrel R., Barbuy B., Friel E., Bienaymé O., Perrin M., Probing the Galactic thick disc vertical properties and interfaces, *A&A*, 2011, vol. 525, p. A90+
- Kaufer A., Stahl O., Tubbesing S., Norregaard P., Avila G., Francois P., Pasquini L., Pizzella A., Performance report on FEROS, the new fiber-linked echelle spectrograph at the ESO 1.52-m telescope. In *Society of Photo-Optical Instrumentation Engineers (SPIE) Conference Series*, vol. 4008 of Presented at the Society of Photo-Optical Instrumentation Engineers (SPIE) Conference, 2000, p. 459
- Kauffmann G., Heckman T. M., White S. D. M., Charlot S., Tremonti C., Peng E. W., Seibert M., Brinkmann J., Nichol R. C., SubbaRao M., York D., The dependence of star formation history and internal structure on stellar mass for 10^5 low-redshift galaxies, *MNRAS*, 2003, vol. 341, p. 54
- Kazantzidis S., Bullock J. S., Zentner A. R., Kravtsov A. V., Moustakas L. A., Cold Dark Matter Substructure and Galactic Disks. I. Morphological Signatures of Hierarchical Satellite Accretion, *ApJ*, 2008, vol. 688, p. 254
- Kennicutt J. R. C., The Global Schmidt Law in Star-forming Galaxies, *ApJ*, 1998, vol. 498, p. 541
- Kereš D., Katz N., Davé R., Fardal M., Weinberg D. H., Galaxies in a simulated Λ CDM universe - II. Observable properties and constraints on feedback, *MNRAS*, 2009, vol. 396, p. 2332
- Kereš D., Katz N., Weinberg D. H., Davé R., How do galaxies get their gas?, *MNRAS*, 2005, vol. 363, p. 2
- Koleva M., de Rijcke S., Prugniel P., Zeilinger W. W., Michielsen D., Formation and evolution of dwarf elliptical galaxies - II. Spatially resolved star formation histories, *MNRAS*, 2009, vol. 396, p. 2133
- Koleva M., Prugniel P., de Rijcke S., Zeilinger W. W., Age and metallicity gradients in early-type galaxies: a dwarf-to-giant sequence, *MNRAS*, 2011, vol. 417, p. 1643
- Kormendy J., Brightness distributions in compact and normal galaxies. II - Structure parameters of the spheroidal component, *ApJ*, 1977, vol. 218, p. 333

- Kormendy J., Drory N., Bender R., Cornell M. E., Bulgeless Giant Galaxies Challenge Our Picture of Galaxy Formation by Hierarchical Clustering, *ApJ*, 2010, vol. 723, p. 54
- Kormendy J., Kennicutt J. R. C., Secular Evolution and the Formation of Pseudobulges in Disk Galaxies, *ARA&A*, 2004, vol. 42, p. 603
- Kriek M., van Dokkum P. G., Franx M., Quadri R., Gawiser E., Herrera D., Illingworth G. D., Labbé I., Lira P., Marchesini D., Rix H.-W., Rudnick G., Taylor E. N., Toft S., Urry C. M., Wuyts S., Spectroscopic Identification of Massive Galaxies at $z \sim 2.3$ with Strongly Suppressed Star Formation, *ApJL*, 2006, vol. 649, p. L71
- Kroupa P., On the variation of the initial mass function, *MNRAS*, 2001, vol. 322, p. 231
- Kroupa P., The Initial Mass Function of Stars: Evidence for Uniformity in Variable Systems, *Science*, 2002, vol. 295, p. 82
- Kupka F., Piskunov N., Ryabchikova T. A., Stempels H. C., Weiss W. W., VALD-2: Progress of the Vienna Atomic Line Data Base, *A&AS*, 1999, vol. 138, p. 119
- La Barbera F., de Carvalho R. R., de La Rosa I. G., Lopes P. A. A., SPIDER - II. The Fundamental Plane of early-type galaxies in grizYJHK, *MNRAS*, 2010, vol. 408, p. 1335
- La Barbera F., de Carvalho R. R., de La Rosa I. G., Lopes P. A. A., Kohl-Moreira J. L., Capelato H. V., SPIDER - I. Sample and galaxy parameters in the grizYJHK wavebands, *MNRAS*, 2010, vol. 408, p. 1313
- La Barbera F., de Carvalho R. R., Kohl-Moreira J. L., Gal R. R., Soares-Santos M., Capaccioli M., Santos R., Sant'anna N., 2DPHOT: A Multi-Purpose Environment for the Two-Dimensional Analysis of Wide-Field Images, *Publications of the Astronomical Society of the Pacific*, 2008, vol. 120, p. 681
- La Barbera F., Ferreras I., de Carvalho R. R., Lopes P. A. A., Pasquali A., de la Rosa I. G., De Lucia G., On the Radial Stellar Content of Early-type Galaxies as a Function of Mass and Environment, *ApJL*, 2011, vol. 740, p. L41
- Larson R. B., Effects of supernovae on the early evolution of galaxies, *MNRAS*, 1974, vol. 169, p. 229

-
- Larson R. B., Tinsley B. M., Caldwell C. N., The evolution of disk galaxies and the origin of S0 galaxies, *ApJ*, 1980, vol. 237, p. 692
- Laws C., González G., Walker K. M., Tyagi S., Dodsworth J., Snider K., Suntzeff N. B., Parent Stars of Extrasolar Planets. VII. New Abundance Analyses of 30 Systems, *AJ*, 2003, vol. 125, p. 2664
- Lecureur A., Hill V., Zoccali M., Barbuy B., Gómez A., Minniti D., Ortolani S., Renzini A., Oxygen, sodium, magnesium, and aluminium as tracers of the galactic bulge formation, *A&A*, 2007, vol. 465, p. 799
- Lépine J. R. D., Acharova I. A., Mishurov Y. N., Corotation, Stellar Wandering, and Fine Structure of the Galactic Abundance Pattern, *ApJ*, 2003, vol. 589, p. 210
- Lintott C., Schawinski K., Bamford S., Slosar A., Land K., Thomas D., Edmondson E., Masters K., Nichol R. C., Raddick M. J., Szalay A., Andreescu D., Murray P., Vandenberg J., Galaxy Zoo 1: data release of morphological classifications for nearly 900 000 galaxies, *MNRAS*, 2011, vol. 410, p. 166
- Lisker T., Early-type dwarf galaxies in clusters: A mixed bag with various origins?, *Astronomische Nachrichten*, 2009, vol. 330, p. 1043
- Lopes P. A. A., de Carvalho R. R., Kohl-Moreira J. L., Jones C., NoSOCS in SDSS - I. Sample definition and comparison of mass estimates, *MNRAS*, 2009a, vol. 392, p. 135
- Lopes P. A. A., de Carvalho R. R., Kohl-Moreira J. L., Jones C., NoSOCS in SDSS - II. Mass calibration of low redshift galaxy clusters with optical and X-ray properties, *MNRAS*, 2009b, vol. 399, p. 2201
- Luck R. E., Heiter U., Dwarfs in the Local Region, *AJ*, 2006, vol. 131, p. 3069
- Mac Low M.-M., Ferrara A., Starburst-driven Mass Loss from Dwarf Galaxies: Efficiency and Metal Ejection, *ApJ*, 1999, vol. 513, p. 142
- Madgwick D. S., Lahav O., Baldry I. K., Baugh C. M., Bland-Hawthorn J., Bridges T., Cannon R., Cole S., Colless M., Collins C., Couch W., et al. The 2dF Galaxy Redshift Survey: galaxy luminosity functions per spectral type, *MNRAS*, 2002, vol. 333, p. 133

- Mahdavi A., Geller M. J., Böhringer H., Kurtz M. J., Ramella M., The Dynamics of Poor Systems of Galaxies, *ApJ*, 1999, vol. 518, p. 69
- Majewski S. R., Munn J. A., Hawley S. L., Absolute Proper Motions to B approximately 22.5: Large-Scale Streaming Motions and the Structure and Origin of the Galactic Halo, *ApJL*, 1996, vol. 459, p. L73
- Mamon G., Dynamical Theory of groups and Clusters of Galaxies. In *N-body Problems and Gravitational Dynamics* , 1993, p. 188
- Mamon G. A., The Evolution of Galaxy Groups and of Galaxies Therein. In *Groups of Galaxies in the Nearby Universe* , 2007, p. 203
- Mamon G. A., Tweed D., Cattaneo A., Thuan T. X., How do dwarf galaxies acquire their mass & when do they form their stars?, *ArXiv e-prints*, 2010
- Martin N. F., Ibata R. A., Conn B. C., Lewis G. F., Bellazzini M., Irwin M. J., McConnachie A. W., Why the Canis Major overdensity is not due to the Warp: analysis of its radial profile and velocities, *MNRAS*, 2004, vol. 355, p. L33
- Masana E., Jordi C., Ribas I., Effective temperature scale and bolometric corrections from 2MASS photometry, *A&A*, 2006, vol. 450, p. 735
- Matteucci F., The chemical evolution of the Milky Way : from light to heavy elements. In *Origin of Matter and Evolution of Galaxies* , vol. 847 of *American Institute of Physics Conference Series*, 2006, p. 79
- Matteucci F., Brocato E., Metallicity distribution and abundance ratios in the stars of the Galactic bulge, *ApJ*, 1990, vol. 365, p. 539
- McWilliam A., High-resolution spectroscopic survey of 671 GK giants. I - Stellar atmosphere parameters and abundances, *ApJS*, 1990, vol. 74, p. 1075
- McWilliam A., Rich R. M., The first detailed abundance analysis of Galactic bulge K giants in Baade's window, *ApJS*, 1994, vol. 91, p. 749

-
- Meléndez J., Asplund M., Alves-Brito A., Cunha K., Barbuy B., Bessell M. S., Chiappini C., Freeman K. C., Ramírez I., Smith V. V., Yong D., Chemical similarities between Galactic bulge and local thick disk red giant stars, *A&A*, 2008, vol. 484, p. L21
- Meléndez J., Asplund M., Gustafsson B., Yong D., The Peculiar Solar Composition and Its Possible Relation to Planet Formation, *ApJ*, 2009, vol. 704, p. L66
- Meléndez J., Barbuy B., Both accurate and precise gf-values for Fe II lines, *A&A*, 2009, vol. 497, p. 611
- Meléndez J., Cohen J. G., The Rise of the AGB in the Galactic Halo: Mg Isotopic Ratios and High Precision Elemental Abundances in M71 Giants, *ApJ*, 2009, vol. 699, p. 2017
- Meléndez J., Ramírez I., Spectroscopic Equilibrium of Iron in Metal-Rich Dwarfs. In *Cosmic Abundances as Records of Stellar Evolution and Nucleosynthesis*, vol. 336 of *Astronomical Society of the Pacific Conference Series*, 2005, p. 343
- Menci N., Fusco-Femiano R., Galaxy Velocity Dispersion Profiles from Merging in Clusters, *ApJ*, 1996, vol. 472, p. 46
- Miller G. E., Scalo J. M., The initial mass function and stellar birthrate in the solar neighborhood, *ApJS*, 1979, vol. 41, p. 513
- Miller S. H., Bundy K., Sullivan M., Ellis R. S., Treu T., The Assembly History of Disk Galaxies. I. The Tully-Fisher Relation to $z \sim 1.3$ from Deep Exposures with DEIMOS, *ApJ*, 2011, vol. 741, p. 115
- Miller S. H., Ellis R. S., Sullivan M., Bundy K., Newman A., Treu T., The Assembly History of Disk Galaxies: II. Probing the Emerging Tully-Fisher Relation During $1 < z < 1.7$, *ArXiv e-prints*, 2012
- Minchev I., Famaey B., A New Mechanism for Radial Migration in Galactic Disks: Spiral-Bar Resonance Overlap, *ApJ*, 2010, vol. 722, p. 112
- Mishenina T. V., Soubiran C., Bienaymé O., Korotin S. A., Belik S. I., Usenko I. A., Kovtyukh V. V., Spectroscopic investigation of stars on the lower main sequence, *A&A*, 2008, vol. 489, p. 923

- Mishenina T. V., Soubiran C., Kovtyukh V. V., Korotin S. A., On the correlation of elemental abundances with kinematics among galactic disk stars, *A&A*, 2004, vol. 418, p. 551
- Moster B. P., Somerville R. S., Maulbetsch C., van den Bosch F. C., Macciò A. V., Naab T., Oser L., Constraints on the Relationship between Stellar Mass and Halo Mass at Low and High Redshift, *ApJ*, 2010, vol. 710, p. 903
- Naab T., Ostriker J. P., A simple model for the evolution of disc galaxies: the Milky Way, *MNRAS*, 2006, vol. 366, p. 899
- Nair P. B., Abraham R. G., A Catalog of Detailed Visual Morphological Classifications for 14,034 Galaxies in the Sloan Digital Sky Survey, *ApJS*, 2010, vol. 186, p. 427
- Neal R. M., , *Journal of Computational and Graphical Statistics*, 2000, vol. 9, p. 249
- Neves V., Santos N. C., Sousa S. G., Correia A. C. M., Israelian G., Chemical abundances of 451 stars from the HARPS GTO planet search program. Thin disc, thick disc, and planets, *A&A*, 2009, vol. 497, p. 563
- Niemi S.-M., Nurmi P., Heinämäki P., Valtonen M., Are the nearby groups of galaxies gravitationally bound objects?, *MNRAS*, 2007, vol. 382, p. 1864
- Nolthenius R., White S. D. M., Groups of galaxies in the CfA survey and in cold dark matter universes, *MNRAS*, 1987, vol. 225, p. 505
- Nomoto K., Tominaga N., Umeda H., Kobayashi C., Maeda K., Nucleosynthesis yields of core-collapse supernovae and hypernovae, and galactic chemical evolution, *Nuclear Physics A*, 2006, vol. 777, p. 424
- Nordström B., Mayor M., Andersen J., Holmberg J., Pont F., Jørgensen B. R., Olsen E. H., Udry S., Mowlavi N., The Geneva-Copenhagen survey of the Solar neighbourhood. Ages, metallicities, and kinematic properties of $\sim 14\,000$ F and G dwarfs, *A&A*, 2004, vol. 418, p. 989
- Olsen L. F., Benoist C., da Costa L., Hansen L., Jørgensen H. E., Multi-object spectroscopy of low redshift EIS clusters. III. Properties of optically selected clusters, *A&A*, 2005, vol. 435, p. 781

-
- Oser L., Ostriker J. P., Naab T., Johansson P. H., Burkert A., The Two Phases of Galaxy Formation, *ApJ*, 2010, vol. 725, p. 2312
- Osmond J. P. F., Ponman T. J., The GEMS project: X-ray analysis and statistical properties of the group sample, *MNRAS*, 2004, vol. 350, p. 1511
- Ostriker J. P., Tremaine S. D., Another evolutionary correction to the luminosity of giant galaxies, *ApJL*, 1975, vol. 202, p. L113
- Pagel B. E. J., *Nucleosynthesis and Chemical Evolution of Galaxies*, 1997
- Panter B., Jimenez R., Heavens A. F., Charlot S., The star formation histories of galaxies in the Sloan Digital Sky Survey, *MNRAS*, 2007, vol. 378, p. 1550
- Paz D. J., Lambas D. G., Padilla N., Merchán M., Shapes of clusters and groups of galaxies: comparison of model predictions with observations, *MNRAS*, 2006, vol. 366, p. 1503
- Pearce F. R., Jenkins A., Frenk C. S., White S. D. M., Thomas P. A., Couchman H. M. P., Peacock J. A., Efstathiou G., Simulations of galaxy formation in a cosmological volume, *MNRAS*, 2001, vol. 326, p. 649
- Perea J., del Olmo A., Moles M., Mass estimation for systems of galaxies, *A&A*, 1990, vol. 237, p. 319
- Pérez-González P. G., Rieke G. H., Villar V., Barro G., Blaylock M., Egami E., Gallego J., Gil de Paz A., Pascual S., Zamorano J., Donley J. L., The Stellar Mass Assembly of Galaxies from $z = 0$ to $z = 4$: Analysis of a Sample Selected in the Rest-Frame Near-Infrared with Spitzer, *ApJ*, 2008, vol. 675, p. 234
- Pierce M. J., Tully R. B., Luminosity-line width relations and the extragalactic distance scale. I - Absolute calibration, *ApJ*, 1992, vol. 387, p. 47
- Plionis M., Basilakos S., Tovmassian H. M., The shape of poor groups of galaxies, *MNRAS*, 2004, vol. 352, p. 1323
- Pompéia L., Barbuy B., Grenon M., Detailed Analysis of Nearby Bulgelike Dwarf Stars. I. Stellar Parameters, Kinematics, and Oxygen Abundances, *ApJ*, 2002, vol. 566, p. 845

- Pompéia L., Barbuy B., Grenon M., Detailed Analysis of Nearby Bulgelike Dwarf Stars. III. α -Element and Heavy-Element Abundances, *ApJ*, 2003, vol. 592, p. 1173
- Pompéia L., Barbuy B., Grenon M., Gustafsson B., Chemical Abundances in Metal-Rich Bulge-like Stars. In *IAU Symposium*, vol. 241 of *IAU Symposium*, 2007, p. 78
- Popesso P., Biviano A., Böhringer H., Romaniello M., RASS-SDSS galaxy cluster survey. V. The X-ray-underluminous Abell clusters, *A&A*, 2007, vol. 461, p. 397
- Press W. H., Flannery B. P., Teukolsky S. A., *Numerical recipes. The art of scientific computing*, 1986
- Puech M., Hammer F., Flores H., Delgado-Serrano R., Rodrigues M., Yang Y., The baryonic content and Tully-Fisher relation at $z \sim 0.6$, *A&A*, 2010, vol. 510, p. A68
- Quinn P. J., Hernquist L., Fullagar D. P., Heating of galactic disks by mergers, *ApJ*, 1993, vol. 403, p. 74
- Raboud D., Grenon M., Martinet L., Fux R., Udry S., Evidence for a signature of the galactic bar in the solar neighbourhood, *A&A*, 1998, vol. 335, p. L61
- Rahimi A., Kawata D., Brook C. B., Gibson B. K., Chemodynamical analysis of bulge stars for simulated disc galaxies, *MNRAS*, 2010, vol. 401, p. 1826
- Ramella M., Geller M. J., Huchra J. P., Groups of galaxies in the Center for Astrophysics redshift survey, *ApJ*, 1989, vol. 344, p. 57
- Ramírez I., Allende Prieto C., Lambert D. L., Oxygen abundances in nearby stars. Clues to the formation and evolution of the Galactic disk, *A&A*, 2007, vol. 465, p. 271
- Ramírez I., Meléndez J., The Effective Temperature Scale of FGK Stars. I. Determination of Temperatures and Angular Diameters with the Infrared Flux Method, *ApJ*, 2005, vol. 626, p. 446
- Rauscher T., Heger A., Hoffman R. D., Woosley S. E., Nucleosynthesis in Massive Stars with Improved Nuclear and Stellar Physics, *ApJ*, 2002, vol. 576, p. 323

-
- Reddy B. E., Lambert D. L., Searching for the metal-weak thick disc in the solar neighbourhood, *MNRAS*, 2008, vol. 391, p. 95
- Reddy B. E., Lambert D. L., Allende Prieto C., Elemental abundance survey of the Galactic thick disc, *MNRAS*, 2006, vol. 367, p. 1329
- Reddy B. E., Tomkin J., Lambert D. L., Allende Prieto C., The chemical compositions of Galactic disc F and G dwarfs, *MNRAS*, 2003, vol. 340, p. 304
- Ribeiro A. L. B., Lopes P. A. A., Trevisan M., Segregation effects according to the evolutionary stage of galaxy groups, *MNRAS*, 2010, vol. 409, p. L124
- Ribeiro A. L. B., Trevisan M., Lopes P. A. A., Schilling A. C., Galaxy distribution and evolution around a sample of 2dF groups, *A&A*, 2009, vol. 505, p. 521
- Richstone D. O., Potter M. D., Galactic mass loss - A mild evolutionary correction to the angular size test, *ApJ*, 1982, vol. 254, p. 451
- Rines K., Diaferio A., CIRS: Cluster Infall Regions in the Sloan Digital Sky Survey. I. Infall Patterns and Mass Profiles, *AJ*, 2006, vol. 132, p. 1275
- Ripley B. D., , *Journal of the Royal Statistical Society*, 1977, vol. 39, p. 172
- Robin A. C., Reylé C., Derrière S., Picaud S., A synthetic view on structure and evolution of the Milky Way, *A&A*, 2003, vol. 409, p. 523
- Roškar R., Debattista V. P., Loebman S. R., Ž. Ivezić Quinn T. R., Implications of Radial Migration for Stellar Population Studies, *ArXiv e-prints*, 2011
- Roškar R., Debattista V. P., Quinn T. R., Wadsley J., Radial Migration in Disk Galaxies I: Transient Spiral Structure and Dynamics, *ArXiv e-prints*, 2011
- Ruchti G. R., Fulbright J. P., Wyse R. F. G., Gilmore G. F., Bienaymé O., et al. Origins of the Thick Disk as Traced by the Alpha Elements of Metal-poor Giant Stars Selected from Rave, *ApJL*, 2010, vol. 721, p. L92
- Sadakane K., Ohkubo M., Takeda Y., Sato B., Kambe E., Aoki W., Abundance Analyses of 12 Parent Stars of Extrasolar Planets Observed with the SUBARU/HDS, *PASJ*, 2002, vol. 54, p. 911

- Salpeter E. E., The Luminosity Function and Stellar Evolution., *ApJ*, 1955, vol. 121, p. 161
- Sánchez-Blázquez P., Peletier R. F., Jiménez-Vicente J., Cardiel N., Cenarro A. J., Falcón-Barroso J., Gorgas J., Selam S., Vazdekis A., Medium-resolution Isaac Newton Telescope library of empirical spectra, *MNRAS*, 2006, vol. 371, p. 703
- Santos N. C., Israelian G., Mayor M., Chemical analysis of 8 recently discovered extra-solar planet host stars, *A&A*, 2000, vol. 363, p. 228
- Santos N. C., Israelian G., Mayor M., The metal-rich nature of stars with planets, *A&A*, 2001, vol. 373, p. 1019
- Santos N. C., Israelian G., Mayor M., Spectroscopic [Fe/H] for 98 extra-solar planet-host stars. Exploring the probability of planet formation, *A&A*, 2004, vol. 415, p. 1153
- Santos N. C., Israelian G., Mayor M., Bento J. P., Almeida P. C., Sousa S. G., Ecuivillon A., Spectroscopic metallicities for planet-host stars: Extending the samples, *A&A*, 2005, vol. 437, p. 1127
- Santos N. C., Israelian G., Mayor M., Rebolo R., Udry S., Statistical properties of exoplanets. II. Metallicity, orbital parameters, and space velocities, *A&A*, 2003, vol. 398, p. 363
- Scalo J. M., The stellar initial mass function, *Fundamentals of Cosmic Physics*, 1986, vol. 11, p. 1
- Schmidt M., The Rate of Star Formation., *ApJ*, 1959, vol. 129, p. 243
- Schönrich R., Binney J., Chemical evolution with radial mixing, *MNRAS*, 2009a, vol. 396, p. 203
- Schönrich R., Binney J., Origin and structure of the Galactic disc(s), *MNRAS*, 2009b, vol. 399, p. 1145
- Schuster W. J., Nissen P. E., Uvby-beta photometry of high-velocity and metal-poor stars. II - Intrinsic color and metallicity calibrations, *A&A*, 1989, vol. 221, p. 65
- Sellwood J. A., Binney J. J., Radial mixing in galactic discs, *MNRAS*, 2002, vol. 336, p. 785

-
- Shen J., Rich R. M., Kormendy J., Howard C. D., De Propris R., Kunder A., Our Milky Way as a Pure-disk Galaxy: A Challenge for Galaxy Formation, *ApJL*, 2010, vol. 720, p. L72
- Silk J., Cosmic Black-Body Radiation and Galaxy Formation, *ApJ*, 1968, vol. 151, p. 459
- Silk J., Feedback in Galaxy Formation. In *IAU Symposium*, vol. 277 of *IAU Symposium*, 2011, p. 273
- Skrutskie M. F., Cutri R. M., Stiening R., Weinberg M. D., Schneider S., et al. The Two Micron All Sky Survey (2MASS), *AJ*, 2006, vol. 131, p. 1163
- Somerville R. S., Hopkins P. F., Cox T. J., Robertson B. E., Hernquist L., A semi-analytic model for the co-evolution of galaxies, black holes and active galactic nuclei, *MNRAS*, 2008, vol. 391, p. 481
- Soubiran C., Bienaymé O., Siebert A., Vertical distribution of Galactic disk stars. I. Kinematics and metallicity, *A&A*, 2003, vol. 398, p. 141
- Soubiran C., Girard P., Abundance trends in kinematical groups of the Milky Way's disk, *A&A*, 2005, vol. 438, p. 139
- Soubiran C., Le Campion J., Cayrel de Strobel G., Caillo A., The PASTEL catalogue of stellar parameters, *A&A*, 2010, vol. 515, p. A111+
- Sousa S. G., Santos N. C., Israelian G., Mayor M., Monteiro M. J. P. F. G., Spectroscopic parameters for a sample of metal-rich solar-type stars, *A&A*, 2006, vol. 458, p. 873
- Sousa S. G., Santos N. C., Israelian G., Mayor M., Monteiro M. J. P. F. G., A new code for automatic determination of equivalent widths: Automatic Routine for line Equivalent widths in stellar Spectra (ARES), *A&A*, 2007, vol. 469, p. 783
- Sousa S. G., Santos N. C., Mayor M., Udry S., Casagrande L., Israelian G., Pepe F., Queloz D., Monteiro M. J. P. F. G., Spectroscopic parameters for 451 stars in the HARPS GTO planet search program. Stellar [Fe/H] and the frequency of exo-Neptunes, *A&A*, 2008, vol. 487, p. 373

- Spiniello C., Koopmans L. V. E., Trager S. C., Czoske O., Treu T., The X-Shooter Lens Survey - I. Dark matter domination and a Salpeter-type initial mass function in a massive early-type galaxy, *MNRAS*, 2011, vol. 417, p. 3000
- Spite M., Étude de l'étoile χ Draconis, *Annales d'Astrophysique*, 1967, vol. 30, p. 211
- Spite M., Huille S., Spite F., Francois P., High resolution observations of stars in the peculiar globular cluster Omega CEN, *A&AS*, 1987, vol. 71, p. 591
- Spite M., Spite F., Barbuy B., Chemical evolution of the Magellanic Clouds. III - Oxygen and carbon abundances in a few F supergiants of the Small Cloud, *A&A*, 1989, vol. 222, p. 35
- Springel V., White S. D. M., Jenkins A., Frenk C. S., Yoshida N., Gao L., Navarro J., Thacker R., Croton D., Helly J., Peacock J. A., Cole S., Thomas P., Couchman H., Evrard A., Colberg J., Pearce F., Simulations of the formation, evolution and clustering of galaxies and quasars, *Nature*, 2005, vol. 435, p. 629
- Steidel C. C., Erb D. K., Shapley A. E., Pettini M., Reddy N., Bogosavljević M., Rudie G. C., Rakic O., The Structure and Kinematics of the Circumgalactic Medium from Far-ultraviolet Spectra of $z \sim 2-3$ Galaxies, *ApJ*, 2010, vol. 717, p. 289
- Stoyan D., Stoyan H., *Fractals, Random Shapes and Point Fields*. Chichester: John Wiley & Sons, 1994
- Strateva I., Ž. Ivezić Knapp G. R., Narayanan V. K., Strauss M. A., et al. Color Separation of Galaxy Types in the Sloan Digital Sky Survey Imaging Data, *AJ*, 2001, vol. 122, p. 1861
- Strauss M. A., Weinberg D. H., Lupton R. H., Narayanan V. K., Annis et al. Spectroscopic Target Selection in the Sloan Digital Sky Survey: The Main Galaxy Sample, *AJ*, 2002, vol. 124, p. 1810
- Tago E., Einasto J., Saar E., Einasto M., Suhhonenko I., Jõeveer M., Vennik J., Heinämäki P., Tucker D. L., Clusters and groups of galaxies in the 2dF galaxy redshift survey: A new catalogue, *Astronomische Nachrichten*, 2006, vol. 327, p. 365
- Takeda Y., Ohkubo M., Sato B., Kambe E., Sadakane K., Spectroscopic Study on the Atmospheric Parameters of Nearby F-K Dwarfs and Subgiants, *PASJ*, 2005, vol. 57, p. 27

-
- Thévenin F., Idiart T. P., Stellar Iron Abundances: Non-LTE Effects, *ApJ*, 1999, vol. 521, p. 753
- Thorén P., Feltzing S., Chemical abundances in cool metal rich disk dwarf stars, *A&A*, 2000, vol. 363, p. 692
- Torres G., Andersen J., Giménez A., Accurate masses and radii of normal stars: modern results and applications, *A&ARv*, 2010, vol. 18, p. 67
- Tovmassian H. M., Plionis M., The Relation Between Morphology and Dynamics of Poor Groups of Galaxies, *ApJ*, 2009, vol. 696, p. 1441
- Tremonti C. A., Heckman T. M., Kauffmann G., Brinchmann J., Charlot S., White S. D. M., Seibert M., Peng E. W., Schlegel D. J., Uomoto A., Fukugita M., Brinkmann J., The Origin of the Mass-Metallicity Relation: Insights from 53,000 Star-forming Galaxies in the Sloan Digital Sky Survey, *ApJ*, 2004, vol. 613, p. 898
- Trevisan M., Barbuy B., Eriksson K., Gustafsson B., Grenon M., Pompéia L., Analysis of old very metal rich stars in the solar neighbourhood: s- and r-process element abundances, 2012, in prep.
- Trevisan M., Ferreras I., de La Rosa I. G., La Barbera F., De Carvalho R. R., Constraints on feedback processes during the formation of early-type galaxies, 2012a, accepted for publication in *ApJL*
- Trevisan M., Ferreras I., de La Rosa I. G., La Barbera F., De Carvalho R. R., Stellar populations in dwarf elliptical galaxies, 2012b, in prep.
- Trujillo I., Conselice C. J., Bundy K., Cooper M. C., Eisenhardt P., Ellis R. S., Strong size evolution of the most massive galaxies since $z \sim 2$, *MNRAS*, 2007, vol. 382, p. 109
- Tully R. B., Fisher J. R., A new method of determining distances to galaxies, *A&A*, 1977, vol. 54, p. 661
- Valenti J. A., Fischer D. A., Spectroscopic Properties of Cool Stars (SPOCS). I. 1040 F, G, and K Dwarfs from Keck, Lick, and AAT Planet Search Programs, *ApJS*, 2005, vol. 159, p. 141

- van Dokkum P. G., Conroy C., Confirmation of Enhanced Dwarf-sensitive Absorption Features in the Spectra of Massive Elliptical Galaxies: Further Evidence for a Non-universal Initial Mass Function, *ApJL*, 2011, vol. 735, p. L13
- van Dokkum P. G., Franx M., Kriek M., Holden B., Illingworth G. D., Magee D., Bouwens R., Marchesini D., Quadri R., Rudnick G., Taylor E. N., Toft S., Confirmation of the Remarkable Compactness of Massive Quiescent Galaxies at $z \sim 2.3$: Early-Type Galaxies Did not Form in a Simple Monolithic Collapse, *ApJL*, 2008, vol. 677, p. L5
- Vazdekis A., Sánchez-Blázquez P., Falcón-Barroso J., Cenarro A. J., Beasley M. A., Cardiel N., Gorgas J., Peletier R. F., Evolutionary stellar population synthesis with MILES - I. The base models and a new line index system, *MNRAS*, 2010, vol. 404, p. 1639
- Villalobos Á., Kazantzidis S., Helmi A., Thick-disk Evolution Induced by the Growth of an Embedded Thin Disk, *ApJ*, 2010, vol. 718, p. 314
- Voit G. M., Tracing cosmic evolution with clusters of galaxies, *Reviews of Modern Physics*, 2005, vol. 77, p. 207
- Wadsley J. W., Stadel J., Quinn T., Gasoline: a flexible, parallel implementation of TreeSPH, *New Astronomy*, 2004, vol. 9, p. 137
- Wallace L., Hinkle K., Livingston W., An atlas of the spectrum of the solar photosphere from 13,500 to 28,000 cm^{-1} (3570 to 7405 Å), 1998
- Welch B. L., , *Biometrika*, 1947, vol. 34, p. 28
- White S. D. M., Rees M. J., Core condensation in heavy halos - A two-stage theory for galaxy formation and clustering, *MNRAS*, 1978, vol. 183, p. 341
- Wishart A. W., The bound-free photo-detachment cross-section of H-, *MNRAS*, 1979, vol. 187, p. 59P
- Yanny B., Newberg H. J., Grebel E. K., Kent S., Odenkirchen M., Rockosi C. M., Schlegel D., Subbarao M., Brinkmann J., Fukugita M., Ž. Ivezić Lamb D. Q., Schneider D. P., York D. G., A Low-Latitude Halo Stream around the Milky Way, *ApJ*, 2003, vol. 588, p. 824

-
- Yanny B., Rockosi C., Newberg H. J., Knapp G. R., Adelman-McCarthy J. K., Alcorn B., Allam S., Allende Prieto C., An D., Anderson K. S. J., Anderson S., Bailer-Jones C. A. L., Bastian S., et al. SEGUE: A Spectroscopic Survey of 240,000 Stars with $g = 14-20$, *AJ*, 2009, vol. 137, p. 4377
- Zoccali M., Hill V., Lecureur A., Barbuy B., Renzini A., Minniti D., Gómez A., Ortolani S., The metal content of bulge field stars from FLAMES-GIRAFFE spectra. I. Stellar parameters and iron abundances, *A&A*, 2008, vol. 486, p. 177
- Zoccali M., Lecureur A., Barbuy B., Hill V., Renzini A., Minniti D., Momany Y., Gómez A., Ortolani S., Oxygen abundances in the Galactic bulge: evidence for fast chemical enrichment, *A&A*, 2006, vol. 457, p. L1
- Zucker D. B., Belokurov V., Evans N. W., Kleyna J. T., Irwin M. J., Wilkinson M. I., Fellhauer M., Bramich D. M., et al. A Curious Milky Way Satellite in Ursa Major, *ApJ*, 2006, vol. 650, p. L41

Appendix

Appendix A

Code for χ^2 -minimization between observed and synthetic spectra

Stellar chemical abundances can be determined from spectral synthesis analysis. The method consists of finding the abundance that results in the synthetic spectra that best fits observed ones. Therefore, it is necessary should vary the abundance of the element, find the position of the local continuum, to convolve the synthetic spectrum with proper FWHM, etc. Thus, the whole process can be very time-consuming and error prone if the fit is done visually. In addition, the visual process is not an objective method, and it is more difficult to calculate the errors involved. For this reason, we developed a code in R¹ that performs the fit between observed and synthetic spectra automatically, by minimizing χ^2 . Figure A.1 shows the structure of the code.

To run the code, it is necessary:

- File containing a list of N_\star stars with their atmospheric parameters;
- solar spectrum and file with solar abundances (if the calibration of atomic parameters is required);
- line list with lines of N_{elem} elements;
- configuration file.

The code returns N_{elem} files, one for each element, and each one containing the abundances of the N_\star stars. The code was tested using the Solar spectrum. Figure A.2 and Table A.1 present some examples of best fits found by the code.

¹ <http://www.r-project.org/>

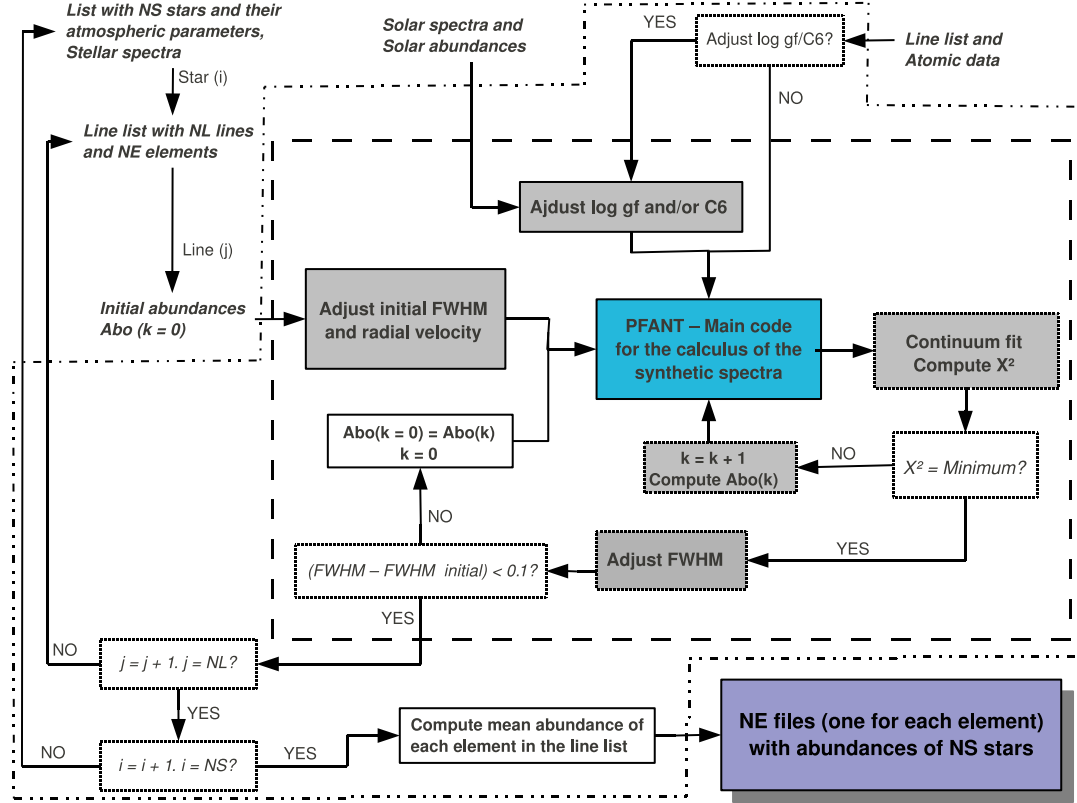


Figure A.1: Diagram presenting the structure of the code for χ^2 -minimization between observed and synthetic spectra. The objects outside the 2-dots-dashed line (— · —) correspond to the input and output.

Table A.1 - Solar abundances obtained with the code. Abundance = $\log(N_X/N_H) + 12$

	Cr I	Cr II	O	Na	Mg	Al	Ca
This code	5.68 ± 0.02	5.66 ± 0.03	$8.68 \pm \text{—}$	6.34 ± 0.03	7.59 ± 0.02	6.47 ± 0.01	6.35 ± 0.03
Grevesse & Sauval (1998)	5.67 ± 0.03	5.67 ± 0.03	8.87 ± 0.07	6.33 ± 0.03	7.58 ± 0.05	6.47 ± 0.07	6.36 ± 0.02

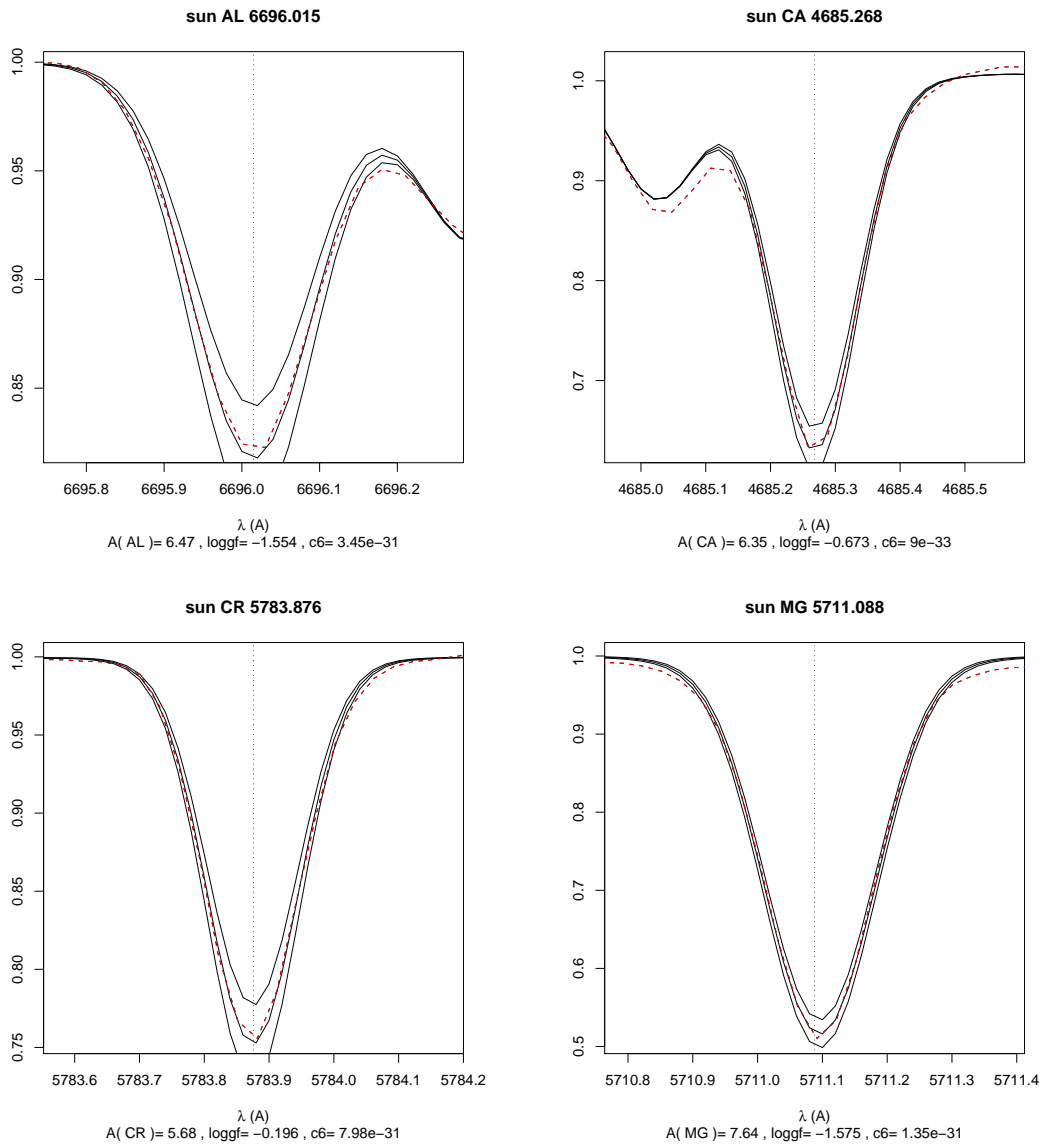


Figure A.2: Best fit between observed (dashed line) and synthetic spectra (solid line). Synthetic spectra shown were calculated with abundances A , $A + 0.1$ e $A - 0.1$.

Appendix B

Tables¹

Table B.1 - Log of spectroscopic observations.

star	α_{J2000} [h m s]	δ_{J2000} [d m s]	date	UT	exp [s]	Airmass	(S/N)
G 161-029	09:25:41.84	-06:46:05.80	2001 Jan 15	04:33:58	4500	1.15	57
BD-02 180	01:21:20.93	-01:43:45.62	2001 Jan 15	00:35:33	3600	1.54	64
BD-05 5798	22:20:19.62	-04:50:06.72	1999 Sep 27	04:54:58	2800	1.37	62
BD-17 6035	20:53:53.32	-16:45:54.98	1999 Sep 24	02:28:19	3600	1.14	65
CD-32 0327	00:15:14.75	-31:19:57.97	1999 Sep 26	06:50:42	3600	1.61	90
CD-40 15036	23:31:31.27	-39:22:33.17	1999 Sep 26	04:14:08	3600	1.15	122
HD 8389	01:03:02.64	-12:57:57.85	2001 Oct 03	05:56:58	1000	1.06	65
HD 9174	01:01:01.00	-19:36:16.21	2001 Oct 03	07:31:10	1800	1.20	86
HD 9424	01:22:22.17	-58:43:11.61	1999 Sep 23	07:28:18	2450	1.21	114
HD 10576	01:32:32.24	-69:59:13.08	1999 Sep 24	07:40:07	2500	1.38	149
HD 11608	01:31:31.44	-21:15:09.83	2001 Oct 04	06:49:09	3800	1.09	80
HD 12789	02:07:06.50	-46:22:29.05	2001 Oct 01	03:31:39	2400	1.16	145
HD 13386	02:08:08.04	-31:04:11.52	2001 Jan 18	01:44:42	2700	1.31	102
HD 15133	02:33:32.89	-28:59:15.63	2001 Jan 16	01:40:25	3000	1.22	79
HD 15555	02:34:34.02	-24:06:14.26	2001 Jan 14	00:36:22	600	1.04	49
HD 16905	02:03:03.19	-61:21:15.27	2001 Jan 18	02:45:49	3600	1.51	70
HD 25061	03:25:25.30	-52:55:51.12	2001 Jan 16	02:36:40	3600	1.20	112
HD 26151	04:21:20.72	-27:25:32.37	2001 Jan 17	02:41:23	2400	1.11	108
HD 26794	04:30:30.30	03:01:19.41	2001 Jan 19	03:23:04	1000	1.49	97
HD 27894	04:47:47.05	-59:24:39.01	2001 Jan 16	03:43:32	3600	1.34	80
HD 30295	04:20:19.98	-61:37:14.49	2001 Jan 17	02:53:03	3000	1.24	114

¹ Full Tables B.1 to B.8 are available at the CDS via anonymous ftp to [cdsarc.u-strasbg.fr](ftp://cdsarc.u-strasbg.fr) (130.79.128.5) or via <http://cdsarc.u-strasbg.fr/viz-bin/qcat?J/A+A/535/A42>

Table B.1 - continued.

star	α_{J2000} [h m s]	δ_{J2000} [d m s]	date	UT	exp [s]	Airmass	(S/N)
HD 31452	04:11:10.69	02:56:03.05	2001 Oct 05	08:32:57	1500	1.18	104
HD 31827	04:18:18.31	-51:02:51.05	2001 Jan 16	04:59:32	2400	1.38	99
HD 35854	05:15:14.74	-32:30:17.15	2001 Jan 17	05:06:33	2100	1.28	142
HD 37986	05:54:53.69	-15:37:49.95	2001 Jan 17	05:45:16	1800	1.50	114
HD 39213	05:16:16.48	-37:30:48.01	2001 Jan 14	01:00:01	2400	1.07	86
HD 39715	05:29:28.58	02:08:32.03	2001 Jan 17	03:57:13	3000	1.28	125
HD 43848	06:31:31.36	-40:31:54.69	2001 Jan 15	01:45:17	2400	4.53	78
HD 77338	09:12:12.49	-25:31:37.42	2001 Jan 15	03:59:10	1800	1.10	95
HD 81767	09:09:09.28	-16:39:43.13	2001 Jan 16	07:59:40	3000	1.15	84
HD 82943	09:51:50.74	-12:07:46.36	2001 Jan 17	07:51:11	480	1.11	185
HD 86065	09:43:42.52	-18:06:26.67	2001 Jan 18	06:11:52	3600	1.02	126
HD 86249	09:13:12.51	-40:47:13.04	2001 Jan 17	08:26:52	2400	1.11	102
HD 87007	10:59:58.59	-10:24:19.39	2001 Jan 19	03:50:51	2700	1.33	119
HD 90054	10:43:43.45	02:37:09.64	2000 Feb 15	06:32:34	720	1.24	106
HD 91585	10:57:57.12	-29:32:00.68	2001 Jan 19	04:44:44	3000	1.14	105
HD 91669	10:54:54.43	-13:47:16.61	2001 Jan 19	05:39:55	3600	1.09	80
HD 93800	10:32:31.69	-06:46:10.60	2001 Jan 19	06:49:50	2700	1.09	77
HD 94374	10:23:22.50	-14:22:28.20	2000 Feb 16	01:15:02	1500	2.14	79
HD 95338	10:26:26.30	-56:37:22.95	2000 Feb 16	03:55:18	2100	1.20	129
HD 104212	12:03:03.36	-46:47:03.09	2000 Feb 17	04:16:40	2400	1.18	163
HD 107509	12:44:44.47	-61:32:19.49	2000 Feb 16	05:43:18	1800	1.22	220
HD 120329	13:16:16.31	-57:15:43.13	2000 Feb 16	07:22:46	1800	1.16	123
HD 143102	16:13:12.76	-56:41:41.73	1999 Sep 23	23:25:27	1800	1.35	109
HD 148530	16:36:35.95	03:15:10.64	1999 Sep 24	00:21:06	2800	2.23	130
HD 149256	16:07:06.75	-36:03:41.99	1999 Sep 22	23:21:49	1800	1.17	92
HD 149606	16:36:36.12	-40:53:17.01	1999 Sep 26	00:33:59	2000	1.49	96
HD 149933	16:46:45.84	00:02:24.60	1999 Sep 25	00:32:24	900	2.06	70
HD 165920	18:18:17.68	-22:54:30.38	1999 Sep 27	01:16:19	2200	1.34	130
HD 168714	18:15:14.59	-55:03:20.60	1999 Sep 26	02:09:56	2000	1.32	96
HD 171999	18:59:58.82	-06:48:19.72	2001 Oct 03	00:38:02	1500	1.29	113
HD 177374	19:45:45.08	-07:27:21.67	2001 Oct 05	01:48:04	3000	1.63	94
HD 179764	19:12:12.08	-09:58:17.48	1999 Sep 23	01:26:26	2000	1.20	113
HD 180865	19:50:49.67	-66:09:07.03	1999 Sep 26	02:58:29	1800	1.51	118
HD 181234	19:00:00.10	-09:19:24.96	1999 Sep 23	02:15:11	1800	1.34	94

Table B.1 - continued.

star	α_{J2000} [h m s]	δ_{J2000} [d m s]	date	UT	exp [s]	Airmass	(S/N)
HD 181433	19:10:09.57	-66:28:07.67	1999 Sep 26	02:54:51	1600	1.21	49
HD 182572	19:58:58.20	11:56:39.90	1999 Sep 23	02:06:02	180	1.61	130
HD 196397	20:26:25.56	-11:52:15.79	1999 Sep 25	03:30:04	1800	1.16	83
HD 196794	20:22:22.05	10:04:32.64	1999 Sep 26	03:35:42	1300	1.79	117
HD 197921	20:10:10.20	-54:46:39.86	1999 Sep 27	04:05:12	2200	1.36	87
HD 201237	21:42:41.69	-19:59:41.40	1999 Sep 22	03:47:06	4400	1.26	93
HD 209721	22:23:22.51	-69:17:13.07	1999 Sep 27	07:01:14	2500	1.83	103
HD 211706	22:08:07.77	-07:18:48.93	1999 Sep 26	05:19:49	2700	1.22	128
HD 213996	22:06:05.67	11:52:53.06	1999 Sep 21	03:23:50	1200	1.33	89
HD 214463	22:48:47.97	-30:12:37.22	1999 Sep 27	06:10:57	2600	1.44	94
HD 218566	23:11:10.73	-02:15:38.67	1999 Sep 27	05:47:13	1100	1.39	92
HD 218750	23:02:01.53	-50:58:06.39	1999 Sep 23	05:17:07	1800	1.15	94
HD 221313	23:17:17.25	-33:04:34.60	1999 Sep 27	07:54:26	3000	1.82	85
HD 221974	23:46:45.78	-17:14:12.49	1999 Sep 21	03:57:29	2000	1.02	80
HD 224230	23:10:10.27	-72:00:07.85	1999 Sep 26	07:55:51	3600	2.36	98
HD 224383	23:34:33.52	-09:38:51.07	1999 Sep 24	06:48:44	2400	1.35	134

Table B.2 - Basic stellar data.

Star	T_{Gen} (K)	V	J	K_S	M_{Bol}	BC _V	π (mas)	d (pc)
G 161-029	4869	10.33	9.52 ± 0.02	8.90 ± 0.02	...	-0.41
BD-02 180	4917	10.09	8.44 ± 0.02	7.89 ± 0.02	5.59	-0.29	14.41 ± 1.62	69 ± 8
BD-05 5798	4875	10.38	8.64 ± 0.03	8.07 ± 0.04	5.68	-0.35	13.48 ± 1.94	74 ± 11
BD-17 6035	4830	10.30	8.53 ± 0.03	7.98 ± 0.02	5.71	-0.35	14.23 ± 2.41	70 ± 12
CD-32 0327	5001	10.41	8.75 ± 0.03	8.16 ± 0.03	5.88	-0.32	14.41 ± 1.77	69 ± 9
CD-40 15036	5341	10.08	8.69 ± 0.02	8.27 ± 0.02	5.08	-0.16	10.75 ± 1.70	93 ± 15
HD 8389	5135	7.85	6.39 ± 0.02	5.92 ± 0.02	5.27	-0.18	33.09 ± 0.99	30 ± 1
HD 9174	5459	8.40	7.13 ± 0.02	6.74 ± 0.03	4.03	-0.10	14.04 ± 1.13	71 ± 6
HD 9424	5332	9.17	7.81 ± 0.03	7.38 ± 0.02	5.17	-0.15	16.94 ± 0.99	59 ± 3
HD 10576	5883	8.51	7.41 ± 0.03	7.07 ± 0.03	3.77	-0.08	11.66 ± 0.73	86 ± 5
HD 11608	4917	9.31	7.61 ± 0.02	7.07 ± 0.03	5.91	-0.31	24.12 ± 1.34	41 ± 2
HD 12789	5706	8.89	7.74 ± 0.02	7.38 ± 0.02	4.00	-0.08	10.92 ± 1.00	92 ± 8
HD 13386	5131	8.91	7.39 ± 0.02	6.97 ± 0.02	5.46	-0.19	22.27 ± 1.09	45 ± 2
HD 15133	5113	9.36	7.85 ± 0.03	7.38 ± 0.02	5.33	-0.20	17.18 ± 1.38	58 ± 5
HD 15555	4793	7.34	5.60 ± 0.02	4.99 ± 0.02	3.42	-0.37	19.45 ± 1.06	51 ± 3
HD 16905	4821	9.44	7.65 ± 0.02	7.09 ± 0.02	6.06	-0.37	24.94 ± 0.93	40 ± 1
HD 25061	5247	9.27	7.84 ± 0.02	7.36 ± 0.02	5.35	-0.18	17.86 ± 0.82	56 ± 3
HD 26151	5285	8.49	7.08 ± 0.02	6.65 ± 0.03	5.02	-0.16	21.79 ± 1.12	46 ± 2
HD 26794	4932	8.78	7.07 ± 0.02	6.49 ± 0.02	5.83	-0.34	30.02 ± 1.68	33 ± 2
HD 27894	4879	9.36	7.64 ± 0.02	7.07 ± 0.03	5.89	-0.34	23.60 ± 0.91	42 ± 2
HD 30295	5350	8.86	7.49 ± 0.02	7.04 ± 0.02	4.88	-0.15	17.14 ± 0.77	58 ± 3
HD 31452	5206	8.43	6.94 ± 0.03	6.47 ± 0.02	5.26	-0.20	25.50 ± 1.27	39 ± 2
HD 31827	5463	8.26	7.00 ± 0.02	6.61 ± 0.02	4.56	-0.10	19.05 ± 0.69	52 ± 2
HD 35854	4943	7.70	6.01 ± 0.03	5.39 ± 0.02	6.08	-0.35	55.76 ± 0.76	18 ± 0
HD 37986	5455	7.36	6.06 ± 0.02	5.62 ± 0.02	5.02	-0.13	36.05 ± 0.92	28 ± 1
HD 39213	5337	8.96	7.61 ± 0.02	7.20 ± 0.02	4.82	-0.13	15.75 ± 0.91	63 ± 4
HD 39715	4781	8.84	6.99 ± 0.03	6.35 ± 0.02	6.28	-0.44	37.57 ± 1.26	27 ± 1
HD 43848	5091	8.65	7.12 ± 0.03	6.61 ± 0.02	5.58	-0.22	26.99 ± 0.83	37 ± 1
HD 77338	5283	8.63	7.22 ± 0.02	6.76 ± 0.02	5.39	-0.16	24.23 ± 1.18	41 ± 2
HD 81767	4943	9.45	7.77 ± 0.02	7.21 ± 0.02	5.74	-0.31	20.89 ± 1.49	48 ± 3
HD 82943	5849	6.54	5.51 ± 0.02	5.11 ± 0.02	4.28	-0.07	36.42 ± 0.84	27 ± 1
HD 86065	4963	9.36	7.65 ± 0.03	7.09 ± 0.02	6.14	-0.33	26.42 ± 1.25	38 ± 2
HD 86249	4935	8.99	7.32 ± 0.02	6.74 ± 0.02	6.02	-0.32	29.57 ± 1.16	34 ± 1
HD 87007	5302	8.82	7.35 ± 0.02	6.89 ± 0.04	5.46	-0.19	23.23 ± 1.41	43 ± 3
HD 90054	5986	7.87	6.85 ± 0.02	6.52 ± 0.02	3.63	-0.05	14.52 ± 0.97	69 ± 5
HD 91585	5077	9.43	7.90 ± 0.03	7.37 ± 0.03	5.66	-0.24	19.67 ± 1.33	51 ± 3
HD 91669	5175	9.70	8.26 ± 0.02	7.77 ± 0.02	4.95	-0.18	12.19 ± 1.52	82 ± 10
HD 93800	5129	9.12	7.58 ± 0.02	7.10 ± 0.02	5.32	-0.22	19.18 ± 1.42	52 ± 4
HD 94374	4825	9.27	7.42 ± 0.02	6.79 ± 0.02	6.13	-0.43	28.70 ± 1.29	35 ± 2
HD 95338	5144	8.62	7.10 ± 0.02	6.59 ± 0.02	5.56	-0.23	27.14 ± 0.91	37 ± 1
HD 104212	5694	8.38	7.24 ± 0.02	6.88 ± 0.03	3.62	-0.08	11.59 ± 1.09	86 ± 8
HD 107509	5944	7.91	6.90 ± 0.02	6.58 ± 0.03	3.68	-0.06	14.65 ± 0.82	68 ± 4
HD 120329	5511	8.34	7.09 ± 0.02	6.69 ± 0.02	4.00	-0.11	14.24 ± 1.05	70 ± 5
HD 143102	5432	7.88	6.59 ± 0.02	6.17 ± 0.02	3.51	-0.12	14.13 ± 0.99	71 ± 5

Table B.2 - continued.

Star	T_{Gen} (K)	V	J	K_S	M_{Bol}	BC_V	π (mas)	d (pc)
HD 148530	5346	8.81	7.42 ± 0.03	6.97 ± 0.02	5.31	-0.17	21.50 ± 1.27	47 ± 3
HD 149256	5271	8.42	7.04 ± 0.02	6.60 ± 0.02	3.89	-0.15	13.32 ± 1.21	75 ± 7
HD 149606	4936	8.95	7.25 ± 0.02	6.72 ± 0.02	6.09	-0.31	30.89 ± 1.37	32 ± 1
HD 149933	5424	8.05	6.72 ± 0.02	6.29 ± 0.03	5.03	-0.14	26.56 ± 1.22	38 ± 2
HD 165920	5261	7.91	6.50 ± 0.03	6.03 ± 0.02	5.22	-0.17	31.27 ± 1.12	32 ± 1
HD 168714	5552	8.90	7.67 ± 0.02	7.31 ± 0.02	4.33	-0.09	12.67 ± 1.51	79 ± 9
HD 171999	5257	8.34	6.89 ± 0.02	6.43 ± 0.02	5.31	-0.18	26.97 ± 1.12	37 ± 2
HD 177374	5011	9.40	7.75 ± 0.03	7.24 ± 0.02	5.44	-0.28	18.35 ± 1.65	54 ± 5
HD 179764	5374	9.01	7.58 ± 0.02	7.11 ± 0.02	4.84	-0.19	15.98 ± 1.30	63 ± 5
HD 180865	5132	8.97	7.45 ± 0.02	6.98 ± 0.02	5.54	-0.21	22.66 ± 1.32	44 ± 3
HD 181234	5220	8.59	7.15 ± 0.03	6.69 ± 0.02	4.97	-0.17	20.49 ± 1.19	49 ± 3
HD 181433	4866	8.40	6.66 ± 0.02	6.09 ± 0.02	5.97	-0.35	38.24 ± 1.15	26 ± 1
HD 182572	5461	5.17	3.55 ± 0.21	3.04 ± 0.32	4.01	-0.26	66.01 ± 0.77	15 ± 1
HD 196397	5267	8.95	7.59 ± 0.02	7.13 ± 0.03	5.20	-0.15	19.01 ± 1.65	53 ± 5
HD 196794	5075	8.52	6.94 ± 0.03	6.41 ± 0.02	5.99	-0.26	35.22 ± 1.14	28 ± 1
HD 197921	4866	9.25	7.49 ± 0.02	6.90 ± 0.02	5.82	-0.37	24.45 ± 1.58	41 ± 3
HD 201237	4886	10.10	8.31 ± 0.02	7.71 ± 0.02	4.97	-0.39	11.23 ± 2.09	89 ± 17
HD 209721	5388	9.51	8.18 ± 0.02	7.77 ± 0.02	4.59	-0.13	11.00 ± 1.26	91 ± 10
HD 211706	5830	8.90	7.84 ± 0.02	7.52 ± 0.02	4.19	-0.07	11.78 ± 1.40	85 ± 10
HD 213996	5203	8.66	7.21 ± 0.03	6.76 ± 0.03	5.30	-0.18	23.10 ± 1.14	43 ± 2
HD 214463	4958	9.67	8.10 ± 0.02	7.59 ± 0.02	5.29	-0.24	14.90 ± 1.77	67 ± 8
HD 218566	4834	8.59	6.82 ± 0.02	6.22 ± 0.02	5.83	-0.38	33.40 ± 1.19	30 ± 1
HD 218750	5122	9.25	7.71 ± 0.02	7.18 ± 0.03	5.34	-0.24	18.45 ± 1.50	54 ± 4
HD 221313	5075	9.90	8.38 ± 0.02	7.85 ± 0.02	5.16	-0.23	12.52 ± 1.79	80 ± 11
HD 221974	5109	9.31	7.80 ± 0.02	7.32 ± 0.02	5.68	-0.20	20.61 ± 1.53	49 ± 4
HD 224230	4900	9.97	8.24 ± 0.03	7.63 ± 0.03	6.16	-0.36	20.43 ± 1.22	49 ± 3
HD 224383	5689	7.89	6.74 ± 0.03	6.33 ± 0.02	4.40	-0.10	20.98 ± 1.24	48 ± 3

Table B.3 - Kinematical data.

star	U	V	W	v_{Helio}	R_{min}	R_{max}	Z_{max}	e	P_{thin}	P_{thick}
	(km s ⁻¹)			(km s ⁻¹)	(kpc)	(kpc)	(kpc)		(%)	(%)
Thin disk										
HD 11608	-37	-37	21	-25.34 ± 0.16	5.58 ± 0.32	9.05 ± 0.52	0.17 ± 0.03	0.24 ± 0.01	84	16
HD 26151	-50	-19	12	-6.87 ± 0.11	6.20 ± 0.36	9.68 ± 0.58	0.07 ± 0.02	0.22 ± 0.01	95	5
HD 26794	71	13	3	56.49 ± 0.17	7.39 ± 0.41	11.14 ± 0.67	0.06 ± 0.03	0.20 ± 0.01	95	5
HD 35854	5	-31	4	23.05 ± 0.23	6.18 ± 0.38	8.55 ± 0.51	0.04 ± 0.02	0.16 ± 0.01	92	8
HD 77338	-39	-27	-25	8.47 ± 0.11	6.05 ± 0.37	9.25 ± 0.56	0.46 ± 0.06	0.21 ± 0.01	84	16
HD 82943	-10	-20	-9	8.25 ± 0.13	6.71 ± 0.41	8.64 ± 0.50	0.19 ± 0.04	0.13 ± 0.01	95	5
HD 86249	12	8	-24	-7.84 ± 0.09	8.51 ± 0.49	8.99 ± 0.58	0.43 ± 0.06	0.03 ± 0.01	96	4
HD 93800	49	-8	-13	3.81 ± 0.11	7.13 ± 0.42	9.33 ± 0.55	0.26 ± 0.04	0.13 ± 0.01	94	6
HD 177374	-91	-15	-20	79.97 ± 0.14	5.78 ± 0.34	11.40 ± 0.72	0.42 ± 0.05	0.33 ± 0.01	82	18
HD 181433	-56	-1	8	60.69 ± 0.17	6.79 ± 0.38	10.47 ± 0.63	0.03 ± 0.02	0.21 ± 0.01	97	3
HD 224230	-78	-16	-6	59.61 ± 0.06	5.88 ± 0.35	10.80 ± 0.67	0.18 ± 0.04	0.29 ± 0.01	92	8
Thick disk										
G 161-029	-149	-89	40	23.00 ± 0.16	0	97
BD-02 180	-1	-82	-46	16.32 ± 0.19	3.82 ± 0.22	8.56 ± 0.48	0.92 ± 0.11	0.38 ± 0.01	0	99
BD-05 5798	15	-54	-53	6.51 ± 0.10	5.14 ± 0.30	8.49 ± 0.47	1.10 ± 0.13	0.25 ± 0.01	4	96
BD-17 6035	35	-83	11	-65.48 ± 0.08	3.62 ± 0.22	8.55 ± 0.51	0.06 ± 0.02	0.40 ± 0.01	1	99
CD-32 0327	52	-69	-10	14.50 ± 0.10	4.17 ± 0.25	8.79 ± 0.54	0.22 ± 0.04	0.36 ± 0.01	5	95
CD-40 15036	88	-80	-9	-12.58 ± 0.06	3.58 ± 0.22	9.36 ± 0.57	0.23 ± 0.04	0.45 ± 0.01	0	99
HD 9424	57	-96	-1	43.61 ± 0.18	3.09 ± 0.17	8.75 ± 0.50	0.11 ± 0.03	0.48 ± 0.01	0	99
HD 10576	56	-93	-19	54.86 ± 0.06	3.23 ± 0.20	8.73 ± 0.51	0.33 ± 0.05	0.46 ± 0.01	0	99
HD 13386	17	-68	-13	32.39 ± 0.10	4.33 ± 0.24	8.57 ± 0.49	0.25 ± 0.04	0.33 ± 0.01	10	90
HD 15133	45	-75	-8	38.43 ± 0.13	3.96 ± 0.23	8.72 ± 0.50	0.19 ± 0.03	0.38 ± 0.01	3	97
HD 15555	74	-56	0	36.18 ± 0.12	4.61 ± 0.25	9.30 ± 0.51	0.10 ± 0.03	0.34 ± 0.01	18	82
HD 16905	-31	-59	-31	64.77 ± 0.14	4.66 ± 0.28	8.82 ± 0.51	0.58 ± 0.07	0.31 ± 0.01	13	87
HD 25061	88	-51	-7	47.55 ± 0.13	4.71 ± 0.27	9.64 ± 0.59	0.19 ± 0.04	0.34 ± 0.01	17	83
HD 27894	63	-73	-41	82.85 ± 0.14	4.05 ± 0.25	8.94 ± 0.54	0.82 ± 0.10	0.38 ± 0.01	0	99
HD 31827	-17	-69	9	44.75 ± 0.28	4.21 ± 0.25	8.63 ± 0.53	0.04 ± 0.01	0.34 ± 0.01	13	86
HD 39213	10	-70	27	49.57 ± 0.09	4.23 ± 0.25	8.51 ± 0.50	0.25 ± 0.04	0.34 ± 0.01	8	92
HD 81767	50	-77	-2	81.81 ± 0.14	3.85 ± 0.22	8.74 ± 0.49	0.11 ± 0.03	0.39 ± 0.01	2	98
HD 90054	5	-99	-17	48.93 ± 0.36	3.06 ± 0.19	8.52 ± 0.50	0.31 ± 0.05	0.47 ± 0.01	0	99
HD 94374	38	-108	-16	75.05 ± 0.17	2.71 ± 0.17	8.59 ± 0.51	0.29 ± 0.05	0.52 ± 0.01	0	99
HD 95338	24	-111	-44	97.05 ± 0.08	2.68 ± 0.17	8.55 ± 0.50	0.88 ± 0.08	0.52 ± 0.01	0	98
HD 104212	30	-96	-32	66.04 ± 0.12	3.18 ± 0.19	8.51 ± 0.49	0.60 ± 0.07	0.46 ± 0.01	0	99
HD 107509	33	-100	-24	70.43 ± 0.13	3.01 ± 0.18	8.56 ± 0.51	0.44 ± 0.06	0.48 ± 0.01	0	99
HD 120329	71	-103	-78	24.85 ± 0.05	3.04 ± 0.19	8.95 ± 0.53	2.02 ± 0.19	0.49 ± 0.01	0	92
HD 143102	53	-92	-20	7.95 ± 0.02	3.26 ± 0.21	8.68 ± 0.53	0.34 ± 0.06	0.45 ± 0.01	0	99
HD 148530	-81	-80	-34	25.77 ± 0.22	3.56 ± 0.20	9.71 ± 0.56	0.68 ± 0.09	0.46 ± 0.01	0	99
HD 149256	-7	-98	-48	25.42 ± 0.08	3.13 ± 0.20	8.46 ± 0.50	0.95 ± 0.12	0.46 ± 0.01	0	99
HD 149606	28	-77	4	-2.27 ± 0.22	3.88 ± 0.23	8.53 ± 0.50	0.04 ± 0.02	0.37 ± 0.01	3	97

Table B.3 - continued.

star	U	V	W	v_{Helio}	R_{min}	R_{max}	Z_{max}	e	P_{thin}	P_{thick}
	(km s ⁻¹)			(km s ⁻¹)	(kpc)	(kpc)	(kpc)		(%)	(%)
HD 149933	22	-63	-9	-13.95 ± 0.06	4.50 ± 0.25	8.49 ± 0.47	0.20 ± 0.03	0.31 ± 0.01	19	81
HD 165920	-66	-49	-42	61.25 ± 0.12	4.86 ± 0.31	9.64 ± 0.60	0.87 ± 0.11	0.33 ± 0.01	11	89
HD 168714	60	-74	17	-9.76 ± 0.26	3.91 ± 0.22	8.82 ± 0.51	0.12 ± 0.03	0.39 ± 0.01	2	97
HD 171999	13	-87	-11	-46.32 ± 0.28	3.49 ± 0.21	8.49 ± 0.49	0.22 ± 0.04	0.42 ± 0.01	1	99
HD 179764	21	-106	6	-66.04 ± 0.17	2.76 ± 0.17	8.46 ± 0.49	0.03 ± 0.02	0.51 ± 0.01	0	99
HD 180865	27	-72	-14	18.41 ± 0.15	4.11 ± 0.23	8.52 ± 0.49	0.26 ± 0.04	0.35 ± 0.01	5	95
HD 181234	5	-92	2	-46.33 ± 0.14	3.28 ± 0.20	8.44 ± 0.51	0.06 ± 0.02	0.44 ± 0.01	0	99
HD 196397	-1	-69	16	-16.94 ± 0.07	4.24 ± 0.24	8.50 ± 0.50	0.11 ± 0.03	0.33 ± 0.01	13	87
HD 201237	-86	-79	-1	30.57 ± 0.34	3.51 ± 0.21	9.74 ± 0.60	0.13 ± 0.03	0.47 ± 0.01	1	99
HD 209721	14	-76	31	7.53 ± 0.11	3.93 ± 0.23	8.43 ± 0.50	0.30 ± 0.04	0.36 ± 0.01	3	97
HD 211706	80	-106	-13	-62.79 ± 0.06	2.68 ± 0.16	9.08 ± 0.53	0.27 ± 0.04	0.54 ± 0.01	0	98
HD 218566	77	-61	-8	-37.21 ± 0.25	4.37 ± 0.25	9.28 ± 0.54	0.19 ± 0.04	0.36 ± 0.01	8	92
HD 218750	-25	-74	13	17.13 ± 0.10	3.98 ± 0.23	8.69 ± 0.51	0.08 ± 0.02	0.37 ± 0.01	6	94
HD 221313	5	-65	-47	41.60 ± 0.21	4.56 ± 0.30	8.48 ± 0.53	0.94 ± 0.12	0.30 ± 0.01	2	98
HD 221974	95	-48	-3	-25.65 ± 0.17	4.74 ± 0.29	9.91 ± 0.62	0.14 ± 0.03	0.35 ± 0.01	19	81
HD 224383	74	-84	-1	-30.47 ± 0.10	3.46 ± 0.20	9.03 ± 0.54	0.11 ± 0.03	0.45 ± 0.01	0	99
Intermediate sample										
HD 8389	45	-28	-25	35.87 ± 0.08	6.19 ± 0.34	8.90 ± 0.51	0.45 ± 0.06	0.18 ± 0.01	76	24
HD 9174	-22	-56	-29	24.51 ± 0.05	4.85 ± 0.31	8.71 ± 0.54	0.54 ± 0.07	0.28 ± 0.01	21	78
HD 12789	74	-35	-12	26.83 ± 0.20	5.52 ± 0.34	9.50 ± 0.61	0.27 ± 0.04	0.26 ± 0.01	60	40
HD 30295	65	-30	-39	46.49 ± 0.11	5.93 ± 0.34	9.35 ± 0.55	0.77 ± 0.09	0.22 ± 0.01	37	63
HD 31452	-6	-62	-10	14.69 ± 0.03	4.57 ± 0.27	8.58 ± 0.48	0.21 ± 0.04	0.31 ± 0.01	25	75
HD 37986	28	-59	1	59.45 ± 0.28	4.70 ± 0.28	8.60 ± 0.51	0.07 ± 0.03	0.29 ± 0.01	32	68
HD 39715	-74	-50	-21	-33.66 ± 0.17	4.71 ± 0.29	9.89 ± 0.62	0.41 ± 0.06	0.35 ± 0.01	29	71
HD 43848	53	-58	1	44.92 ± 0.12	4.66 ± 0.27	8.85 ± 0.52	0.07 ± 0.03	0.31 ± 0.01	24	76
HD 86065	69	-44	2	55.30 ± 0.12	5.18 ± 0.29	9.27 ± 0.52	0.07 ± 0.03	0.28 ± 0.01	51	49
HD 87007	40	-47	-13	30.30 ± 0.09	5.22 ± 0.30	8.66 ± 0.50	0.25 ± 0.04	0.25 ± 0.01	53	47
HD 91585	100	-41	5	44.48 ± 0.12	5.00 ± 0.29	10.20 ± 0.63	0.04 ± 0.02	0.34 ± 0.01	30	70
HD 91669	-76	-18	-28	-12.40 ± 0.12	5.88 ± 0.34	10.81 ± 0.67	0.57 ± 0.08	0.29 ± 0.01	79	21
HD 182572	116	-31	-19	-99.86 ± 0.09	5.15 ± 0.30	11.08 ± 0.69	0.38 ± 0.04	0.37 ± 0.01	21	79
HD 196794	57	-37	-14	-52.78 ± 0.07	5.58 ± 0.33	9.06 ± 0.54	0.28 ± 0.04	0.24 ± 0.01	66	34
HD 197921	64	-42	3	-38.57 ± 0.13	5.29 ± 0.31	9.16 ± 0.55	0.06 ± 0.02	0.27 ± 0.01	60	40
HD 213996	-90	-38	5	-17.99 ± 0.12	4.99 ± 0.28	10.62 ± 0.63	0.05 ± 0.02	0.36 ± 0.01	65	35
HD 214463	10	-56	-17	3.26 ± 0.25	4.87 ± 0.29	8.49 ± 0.50	0.31 ± 0.04	0.27 ± 0.01	34	66

Table B.4 - Selected data from the PASTEL catalogue.

Star	T_{eff}	$\log g$	[Fe/H]	Reference
HD 8389	5283 ± 64	4.37 ± 0.12	0.34 ± 0.05	Sousa et al. (2008)
	5378 ± 84	4.50 ± 0.12	0.47 ± 0.08	Sousa et al. (2006)
HD 9424	5420 ± 43	Masana et al. (2006)
HD 10576	5882 ± 56	Masana et al. (2006)
HD 13386	5226 ± 56	4.28 ± 0.09	0.26 ± 0.06	Sousa et al. (2006)
	5361 ± 43	Masana et al. (2006)
HD 15555	4820 ± 43	González Hernández & Bonifacio (2009)
	4855 ± 53	Ramírez & Meléndez (2005)
	4855 ± 67	Alonso et al. (1999)
HD 25061	5321 ± 39	Masana et al. (2006)
HD 26151	5348 ± 44	4.47 ± 0.06	0.26 ± 0.03	Valenti & Fischer (2005)
	5353 ± 45	Masana et al. (2006)
	5388 ± 56	4.31 ± 0.08	0.28 ± 0.07	Sousa et al. (2006)
HD 26794	4909 ± 44	4.74 ± 0.06	0.10 ± 0.03	Valenti & Fischer (2005)
	$4950 \pm \dots$...	0.04 ± 0.10	Favata et al. (1997)
HD 27894	4875 ± 81	4.22 ± 0.26	0.30 ± 0.07	Santos et al. (2005)
	4952 ± 105	4.39 ± 0.20	0.20 ± 0.08	Sousa et al. (2008)
HD 30295	5291 ± 76	4.08 ± 0.21	0.15 ± 0.07	Bond et al. (2006)
	5417 ± 44	4.50 ± 0.06	0.28 ± 0.03	Valenti & Fischer (2005)
	5421 ± 42	Masana et al. (2006)
HD 31452	5262 ± 39	Masana et al. (2006)
HD 31827	5402 ± 59	3.84 ± 0.20	0.20 ± 0.08	Bond et al. (2006)
	5614 ± 44	4.39 ± 0.06	0.41 ± 0.03	Valenti & Fischer (2005)
HD 35854	4886 ± 34	Masana et al. (2006)
	4928 ± 56	4.46 ± 0.11	-0.13 ± 0.03	Sousa et al. (2008)
	4948 ± 44	4.61 ± 0.06	-0.04 ± 0.03	Valenti & Fischer (2005)
HD 37986	$5455 \pm \dots$	$4.40 \pm \dots$	0.27 ± 0.02	Feltzing & Gustafsson (1998)
	5507 ± 38	4.29 ± 0.06	0.26 ± 0.03	Sousa et al. (2008)
	5586 ± 42	4.38 ± 0.05	0.35 ± 0.05	Sousa et al. (2006)
HD 39213	5288 ± 59	4.00 ± 0.21	0.20 ± 0.07	Bond et al. (2006)
	5457 ± 44	4.36 ± 0.06	0.36 ± 0.03	Valenti & Fischer (2005)
HD 39715	4798 ± 44	4.75 ± 0.06	-0.04 ± 0.03	Valenti & Fischer (2005)
	4834 ± 51	González Hernández & Bonifacio (2009)
HD 77338	$5290 \pm \dots$	$4.60 \pm \dots$	$0.30 \pm \dots$	Thorén & Feltzing (2000)
	$5290 \pm \dots$	$4.90 \pm \dots$	0.22 ± 0.02	Feltzing & Gustafsson (1998)

Table B.4 - continued.

Star	T_{eff}	$\log g$	[Fe/H]	Reference
HD 82943	5900 ± 50	4.40 ± 0.05	0.24 ± 0.04	Heiter & Luck (2003)
	5914 ± ...	4.34 ± ...	0.24 ± ...	Sadakane et al. (2002)
	5927 ± 100	4.36 ± 0.10	0.23 ± 0.04	Luck & Heiter (2006)
	5939 ± 51	Masana et al. (2006)
	5952 ± 71	Ramírez & Meléndez (2005)
	5989 ± 20	4.43 ± 0.02	0.26 ± 0.01	Sousa et al. (2008)
	5997 ± 44	4.42 ± 0.06	0.27 ± 0.03	Valenti & Fischer (2005)
	6002 ± 15	4.42 ± 0.04	0.27 ± 0.02	Takeda et al. (2005)
	6005 ± 41	4.45 ± 0.13	0.32 ± 0.05	Santos et al. (2004)
	6008 ± 34	4.43 ± 0.06	0.26 ± 0.03	Laws et al. (2003)
	6010 ± 50	4.62 ± 0.20	0.32 ± 0.06	Santos et al. (2000)
	6025 ± 40	4.54 ± 0.10	0.33 ± 0.06	Santos et al. (2001)
	6025 ± 50	4.54 ± 0.15	0.32 ± 0.06	Santos et al. (2003)
	6028 ± 19	4.46 ± 0.02	0.29 ± 0.02	Santos et al. (2004)
HD 86065	5026 ± 60	4.50 ± 0.12	-0.06 ± 0.03	Sousa et al. (2008)
HD 86249	4961 ± 34	Masana et al. (2006)
HD 87007	5242 ± 61	González Hernández & Bonifacio (2009)
	5263 ± 70	Masana et al. (2006)
	5300 ± ...	4.40 ± ...	0.27 ± ...	Thorén & Feltzing (2000)
	5300 ± ...	4.70 ± ...	0.27 ± 0.02	Feltzing & Gustafsson (1998)
HD 90054	6080 ± 55	Masana et al. (2006)
HD 104212	5996 ± 52	Masana et al. (2006)
HD 107509	6069 ± 58	Masana et al. (2006)
HD 120329	5636 ± 49	Masana et al. (2006)
HD 148530	5402 ± 44	Masana et al. (2006)
HD 149933	5735 ± 49	Masana et al. (2006)
HD 165920	5339 ± 55	4.39 ± 0.08	0.29 ± 0.04	Sousa et al. (2008)
	5346 ± 48	4.36 ± 0.07	0.31 ± 0.05	Sousa et al. (2006)
HD 171999	5249 ± ...	4.65 ± ...	0.40 ± 0.02	Feltzing & Gustafsson (1998)
	5327 ± 34	Masana et al. (2006)
HD 180865	5255 ± 42	Masana et al. (2006)
HD 181234	5262 ± 67	Ramírez & Meléndez (2005)
	5354 ± 44	4.47 ± 0.06	0.36 ± 0.03	Valenti & Fischer (2005)
	5476 ± 44	Masana et al. (2006)
	5530 ± 60	González Hernández & Bonifacio (2009)

Table B.4 - continued.

Star	T_{eff}	$\log g$	[Fe/H]	Reference
HD 181433	4954 ± 34	Masana et al. (2006)
	4962 ± 134	4.37 ± 0.26	0.33 ± 0.13	Sousa et al. (2008)
HD 182572	5109 ± 478	González Hernández & Bonifacio (2009)
	$5380 \pm \dots$	$3.92 \pm \dots$	$0.15 \pm \dots$	McWilliam (1990)
	$5400 \pm \dots$	$4.00 \pm \dots$	$0.35 \pm \dots$	Feltzing & González (2001)
	5469 ± 69	Ramírez & Meléndez (2005)
	5528 ± 28	Blackwell & Lynas-Gray (1998)
	$5561 \pm \dots$	di Benedetto (1998)
	5566 ± 20	4.11 ± 0.06	0.33 ± 0.03	Takeda et al. (2005)
	$5600 \pm \dots$	$4.13 \pm \dots$	$0.37 \pm \dots$	Bensby et al. (2005)
	5610 ± 80	4.19 ± 0.10	0.37 ± 0.07	Fuhrmann (2000)
	5619 ± 8	$4.00 \pm \dots$	$0.38 \pm \dots$	Mishenina et al. (2008)
	5656 ± 44	4.32 ± 0.06	0.40 ± 0.03	Valenti & Fischer (2005)
	5730 ± 100	4.24 ± 0.10	0.44 ± 0.10	Luck & Heiter (2006)
	$5730 \pm \dots$	$4.43 \pm \dots$	0.42 ± 0.02	Feltzing & Gustafsson (1998)
	5750 ± 50	4.35 ± 0.05	0.45 ± 0.08	Heiter & Luck (2003)
HD 197921	4948 ± 33	Masana et al. (2006)
HD 211706	6023 ± 61	Masana et al. (2006)
HD 218566	4927 ± 44	4.81 ± 0.06	0.38 ± 0.03	Valenti & Fischer (2005)
HD 218750	5227 ± 39	Masana et al. (2006)
HD 224383	$5729 \pm \dots$	$4.40 \pm \dots$	-0.07 ± 0.03	Ramírez et al. (2007)
	5751 ± 48	Masana et al. (2006)
	5754 ± 44	4.31 ± 0.06	-0.04 ± 0.03	Valenti & Fischer (2005)

Table B.5 - Si, Ca, and Ti line list.

Species	λ (Å)	χ_{exc} (eV)	$\log gf$ (Sun)	$\log gf$ (BFL04)	$\log gf$ (NIST)	$\log gf$ (VALD)	$\log gf$ (BZO+09)
Si I	5665.56	4.92	-2.01	-1.94	-2.04	-1.75	...
Si I	5684.48	4.95	-1.63	-1.55	-1.42	-1.73	...
Si I	5690.43	4.93	-1.81	-1.77	-1.87	-1.77	...
Si I	5701.10	4.93	-2.00	-1.95	-2.05	-1.58	...
Si I	5708.40	4.95	-1.40	...	-1.47	-1.03	...
Si I	5772.15	5.08	-1.65	-1.65	-1.75	-1.36	...
Si I	5793.07	4.93	-1.96	-1.96	-2.02	-2.48	...
Si I	5797.86	4.95	-1.94	-1.95	-2.05	-3.54	...
Si I	5948.54	5.08	-1.27	-1.13	-1.23	-0.78	...
Si I	6125.02	5.61	-1.49	-1.52	...	-1.46	...
Si I	6142.48	5.61	-1.43	-1.50	...	-1.30	-1.50
Si I	6145.02	5.61	-1.37	-1.45	...	-1.31	-1.45
Si I	6155.13	5.61	-0.73	-0.72	...	-0.75	-0.85
Si I	6237.32	5.61	-0.99	-1.05	...	-0.98	-1.01
Si I	6243.82	5.61	-1.22	-1.29	...	-1.24	-1.30
Si I	6244.47	5.61	-1.26	-1.32	...	-1.09	...
Si I	6414.99	5.87	-0.92	-1.04	-1.13
Si I	6721.84	5.86	-1.11	...	-0.94	-1.52	-1.17
Si I	6741.63	5.98	-1.58	-1.65	...	-1.43	...
Si I	7405.77	5.61	-0.45	-0.72	...	-0.31	...
Si I	7415.95	5.61	-0.50	-0.76	...	-0.39	...
Si I	7423.50	5.61	-0.39	-0.65	...	-0.18	...
Ca I	4578.55	2.52	-0.76	-0.92	-0.56	-0.70	...
Ca I	4685.27	2.93	-0.88	-0.93	-0.88	-0.88	...
Ca I	5260.39	2.52	-2.00	-1.78	-1.90	-1.72	...
Ca I	5261.70	2.52	-0.55	-0.45	-0.73	-0.58	...
Ca I	5349.47	2.70	-0.50	-0.64	...	-0.31	...
Ca I	5512.98	2.93	-0.26	-0.56	-0.30	-0.46	...
Ca I	5581.97	2.52	-0.35	-0.52	-0.71	-0.56	...
Ca I	5590.11	2.52	-0.52	-0.52	-0.71	-0.57	...
Ca I	5867.56	2.93	-1.60	-1.60	...	-1.57	...
Ca I	6102.73	1.88	-0.55	-0.65	-0.79	-0.79	...
Ca I	6122.22	1.88	-0.06	-0.37	-0.32	-0.32	...

Notes. BFL04: Bensby et al. (2004); BZO+09: Barbuy et al. (2009).

Table B.5 - continued.

Species	λ (Å)	χ_{exc} (eV)	$\log gf$ (Sun)	$\log gf$ (BFL04)	$\log gf$ (NIST)	$\log gf$ (VALD)	$\log gf$ (BZO+09)
Ca I	6161.30	2.52	-1.33	-1.26	-1.03	-1.27	-1.02
Ca I	6166.44	2.52	-1.07	-1.17	-0.90	-1.14	-0.90
Ca I	6169.04	2.52	-0.64	-0.84	-0.54	-0.80	-0.54
Ca I	6169.56	2.52	-0.27	-0.62	-0.27	-0.48	-0.27
Ca I	6717.70	2.71	-0.32	-0.44	-0.61	-0.52	...
Ti I	5662.16	2.32	-0.12	...	-0.11	0.01	...
Ti I	5689.49	2.30	-0.51	...	-0.47	-0.36	...
Ti I	5766.33	3.29	+0.31	0.39	...
Ti I	5866.45	1.07	-0.88	-0.78	-0.84	-0.84	...
Ti I	5922.11	1.05	-1.49	...	-1.47	-1.47	...
Ti I	5937.81	1.07	-1.92	...	-1.89	-1.89	...
Ti I	5941.75	1.05	-1.45	...	-1.52	-1.51	...
Ti I	5953.16	1.89	-0.24	...	-0.33	-0.33	...
Ti I	5965.83	1.88	-0.44	...	-0.41	-0.41	...
Ti I	5978.54	1.87	-0.58	...	-0.50	-0.50	...
Ti I	6064.63	1.05	-1.89	...	-1.94	-1.94	...
Ti I	6091.17	2.27	-0.54	...	-0.42	-0.42	...
Ti I	6126.22	1.07	-1.46	-1.37	-1.42	-1.43	-1.43
Ti I	6258.10	1.44	-0.46	-0.30	-0.36	-0.36	-0.36
Ti I	6261.10	1.43	-0.53	-0.42	-0.48	-0.48	-0.48
Ti I	6303.76	1.44	-1.73	-1.51	-1.57	-1.57	-1.57
Ti I	6312.22	1.46	-1.63	...	-1.55	-1.55	...
Ti I	6554.24	1.44	-1.28	...	-1.22	-1.22	-1.22
Ti I	6556.08	1.46	-1.16	...	-1.08	-1.07	-1.07
Ti I	6743.12	0.90	-1.70	-1.63	-1.63	-1.63	-1.73

Notes. BFL04: Bensby et al. (2004); BZO+09: Barbuy et al. (2009).

Table B.6 - Fe I and Fe II line list.

Ion	λ (Å)	χ_{ex} (eV)	C6	log gf (Sun)	log gf (VALD)	log gf (FW06)	log gf (MAGY09)
Fe I	5522.45	4.21	3.0200e-31	-1.49	-1.55	-1.52	...
Fe I	5546.51	4.37	3.9100e-31	-1.18	-1.31	-1.28	...
Fe I	5560.21	4.43	4.7900e-31	-1.14	-1.19	-1.16	...
Fe I	5577.02	5.03	1.0000e-32	-1.61	-1.55
Fe I	5618.63	4.21	2.9000e-31	-1.39	-1.28	-1.28	...
Fe I	5619.61	4.39	3.7100e-31	-1.51	-1.70	-1.67	...
Fe I	5635.83	4.26	5.2400e-31	-1.65	-1.89	-1.86	...
Fe I	5638.26	4.22	2.8800e-31	-0.83	-0.87	-0.84	-0.84
Fe I	5651.48	4.47	4.8300e-31	-1.86	-2.00	...	-1.75
Fe I	5652.33	4.26	3.1200e-31	-1.81	-1.95	-1.92	...
Fe I	5661.35	4.28	3.2400e-31	-1.91	-1.74	-1.76	-1.76
Fe I	5662.52	4.18	3.0000e-31	-0.65	-0.57	-0.57	-0.57
Fe I	5679.02	4.65	8.1300e-31	-0.84	-0.92	-0.90	-0.75
Fe I	5701.55	2.56	4.9500e-32	-2.22	-2.22	-2.22	-2.22
Fe I	5705.47	4.30	3.0200e-31	-1.52	-1.35	-1.36	-1.35
Fe I	5741.85	4.26	2.8300e-31	-1.71	-1.85	-1.67	...
Fe I	5753.13	4.26	2.9900e-31	-0.77	-0.69	-0.69	...
Fe I	5775.08	4.22	2.5000e-31	-1.16	-1.30	-1.30	...
Fe I	5778.46	2.59	4.9500e-32	-3.57	-3.43	-3.43	...
Fe I	5809.22	3.88	5.6500e-31	-1.73	-1.84	-1.79	-1.71
Fe I	5849.69	3.69	5.5900e-32	-3.14	-2.99
Fe I	5852.22	4.55	4.8000e-31	-1.24	-1.33	-1.30	...
Fe I	5855.08	4.61	5.7400e-31	-1.60	-1.48	-1.48	-1.48
Fe I	5858.78	4.22	3.4600e-31	-2.17	-2.26
Fe I	5861.11	4.28	4.2600e-31	-2.51	-2.45
Fe I	5905.67	4.65	6.2300e-31	-0.87	-0.73	-0.77	-0.77
Fe I	5934.65	3.93	5.6900e-31	-1.26	-1.17	-1.12	-1.12
Fe I	5956.69	0.86	1.5500e-32	-4.59	-4.61	-4.61	-4.61
Fe I	6027.05	4.08	1.5000e-31	-1.23	-1.09	-1.09	-1.09
Fe I	6054.07	4.37	2.8300e-31	-2.31
Fe I	6079.01	4.65	5.1300e-31	-1.06	-1.12	-1.10	...
Fe I	6082.71	2.22	3.2700e-32	-3.61	-3.57	-3.57	...

Notes. FW06: Fuhr & Wiese (2006); MAGY09: Meléndez et al. (2009);
MB09: Meléndez & Barbuy (2009)

Table B.6 - continued.

Ion	λ (Å)	χ_{ex} (eV)	C6	log gf (Sun)	log gf (VALD)	log gf (FW06)	log gf (MAGY09)
(1)	(2)	(3)	(4)	(5)	(6)	(7)	(8)
Fe I	6093.64	4.61	4.4100e-31	-1.39	-1.50	-1.47	-1.30
Fe I	6127.90	4.14	1.5000e-31	-1.43	-1.40	-1.40	...
Fe I	6151.62	2.18	2.5500e-32	-3.36	-3.30	-3.30	-3.30
Fe I	6157.73	4.07	1.5000e-31	-1.38	-1.26	-1.22	...
Fe I	6159.38	4.61	4.0900e-31	-1.99	-1.97
Fe I	6165.37	4.14	1.5700e-31	-1.55	-1.47	-1.47	-1.46
Fe I	6170.51	4.79	7.2600e-31	-0.46	-0.44	...	-0.29
Fe I	6173.34	2.22	2.6500e-32	-2.90	...	-2.88	-2.88
Fe I	6180.20	2.73	4.1100e-32	-2.62	-2.59	-2.65	...
Fe I	6187.99	3.94	4.9000e-31	-1.73	-1.72	-1.67	...
Fe I	6200.31	2.61	4.5800e-32	-2.43	-2.44	-2.44	-2.44
Fe I	6213.43	2.22	2.6200e-32	-2.64	-2.48	-2.48	-2.52
Fe I	6219.28	2.20	2.5800e-32	-2.51	-2.43	-2.43	...
Fe I	6220.78	3.88	4.1500e-31	-2.38	-2.46
Fe I	6226.74	3.88	4.1500e-31	-2.16	-2.22
Fe I	6229.23	2.84	4.5800e-32	-2.92	-2.81	-2.81	...
Fe I	6240.65	2.22	3.1400e-32	-3.36	-3.23	-3.17	-3.23
Fe I	6265.13	2.18	2.4800e-32	-2.56	-2.55	-2.55	-2.55
Fe I	6270.23	2.86	4.5800e-32	-2.63	-2.46	-2.61	-2.54
Fe I	6297.79	2.22	2.5800e-32	-2.83	-2.74	-2.74	...
Fe I	6311.50	2.83	4.3900e-32	-3.09	-3.14	-3.14	...
Fe I	6315.81	4.07	9.4300e-32	-1.73	-1.71	-1.66	...
Fe I	6322.69	2.59	4.4200e-32	-2.37	-2.43	-2.43	...
Fe I	6380.74	4.19	1.5000e-31	-1.38	-1.38	-1.38	...
Fe I	6392.54	2.28	3.3800e-32	-4.06	-4.03
Fe I	6419.95	4.73	4.6600e-31	-0.38	...	-0.27	-0.27
Fe I	6436.41	4.19	9.4300e-32	-2.38	-2.46
Fe I	6481.87	2.28	3.3300e-32	-2.98	-2.98	-2.98	...
Fe I	6518.37	2.83	4.1400e-32	-2.58	-2.46	-2.30	...
Fe I	6569.22	4.73	4.0300e-31	-0.61	-0.42	-0.45	...
Fe I	6574.23	0.99	3.0000e-32	-4.99	-5.02	-5.00	...

Notes. FW06: Fuhr & Wiese (2006); MAGY09: Meléndez et al. (2009);
MB09: Meléndez & Barbuy (2009)

Table B.6 - continued.

Ion	λ (Å)	χ_{ex} (eV)	C6	log gf (Sun)	log gf (VALD)	log gf (FW06)	log gf (MAGY09)
(1)	(2)	(3)	(4)	(5)	(6)	(7)	(8)
Fe I	6593.87	2.43	3.6900e-32	-2.44	-2.42	-2.42	...
Fe I	6597.56	4.79	4.7600e-31	-1.01	-1.07	-1.05	...
Fe I	6608.02	2.28	3.2700e-32	-4.03	-4.03
Fe I	6625.02	1.01	9.4300e-32	-5.31	-5.35	-5.34	...
Fe I	6627.54	4.55	3.1200e-31	-1.53	-1.68
Fe I	6633.75	4.56	4.5400e-31	-0.80	-0.80	-0.80	...
Fe I	6634.11	4.79	4.6000e-31	-1.08
Fe I	6646.93	2.61	4.2300e-32	-4.05	-3.99
Fe I	6653.85	4.14	5.6900e-31	-2.52
Fe I	6696.32	2.68	4.9000e-31	-3.73
Fe I	6699.14	4.59	3.0400e-32	-2.15	-2.10	-2.10	...
Fe I	6703.57	2.76	3.6600e-32	-3.06	-3.16	-3.06	-3.02
Fe I	6704.48	4.22	3.0000e-32	-2.60	-2.66
Fe I	6710.32	1.48	2.0100e-32	-4.90	-4.88
Fe I	6713.77	4.79	4.3000e-31	-1.49	-1.60	...	-1.40
Fe I	6716.24	4.58	2.4800e-32	-1.78	-1.92
Fe I	6725.35	4.10	4.8200e-31	-2.29	-2.30
Fe I	6726.67	4.61	4.5000e-31	-1.09	-1.13	...	-1.03
Fe I	6733.15	4.64	3.4100e-31	-1.47	-1.58
Fe I	6739.52	1.56	2.1000e-32	-4.96	-4.79	-4.79	...
Fe I	6745.10	4.58	2.1000e-32	-2.16	-2.16
Fe I	6745.96	4.07	9.4300e-32	-2.80	-2.77
Fe I	6750.15	2.42	4.1100e-32	-2.68	-2.62	-2.62	-2.62
Fe I	6752.71	4.64	3.3700e-31	-1.29	-1.20	-1.20	...
Fe I	6786.86	4.19	5.7400e-31	-1.98	-2.07	-2.02	...
Fe I	6793.27	4.07	3.0000e-31	-2.40	-2.33	-2.33	...
Fe I	6804.00	4.65	3.5300e-31	-1.52	-1.50	-1.50	...
Fe I	6804.27	4.58	2.4600e-32	-1.87	-1.81	-1.81	...
Fe I	6806.85	2.73	3.4600e-32	-3.15	-3.21	-2.13	...
Fe I	6810.26	4.61	4.5000e-31	-1.09	-0.99	-0.99	-0.99
Fe I	6820.37	4.64	4.8800e-31	-1.19	-1.32	-1.29	...

Notes. FW06: Fuhr & Wiese (2006); MAGY09: Meléndez et al. (2009);
MB09: Meléndez & Barbuy (2009)

Table B.6 - continued.

Ion	λ (Å)	χ_{ex} (eV)	C6	$\log gf$ (Sun)	$\log gf$ (VALD)	$\log gf$ (FW06)	$\log gf$ (MAGY09)
(1)	(2)	(3)	(4)	(5)	(6)	(7)	(8)
Fe I	6828.59	4.64	3.2700e-31	-0.92	-0.92	-0.89	...
Fe I	6842.69	4.64	4.8000e-31	-1.23	-1.32	-1.29	...
Fe I	6843.66	4.55	2.9400e-31	-0.87	-0.93	-0.89	...
Fe II	5991.38	3.15	7.7500e-33	-3.63	-3.65	-3.65	-3.54
Fe II	6084.11	3.20	7.8700e-33	-3.90	-3.88	-3.88	-3.79
Fe II	6113.33	3.22	7.8700e-33	-4.22	-4.23	-4.23	-4.14
Fe II	6149.26	3.89	3.4000e-33	-2.77	-2.84	-2.84	-2.69
Fe II	6247.56	3.89	9.4300e-33	-2.39	-2.44	-2.43	-2.30
Fe II	6369.46	2.89	7.4200e-33	-4.17	-4.23	-3.47	-4.11
Fe II	6432.68	2.89	7.4200e-33	-3.60	...	-3.50	-3.57
Fe II	6456.38	3.90	9.3000e-33	-2.17	-2.19	-2.19	-2.05
Fe II	6516.08	2.89	7.4200e-33	-3.33	-3.43	-3.37	-3.31

Notes. FW06: Fuhr & Wiese (2006); MAGY09: Meléndez et al. (2009);
MB09: Meléndez & Barbuy (2009)

Table B.7 - Photometric and adopted spectroscopic stellar parameters.

Star	T_{eff}	$\log g$	ξ	[Fe I/H] _{Gen}	[Fe I/H]	[Fe II/H]	Mass	Age
	K	dex	km s ⁻¹	dex	dex	dex	(M_{\odot})	(Gyr)
(1)	(2)	(3)	(4)	(5)	(6)	(7)		
Thin disk								
HD 11608	4966 ± 47	4.57 ± 0.06	0.30 ± 0.31	0.60	0.39 ± 0.05	0.42 ± 0.13	0.88 ± 0.06	5.6 ± 2.9
HD 26151	5383 ± 47	4.41 ± 0.05	0.67 ± 0.03	0.42	0.33 ± 0.05	0.34 ± 0.08	0.97 ± 0.07	8.2 ± 2.4
HD 26794	4920 ± 52	4.49 ± 0.06	0.30 ± 0.12	0.30	0.07 ± 0.04	0.10 ± 0.12	0.78 ± 0.05	11.8 ± 2.2
HD 35854	4901 ± 37	4.57 ± 0.03	0.30 ± 0.09	0.33	-0.04 ± 0.03	-0.00 ± 0.12	0.76 ± 0.05	9.0 ± 0.8
HD 77338	5346 ± 42	4.55 ± 0.05	0.44 ± 0.08	0.43	0.41 ± 0.05	0.49 ± 0.08	0.98 ± 0.07	2.0 ± 1.2
HD 82943	5929 ± 45	4.35 ± 0.04	1.22 ± 0.03	0.34	0.23 ± 0.05	0.26 ± 0.07	1.14 ± 0.08	3.0 ± 0.7
HD 86249	4957 ± 42	4.59 ± 0.05	0.30 ± 0.11	0.32	0.12 ± 0.04	0.20 ± 0.10	0.82 ± 0.06	7.3 ± 2.1
HD 93800	5181 ± 43	4.44 ± 0.07	0.30 ± 0.09	0.43	0.49 ± 0.04	0.57 ± 0.09	0.92 ± 0.07	8.8 ± 3.5
HD 177374	5044 ± 45	4.38 ± 0.08	0.30 ± 0.10	0.40	-0.08 ± 0.04	0.12 ± 0.10	0.79 ± 0.05	13.7 ± 1.0
HD 181433	4902 ± 41	4.57 ± 0.04	0.30 ± 0.21	0.65	0.41 ± 0.04	0.52 ± 0.12	0.86 ± 0.06	6.7 ± 1.8
HD 224230	4873 ± 54	4.58 ± 0.06	0.30 ± 0.17	0.34	-0.08 ± 0.04	0.11 ± 0.13	0.75 ± 0.05	9.4 ± 2.4
Thick disk								
G 161-029	4798 ± 34	4.60 ^a ± 0.04	0.30 ± 0.63	0.42	0.01 ± 0.09	0.12 ± 0.13
BD-02 180	5004 ± 57	4.46 ± 0.10	0.30 ± 0.17	0.45	0.33 ± 0.04	0.45 ± 0.08	0.86 ± 0.06	10.3 ± 4.0
BD-05 5798	4902 ± 65	4.44 ± 0.13	0.64 ± 0.05	0.57	0.20 ± 0.05	0.27 ± 0.13	0.82 ± 0.06	11.4 ± 3.7
BD-17 6035	4892 ± 73	4.43 ± 0.15	0.85 ± 0.03	0.60	0.09 ± 0.05	0.17 ± 0.14	0.79 ± 0.06	11.5 ± 3.2
CD-32 0327	4957 ± 66	4.52 ± 0.11	0.34 ± 0.06	0.49	-0.01 ± 0.06	0.19 ± 0.10	0.79 ± 0.05	10.3 ± 3.5
CD-40 15036	5429 ± 66	4.41 ± 0.14	0.58 ± 0.04	0.07	-0.03 ± 0.07	-0.03 ± 0.09	0.89 ± 0.07	9.8 ± 4.6
HD 9424	5449 ± 48	4.48 ± 0.06	0.66 ± 0.03	0.12	0.12 ± 0.06	0.10 ± 0.08	0.95 ± 0.07	6.1 ± 3.2
HD 10576	5929 ± 67	4.14 ± 0.06	1.36 ± 0.06	0.11	0.02 ± 0.07	0.02 ± 0.08	1.12 ± 0.08	5.8 ± 0.9
HD 13386	5269 ± 43	4.54 ± 0.05	0.46 ± 0.04	0.35	0.36 ± 0.05	0.34 ± 0.09	0.96 ± 0.07	3.6 ± 2.4
HD 15133	5223 ± 46	4.47 ± 0.08	0.30 ± 0.05	0.52	0.46 ± 0.04	0.51 ± 0.09	0.94 ± 0.07	6.9 ± 3.7
HD 15555	4867 ± 40	3.69 ± 0.06	1.04 ± 0.03	0.32	0.37 ± 0.05	0.38 ± 0.11	1.22 ± 0.10	6.3 ± 0.9
HD 16905	4866 ± 42	4.58 ± 0.05	0.30 ± 0.14	0.53	0.27 ± 0.04	0.44 ± 0.12	0.83 ± 0.06	7.4 ± 1.8
HD 25061	5307 ± 49	4.49 ± 0.05	0.77 ± 0.03	0.40	0.18 ± 0.05	0.19 ± 0.09	0.92 ± 0.06	6.7 ± 3.3
HD 27894	4920 ± 45	4.54 ± 0.05	0.30 ± 0.12	0.50	0.37 ± 0.04	0.51 ± 0.10	0.86 ± 0.06	7.7 ± 2.3
HD 31827	5608 ± 49	4.35 ± 0.04	0.82 ± 0.03	0.40	0.48 ± 0.05	0.49 ± 0.08	1.08 ± 0.07	4.8 ± 0.9
HD 39213	5473 ± 48	4.38 ± 0.06	0.74 ± 0.04	0.39	0.45 ± 0.06	0.44 ± 0.08	1.02 ± 0.07	6.3 ± 2.0
HD 81767	4966 ± 52	4.49 ± 0.07	0.30 ± 0.11	0.49	0.22 ± 0.05	0.25 ± 0.13	0.83 ± 0.05	10.4 ± 3.0
HD 90054	6047 ± 52	4.18 ± 0.06	1.52 ± 0.05	0.39	0.29 ± 0.06	0.33 ± 0.07	1.28 ± 0.08	3.2 ± 0.4
HD 94374	5000 ± 38	4.63 ± 0.05	0.30 ± 0.08	0.28	-0.10 ± 0.03	-0.18 ± 0.13	0.79 ± 0.05	4.8 ± 2.4
HD 95338	5175 ± 42	4.52 ± 0.04	0.43 ± 0.05	0.34	0.21 ± 0.04	0.22 ± 0.09	0.90 ± 0.06	6.3 ± 2.6
HD 104212	5833 ± 53	4.07 ± 0.09	1.21 ± 0.03	0.09	0.13 ± 0.06	0.07 ± 0.07	1.14 ± 0.08	5.9 ± 0.8
HD 107509	6102 ± 60	4.18 ± 0.06	1.80 ± 0.06	0.08	0.03 ± 0.06	-0.06 ± 0.08	1.21 ± 0.09	3.9 ± 0.5
HD 120329	5617 ± 48	4.14 ± 0.07	1.22 ± 0.02	0.27	0.31 ± 0.06	0.39 ± 0.07	1.11 ± 0.08	7.3 ± 1.0
HD 143102	5547 ± 48	3.94 ± 0.07	1.13 ± 0.03	0.01	0.16 ± 0.06	0.21 ± 0.08	1.16 ± 0.08	6.8 ± 1.0
HD 148530	5392 ± 53	4.49 ± 0.06	0.72 ± 0.04	0.11	0.03 ± 0.06	0.02 ± 0.09	0.90 ± 0.08	7.1 ± 3.6
HD 149256	5406 ± 47	4.01 ± 0.08	1.15 ± 0.02	0.27	0.34 ± 0.06	0.38 ± 0.08	1.08 ± 0.08	8.9 ± 1.5

Notes. ^(a) Spectroscopic gravity. Other $\log g$ s were derived using HIPPARCOS parallaxes.

Table B.7 - continued.

Star	T_{eff}	$\log g$	ξ	$[\text{Fe I}/\text{H}]_{\text{Gen}}$	$[\text{Fe I}/\text{H}]$	$[\text{Fe II}/\text{H}]$	Mass	Age
	K	dex	km s^{-1}	dex	dex	dex	(M_{\odot})	(Gyr)
(1)	(2)	(3)	(4)	(5)	(6)	(7)		
HD 149606	4976 ± 50	4.63 ± 0.05	0.30 ± 0.08	0.35	0.20 ± 0.05	0.41 ± 0.11	0.85 ± 0.10	4.1 ± 2.6
HD 149933	5486 ± 49	4.44 ± 0.05	1.11 ± 0.02	0.31	0.13 ± 0.06	0.17 ± 0.08	0.95 ± 0.06	7.2 ± 2.9
HD 165920	5336 ± 44	4.47 ± 0.04	0.64 ± 0.03	0.40	0.36 ± 0.05	0.40 ± 0.08	0.97 ± 0.07	5.2 ± 2.5
HD 168714	5686 ± 48	4.30 ± 0.11	0.79 ± 0.03	0.47	0.48 ± 0.06	0.47 ± 0.08	1.12 ± 0.07	4.0 ± 1.1
HD 171999	5304 ± 45	4.49 ± 0.05	0.58 ± 0.03	0.33	0.29 ± 0.05	0.35 ± 0.08	0.96 ± 0.09	6.0 ± 2.8
HD 179764	5323 ± 48	4.28 ± 0.08	0.92 ± 0.04	0.16	-0.05 ± 0.05	0.03 ± 0.09	0.85 ± 0.06	14.6 ± 0.6
HD 180865	5218 ± 44	4.53 ± 0.06	0.48 ± 0.06	0.31	0.21 ± 0.05	0.27 ± 0.09	0.91 ± 0.06	5.9 ± 3.1
HD 181234	5311 ± 45	4.37 ± 0.06	0.30 ± 0.07	0.30	0.45 ± 0.04	0.52 ± 0.09	0.96 ± 0.06	9.4 ± 2.2
HD 196397	5404 ± 54	4.49 ± 0.08	0.55 ± 0.07	0.36	0.38 ± 0.06	0.43 ± 0.09	0.99 ± 0.07	3.7 ± 2.8
HD 201237	4829 ± 82	4.14 ± 0.16	0.50 ± 0.05	0.50	0.00 ± 0.04	-0.06 ± 0.18	0.77 ± 0.05	13.8 ± 0.9
HD 209721	5503 ± 51	4.30 ± 0.10	1.05 ± 0.03	0.35	0.28 ± 0.05	0.23 ± 0.08	1.00 ± 0.08	8.8 ± 2.1
HD 211706	6017 ± 69	4.33 ± 0.11	1.44 ± 0.08	0.09	0.09 ± 0.07	0.07 ± 0.08	1.14 ± 0.08	3.0 ± 1.5
HD 218566	4849 ± 42	4.48 ± 0.04	0.30 ± 0.68	0.46	0.28 ± 0.14	0.43 ± 0.22	0.81 ± 0.06	11.5 ± 1.9
HD 218750	5134 ± 49	4.41 ± 0.08	0.37 ± 0.08	0.31	0.17 ± 0.05	0.23 ± 0.09	0.85 ± 0.06	12.8 ± 2.4
HD 221313	5153 ± 55	4.36 ± 0.13	0.62 ± 0.04	0.50	0.31 ± 0.05	0.34 ± 0.10	0.90 ± 0.06	12.0 ± 3.6
HD 221974	5213 ± 52	4.60 ± 0.07	0.30 ± 0.11	0.49	0.46 ± 0.05	0.56 ± 0.11	0.95 ± 0.07	2.2 ± 1.8
HD 224383	5760 ± 53	4.28 ± 0.06	1.16 ± 0.09	0.00	-0.10 ± 0.06	-0.15 ± 0.08	0.98 ± 0.07	9.0 ± 1.3
Intermediate population								
HD 8389	5274 ± 42	4.47 ± 0.04	0.33 ± 0.12	0.47	0.58 ± 0.04	0.58 ± 0.08	0.96 ± 0.07	5.4 ± 1.8
HD 9174	5599 ± 55	4.15 ± 0.08	0.95 ± 0.02	0.36	0.41 ± 0.07	0.35 ± 0.08	1.13 ± 0.08	6.7 ± 1.0
HD 12789	5810 ± 47	4.21 ± 0.09	1.15 ± 0.03	0.31	0.27 ± 0.06	0.36 ± 0.07	1.17 ± 0.08	4.9 ± 0.9
HD 30295	5406 ± 45	4.36 ± 0.05	0.72 ± 0.03	0.41	0.32 ± 0.05	0.33 ± 0.08	0.97 ± 0.07	9.1 ± 1.8
HD 31452	5250 ± 45	4.44 ± 0.05	0.61 ± 0.05	0.30	0.23 ± 0.05	0.19 ± 0.09	0.90 ± 0.06	10.0 ± 3.1
HD 37986	5503 ± 44	4.47 ± 0.04	0.95 ± 0.02	0.47	0.30 ± 0.05	0.33 ± 0.08	1.02 ± 0.07	4.0 ± 1.6
HD 39715	4741 ± 63	4.57 ± 0.04	0.30 ± 0.15	0.33	-0.10 ± 0.03	0.07 ± 0.15	0.72 ± 0.05	9.6 ± 1.6
HD 43848	5161 ± 41	4.54 ± 0.04	0.30 ± 0.08	0.52	0.43 ± 0.04	0.46 ± 0.09	0.94 ± 0.06	3.7 ± 1.7
HD 86065	4938 ± 48	4.62 ± 0.05	0.30 ± 0.10	0.36	0.09 ± 0.04	0.21 ± 0.12	0.82 ± 0.06	6.0 ± 2.6
HD 87007	5282 ± 59	4.54 ± 0.06	0.61 ± 0.04	0.44	0.29 ± 0.06	0.45 ± 0.09	0.95 ± 0.06	4.0 ± 2.9
HD 91585	5144 ± 50	4.55 ± 0.07	0.48 ± 0.07	0.30	0.25 ± 0.05	0.33 ± 0.10	0.91 ± 0.09	5.4 ± 3.5
HD 91669	5278 ± 57	4.34 ± 0.11	0.64 ± 0.04	0.42	0.44 ± 0.05	0.45 ± 0.09	0.95 ± 0.06	10.1 ± 3.4
HD 182572	5700 ± 32	4.18 ± 0.03	1.00 ± 0.02	0.31	0.48 ± 0.04	0.39 ± 0.07	1.16 ± 0.07	4.5 ± 0.2
HD 196794	5094 ± 44	4.64 ± 0.04	0.30 ± 0.05	0.33	0.06 ± 0.05	0.16 ± 0.09	0.84 ± 0.06	3.7 ± 2.0
HD 197921	4866 ± 45	4.48 ± 0.06	0.30 ± 0.15	0.39	0.22 ± 0.04	0.33 ± 0.10	0.80 ± 0.05	11.3 ± 2.4
HD 213996	5314 ± 53	4.49 ± 0.05	0.75 ± 0.04	0.43	0.33 ± 0.05	0.35 ± 0.10	0.96 ± 0.09	5.1 ± 3.0
HD 214463	5122 ± 47	4.40 ± 0.11	0.80 ± 0.04	0.33	0.34 ± 0.05	0.30 ± 0.09	0.90 ± 0.06	11.8 ± 3.7

Notes. ^(a) Spectroscopic gravity. Other $\log g$ s were derived using HIPPARCOS parallaxes.

Table B.8 - Final abundances of C, Ni, O and Mg.

Star	[C/H]	[C/Fe]	[Ni/H]	[Ni/Fe]	[O/H]	[O/Fe]	[Mg/H]	[Mg/Fe]
Thin disk								
HD 11608	0.26	-0.13	0.52 ± 0.06	0.13	0.24	-0.15	0.36	-0.03
HD 26151	0.24	-0.09	0.42 ± 0.05	0.09	0.31	-0.02
HD 26794	0.07	-0.00	0.10 ± 0.03	0.03	0.25	0.18	0.15	0.08
HD 35854	-0.00	0.04	-0.03 ± 0.03	0.01	0.05	0.09	-0.07	-0.03
HD 77338	0.44	0.03	0.52 ± 0.04	0.11	0.33	-0.08
HD 82943	0.18	-0.05	0.25 ± 0.06	0.02	0.45	0.22	0.16	-0.07
HD 86249	0.15	0.03	0.12 ± 0.03	0.00	0.02	-0.10
HD 93800	0.44	-0.05	0.64 ± 0.04	0.15	-0.03	-0.52	0.46	-0.03
HD 177374	0.32	0.40	-0.01 ± 0.03	0.07	0.19	0.27
HD 181433	0.56 ± 0.04	0.15	0.42	0.01	0.44	0.03
HD 224230	0.10	0.18	-0.05 ± 0.03	0.02	-0.01	0.07	-0.06	0.03
Thick disk								
G 161-029	0.04	0.03	0.10 ± 0.09	0.08	0.10	0.09
BD-02 180	0.35	0.02	0.41 ± 0.04	0.08	0.60	0.27	0.30	-0.03
BD-05 5798	0.28	0.08	0.19 ± 0.04	-0.01	0.25	0.05
BD-17 6035	0.31	0.22	0.12 ± 0.04	0.03	0.26	0.17
CD-32 0327	0.09 ± 0.04	0.11	0.11	0.19
CD-40 15036	-0.01	0.02	-0.02 ± 0.07	0.00	-0.14	-0.01
HD 9424	0.17	0.05	0.17 ± 0.05	0.05	0.09	-0.03	0.10	-0.02
HD 10576	-0.01 ± 0.07	-0.03	0.25	0.23	0.00	-0.02
HD 13386	0.25	-0.11	0.41 ± 0.04	0.05	0.07	-0.29	0.30	-0.16
HD 15133	0.25	-0.21	0.59 ± 0.04	0.13	0.27	-0.19	0.37	-0.09
HD 15555	-0.11	-0.48	0.51 ± 0.04	0.14	0.35	-0.02	0.33	-0.04
HD 16905	0.23	-0.04	0.38 ± 0.04	0.11	0.28	0.01	0.26	-0.01
HD 25061	0.13	-0.05	0.23 ± 0.04	0.05	0.12	-0.06
HD 27894	0.25	-0.12	0.43 ± 0.04	0.06	0.32	-0.05	0.34	-0.03
HD 31827	0.46	-0.02	0.59 ± 0.05	0.11	0.02	-0.46	0.47	-0.01
HD 39213	0.59 ± 0.05	0.14	0.39	-0.06
HD 81767	-0.01	-0.23	0.22 ± 0.03	0.00	0.28	0.06	0.16	-0.06
HD 90054	0.31	0.02	0.31 ± 0.06	0.02	0.17	-0.12	0.22	-0.07
HD 94374	0.25	0.35	-0.08 ± 0.03	0.02	-0.04	0.06
HD 95338	0.06	-0.15	0.25 ± 0.04	0.04	0.06	-0.15	0.18	-0.03
HD 104212	0.11	-0.02	0.13 ± 0.07	0.00	0.35	0.22	0.07	-0.06
HD 107509	-0.05	-0.08	0.00 ± 0.07	-0.02	0.13	0.10	0.01	0.05
HD 120329	0.39	0.08	0.33 ± 0.06	0.02	0.29	-0.02
HD 143102	0.17 ± 0.06	0.01	0.17	0.01	0.10	-0.06
HD 148530	0.06	0.03	0.04 ± 0.05	0.01	0.32	0.29	0.07	0.04
HD 149256	0.40 ± 0.05	0.06	0.61	0.27	0.37	0.03
HD 149606	0.24	0.04	0.22 ± 0.04	0.02	0.40	0.20	0.17	-0.03
HD 149933	0.21	0.08	0.23 ± 0.05	0.10	0.10	-0.03	0.21	0.05
HD 165920	0.34	-0.02	0.42 ± 0.04	0.06	0.17	-0.19	0.29	-0.07

Table B.8 - continued.

Star	[C/H]	[C/Fe]	[Ni/H]	[Ni/Fe]	[O/H]	[O/Fe]	[Mg/H]	[Mg/Fe]
HD 168714	0.35	-0.13	0.62 ± 0.05	0.14	0.44	-0.04
HD 171999	0.30	0.01	0.33 ± 0.04	0.04	0.27	-0.02	0.24	-0.05
HD 179764	-0.02 ± 0.05	0.03	0.04	0.09	0.02	0.07
HD 180865	0.20	-0.01	0.28 ± 0.04	0.07	0.39	0.18	0.26	0.05
HD 181234	0.30	-0.15	0.55 ± 0.04	0.10	0.37	-0.08	0.44	-0.01
HD 196397	0.37	-0.01	0.46 ± 0.05	0.08	0.32	-0.06
HD 201237	-0.19	-0.19	0.03 ± 0.04	0.03	0.12	0.12	0.01	0.01
HD 209721	0.35	0.07	0.36 ± 0.05	0.08	0.17	-0.11	0.32	0.04
HD 211706	0.09	0.00	0.11 ± 0.08	0.02	0.02	-0.07
HD 218566	0.21	-0.07	0.39 ± 0.15	0.11	0.17	-0.11	0.12	0.10
HD 218750	0.22	0.05	0.21 ± 0.04	0.04	0.24	0.07
HD 221313	0.41 ± 0.04	0.10	0.52	0.21	0.33	0.02
HD 221974	0.39	-0.07	0.59 ± 0.04	0.13	0.40	-0.06	0.37	-0.09
HD 224383	-0.03	0.07	-0.10 ± 0.06	-0.01	-0.04	0.06
Intermediate population								
HD 8389	0.46	-0.12	0.71 ± 0.04	0.22	0.35	-0.23	0.45	-0.13
HD 9174	0.51 ± 0.06	0.10	0.55	0.14	0.33	-0.08
HD 12789	0.34 ± 0.06	0.07	0.44	0.17	0.14	-0.13
HD 30295	0.33	0.01	0.37 ± 0.04	0.05	0.34	0.02	0.33	0.01
HD 31452	0.25 ± 0.04	0.02	0.15	-0.08
HD 37986	0.34	0.04	0.35 ± 0.04	0.05	0.22	-0.08	0.26	-0.04
HD 39715	-0.10 ± 0.03	0.01	-0.13	-0.03
HD 43848	0.29	-0.14	0.53 ± 0.04	0.10	0.36	-0.07	0.38	-0.15
HD 86065	0.11	0.02	0.13 ± 0.04	0.04	0.17	0.08	0.09	-0.00
HD 87007	0.23	-0.06	0.39 ± 0.04	0.10	0.14	-0.15	0.31	0.02
HD 91585	0.28	0.03	0.34 ± 0.04	0.09	0.44	0.19	0.33	0.08
HD 91669	0.32	-0.12	0.54 ± 0.04	0.10	0.31	-0.13	0.38	-0.06
HD 182572	0.29	-0.19	0.52 ± 0.04	0.04	0.44	-0.04	0.44	-0.04
HD 196794	-0.02	-0.08	0.08 ± 0.04	0.02	0.14	0.08	0.00	-0.06
HD 197921	0.12	-0.10	0.30 ± 0.04	0.08	0.27	0.05	0.29	0.07
HD 213996	0.27	-0.06	0.39 ± 0.04	0.06	0.22	-0.11	0.30	-0.03
HD 214463	0.22	-0.12	0.43 ± 0.03	0.09	0.27	-0.07	0.28	-0.06

Table B.9 - Final abundances of Ca, Si and Ti.

Star	[Ca/H]	[Ca/Fe]	[Si/H]	[Si/Fe]	[Ti/H]	[Ti/Fe]
Thin disk						
HD 11608	0.33 ± 0.10	-0.06	0.40 ± 0.06	0.01	0.35 ± 0.09	-0.04
HD 26151	0.34 ± 0.04	0.01	0.35 ± 0.04	0.02	0.35 ± 0.09	0.02
HD 26794	0.11 ± 0.09	0.04	0.11 ± 0.05	0.04	0.15 ± 0.11	0.08
HD 35854	-0.05 ± 0.11	-0.01	-0.04 ± 0.05	-0.00	-0.10 ± 0.08	-0.06
HD 77338	0.34 ± 0.06	-0.07	0.47 ± 0.05	0.06	0.32 ± 0.08	-0.09
HD 82943	0.30 ± 0.05	0.07	0.26 ± 0.05	0.03	0.20 ± 0.07	-0.03
HD 86249	0.11 ± 0.10	-0.01	0.10 ± 0.05	-0.02	0.04 ± 0.09	-0.08
HD 93800	0.38 ± 0.10	-0.11	0.51 ± 0.05	0.02	0.42 ± 0.08	-0.07
HD 177374	0.04 ± 0.14	0.12	0.13 ± 0.05	0.21	-0.24 ± 0.09	-0.16
HD 181433	0.30 ± 0.13	-0.11	0.52 ± 0.05	0.11	0.37 ± 0.08	-0.04
HD 224230	-0.18 ± 0.20	-0.10	-0.14 ± 0.06	-0.07	-0.09 ± 0.11	-0.01
Thick disk						
G 161-029	0.00 ± 0.12	-0.01	0.05 ± 0.06	0.04	0.04 ± 0.12	0.02
BD-02 180	0.35 ± 0.04	0.02	0.34 ± 0.06	0.01	0.41 ± 0.11	0.08
BD-05 5798	0.16 ± 0.15	-0.04	0.14 ± 0.06	-0.06	0.19 ± 0.13	-0.01
BD-17 6035	0.06 ± 0.18	-0.03	0.10 ± 0.06	0.01	0.05 ± 0.17	-0.04
CD-32 0327	-0.02 ± 0.19	-0.01	0.03 ± 0.05	0.04	-0.01 ± 0.15	0.01
CD-40 15036	-0.02 ± 0.11	0.01	-0.03 ± 0.03	0.00	0.00 ± 0.12	0.03
HD 9424	0.12 ± 0.10	-0.00	0.16 ± 0.04	0.04	0.20 ± 0.09	0.08
HD 10576	-0.00 ± 0.11	-0.02	0.03 ± 0.05	0.00	0.04 ± 0.10	0.02
HD 13386	0.34 ± 0.08	-0.02	0.32 ± 0.05	-0.04	0.35 ± 0.09	-0.01
HD 15133	0.48 ± 0.10	0.02	0.44 ± 0.05	-0.02	0.51 ± 0.09	0.05
HD 15555	0.17 ± 0.08	-0.20	0.45 ± 0.05	0.08	0.27 ± 0.09	-0.10
HD 16905	0.24 ± 0.08	-0.03	0.36 ± 0.05	0.09	0.25 ± 0.09	-0.02
HD 25061	0.20 ± 0.09	0.02	0.17 ± 0.04	-0.01	0.18 ± 0.09	-0.00
HD 27894	0.32 ± 0.10	-0.05	0.41 ± 0.05	0.04	0.40 ± 0.10	0.03
HD 31827	0.45 ± 0.05	-0.03	0.55 ± 0.04	0.07	0.41 ± 0.09	-0.07
HD 39213	0.45 ± 0.05	-0.00	0.48 ± 0.04	0.03	0.50 ± 0.08	0.05
HD 81767	0.21 ± 0.09	-0.01	0.21 ± 0.05	-0.01	0.18 ± 0.11	-0.04
HD 90054	0.24 ± 0.15	-0.05	0.26 ± 0.05	-0.03	0.22 ± 0.08	-0.07
HD 94374	0.18 ± 0.09	0.28	-0.23 ± 0.04	-0.13	0.18 ± 0.08	0.28
HD 95338	0.14 ± 0.05	-0.07	0.19 ± 0.04	-0.02	0.17 ± 0.09	-0.04
HD 104212	0.13 ± 0.07	0.00	0.14 ± 0.04	0.01	0.14 ± 0.08	0.01
HD 107509	-0.03 ± 0.23	-0.06	0.03 ± 0.05	-0.00	0.02 ± 0.08	-0.00
HD 120329	0.26 ± 0.06	-0.05	0.34 ± 0.04	0.03	0.29 ± 0.09	-0.02
HD 143102	0.09 ± 0.06	-0.07	0.20 ± 0.04	0.04	0.13 ± 0.08	-0.03
HD 148530	0.04 ± 0.11	0.01	0.06 ± 0.04	0.03	0.04 ± 0.10	0.01
HD 149256	0.24 ± 0.08	-0.10	0.40 ± 0.05	0.06	0.34 ± 0.09	0.00
HD 149606	0.12 ± 0.14	-0.08	0.16 ± 0.05	-0.04	0.13 ± 0.10	-0.07
HD 149933	0.11 ± 0.12	-0.02	0.19 ± 0.04	0.06	0.13 ± 0.09	-0.00
HD 165920	0.33 ± 0.06	-0.03	0.40 ± 0.04	0.04	0.30 ± 0.08	-0.06

Table B.9 - continued.

Star	[Ca/H]	[Ca/Fe]	[Si/H]	[Si/Fe]	[Ti/H]	[Ti/Fe]
HD 168714	0.46 ± 0.12	-0.02	0.41 ± 0.04	-0.07	0.37 ± 0.09	-0.11
HD 171999	0.23 ± 0.10	-0.06	0.32 ± 0.04	0.03	0.20 ± 0.09	-0.09
HD 179764	-0.04 ± 0.06	0.01	0.08 ± 0.04	0.13	-0.10 ± 0.09	-0.05
HD 180865	0.21 ± 0.07	-0.00	0.24 ± 0.04	0.03	0.28 ± 0.10	0.07
HD 181234	0.48 ± 0.10	0.03	0.52 ± 0.04	0.07	0.49 ± 0.08	0.04
HD 196397	0.33 ± 0.09	-0.05	0.41 ± 0.05	0.03	0.36 ± 0.10	-0.02
HD 201237	0.10 ± 0.17	0.10	0.05 ± 0.07	0.05	0.07 ± 0.17	0.07
HD 209721	0.25 ± 0.12	-0.03	0.29 ± 0.04	0.01	0.26 ± 0.09	-0.02
HD 211706	0.09 ± 0.15	-0.00	0.09 ± 0.05	-0.00	0.10 ± 0.10	0.01
HD 218566	0.26 ± 0.09	-0.02	0.34 ± 0.08	0.06	0.24 ± 0.15	-0.04
HD 218750	0.14 ± 0.12	-0.03	0.23 ± 0.05	0.06	0.17 ± 0.09	-0.00
HD 221313	0.34 ± 0.13	0.03	0.31 ± 0.05	0.00	0.35 ± 0.11	0.04
HD 221974	0.40 ± 0.09	-0.06	0.47 ± 0.05	0.01	0.48 ± 0.10	0.02
HD 224383	-0.10 ± 0.13	0.00	-0.14 ± 0.04	-0.05	-0.02 ± 0.08	0.07
Intermediate population						
HD 8389	0.54 ± 0.10	-0.04	0.60 ± 0.05	0.02	0.57 ± 0.08	-0.01
HD 9174	0.36 ± 0.09	-0.05	0.50 ± 0.05	0.09	0.38 ± 0.10	-0.03
HD 12789	0.28 ± 0.05	0.01	0.31 ± 0.05	0.04	0.27 ± 0.08	0.00
HD 30295	0.33 ± 0.07	0.01	0.32 ± 0.04	0.00	0.30 ± 0.09	-0.02
HD 31452	0.19 ± 0.08	-0.04	0.23 ± 0.04	0.00	0.19 ± 0.09	-0.04
HD 37986	0.25 ± 0.04	-0.05	0.36 ± 0.04	0.06	0.27 ± 0.08	-0.03
HD 39715	-0.09 ± 0.11	0.01	-0.13 ± 0.06	-0.03	-0.14 ± 0.13	-0.04
HD 43848	0.35 ± 0.08	-0.08	0.40 ± 0.05	-0.03	0.37 ± 0.08	-0.06
HD 86065	0.03 ± 0.09	-0.06	0.11 ± 0.05	0.02	0.02 ± 0.10	-0.08
HD 87007	0.24 ± 0.09	-0.05	0.38 ± 0.05	0.09	0.23 ± 0.12	-0.06
HD 91585	0.23 ± 0.10	-0.02	0.29 ± 0.05	0.04	0.27 ± 0.10	0.02
HD 91669	0.41 ± 0.09	-0.03	0.48 ± 0.05	0.04	0.38 ± 0.12	-0.06
HD 182572	0.50 ± 0.05	0.02	0.46 ± 0.04	-0.02	0.50 ± 0.06	0.02
HD 196794	0.10 ± 0.07	0.04	0.04 ± 0.04	-0.03	0.08 ± 0.10	0.01
HD 197921	0.22 ± 0.11	0.00	0.24 ± 0.05	0.02	0.24 ± 0.10	0.02
HD 213996	0.34 ± 0.07	0.01	0.35 ± 0.05	0.02	0.35 ± 0.10	0.02
HD 214463	0.38 ± 0.11	0.04	0.32 ± 0.05	-0.02	0.32 ± 0.10	-0.02